

Element-specific detection of magnetization dynamics using Scanning Transmission X-ray Microscopy

Dissertation

zur Erlangung des akademischen Grades Dr. rer. nat.

vorgelegt bei der Fakultät für Physik der Universität Duisburg-Essen von

Thomas Feggeler

aus

Essen

Datum der Disputation: 20.11.2020

1. Gutachter: Prof. Dr. Heiko Wende

2. Gutachter: Prof. Dr. Hendrik Ohldag

“L'avenir, tu n'as point à le prévoir mais à le permettre.”

Antoine de Saint-Exupéry, *Citadelle* (1948)

Kurzfassung

Elementspezifische Detektion von Magnetisierungsdynamik mittels Scanning Transmission X-ray Microscopy

In dieser Arbeit wurde die Magnetisierungsdynamik von mikro- und nanometergroßen Proben elementspezifisch und orts aufgelöst (< 50 nm) mittels Scanning X-ray Microscopy detektierter ferromagnetische Resonanz (STXM-FMR) gemessen, die zeitaufgelöste Messungen < 20 ps ermöglicht.

STXM-FMR hat den Ursprung von Resonanzen in einer Py/Co-Disk/Streifen-Doppelschicht Mikrostruktur ($2,5 \mu\text{m}$ 30 nm/ $2 \mu\text{m}$ $0,5 \mu\text{m}$ 30 nm) gezeigt, die durch konventionelle ferromagnetische Resonanz (FMR) detektiert wurden. Es werden uniforme Resonanzen in Py und Co und eine austauschgekoppelte Resonanz beider Probenteile nachgewiesen. Die elementspezifischen Messungen an den Ni L_3 - und Co L_3 -Röntgenabsorptionskanten zeigten einen Drehimpulsübergang von Py auf Co und umgekehrt bei den jeweiligen Hauptresonanzen. Bei der gekoppelten Resonanz konnte ein erweiterter Präzessionskegel der Magnetisierung nachgewiesen werden. Durch eine Amplituden- und Phasenanalyse der STXM-FMR-Daten an der Co L_3 -Kante konnte eine inhomogene Anregung des Streifens aufgrund des Streufeldinflusses an den Streifenkanten aufgezeigt werden. Uniforme und nicht-uniforme Spinwellen wurden für einen einzelnen Py-Streifen ($5 \mu\text{m} \cdot 1 \mu\text{m} \cdot 30$ nm) und für zwei Streifen mit gleichen Abmessungen in T- und L-förmigen Geometrien mit STXM-FMR untersucht, welche gerichtete Oszillationen zeigen. Mikromagnetische Simulationen bestätigen dieses unerwartete Verhalten, welches auf die Streufeldverteilung zurückgeführt wird, die zu zusätzlichen Resonanzmoden an den Streifenkanten führt, wodurch ein Phasengradient der Magnetisierung erzeugt wird, der die gerichtete Oszillation der Spinwellen-Moden verursacht. STXM-FMR-Messungen von Yttrium-Eisen-Granat-Nanopartikeln zeigten eine Verteilung von Anregungen mit unterschiedlicher Phase im untersuchten YIG-Partikelagglomerat. Erstmals konnte die FMR von Segmenten einer bi-segmentierten Fe_3O_4 -Nanopartikelkette mit einer räumlichen Auflösung von < 50 nm elementspezifisch und orts aufgelöst gemessen werden.



Abstract

Element-specific detection of magnetization dynamics using Scanning Transmission X-ray Microscopy

In this thesis, the magnetization dynamics of micro- and nanometer-sized samples were element specifically and spatially resolved (< 50 nm) measured by Scanning Transmission X-ray Microscopy detected Ferromagnetic Resonance (STXM-FMR), which offers time-resolved measurements at < 20 ps.

STXM-FMR has clarified the origin of resonances in a Py/Co disk/stripe bilayer microstructure ($2.5 \mu\text{m} \cdot 30 \text{ nm} / 2 \mu\text{m} \cdot 0.5 \mu\text{m} \cdot 30 \text{ nm}$) detected by conventional Ferromagnetic Resonance (FMR). Uniform resonances in Py and Co and an exchange coupled resonance of both constituents are revealed. The element-specific measurements at the Ni L_3 and Co L_3 X-ray absorption edges showed an angular momentum transfer from Py to Co and vice versa at the Py and Co resonance, respectively. At the coupled resonance, an enhanced precession cone of the magnetization could be shown. Due to an amplitude and phase analysis of the STXM-FMR data at the Co L_3 edge, an inhomogeneous excitation of the stripe due to the stray field influence at the stripe edges could be revealed. Uniform and non-uniform spin waves have been investigated by STXM-FMR for a single Py stripe ($5 \mu\text{m} \cdot 1 \mu\text{m} \cdot 30 \text{ nm}$) and for two stripes with the same dimensions in T- and L- shaped geometries, showing a directed oscillatory behavior of the modes. These unexpected observations are confirmed by micromagnetic simulations. They are attributed to the stray field distribution, which results in the excitation of additional resonant modes at the stripe edges, which generate a phase gradient of the magnetization causing the spin wave modes' directed oscillation.

STXM-FMR measurements of Yttrium Iron Garnet nanoparticles revealed a distribution of excitations with different phase in the investigated YIG particle agglomerate. For the first time the resonant response of segments of a bi-segmented Fe_3O_4 nanoparticle chain with a spatial resolution of $< 50\text{nm}$ could be element-specifically and spatially resolved measured.



Declaration

Ich, Thomas Feggeler, reiche hiermit meine Dissertation mit dem Thema:

Element-specific detection of magnetization dynamics using Scanning Transmission X-ray Microscopy

zur Erlangung des akademischen Grades eines Doktors der Naturwissenschaften (Dr. rer. nat.) ein. Ich versichere hiermit, dass ich meine Dissertation selbstständig verfasst und in keinem weiteren Promotionsverfahren eingereicht habe. Es wurden keine anderen als die angegebenen Quellen und Hilfsmittel verwendet, alle wörtlich oder inhaltlich übernommenen Stellen sind durch Zitate angemessen kenntlich gemacht.

Duisburg, den 22. Juli 2020

Thomas Feggeler



Funding:

This work has been funded by German Research Foundation (DFG) grant OL513/1-1, Austrian Science Fund (FWF) grant I 3050-N36 and the University of Duisburg-Essen.

SLAC National Accelerator Laboratory facility usage:

Use of the Stanford Synchrotron Radiation Lightsource, SLAC National Accelerator Laboratory, is supported by the U.S. Department of Energy, Office of Science, Office of Basic Energy Sciences under Contract No. DE-AC02-76SF00515.

Acknowledgements

This thesis was done in collaboration with a multitude of collaborators and I'd like to point out the role of these people and express my appreciation and gratitude to everyone for their professional and moral support.

I'm very thankful to Dr. Katharina Ollefs, Prof. Dr. Heiko Wende, Prof. Dr. Michael Farle and Dr. Ralf Meckenstock, who gave me the opportunity to do my PhD thesis under their supervision in the DFG project OL513/1 / FWF project I 3050-N36. I'm very grateful to the German Research Foundation (DFG) and the Austrian Science Fund (FWF) for the financial support of the project. I like to thank our project collaborators Dr. Hendrik Ohldag from SLAC National Accelerator Laboratory Menlo Park, CA and Prof. Dr. Andreas Ney, Dr. Taddäus Schaffers, Santa Pile, Dr. Martin Buchner and Dr. Verena Ney from the Johannes Kepler University Linz, Austria for their continuing contribution to the joint project. I also like to thank C. Schöppner, who fabricated the Py/Co bilayer microstructure and took part in the STXM-FMR measurements as part of his PhD thesis. The in total five measurement beamtimes were performed by different teams, which are enumerated in the following table. I'd like to thank all participants for the productive and nice collaboration during these beamtimes.

April 2017:	February 2018	July 2018
R. Meckenstock D. Spoddig H. Ohldag A. Ney T. Schaffers M. Buchner	R. Meckenstock D. Spoddig H. Ohldag A. Ney T. Schaffers S. Pile	K. Ollefs H. Ohldag A. Ney V. Ney S. Pile
November 2018:	April 2019:	
H. Ohldag A. Ney S. Pile	R. Meckenstock H. Ohldag A. Ney V. Ney	

Table I: Teams of the joint measurement beamtimes at SLAC.

In the following I would like to express my personal gratitude and appreciation to all the people who supported me professionally and personally.

I'm very grateful to Dr. Katharina Ollefs, who led this project in an outstanding way. You supported me and my work all the time over the last years and always took

time to discuss about our data and the future plans of our project. Thank you for your ongoing enthusiasm and encouragements concerning our project and the everyday life.

My dear thanks go to Prof. Dr. Michael Farle, who continuously supported my work and gave me the opportunity to perform my research at his laboratories. I would like to thank him for his helpful guidance over all these years. I'm very thankful to him and Prof. Dr. Heiko Wende for continuing my employment during these times of COVID-19, which allowed me to finish my PhD thesis.

I'm very thankful to Prof. Dr. Heiko Wende, for his always ongoing support for my research and the helpful discussions about the measurement results. I like to express my gratitude for the opportunity to use his chemistry laboratory equipment for the preparation of the magnetotactic bacteria. I'm grateful to him for the extension of my work contract together with Prof. Dr. Michael Farle during the COVID-19 times.

I'm expressing my dear gratitude to Dr. Ralf Meckenstock. Your support and guidance over the many years gave me the opportunity to pursue my research and finally to do this PhD thesis. I'm grateful for all the hours you took your time for discussions and measurements at our labs here and at the beamtimes. Thank you for the wonderful time we have spent together in our office.

I'd like to thank Dr. Detlef Spoddig for your ongoing support and enthusiasm for my work. I learned from you the optical lithography for the fabrication of our micro-resonators and lots of technical details concerning the lab equipment, like the FMR spectrometers, I used over the years. I'm thankful that you were always there to support the sample preparations for the beamtimes, without your skills and knowledge the transfer of the magnetotactic bacteria to the micro-resonators would not have been possible.

I'm very grateful to Dr. Hendrik Ohldag, without your support at the beamline, none of our STXM-FMR measurements would have been possible. Your great support of

my research and our good discussions were essential for the success of our project and our joint publications.

I'd like to express my dear thanks to Prof. Dr. Michael Winklhofer, who greatly supports my research since the beginning of my Master thesis. I learned from you everything about magnetotactic bacteria and the sample preparation process. You have been always there to support me with knowledge and even measurement equipment, like the optical microscopes I used for the preparation of the bacteria samples.

My kind thanks go Benjamin Zingsem for his always present willingness to discuss about my research and the development of the color-coded phase and amplitude analysis. I'd like to thank him for the fruitful joint work on our Nature Communications paper and the connected research. I'm thankful to him for taking care of the organizational procedures to hand in our joint patent (together with Prof. Dr. Michael Farle and Irene Iglesias) on 360° domain walls.

I like to thank Prof. Dr. Andreas Ney for the fruitful collaboration in the years of our joint project. I'm grateful to him for taking care of all the administrative and organizational work, which had to be performed to organize our beamtimes. I'm thankful for the nice and fruitful hours of measuring and discussing during the beamtimes and for his support for the experiments.

I'm expressing my dear thanks to Santa Pile for the nice time we had during the last years and our many good discussions. I'm thankful to her for the preparation of the Py stripe samples. Due to these great samples our investigations on spin waves in these stripes were possible.

My thanks go to Dr. Taddäus Schaffers for the productive and nice time during the beamtimes and for his support for the performed experiments there.

I would like to thank Dr. Ulf Wiedwald for providing the YIG nanoparticles for our measurement and for his help in the micro-resonator sample preparation for these samples. I'm grateful for his ongoing interest in my research and for willingness to discuss about the results.

I'm very thankful to Dr. Sebastian Wintz for the support of our project with beam-times at the MAXYMUS beamline at BESSY II. Thank you for giving me the opportunity to measure at MAXYMUS again and again.

Many thanks to Prof. Dr. Mehmet Acet for the great discussions we had over the years and the nice time we spent at the MMM conference at Las Vegas. Your nearly infinite knowledge about materials is extraordinary.

I like to thank Dr. Marina Spasova for the professional and moral support during my PhD time. The discussions with you helped me to view my work with a very helpful different perspective.

I'm thankful to Philipp Kükenbrink for the manufacturing of the STXM-FMR sample holders and to Daniel Scholz for technical support.

I want to express my dear thanks to Sabina Grubba, Christiane Leuchtenberger, and Helga Mundt for their never-ending support in all administrative topics. Without this support doing science would not be possible!

I'm thanking Merve Felek for the fabrication of one batch of the used micro-resonators.

I like to thank Samira Webers and Lea Spieker for proof-reading my thesis. I appreciate your support very much.

I like to express my dear thanks to my friend Iuliia Novoselova. Thank you for your support and all the encouragements you gave to me over the time of writing and for the nice time we spent in the Farle Group.

I want to thank my dear friend Irene Iglesias for her constant support. Your strong belief in my work and me and your encouragements are just awesome, and I'm very grateful for the great time we had in the last months. I'm very glad and thankful for our friendship. Thanks to this friendship I could get to know Nico Rothenbach. I'm

very happy and grateful for your ongoing friendship and support. The times we all spent together in the last months was amazing! Many many thanks Nico!

I'm very grateful to had the chance of getting to know Dr. Anna Semisalova. You became a very close friend to me in the short time we know each other. Thank you so much for your always present wonderful friendship, support, and encouragement and that you always believed in me.

A very close friend, whom I met this year at Klosters, is Dr. Natalia Shkodich. Since February you gave me support and encouragement over the last months and I value our nearly daily chats so much. You are a wonderful friend and I'm very thankful to have got to know you.

I'm very thankful to my friend Marc Stevens for the great time we experienced in the last year in our group and at Klosters. Thank you very much for your moral support in the phase of writing my thesis. I value your friendship very much!

I cannot imagine the time before Tanja Strusch became one of my closest friends. Your never-ending support in all aspects of life is so great and outstanding and I want to express my dearest gratitude for you being such a wonderful friend! In the last months you encouraged and supported me every day, especially in times, which were not so easy. Thank you so much for your everlasting great friendship during all ups and downs.

I like to thank all members of the groups of Prof. Farle and Prof. Wende for the amazing and interesting years and their support.

I'm very thankful to Renate and Günter Stieglitz, who outstandingly supported me over so many years in such a great way. My dearest gratitude goes to my mother Margret Feggeler. Your unconditional support of my decisions in life and your encouragement to pursue my way made this PhD project possible. Thank you so much for being always there for me in all life situations and for your infinite trust and belief in me every single day. Without your guidance and support my life so far would not have been possible.



Abbreviations

CUDA	Compute Unified Device Architecture
ESR	Electron Spin Resonance
FMR	Ferromagnetic Resonance
GPU	Graphics Processing Unit
HSB	Hue Saturation Brightness
HSL	Hue Saturation Lightness
OOMMF	Object-Orientated-Micromagnetic-Framework
SEM	Scanning Electron Microscope
STXM	Scanning Transmission X-ray Microscopy
STXM-FMR	Scanning Transmission X-ray Microscopy detected Ferro- magnetic Resonance
TEM	Transmission Electron Microscopy
XDMR	X-ray Detected Magnetic Resonance
XFMR	X-ray detected Ferromagnetic Resonance
XMCD	X-ray Magnetic Circular Dichroism



Table of contents

1. Introduction	1
2. Fundamentals	5
2.1. Magnetic anisotropies	6
2.1.1. Magnetic shape anisotropy.....	7
2.1.2. Magneto crystalline anisotropy.....	8
2.2. Ferromagnetic Resonance (FMR).....	10
2.3. Spin waves	12
2.4. X-ray Magnetic Circular Dichroism (XMCD)	14
3. Experimental and computational techniques	19
3.1. Micro-resonator based ferromagnetic resonance.....	19
3.2. X-ray detected magnetic/ferromagnetic resonance (XDMR / XFMR).....	21
3.3. Scanning Transmission X-ray Microscopy detected ferromagnetic resonance ..	23
3.4. Color-coded fit analysis of STXM-FMR data	28
3.5. Micromagnetic simulations.....	30
4. Magnetization dynamics on micrometer sized sample structures.....	33
4.1. Magnetization dynamics of a Py/Co multilayer sample	33
4.1.1. The Py disk/Co stripe bilayer microstructure	33
4.1.2. Conventional FMR measurements of the sample	35
4.1.3. Element-specific magnetization dynamics of the Py/Co bilayer microstructure.....	36
4.2. Visualization of standing spin waves in different Py stripe arrangements.....	47
4.2.1. Sample overview	47
4.2.2. Micromagnetic simulations of the Py stripe ensembles	49
4.2.3. STXM-FMR experiment introduction	59
4.2.4. Py single stripe.....	60
4.2.5. Py T-shape stripe geometry	73
4.2.6. Py L-shape stripe geometry.....	85
4.2.7. Summary.....	96

5. Magnetization dynamics of nanometer sized sample structures.....	99
5.1. Visualization of the magnetization dynamics of Yttrium Iron Garnet nanoparticles	
99	
5.1.1. Sample overview	99
5.1.2. Ferromagnetic Resonance measurement of the YIG sample	100
5.1.3. STXM-FMR measurements of the YIG sample	101
5.2. STXM-FMR measurements of nanoparticle chains in bacteria Magnetospirillum	
Magnetotacticum	105
5.2.1. Magnetospirillum Magnetotacticum	105
5.2.2. Sample preparation	107
5.2.3. STXM-FMR measurements of the triple chain magnetosome ensemble	110
5.2.4. Micromagnetic simulations of the triple chain magnetosome ensemble.....	113
5.2.5. STXM-FMR measurements of a single bi-segmented magnetosome chain	117
5.2.6. Micromagnetic simulations of the single bi-segmented magnetosome chain	119
6. Conclusion and outlook	125
7. Appendix.....	129
7.1. Equations to calculate the demagnetization factors for rectangular ferromagnetic	
samples	129
7.2. Tabular overview on other spatially- and/or time resolved magnetization	
detection methods	133
7.3. Complete dataset of the presented STXM-FMR measurements.....	135
7.4. Micromagnetic simulations of the Py stripe arrangements.....	139
7.4.1. Averaged free energy densities of the L- shaped Py stripe arrangement	139
7.5. STXM-FMR images of the Py stripe arrangements	141
7.5.1. Single Py stripe	141
7.5.2. T-shaped sample geometry	146
7.5.3. L-shaped sample geometry	148
8. List of figures.....	151
9. List of tables.....	165
10. List of references	167
11. List of publications and conference contributions	189

1. Introduction

The challenges encountered in the development of computer and information technology, e. g. heat dissipation and power consumption [1], require new technological approaches to overcome these limitations. The use of spins as information units is proposed in spintronics and magnonics [2-5]. Chumak et al. have successfully demonstrated the functionality of magnon based logic devices, showing the first magnon based transistor [6]. Further investigations are reported in e. g. [7, 8]. The use of magnetic nanoparticles for soliton based logic devices was first suggested in [9] and further investigated in e. g. [10]. A magnon based approach of realizing logic devices using magnetic nanoparticles, which are naturally grown inside magnetotactic bacteria, was introduced in [11]. Here, the magnon dispersion can be manipulated by changing the nanoparticles' arrangement within the body of the bacteria, which can be achieved by modifying the DNA of the bacteria [11].

The development in these fields requires to understand the static and dynamic properties of the magnetization in such systems. Standard devices to measure the field- and temperature-dependent magnetization are Vibrating Sample Magnetometer (VSM) [12] and Superconducting Quantum Interference Device (SQUID) [13]. A standard technique to probe dynamic magnetization properties is Ferromagnetic resonance (FMR) [14] (chapter 2.2). To measure samples with a small amount of material, e. g. magnetic nanoparticles, FMR based on so-called micro-resonators is used [15-18]. The conventional FMR measurement technique lacks spatial resolution in the micro- and nanometer scale. This makes it impossible to assign the resonant response to single particles or elements, which is needed to understand and control the dynamic behavior e. g. of spintronic devices and magnetic nanoparticles used for computational applications [9-11], as well as for biomedical [19-22] and nano-mechanical [23, 24] applications. Micromagnetic simulations [25-29] have proven to be a valuable addition to conventional FMR measurements (see e. g. chapter 4, 5.2 and [11, 30]), allowing to simulate the dynamic excitation of a micro- or nanostructured sample and extract its spatial dependent information, e. g. [11].

For the experimental visualization of magnetization dynamics several spatially resolved techniques are available, differing in their advantages. Brillouin Light Scattering (BLS) [31, 32] is a non-element-specific technique allowing time-resolved measurements in the nanoseconds regime with a spatial resolution of ~ 250 nm (microBLS [32]) and < 55 nm with additional near field optics [31]. Time-resolved Magneto-optical Kerr-Effect (TR-MOKE) offers no element-specificity, but high time resolutions in the ps to fs regime [33]. The spatial resolution is < 300 nm and < 50 nm with near field optics [33]. Scanning Electron Microscopy with Polarization Analysis (SEMPA) and Spin-Polarized Low-Energy Electron Microscopy (SPLEEM) offer non-element specific measurements of the magnetization with a spatial resolution of ≥ 3 nm (SEMPA) [34] and 10 nm to 20 nm (SPLEEM) [35]. The time resolution is in the several hundreds of ps regime for SEMPA [34] and in the seconds regime for SPLEEM [36]. The non-element specific Ultrafast Lorentz Microscopy offers a spatial resolution on the atomic length scale, and the time-resolved detection of excitations in the MHz regime was demonstrated in [37]. Femtosecond Lorentz Microscopy with > 100 nm spatial resolution with a time resolution of 700 fs was shown in [38]. A new approach detecting FMR excitations (up to the X-band [39] regime) with ps time resolution using a Transmission Electron Microscope was developed by B. Zingsem in his PhD project [40]. The current instrument offers nanometer spatial resolution, which was demonstrated on Fe_3O_4 nanoparticles inside a magnetotactic bacterium [40]. The work is not published as of July 2020.

An element-specific pump-probe technique with a time resolution down to 10 ps is X-ray excited Photoemission Electron Microscopy (X-PEEM) [41]. The detection of excitations in the low GHz regime (1.25 GHz in [41]) is demonstrated in [41]. The spatial resolution is < 10 nm using UV excitations (PEEM) [42]. FMR excitations up to 15 GHz of periodic sample arrangements can element-specifically be probed by X-ray Diffractive Ferromagnetic Resonance (DFMR) with ≤ 1 nm spatial resolution and ps time resolution [43].

A tabular overview of several spatially and in part time-resolved techniques for the detection of the magnetization is given in the appendix in chapter 7.2.

In this work the element-specific, time (≥ 17 ps) and spatially (< 50 nm) resolved technique of Scanning Transmission X-ray Microscopy detected Ferromagnetic Resonance (STXM-FMR) [30, 44-48] is used, which combines high spatial and temporal resolution and allows to detect continuous wave excitations of the magnetization up to 10 GHz in periodic and non-periodic micro- and nanostructures (STXM mapping) [44]. As for X-PEEM the element specificity is achieved due to the use of the X-ray Magnetic Circular Dichroism (XMCD) effect, making possible the characterization of multimaterial sample systems e. g. in the scope of the research on spin valves [49-51] or magnetocaloric materials [52].

In the field of spintronic spin currents in multimaterial devices are investigated e. g. [2, 3, 53, 54]. In this thesis this topic is addressed by STXM-FMR measurements on a prototype Permalloy (Py)/Cobalt (Co) disk/stripe bilayer microstructure to examine the coupling and angular momentum transfer behavior of such a multimaterial systems (chapter 4.1) [48].

To understand the influence of magnetic dipolar coupling on uniform- and non-uniform spin waves, such excitations were investigated by STXM-FMR in micrometer-sized Py stripe ensembles arranged as a single stripe and in T- and L-shape geometries consisting of two stripes (chapter 4.2). Micromagnetic simulations were exploited to elucidate the stray field influence on the oscillation of the experimentally observed spin wave modes. The measurement and simulation data were published in part in [30].

To demonstrate a first proof of nanometer scale resolution of STXM-FMR, the resonant response of a cluster of Yttrium Iron Garnet (YIG) nanoparticles was measured. The findings are shown in chapter 5.1.

The investigations on biomagnonic computing presented in [11] opened the pathway to the research of magnonic logic devices based on biologically produced nanoparticle ensembles with different arrangements. STXM-FMR offers the needed spatial and time resolution for the development of such logic devices operating in the GHz regime. This is proved by the first element-specific, spatially, and time resolved

measurements of FMR of Fe_3O_4 nanoparticle chains situated within magnetotactic bacteria. The investigations are presented in chapter 5.2.

As the gathered STXM-FMR and micromagnetic datasets are too numerous to be presented in total within this thesis' main body, these findings are shown in the appendix (chapter 7). The fundamental physical concepts and the elucidation of the experimental techniques are presented in chapter 2 and 3.

2. Fundamentals

This chapter summarizes the contributions of magnetic anisotropies and magnetic interactions to the free energy density of a sample system, followed by descriptions of ferromagnetic resonance, and the X-ray magnetic circular dichroism effect. For detailed descriptions of magnetic interactions like spin-orbit coupling [14, 55-57], magnetic dipolar interaction [56], and magnetic exchange interaction [58-60], the reader is directed to the corresponding here given literature. The used coordinate system is shown in Figure 1. The angular dependencies of the magnetization, as shown in Figure 1, also can be described in the framework of directional cosines, which are defined as [56]:

$$\begin{aligned}\alpha_1 &= \sin \theta \cos \phi \\ \alpha_2 &= \sin \theta \sin \phi \\ \alpha_3 &= \cos \theta\end{aligned}\tag{1}$$

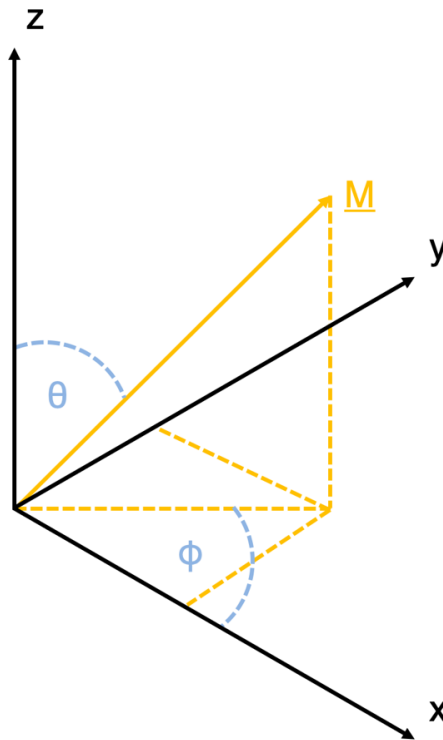


Figure 1: Coordinate system and angular dependencies of the magnetization used in this work. The in-plane rotation angle of the magnetization \underline{M} is denoted as ϕ , while the out-of-plane rotation angle is denoted as θ . Figure redrawn from [56].

2.1. Magnetic anisotropies

Due to the coupling of the magnetic moments $\underline{\mu}$ by magnetic exchange interaction in ferro-, ferri- and antiferromagnetic materials [58-60], the magnetization \underline{M} is the investigated quantity in such materials. It is defined with the volume V as [57]:

$$\underline{M} = \frac{\sum \underline{\mu}}{V} \quad (2).$$

The magnetization prefers its orientation into certain so-called easy directions, which are defined e. g. by the crystallographic axis of a sample or its shape [56]. By applying an external magnetic field \underline{B}_{Ext} , \underline{M} can be rotated into arbitrary directions depending on the field strength necessary to overcome the corresponding anisotropy energy or anisotropy field, respectively. The so-called effective magnetic field \underline{B}_{Eff} , combines the contributions of magnetic anisotropies \underline{B}_{Anis} , the demagnetization field \underline{B}_{Demag} , high-frequency magnetic excitations \underline{b}_{hf}^* and other magnetic interactions \underline{B}_{IA} (e. g. the antisymmetric exchange called Dzyaloshinskii–Moriya interaction (DMI) [61, 62]):

$$\underline{B}_{Eff} = \underline{B}_{Ext} + \underline{b}_{hf} + \underline{B}_{Demag} + \underline{B}_{Anis} + \underline{B}_{IA} \quad (3).$$

The statistical canonical ensemble is used to describe the energy of the designated sample systems [63]. It defines the total differential of the free energy density dF with the total differentials of the internal energy dU , the entropy dS , and the volume dV , together with the temperature T and the ambient pressure p as [63]:

$$\begin{aligned} dF &= \underbrace{dU}_{Tds - pdV + \underline{B}_{Eff}d\underline{M}} - TdS - SdT - pdV \\ &= -pdV + \underline{B}_{Eff}d\underline{M} - SdT \end{aligned} \quad (4).$$

In the case of no volume change and a constant temperature equation (4) can be written as [63]:

* Dynamic quantities are indicated by small letters in this thesis.

$$dF = \underline{B}_{\text{Eff}} d\underline{M} \quad (5).$$

The typical way to describe the different magnetic contributions of a corresponding sample system uses free energy density terms. Using the term F_{Zeeman} [57] to express the influence of an external magnetic field, equation (3) can be rewritten as [14]:

$$F = \frac{F_{\text{Zeeman}}}{-\underline{B}_{\text{Ext}} \underline{M}} + F_{\text{hf}} + F_{\text{Demag, Shape}} + F_{\text{Anis}} + F_{\text{IA}} \quad (6).$$

For the free energy density terms above the angular dependencies of the magnetization (Figure 1) are described with the directional cosines (chapter 2) [56].

2.1.1. Magnetic shape anisotropy

The magnetic shape anisotropy originates in the magnetic dipolar interaction and is governed by the shape of the sample, resulting in preferred directions of the magnetization, with the special case of spherical bodies, which show an isotropic behavior of \underline{M} [56]. From the poles at the edges of a sample, a stray field is formed (Figure 2), while inside the sample a demagnetization field is generated, which points into the opposite direction of the orientation of \underline{B} [57]. To minimize the internal energy magnetic domains are formed in the body, which minimize the stray field (Figure 2) [57].

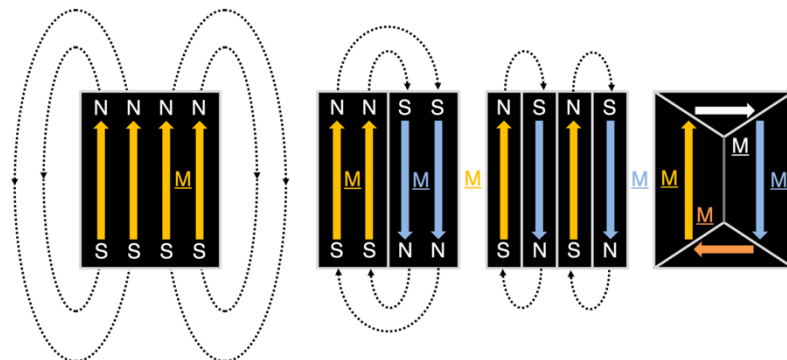


Figure 2: Visualization of the minimization of the stray field and the formation of magnetic domains. Figure adapted and redrawn from [57].

Due to the shape of a sample, the magnetization aligns along preferred directions, e. g. along the long edge of the schematically displayed sample in Figure 2. The influence of the sample shape on the demagnetization field $\underline{B}_{\text{Demag}}$ is defined by the demagnetization tensor \underline{N} [56]:

$$\underline{N} = \begin{pmatrix} N_1 & 0 & 0 \\ 0 & N_2 & 0 \\ 0 & 0 & N_3 \end{pmatrix} \quad (7).$$

A perfectly spherical body has the relation $N_1 = N_2 = N_3 = 1/3$, showing no anisotropy behavior [56]. For many samples an ellipsoidal approximation of the shape can be used, as shown for a variety of aspect ratios in [64]. Aharoni derived an analytical expression for the demagnetization factors of rectangular ferromagnetic prisms in [65]. The equations are presented in the appendix in chapter 7.1. With equation (7) the free energy density is written as [56, 66]:

$$F_{\text{Demag, Shape}} = \frac{1}{2V} \int \underbrace{\mu_0 \underline{M} \underline{N} \underline{M}}_{-\underline{B}_{\text{Demag}}} dV \quad (8)$$

where μ_0 is the magnetic permeability of the vacuum. Equation (8) can be rewritten using the definitions in equation (1) [56]:

$$F_{\text{Demag, Shape}} = \frac{1}{2V} \int (N_1 \alpha_1^2 + N_2 \alpha_2^2 + N_3 \alpha_3^2) \mu_0 \underline{M}^2 dV = \frac{\mu_0}{2} \underline{M} \underline{N} \underline{M} \quad (9).$$

2.1.2. Magneto crystalline anisotropy

The magneto crystalline anisotropy is governed by the spin-orbit interaction e. g. [55-57] and causes the orientation of the magnetization along certain preferred crystallographic directions. In case of a uniaxial magneto crystalline anisotropy the free energy density is defined with the uniaxial anisotropy constants K_{Uj} as [14]:

$$F_{\text{uniaxial}} = K_{U0} + K_{U2} \alpha_3^2 + K_{U4} \alpha_3^4 + K_{U6} (\alpha_1^4 + \alpha_2^4) + \dots \quad (10).$$

The cubic magneto crystalline anisotropy is written with the cubic anisotropy constants K_j as [14, 56, 57]:

$$F_{\text{cubic}} = K_0 + K_4(\alpha_1^2\alpha_2^2 + \alpha_1^2\alpha_3^2 + \alpha_2^2\alpha_3^2) + K_6(\alpha_1^2\alpha_2^2\alpha_3^2) + \dots \quad (11)$$

using the nomenclature defined in [67].

2.2. Ferromagnetic Resonance (FMR)

For a detailed description of ferromagnetic resonance the reader is directed to Vonsovskii [14] and Gilbert [68]. The magnetization \underline{M} is excited by an applied high-frequency continuous wave magnetic field \underline{b}_{hf} in the form of microwaves, which is polarized with an angle of 90° to a static magnetic bias field [14]. In resonance, \underline{b}_{hf} is absorbed by the sample [14]. For the mathematical description a classical approach of a precessing magnetization around the effective magnetic field \underline{B}_{eff} is used [14]. Interactions of the magnetic moments between each other and with the sample material itself cause a damped precession [14]. This model is expressed by the Landau-Lifshitz equation [14, 69], which is formulated with the damping term derived by Gilbert [68] in equation (12):

$$\frac{d\mathbf{M}}{dt} = -\gamma(\mathbf{M} \times \mathbf{B}_{eff}) + \frac{\alpha}{M} \left(\mathbf{M} \times \frac{d\mathbf{M}}{dt} \right) \quad (12)$$

with the gyromagnetic ratio γ . The damping parameter α using the damping frequency λ [14] is specified as [68]:

$$\alpha = \frac{\lambda}{\gamma M} \quad (13).$$

The resonance frequency ω_r , at which the resonant absorption of the high-frequency magnetic field occurs, is given with θ_0 , as the angle of the orientation of \underline{B}_{eff} , in equation (14) [14]:

$$\omega_r = \frac{\gamma \sqrt{1 + \alpha^2}}{M \sin \theta_0} \sqrt{\frac{\partial^2 F}{\partial \theta^2} \frac{\partial^2 F}{\partial \phi^2} \left(\frac{\partial^2 F}{\partial \theta \partial \phi} \right)^2} \quad (14).$$

The resonance linewidth is defined in [14] as:

$$\Delta\omega = \frac{d\omega}{dB} \Delta B = \frac{\alpha\gamma}{M} \left(\frac{\partial^2 F}{\partial \theta^2} + \frac{\partial^2 F}{\partial \phi^2} \frac{1}{\sin^2 \theta_0} \right) \quad (15).$$

The absorption of the high-frequency magnetic field in ferromagnetic resonance is described by the imaginary part of a component of the high frequency susceptibility tensor $\underline{\chi}$ [14]:

$$\underline{\chi} = \begin{pmatrix} \chi_{xx} & i\chi_{xy} & 0 \\ -i\chi_{yx} & \chi_{yy} & 0 \\ 0 & 0 & 0 \end{pmatrix} \quad (16).$$

It can be shown that the absorbed microwave power p_{hf} is proportional to the imaginary part of a component of $\underline{\chi}$, depending on the geometry of the experiment (see chapter 3.1). Therefore, one employs the complex Poynting theorem, which defines the complex conjugated current density \underline{j}^* of the microwave [70]. It includes the complex Poynting vector \underline{S} , the sample volume V and the electric and magnetic energy densities ω_e and ω_m , with the electric field vector \underline{e} , the complex conjugated electric flux density \underline{d}^* , the high-frequency magnetic flux density \underline{b}_{hf} and the complex conjugated magnetic field vector \underline{h}^* [70]:

$$\frac{1}{2} \int \underline{j}^* \underline{e} d^3r = -2i\omega \int \left(\underbrace{\frac{1}{4}(\underline{e} \underline{d}^*)}_{\omega_e} - \frac{1}{4}(\underline{b}_{hf} \underline{h}^*) \right) d^3r - \oint \underline{S} \underline{n} da \quad \text{with} \quad \underline{S} = \frac{1}{2}(\underline{e} \times \underline{h}^*) \quad (17).$$

$-2i\omega V(\omega_e - \omega_m)$

For the absorption of the high frequency magnetic field follows in general:

$$p_{hf} = \text{Re} \left(\frac{i\omega V}{2} \omega_m \right) = \text{Re} \left(\frac{i\omega V}{2} \underline{b}_{hf} \underline{h}^* \right) = \text{Re} \left(\frac{i\omega V}{2} \underbrace{\mu_0 (\underline{\chi} + 1)}_{\underline{b}_{hf}} \underline{h} \underline{h}^* \right) \quad (18).$$

The proportionality of p_{hf} to the imaginary part of a component χ_{jj} of $\underline{\chi}$ can be shown by rewriting equation (18) as:

$$p_{hf} = \text{Re} \left(\frac{i\omega V \mu_0}{2} (\chi'_{jj} - i\chi''_{jj} + 1) h^2 \right) = \frac{\omega V \mu_0 h^2}{2} \chi''_{jj}. \quad (19).$$

Taking into account the high frequency magnetization component $\underline{m}_{\text{hf}}$, which slightly pushes the magnetization away from the direction of the saturation magnetization \underline{M}_s [14], \underline{M} can be written as:

$$\underline{M} = \underline{M}_s + \underline{m}_{\text{hf}} e^{i\omega t} \quad \text{with} \quad \underline{m}_{\text{hf}} = \frac{1}{\mu_0} \underline{\chi} \underline{b}_{\text{hf}} \quad \text{and} \quad |\underline{m}_{\text{hf}}| \ll |\underline{M}_s| \quad (20).$$

2.3. Spin waves

Dynamically excited dipolarly or exchange coupled magnetic moments respond to the excitation with a coupled oscillation of these moments [71]. This kind of oscillation is called spin wave [57]. Having its energy is quantized a spin wave can be viewed as quantum mechanical quasi-particle with the name magnon [71]. Depending on whether exchange or magnetic dipolar coupling are the predominant origin of the spin wave, one differs exchange- and dipolarly coupled (magnetostatic) spin waves, respectively [57]. In a simple model, which regards the spin as a vector quantity, each spin-vector \underline{s} of an ensemble of spins is connected to a magnetic moment $\underline{\mu}_s$ [57]:

$$\underline{\mu}_s = -g_s \mu_B \frac{\underline{s}}{\hbar} \quad (21).$$

Here g_s is the spin g -factor, μ_B the Bohr magneton and \hbar the Planck constant divided by 2π . The angular momentum \underline{l} of an electron is defined by [57]:

$$\underline{\mu}_l = -g_l \mu_B \frac{\underline{l}}{\hbar} \quad (22)$$

where \underline{l} is the angular momentum and g_l its g -factor [57]. Under Russel-Saunders coupling [57] the magnetic moment of an atom is then written as [57]:

$$\mu_i = -g_j \mu_B \frac{J_i}{\hbar} \quad (23)$$

with the total angular momentum [57]:

$$\underline{j} = (\sum_i \underline{s}_i) + (\sum_i \underline{l}_i) \quad (24).$$

The basic description of an exchange coupled spin wave uses a model of a linear arrangement of spins with the total exchange energy E_{Exch} of all constituents defined as (A : exchange constant) [57]:

$$E_{\text{Exch}} = \frac{A}{\hbar^2} \sum_{i=1}^n \underline{s}_i (\underline{s}_{i-1} + \underline{s}_{i+1}) \quad (25).$$

For such a chain a dispersion relation can be derived from this equation describing the precessional motion of the spins with a phase, shifted by $k \cdot d$ (k : one dimensional wave vector, d distance) [57]:

$$\omega = \frac{g_s \mu_B B_{\text{Eff}}}{\hbar} + \frac{2 A s}{\hbar^2} (1 - \cos(k d)) \quad (26).$$

An in-phase precessional motion is given for the case $k = 0$ [57], describing a so-called uniform spin wave mode [71]. The three-dimensional description using the atomic lattice vectors \underline{r}_i is given as [57]:

$$\omega = \frac{g_s \mu_B B_{\text{Eff}}}{\hbar} + \frac{2 A s}{\hbar^2} \sum_{i=0}^n (1 - \cos(\underline{k} \cdot \underline{r}_i)) \quad (27).$$

For magnetostatic spin waves the general dispersion relation is defined as [71]:

$$\omega = \left((-\gamma B_{\text{eff}}) \left((-\gamma B_{\text{eff}}) + (-\gamma \mu_0 M_s) \sin^2(\theta) \right) \right)^{\frac{1}{2}} \quad (28)$$

with the propagation angle θ regarding the direction of B_{Eff} [71]. This equation can be expanded to include exchange coupling by adding the exchange term $A \cdot k^2$ [71]:

$$\omega = \left((-\gamma B_{\text{eff}} + (-\gamma \mu_0 M_s) A k^2) \left((-\gamma B_{\text{eff}}) + (-\gamma \mu_0 M_s) (A k^2 + \sin^2(\theta)) \right) \right)^{\frac{1}{2}} \quad (29).$$

For large $A \cdot k^2$ the spin wave is governed by exchange coupling [71], while for $A \cdot k^2 \ll 1$ results a magnetostatic spin wave governed by magnetic dipolar coupling [71].

Kittel theoretically described in 1958 the excitation of standing exchange and dipolar coupled non-uniform spin wave modes by a homogeneous high-frequency magnetic field, as a result of boundary conditions assuming the surface magnetic moments being pinned by surface anisotropy [72]. A theoretical framework to calculate standing spin waves in ferromagnetic thin films was presented by Hartwell in [73]. The first experiments confirming Kittel's theory were performed on Permalloy (Py) thin films in 1958 by Seavey and Tannenwald in [74]. A pinning caused by magnetic dipolar interaction due to the influence of an inhomogeneous demagnetization field at the edge sides of rectangular geometries is described in [75]. The excitation of standing spin waves is expected for the Py stripe samples measured by STXM-FMR. The results are presented in chapter 4.2.

2.4. X-ray Magnetic Circular Dichroism (XMCD)

The alignment and the size of magnetic moments can be probed by X-ray magnetic circular dichroism (XMCD) [76]. A necessary condition is a parallel orientation of the magnetic moments, as the XMCD effect cancels out for antiparallel spin arrangements [76]. The highest magnitude of XMCD is achieved in parallel/antiparallel orientation of the magnetic moments with respect to the angular momentum of the incident X-rays [76]. In the measurements performed in this thesis circularly polarized X-rays are measured after they were transmitted through the sample. The X-ray absorption intensity I in a transmission experiment with a uniform absorption of the X-rays with energy $E_{X\text{-ray}}$ is defined with the intensity before the transmission I_0 , the X-ray absorption coefficient μ_A , the X-ray absorption cross-section, the atomic number density ρ_A and the sample thickness d as [76]:

$$I = I_0 e^{-\mu_A(E_{X\text{-ray}})d} = I_0 e^{-\rho_A \sigma_{\text{Abs}} d} \quad (30).$$

The absorption of X-rays by electrons at the core energy levels, as schematically illustrated in Figure 3, results in so-called X-ray absorption edges [77].

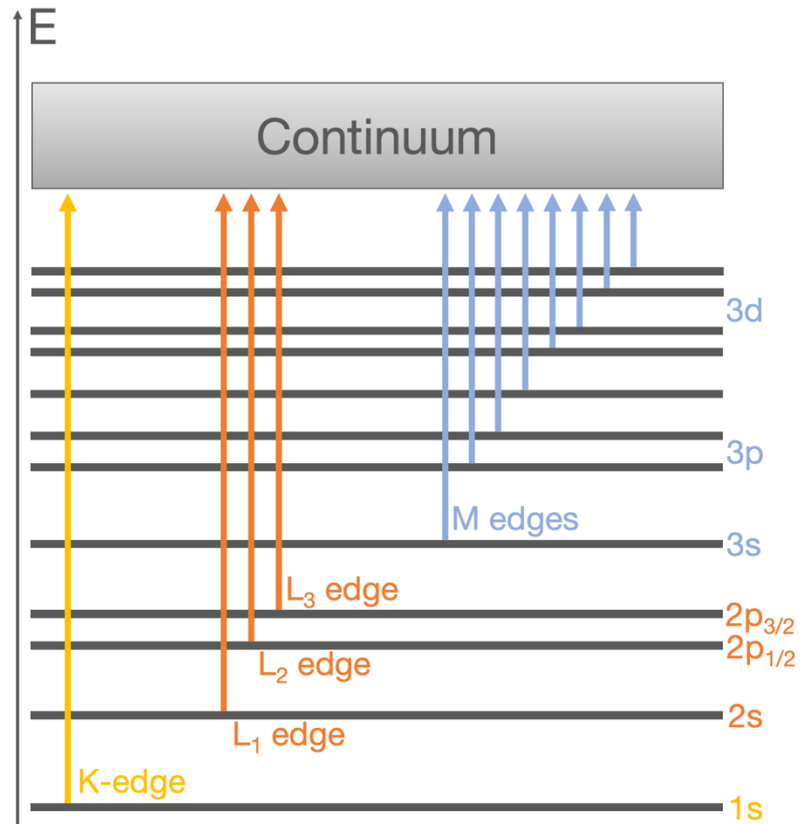


Figure 3: Schematic representation of X-ray absorption edges. As the experiments in this thesis are performed at the L_3 edge, the L edges are highlighted in the figure. Figure adapted from [77].

The X-ray absorption cross-section and therefore the X-ray absorption coefficient is proportional to the transition probability from an initial energy state to the final state. The transition probability T per unit time is given by [76]:

$$T = \frac{2\pi}{\hbar} \left| \langle \psi_{\text{fin}} | H | \psi_{\text{init}} \rangle + \sum_n \frac{\langle \psi_{\text{fin}} | H | \psi_n \rangle \langle \psi_n | H | \psi_{\text{init}} \rangle}{E_{\text{init}} - E_n} \right|^2 \delta(E_{\text{init}} - E_{\text{fin}}) \rho(E_{\text{fin}}) \quad (31)$$

where $\psi_{\text{init},n,\text{fin}}$ are the initial, intermediate and final states, $E_{\text{init},n,\text{fin}}$ are the corresponding energies and ρ_{fin} is the density of final states [76]. H is the Hamilton operator which is defined for X-ray absorption as [76]:

$$H = \frac{e}{m} \underline{p} \underline{A} \quad \underline{A} = \sigma_{+/-} A_0 e^{ikr} \quad (32).$$

Here e is the electron charge, \mathbf{p} is the electron momentum vector and \mathbf{A} the vector potential [76, 78], which is defined as a plane wave using the X-ray photon polarization $\sigma_{+/-}$, the amplitude A_0 , the wave vector \mathbf{k} and the position vector \mathbf{r} [78]. With the approximation of the transition of electric dipoles the corresponding selection rules for the states $|\psi\rangle$ defined by the quantum numbers n (principal quantum number), l (angular momentum quantum number), m_l (magnetic quantum number), s (spin quantum number) and m_s (secondary spin quantum number) can be derived from these equations [76]:

$$\begin{aligned} \Delta l &= \pm 1 \\ \Delta m_l &= 0, \pm 1 \\ \Delta s &= 0 \\ \Delta m_s &= 0 \end{aligned} \tag{33}.$$

The following description of the XMCD effect in this chapter uses the two-step model [79-81] and follows the descriptions in [79]. The angular momentum of circularly polarized X-ray photons is transferred to core energy level electrons and results in an excitation of these, influencing the orbital momentum and/or the spin of the corresponding electron [79]. The splitting of the total angular momentum to orbital momentum and spin is governed by spin-orbit coupling, which is an essential requirement for a spin polarization of the excited electrons [79]. The spin polarization depends on the helicity of the X-ray photons and the composition of the total angular momentum quantum number j due to spin-orbit coupling, which is shown here for the L_2 and L_3 X-ray absorption edges [79]:

$$L_2 \text{ edge: } j=l-s \qquad L_3 \text{ edge: } j=l+s \tag{34}$$

A visualization of the excitation process from the $-2p_{1/2}$ and $-2p_{3/2}$ energy levels to the d-states is depicted in Figure 4. An excitation from the $-2p_{1/2}$ energy level results in an expectation value $+3/4$ of the l_z component of the angular momentum vector and in an expectation value of $-1/2$ of the σ_z component of the spin polarization, which are both oriented parallel to the wavevector $\mathbf{k} = (0, 0, k_z)$ of the incident X-rays [79]. For excitations from the $-2p_{3/2}$ energy level $\langle l_z \rangle$ and $\langle \sigma_z \rangle$ are $+3/4$ and

$1/4$ respectively [79]. The transition of these electrons at the core energy level depends on the number of empty spin-up and spin-down d-states located at an energy closely higher than the Fermi energy [79]. Under the circumstance of a spin polarization at the d-states being oriented along the direction of the k-vector of the X-rays, left circularly polarized X-rays are stronger absorbed at the L_3 absorption edge, while less absorption is observed at the L_2 absorption edge and vice versa for right circularly polarized X-rays, when comparing these processes to the absorption of unpolarized X-ray radiation [79].

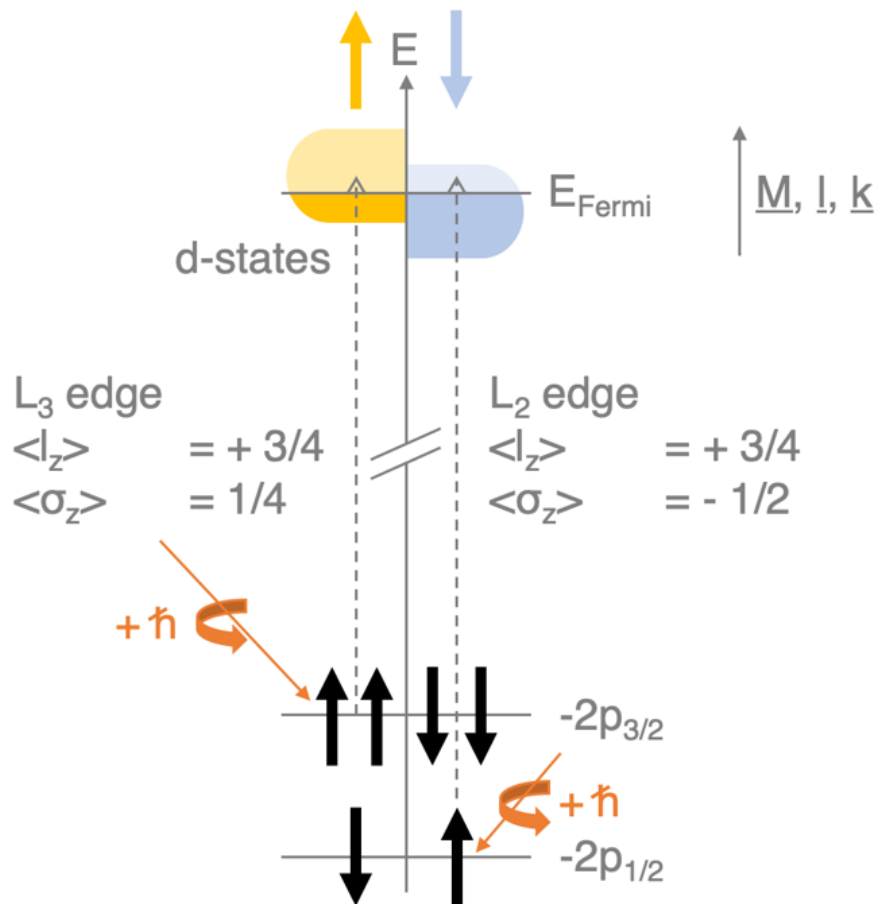


Figure 4: Schematic representation of excitations at the L_2 and L_3 edge. The “-” sign denotes the odd parity of the term symbols. Figure redrawn and adapted from [79].

The difference ΔM of both absorption signals at the same X-ray absorption edge is called X-ray magnetic circular dichroism (XMCD) [79]. It can be defined as the difference of a parallel and antiparallel magnetization M within a material, which is equal to the difference $M^{-/+}(B)$ generated by an antiparallel helicity of the X-rays, which is equal to a measurement performed with an equal polarization but an antiparallel orientation of the external magnetic field B [79]:

$$\Delta M = M^{\uparrow\downarrow} - M^{\uparrow\uparrow} = M^{\cdot}(B) - M^{+}(B) = M^{+}(-B) - M^{+}(B) \quad (35)$$

By employing sum rules the ground state properties, as the orbital momentum, can be extracted from XMCD measurements [79]. For a detailed description the reader is directed to [76] and [79].

3. Experimental and computational techniques

In this chapter the experimental techniques of micro-resonator based ferromagnetic resonance and Scanning Transmission X-ray Microscopy detected Ferromagnetic Resonance (STXM-FMR) are described. In addition, the basic principles of micro-magnetic simulations using MuMax3 [29, 82-84] are presented.

3.1. Micro-resonator based ferromagnetic resonance

The ferromagnetic resonance experiments (see chapter 2.2) were performed using an electro magnet (Bruker) with a field accuracy of ± 0.5 mT and an X-band [39] microwave bridge model E-102 by Varian with a frequency range between 8.8 GHz and 9.6 GHz. A schematic representation of the setup is shown in Figure 5.

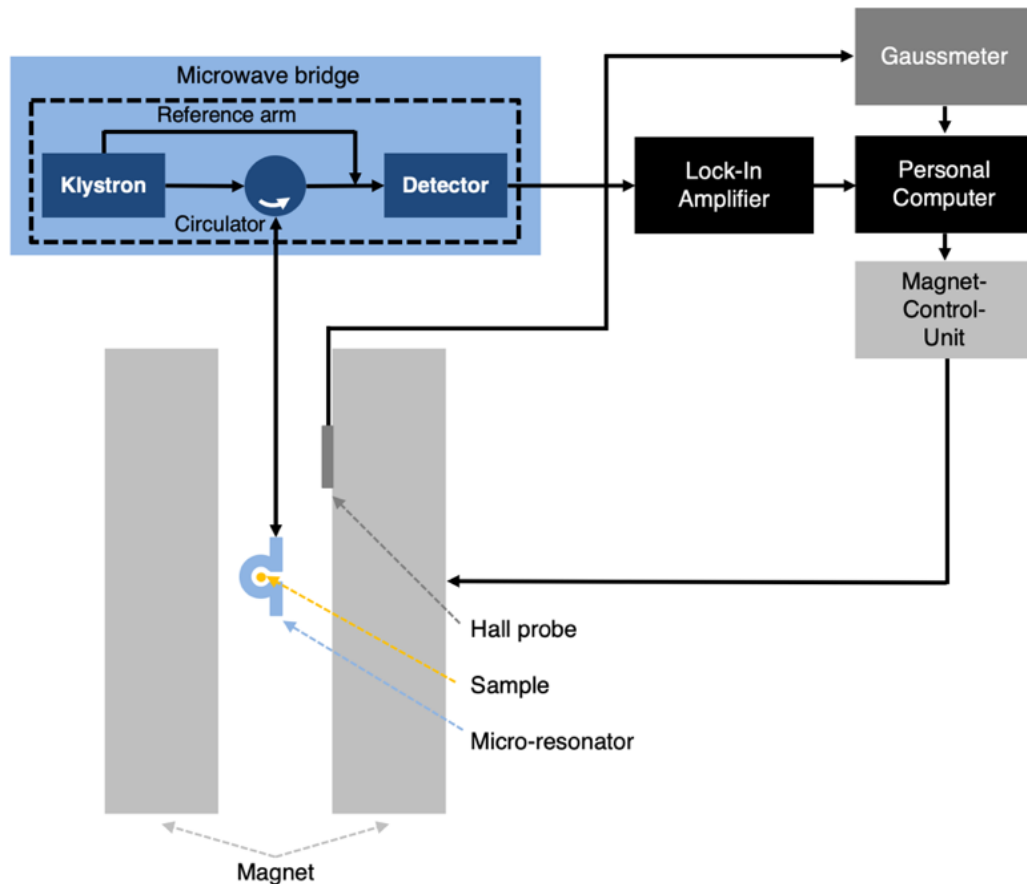


Figure 5: Schematic representation of the ferromagnetic resonance spectrometer used for the conventional FMR measurements. For cavity based FMR measurements the micro-resonator is replaced by a resonant cavity. Figure adapted from [85].

A Hall probe measures the magnetic field strength (gaussmeter model 425 by Lake Shore Cryotronics, accuracy for the measurement range of 3500 mT: $\pm 0.05\%$ of range: ± 1.75 mT [86]). Micro-resonators with a sensitivity of $10^6 \mu_B$ are employed [15, 18], which enable the detection of the FMR signal of Fe_3O_4 ($4.0 \mu_B$ per formula unit [87]) cubes with an edge length of about 35 nm [11]. The micro-resonators are fabricated using optical lithography.

The used setup corresponds to the general operation and nomenclature as described in e. g. [88]. A klystron is used by the microwave bridge to generate microwave radiation in the given frequency range. A part of this radiation is guided as a preload voltage to the microwave detector. This part of the microwave bridge is called reference arm. The remaining microwave radiation enters a circulator, which directs the radiation to the sample and guides, on the other hand, the reflected microwave radiation to the microwave detector. In addition, a slide screw tuner is included in the setup to tune the phase of the microwave and to match the impedance within the transmission line so that no microwave radiation is reflected out of the resonator. When the sample absorbs the microwave power at resonance, this tuning is disturbed, and the microwave power is reflected to the microwave detector. To measure the absorption of the microwave only, the dispersion signal has to be canceled by tuning the microwave frequency to the eigenfrequency of the used resonator during the experiment using an automated frequency control (AFC) [89]. These adjustments are necessary, as the eigenfrequency of the resonator including the sample changes in case of resonance, or e. g. due to temperature variations [90].

The sensitivity of the detection of the FMR signal is increased using lock-in amplifier technique with a Stanford Research System lock-in amplifier model SR830. A field modulation is used; its frequency serves as a reference for the lock-in amplifier, so the modulation-frequency-dependent FMR signal is detected [91]. Next to the field modulation technique, an amplitude modulation of the microwave is possible for conventional FMR detection. For angular dependent measurements, the electro-magnet can be rotated using a stepper motor.

3.2. X-ray detected magnetic/ferromagnetic resonance (XDMR / XFMR)

X-ray detected magnetic/ferromagnetic resonance probes element-specifically the average precession cone of the magnetization with respect to its orbital and spin portion [92]. A review on X-ray detected magnetic resonance was published in 2011 in [93]. In general, two experimental geometries are used corresponding to the longitudinal and transverse XMCD effect [92]. A schematic representation is shown in Figure 6. Here θ is the precession angle of the magnetization, which is in the size of 0.1° [44] to 0.15° [46] in the performed experiments in this thesis.

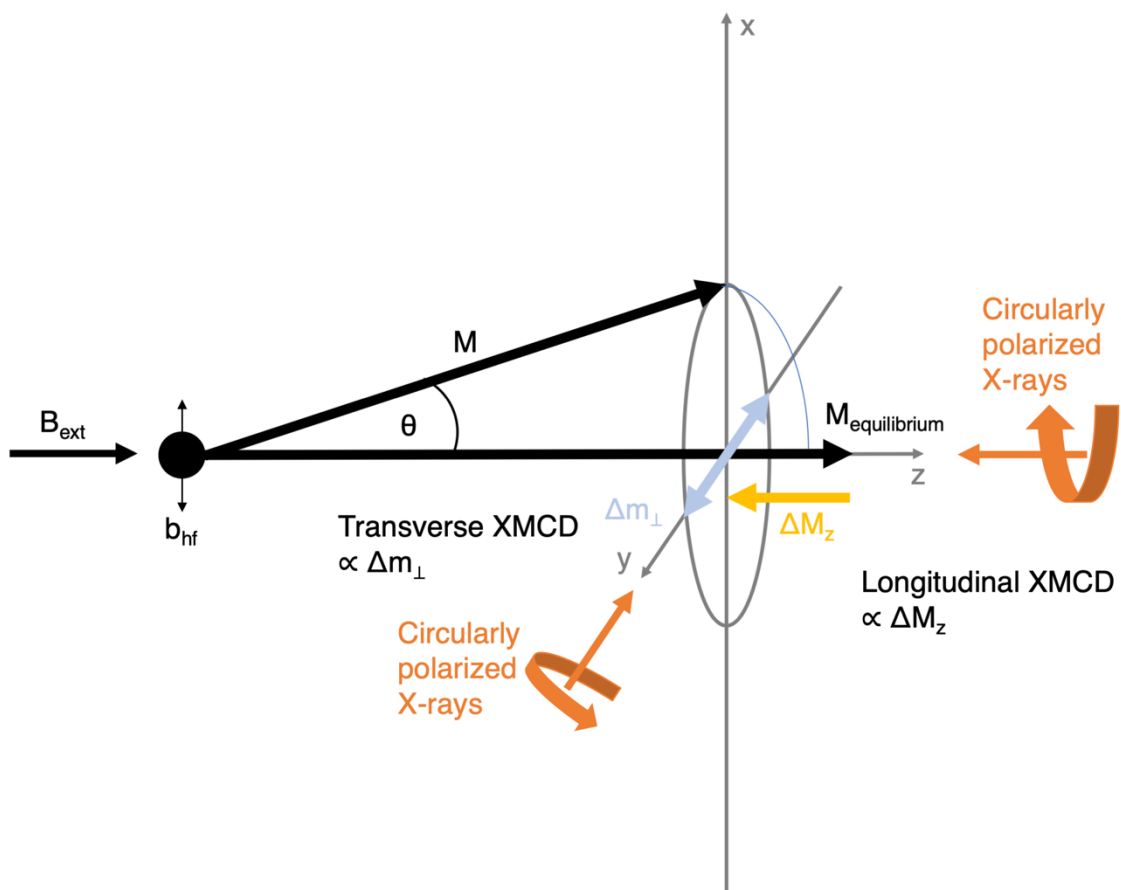


Figure 6: Schematic visualization of the transverse and longitudinal XMCD geometries for X-ray detected magnetic resonance. Figure redrawn and adapted from [92].

The shortening of the magnetization vector ΔM_z between the precessing magnetization M and the equilibrium magnetization $M_{\text{Equilibrium}}$ is detected in the longitudinal geometry, having the propagation direction of the X-rays parallel to the external

magnetic field B_{Ext} and $M_{\text{Equilibrium}}$ [92]. The oscillation of the high-frequency magnetization Δm_{\perp} is time and phase-resolved probed in the transverse geometry, having the propagation direction of the X-rays perpendicular to B_{Ext} , $M_{\text{Equilibrium}}$ and the high-frequency magnetic flux b_{hf} [92]. To scan the oscillation of the magnetization at frequencies in the gigahertz regime, a fast X-ray diode is necessary, while in the longitudinal geometry a proportionality of the detected signal to the microwave power is given, allowing a low-frequency amplitude modulation for detection [92]. XFMR requires a significantly higher demand on microwave power (six orders of magnitude) than the standard FMR technique.

The first works reporting the detection of ferromagnetic resonance using circularly polarized X-rays are by Bailey et al. [94] and Boero et al. [95]. Bailey et al. presented pump-probe XMCD detected measurements of a $\text{Ni}_{81}\text{Fe}_{19}$ film with 50 nm thickness with a time resolution of ± 45 ps using excitation frequencies up to 2.6 GHz and X-ray energies of 701 eV for the Fe L_3 edge and 844 eV for the Ni L_3 edge [94]. Boero et al. showed the detection of FMR excitation of a YIG sample with the dimensions $1 \text{ mm} \cdot 1 \text{ mm} \cdot 0.05 \text{ mm}$ using an excitation frequency of 2.47 GHz [95]. The measurement was performed in the longitudinal geometry using X-rays with the energy of 709.4 eV and 722.8 eV and a focus of $0.2 \text{ mm} \cdot 1 \text{ mm}$, and the high-frequency magnetic field (100 mW) orientated in the film plane [95]. A multifrequency continuous wave setup operating at low microwave powers in the longitudinal experimental geometry was introduced in [96], using an electrical short for the high-frequency magnetic field excitation [96]. Also in the longitudinal experimental geometry a was shown by Boero et al. showed the successful element-specific detection of the high-power continuous wave excitation FMR of a doped Py film ($\text{Ni}_{73}\text{Fe}_{18}\text{Gd}_7\text{Co}_2$) with a thickness of 15 nm, probing the sample at the L_2 and L_3 edges of Fe Co and Ni [97]. The possible use of the STXM technique to detect FMR on the nanoscale is predicted [97].

In transverse geometry, a scan on the sub-micron scale ($<0.75 \mu\text{m}$) of the magnetic high-frequency susceptibility in ferromagnetic heterostructures was demonstrated using a time-resolved STXM pump-probe experiment in [98]. Spin pumping in spin valves was investigated utilizing phase-resolved XFMR of a sample consisting of

Co₅₀Fe₅₀(3 nm)/Cu(6 nm)/Ni₈₀Fe₂₀(5 nm) with the dimension of 190 μm x 400 μm [99].

Puzic et al. used a Scanning Transmission X-ray Microscope in transverse geometry to spatially detect the ferromagnetic eigenmodes in patterned Py films with 1 μm · 1 μm and a thickness of 50 nm [100]. The observations of the eigenmodes were performed in the frequency domain with so-called Spatially Resolved Ferromagnetic Resonance (SR-FMR)[†] [100]. The spatially and time-resolved detection of the eigenmodes was achieved by alternating the phase between excitation and the synchrotron [100]. These experiments were the predecessor to the Scanning Transmission X-ray Microscopy detected Ferromagnetic Resonance (STXM-FMR) by Bonetti et al. [44], which was used in this thesis.

3.3. Scanning Transmission X-ray Microscopy detected ferromagnetic resonance

The method of Scanning Transmission X-ray Microscopy detected Ferromagnetic Resonance (STXM-FMR) was introduced by Bonetti et al. in [44]. Descriptions of the method can be found in [45-48]. The following chapter summarizes the measurement technique according to [44]. The measurement method is a combination of a micro-resonator based FMR spectrometer (see chapter 3.1) and a specially designed Scanning Transmission X-ray Microscope (STXM) measuring in the transverse geometry [48, 101] (Figure 6), which allows the element-specific detection of the probability value of the magnetization with nm spatial resolution [101] at Stanford Synchrotron Radiation Lightsource at SLAC National Accelerator Laboratory, Menlo Park, CA in the United States [44]. Due to the mapping by STXM, the magnetization dynamics of periodic, as well as non-periodic micro- and nanostructures can be probed. A schematic representation of the experimental setup is shown in Figure 7. The STXM and the used electromagnet are located within a vacuum chamber (base pressure 10⁻⁷ Torr), which reduces damping effects on the propagating X-rays and the adsorption of hydrocarbons on the sample [44]. The X-ray radiation generated

[†] A synchronization scheme was implemented between the frequency of the sinusoidal magnetic excitation (250 MHz) and the synchrotron frequency (500 MHz at the Advanced Light Source at Lawrence Berkeley National Laboratory, Berkeley, CA, United States) [100].

by the synchrotron is in the energy range from 200 eV to 1200 eV [44] and is focused onto the sample with a zone plate, allowing a spatial resolution down to $1.22 \cdot 35 \text{ nm}$ (angular resolution) [101]. An order sorting aperture (OSA) is positioned between the zone plate and the sample itself, allowing only the X-rays with the highest intensity to pass [44]. The transmitted X-ray radiation is detected by an avalanche photodiode type Hamamatsu S12426 [44], which is located below the sample. The sample is prepared in a micro-resonator with an excitation loop diameter of $20 \mu\text{m}$, which is mounted onto a sample holder, both are pictured in Figure 8. The micro-resonator loop is positioned on a Si_3N_4 membrane with 200 nm thickness to allow X-ray radiation to be transmitted through the sample and the membrane. The sample holder design was created by T. Schaffers and co-workers.

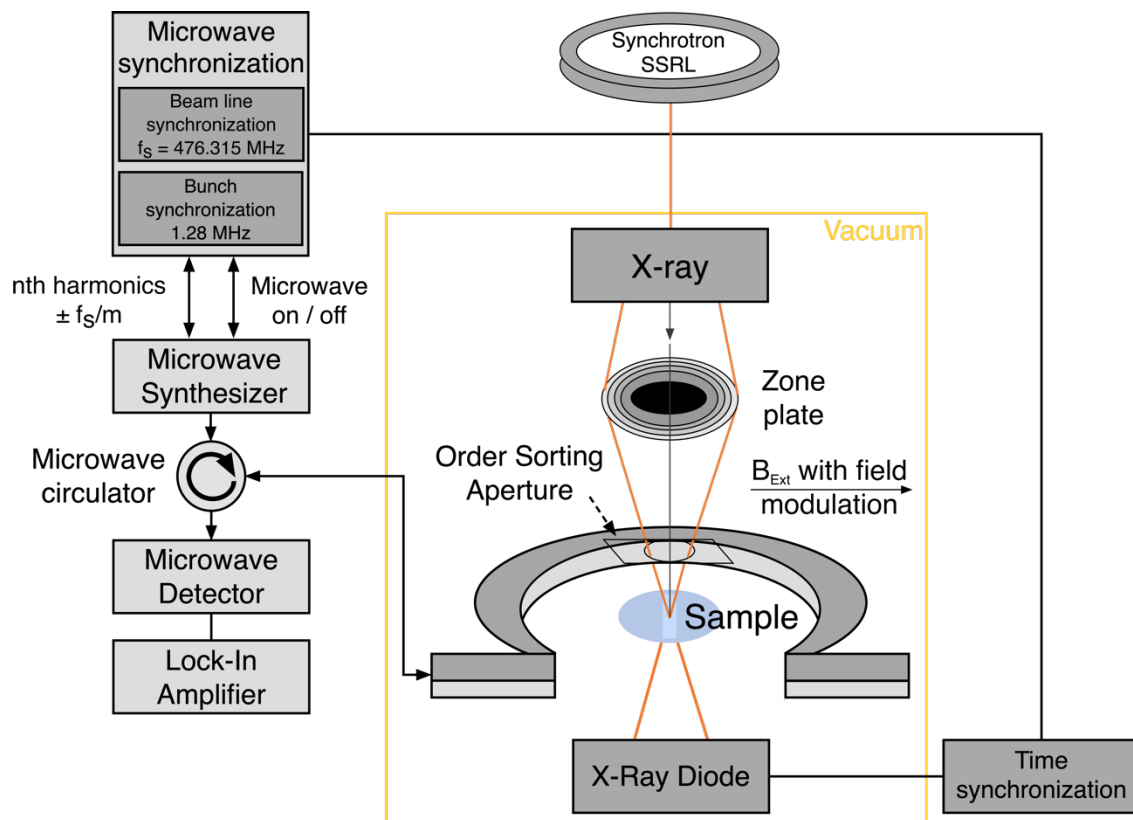
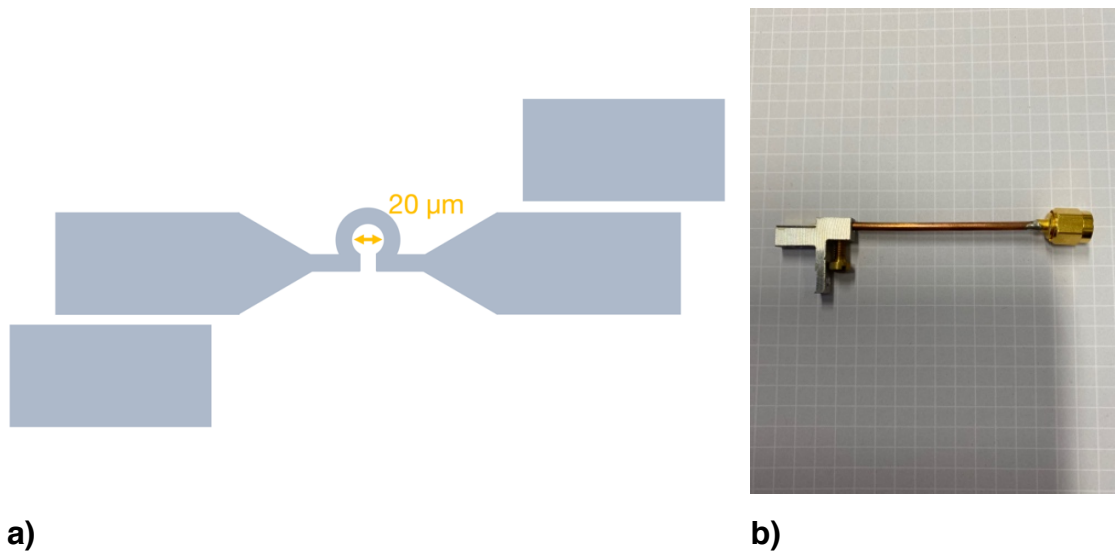


Figure 7: Schematic representation of the STXM-FMR setup at the Stanford Synchrotron Radiation Lightsource at SLAC National Accelerator Laboratory. The electromagnet is not shown for better visibility. Figure adapted from [48].



a) Schematic representation of a strip-line micro-resonator, allowing measurements in reflection and transmission geometries. **b)** Example picture of the sample holder with the attached semi-rigid cable to deliver the microwave power to the sample.

The maximal static bias field available for the setup is at 200 mT. The continuous-wave excitation of the sample is generated by a microwave synthesizer type MG3692B by Anritsu with a maximum power of 19 dBm and a frequency range from 2 GHz to 20 GHz [102]. The oscillation plane of the high-frequency magnetic field is parallel to the propagation direction of the X-rays. All measurements are performed at room temperature. For the employed quasi-stroboscopic detection of the magnetization dynamics, the microwave excitation is phased-locked to the synchrotron operating frequency ($f_s = 476$ MHz [44]) [44]. The phase lock is generated to a microwave (MW) frequency corresponding to a higher harmonic n of the synchrotron frequency \pm a subharmonic f_s/m , where m is the number of scanned phases of the magnetization oscillation [44]:

$$f_{\text{MW}} = f_s \left(n \pm \frac{1}{m} \right) \quad (36).$$

By that m phases with a fixed phase difference of 60° of the magnetization oscillation are probed for each scanned pixel, as the X-ray photons following to each other are probing a different phase of the magnetization oscillation, while all m^{th} X-ray photons probe an equal phase [44]. Using an PID controller (Stanford Research Systems

SIM960, [44]), the phase lock of the microwave excitation to the synchrotron frequency is kept stable [44]. In total 12 STXM-FMR images are taken to monitor the magnetization precession up to 10 GHz with a time distance down to 17 ps (at 10 GHz) [44]. Six images are taken with and six images without applied microwave excitation ($m = 6$) [48]. By subtracting or dividing these datasets (for details see chapter 3.4), the microwave induced X-ray transmission can be extracted [48, 103]. A PIN diode is used to alternately turn the microwave excitation on and off with a frequency of 1.28 MHz, which corresponds to the orbiting frequency of the electron bunches in the synchrotron storage ring [44]. This ensures that the same electron bunch is used for the six scanned points in time (phases) of the magnetization oscillation [44]. A comprehensive description of the microwave synchronization is given in [44]. The data is stored in a time synchronization device called “time machine”, which provides storage slots named as channels for the 12 STXM-FMR images [48]. The time machine data is read out by a custom software and stored within text files for each channel.

The measurement principle is graphically elucidated in Figure 9 in the scope of the STXM-FMR measurement at the Co L_3 edge of a Py/Co disk/stripe bilayer microstructure, which is analyzed in detail in chapter 4.1. In the first column the time steps, at which the STXM-FMR data is recorded, are shown in combination with the recorded phase, relative to the time point $t = 0$ [48]. Column two and three show the STXM-FMR data recorded with and without microwave excitation [48]. In the fourth column the uniform resonant response of the Co stripe is visualized, after performing the difference operation of the data shown in column two and three [48]. Darker contrast represents a lower X-ray absorption with respect to the average contrast value, which is represented by grey color [48]. In consequence brighter contrast represents higher X-ray absorption with respect to the average [48]. The STXM-FMR is measured as follows. A pre-characterization of the sample to investigate the resonance fields corresponding to a certain excitation frequency is done by conventional FMR measurements and/or by micromagnetic simulations, when the magnetic parameters of a sample (e. g. exchange stiffness, saturation magnetization, magnetic anisotropies) are well known.

Co L ₃ -edge			
$\varphi[^\circ] / t[\text{ps}]$	MW on	MW off	Difference
0 / 0			
60 / 18			
120 / 37			
180 / 55			
240 / 74			
300 / 92			
360 / 110			

Figure 9: STXM-FMR at the Co L₃ edge of a Py/Co disk-stripe bilayer microstructure. The blue rectangular marks the recorded dataset. The first row is the same dataset as the last one to show a complete magnetization oscillation. 1st column: Timepoints and the recorded phase relative to the time $t = 0$. The 2nd and 3rd columns: STXM-FMR data recorded with microwave on (MW on) and off (MW off). 4th column: Difference of column 3 and 2 (MW off – MW on). This dataset is analyzed in detail in chapter 4.1. Image adapted from [48].

After setting the external static magnetic bias field to the value known for a certain excitation at a given microwave excitation frequency, the sample is scanned with the X-ray beam. The magnet was calibrated using Hall sensors of the type HGT-2101 [47]. The static field varies in the range of ± 4 mT depending on the position of the Hall probe at the sample holder.

Except for the YIG nanoparticle STXM-FMR measurements (chapter 5.1), which were performed with a negative helicity of the X-ray photons, all other STXM-FMR measurements in this thesis were done with a positive helicity.

3.4. Color-coded fit analysis of STXM-FMR data

A color-coded fit analysis of the STXM-FMR data was developed by B. Zingsem and R. Meckenstock with additional contribution of the author to visualize the phase and amplitude distribution [103] of the measurement data; the current chapter follows this presentation. To extract the microwave induced X-ray transmission [48], the datasets recorded with microwave on and off have to be post-processed by subtracting or dividing the datasets [103]:

$$\frac{\text{count rate}_{\text{MW on, } x,y}(t)}{\text{count rate}_{\text{MW off, } x,y}(t)} = \frac{\text{count rate}_{\text{MW on, } x,y}(t) - \text{count rate}_{\text{MW off, } x,y}(t)}{\text{count rate}_{\text{MW off, } x,y}(t)} + 1 \quad (37).$$

By employing equation (37) assuming a constant detected count rate in the experiment for the state without applied microwave radiation it follows [103]:

$$\frac{\text{count rate}_{\text{MW on, } x,y}(t)}{\text{count rate}_{\text{MW off, } x,y}(t)} \sim \text{count rate}_{\text{MW on, } x,y}(t) - \text{count rate}_{\text{MW off, } x,y}(t) \quad (38).$$

This basically means that both operations result in a comparable result, which strongly depends on the signal to noise ratio [103].

The resulting six STXM-FMR images are fitted pixel-by-pixel with a sinusoidal function to obtain the phase relative to the timepoint $t = 0$, and the amplitude for the recorded magnetization oscillation. In the result the hue is used to code the relative phase, the brightness corresponds to the amplitude, and the saturation represents the fit accuracy [103]. A visualization of the analysis steps performed in the scope of this method is shown in Figure 10 for an example of a $5 \mu\text{m} \times 1 \mu\text{m} \times 0.03 \mu\text{m}$ polycrystalline Py stripe sample, which will be discussed in detail in chapter 4.2. The STXM image of this sample is shown in Figure 10 i). The phase relative to $t = 0$ is shown in subfigure ii), while the fit accuracy (p-value) and the amplitude distribution are shown in the subfigures iii) and iv). An example fit of the fitted sinus function for the red highlighted pixels in Figure 10 i) is depicted in the image part b), while the color code is visualized in c). For an extended description of the analyses method the reader is referred to [103].

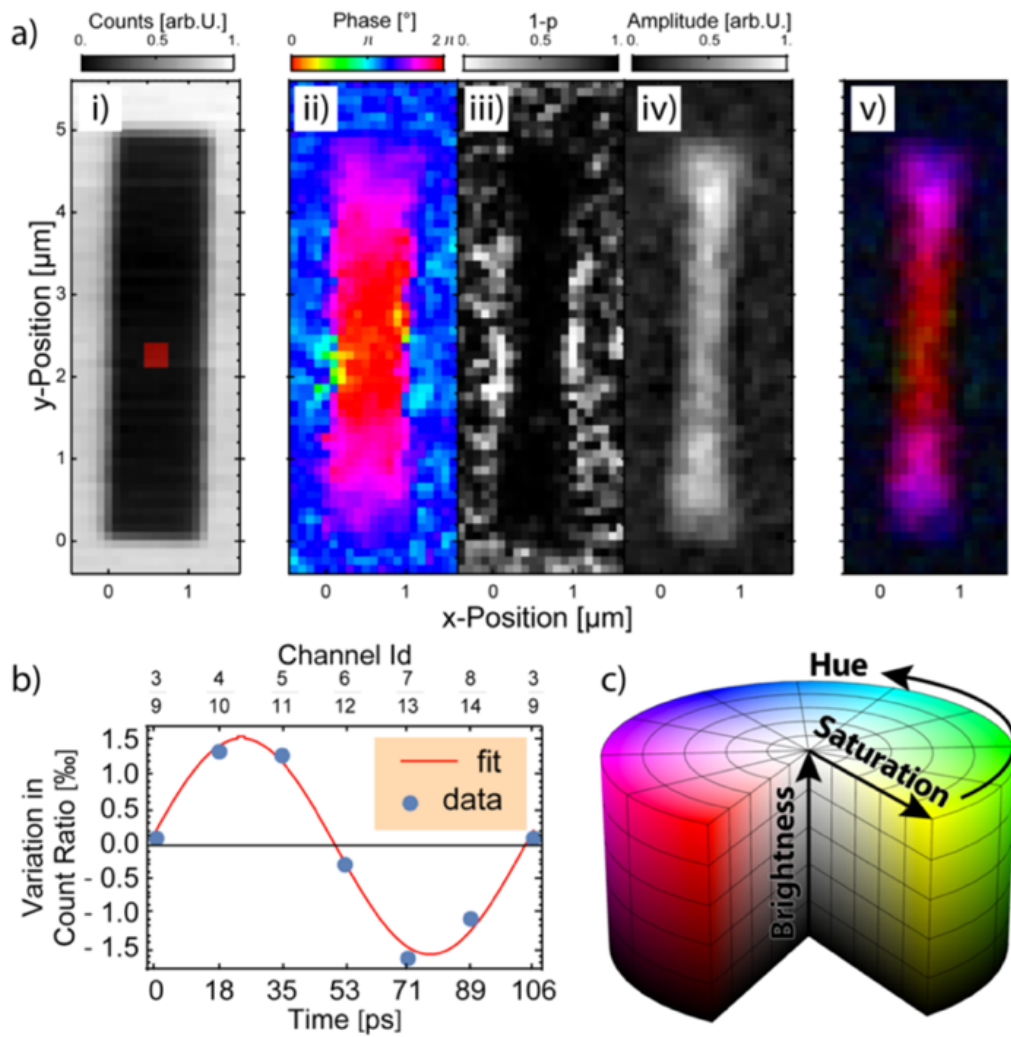


Figure 10: Color code fit analysis. a): Image i) STXM-FMR image of a Py stripe (see chapter 4.2). Images ii), iii) and iv): Extracted relative phase, fit accuracy and amplitude. Image v): Combination of the images ii) to iv). b): Example fit of the red marked square in a) i). c): Color code to visualize i) to v) in a). Figure taken from [103].

3.5. Micromagnetic simulations

All micromagnetic simulations in the thesis's scope were performed using the open-source software package MuMax3 [29, 82-84, 104]. To massively increase the computational performance of the calculations, parts of the calculations are processed on graphics processing units (GPU), employing the CUDA computational libraries of the Nvidia company [105]. A limitation of this approach is the resulting mandatory use of GPU's manufactured by Nvidia. MuMax3 is a finite difference in time domain micromagnetic simulator, which numerically solves a system of equations of motion (Landau-Lifshitz-Gilbert equation) of a discretized sample magnetization using orthorhombic cells [29]. All calculations are performed with single precision [29], which makes a verification of the obtained results by repeating the simulations recommendable. The coordination system and cell indexing within a MuMax3 simulation grid is schematically displayed in Figure 11.

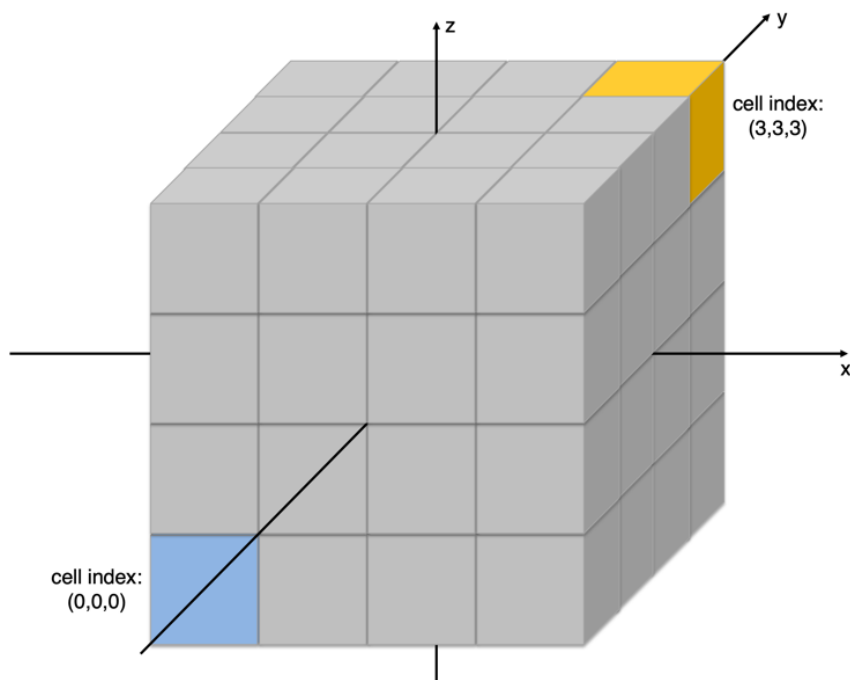


Figure 11: Coordination system and cell indexing of MuMax3. Figure adapted from [85].

Here the lowest plane of cells starts as cell plane 0 with increasing numbers for the cell planes and cell coordinates within a plane, simulated samples can be shifted within this simulation grid using so-called translation commands [29, 104]. The

simulated sample structures itself are created using basic predefined shapes or by reading in image data of the desired sample structure [29, 104]. For each cell of such a simulation grid the exchange stiffness A_{ex} , saturation magnetization M_{sat} , anisotropy parameters and directions and other quantities, which are specified in detail in [29, 104], can be defined [29, 104]. It also is possible to assign these quantities to certain parts of a simulated geometry by introducing up to 256 so-called material regions [29, 104]. The cell size should be selected below the exchange length l_{ex} [106] to ensure the correct calculation of magnetic exchange [107]. The exchange length is defined as [106]:

$$l_{ex} = \sqrt{\frac{A_{ex}}{\frac{1}{2}\mu_0 M_{sat}^2}} \quad (39)$$

To improve simulation performance, three-dimensional periodic boundary conditions can be applied. [29, 104]. There are 4 types of numerical solvers for differential equations available within MuMax3, all employing Runge-Kutta (RK) methodology [29]. In addition predefined energy minimization functions are available called “relax()” [29] and “minimize()” [108]. The implemented Runge-Kutta methods are displayed in table. A detailed description of these methods can be found in [109].

Runge-Kutta method	Convergence order	Consistence order
RK1	1	1
RK12	2	1
RK32	3	2
RK45	5	4

Table 1: Available Runge-Kutta methods within MuMax3 [29, 85].

For a detailed description of the available functions and commands the reader is referred to [29, 85, 104].

The stray field visualizations in the scope of this work have been created using a Matlab (Mathworks company) program written by Z. Li and expanded by the author [85].

All two-dimensional representations of the magnetization data have been created using the mmDisp program of the Object Oriented MicroMagnetic Framework (OOMMF) [27].

All three-dimensional visualizations of the magnetization vector field from MuMax3 simulations have been created using the Muvview software [110]. The three-dimensional visualization uses the color code shown in Figure 12.

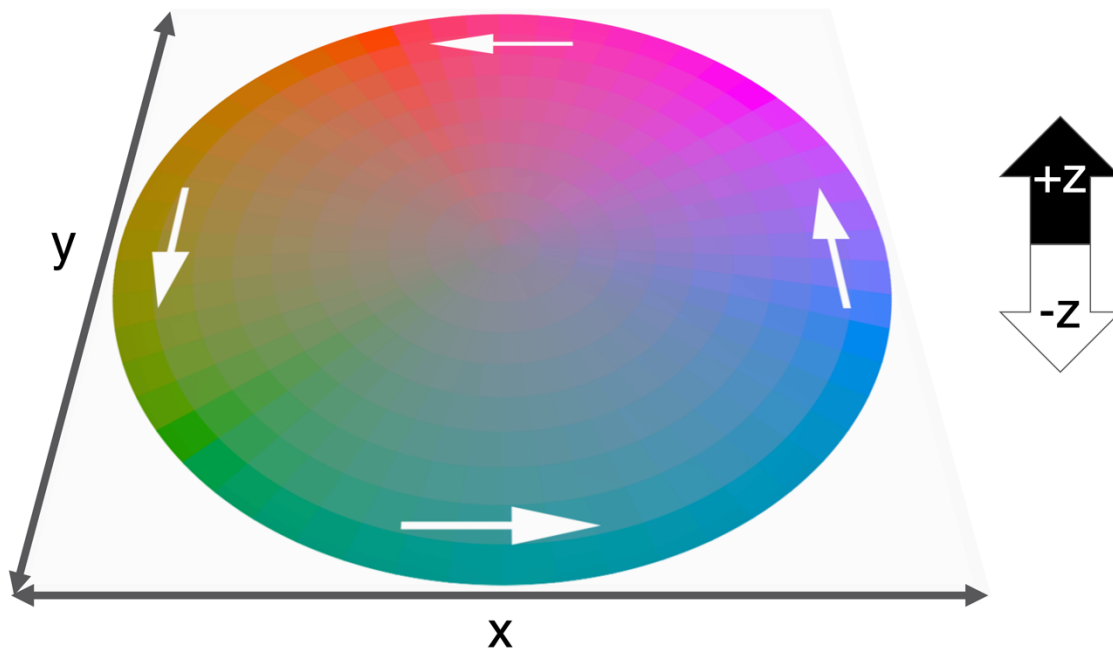


Figure 12: Color wheel indicating the in-plane orientation of the simulated magnetization. Out-of-plane magnetization orientations are colored black for the +z direction and white for the -z direction. Intermediate out-of-plane components are using a color mixture of the in-plane and out-of-plane colors. The color wheel was created using the software WheelMasks by Roger Tallada and enhanced using Adobe Photoshop CC 2015. Figure taken from [85].

4. Magnetization dynamics on micrometer sized sample structures

4.1. Magnetization dynamics of a Py/Co multilayer sample

In the process of the development of spintronic devices [2, 3, 5] the investigation of interlayer coupling and spin currents in multilayered samples is essential and requires studying the behavior at the interfaces of multi-material systems under high-frequency excitations [48]. A standard technique used in this research is Ferromagnetic Resonance [48, 111]. FMR measurements of ultrathin equally sized ferromagnetic multilayer systems revealed two uniform resonances attributed to in-phase and out-of-phase optical or acoustical mode, see e. g. [111]. Future spintronic devices are expected to consist of microstructured multimaterial systems, e. g. [2], in this scope a prototype system consisting of a Cobalt (Co) stripe deposited on a Permalloy (Py) disk (see chapter 4.1.1 for sample details) was element-specifically investigated by STXM-FMR, showing a different behavior than for the aforementioned equally sized bilayers. The measurements were performed in January 2015 by S. Bonetti, R. Meckenstock, A. Ney, H. Ohldag, C. Schöppner and D. Spoddig. The measurement results were published in part in [46] and in the PhD thesis of T. Schaffers [47]. The final analysis was submitted to Physical Review Applied in July 2020 [48].

4.1.1. The Py disk/Co stripe bilayer microstructure

The sample system consists of a polycrystalline Py disk (2.5 μm diameter, 30 nm thickness) with a polycrystalline Co stripe on top (2 μm length, 0.5 μm width, 30 nm thickness) [48], fabricated by a three-step lithography process and depositing the materials by electron beam deposition [48, 112]. The sample was prepared by C. Schöppner in a micro-resonator [15, 16, 18, 113] positioned on a Si_3N_4 membrane with 200 nm thickness. The sample system is depicted in Figure 13 using SEM and STXM methods. Py ($\text{Ni}_{80}\text{Fe}_{20}$) has an average magnetic moment of 1.02 μ_{B} per unit cell [114] with a lattice constant ~ 0.355 nm [115], resulting in $\sim 3.4 \cdot 10^9$ μ_{B} in the disk volume. With an average magnetic moment of 1.7 μ_{B} per atom [56] the Co stripe volume contains about $4.6 \cdot 10^9$ μ_{B} using a unit cell volume of 0.0661 nm³ [116]. An

X-ray beam focused to 35 nm on the sample scans a volume containing of about $6.6 \cdot 10^5 \mu_B$ (Py) and $4.5 \cdot 10^6 \mu_B$ (Co) taking into account the aforementioned parameters.

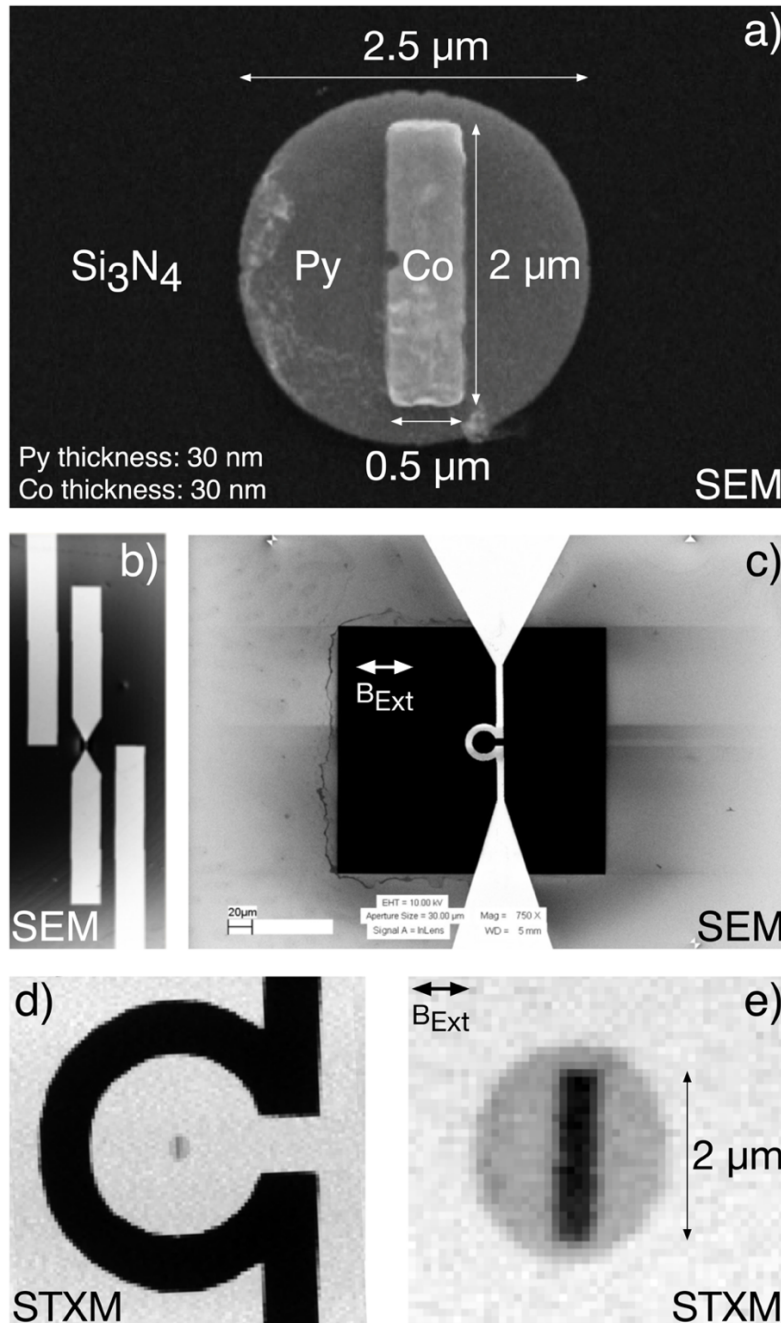


Figure 13: **a)** SEM image of the Py/Co multilayer sample on a Si_3N_4 membrane, indicating the sample dimensions. **b)** SEM image of the stripline micro resonator, **c)** magnification of the membrane area of the micro resonator. **d)** STXM image of the resonator loop including the sample. **e)** STXM image of the sample with a spatial resolution of 35 nm and a step-size of 100 nm. SEM images were taken by D. Spoddig and C. Schöppner. Image adapted from [48].

The demagnetization factors for the Co stripe, calculated using equations (A1) to (A3) are $N_1 = 0.078$, $N_2 = 0.903$ and $N_3 = 0.019$. Due to shape anisotropy, the easy axis of the Co stripe is directed along the long stripe axis, resulting in $\underline{B}_{\text{Ext}}$ orientated perpendicularly to this axis in the experiment. For a disk having $\underline{B}_{\text{Ext}}$ orientated in the disk plane as given for the experiment, the demagnetization factors are ~ 0 [117].

4.1.2. Conventional FMR measurements of the sample

The conventional FMR measurements were performed at room temperature by R. Meckenstock and C. Schöppner. The measurements were done with a power of 10 mW using an excitation frequency of 9.27 GHz [48]. The static magnetic bias field was changed from 0 mT to 400 mT in 0.5 mT steps. The field was orientated perpendicularly to the long side of the Co stripe, as indicated in Figure 13 c) and e). The signal to noise ratio is > 10 . The measured FMR-spectrum is shown in Figure 14. The error bar of $|\underline{B}_{\text{Ext}}|$ is ± 0.5 mT.

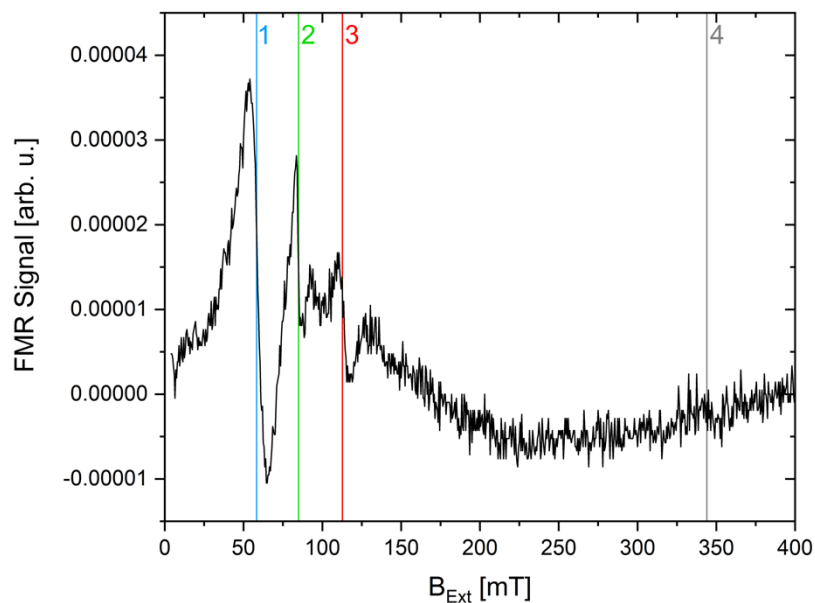


Figure 14: Conventional FMR spectra of the Py/Co multilayer sample. FMR-spectrum up to 400 mT, showing the main resonance modes as 1 (Py), 2 (coupled resonance), 3 (Co) and 4 (Co, edge resonance mode). Image taken from [48].

The spectrum in Figure 14 shows four main resonances indicated as 1, 2, 3 and 4 at 58.3 mT, 84.9 mT, 112.7 mT and 344 mT, respectively [48]. Resonance 1 has the highest intensity followed by resonance 2, 3, and 4. The linewidth is 15 mT for resonance 1, 5 mT for resonance 2, 10 mT for resonance 3 and 8 mT for resonance 4 [48]. The disk shape of the Py part of the sample favors no in-plane easy or hard axis of the shape anisotropy leading in combination with its higher volume to the assignment of resonance 1 (highest intensity) to the Py disk [48], even though Py has a lower saturation magnetization (860 kA/m [13]) than Co (1420 kA/m [13]) [48]. Due to shape anisotropy (see chapter 2.1.1), resonance 3 is assigned to the Co stripe, having its easy anisotropy axis orientated perpendicularly to $\underline{B}_{\text{Ext}}$ [48]. A comparable behavior is demonstrated with FMR measurements of a Co stripe in [16]. Due to the polycrystalline character of both layers, an influence of the magneto crystalline anisotropy is not taken into account [48]. The resonance indicated as 4 in Figure 14 is ascribed as an edge mode of the Co stripe [16, 113, 118] originating in the missing alignment of the magnetic moments at the long sides of the Co stripe [48, 113, 118]. In consequence the resonance of the stripe edges at a higher resonance field [48]. Investigations on edge modes in Py are reported e. g. in [33, 119-122]. The origin of resonance 2 is assumed to be a coupled resonance of both materials [48]. To identify the origin of the resonances STXM-FMR was employed (chapter 3.3).

4.1.3. Element-specific magnetization dynamics of the Py/Co bilayer microstructure

STXM-FMR measurements on the Py/Co bilayer microstructure were performed at the Co L_3 edge (nominal value: 779 eV) for the detection of the magnetization dynamics in the Co stripe and at the Ni L_3 edge (nominal value: 852 eV) for the measurements of the Py disk [48]. The microwave excitation was set to 9.129 GHz [48] with a power of 17 dBm, which corresponds to the 19th harmonic (9.04 GHz) of the synchrotron frequency with an added subharmonic of 1/6th. Due to the limitation of a maximal external bias field of 200 mT at the SSRL, only the formerly introduced resonances 1-3 could be imaged. The STXM-FMR measurements were done for both absorption edges at 58.3 mT (resonance 1), 84.9 mT (resonance 2), and 112.7 mT (resonance 3) [48]. The selected step size for the scan was 100 nm with a dwell time between the single pixel's scans of 5000 ms.

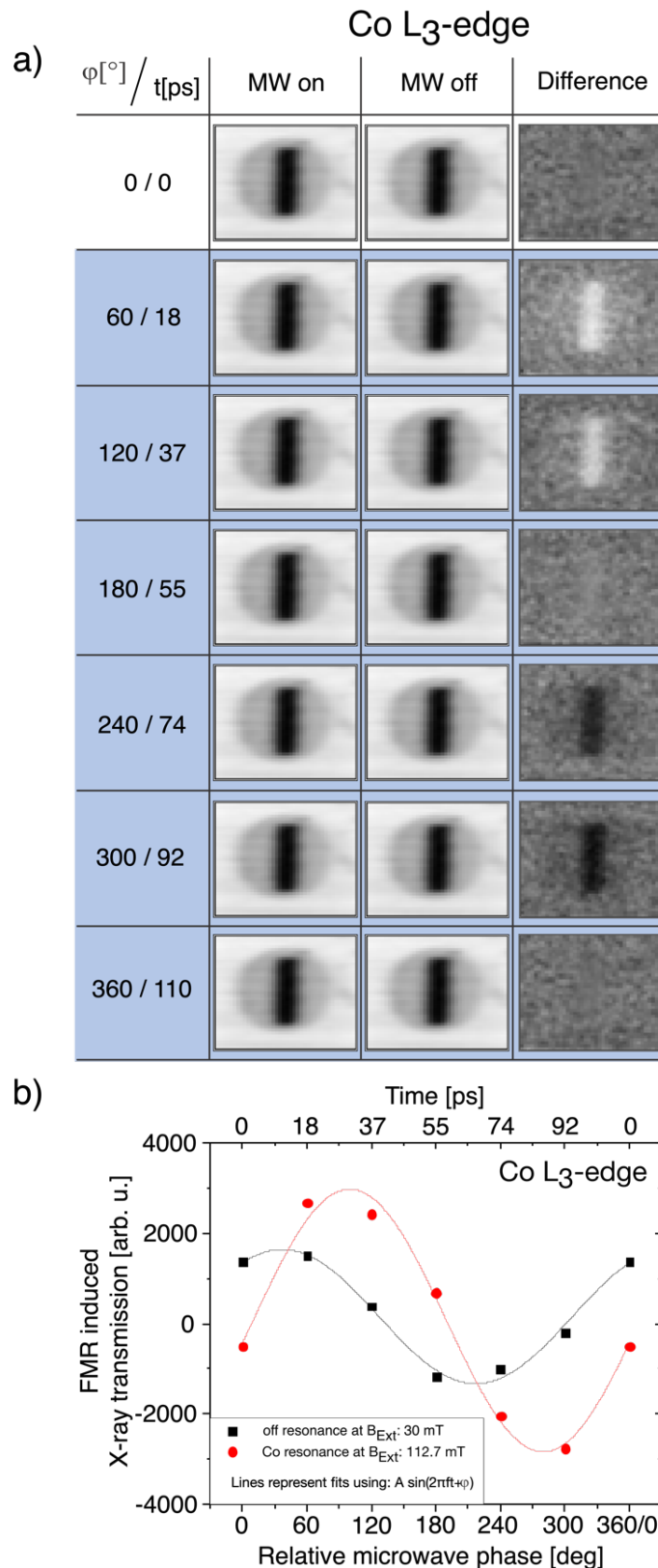
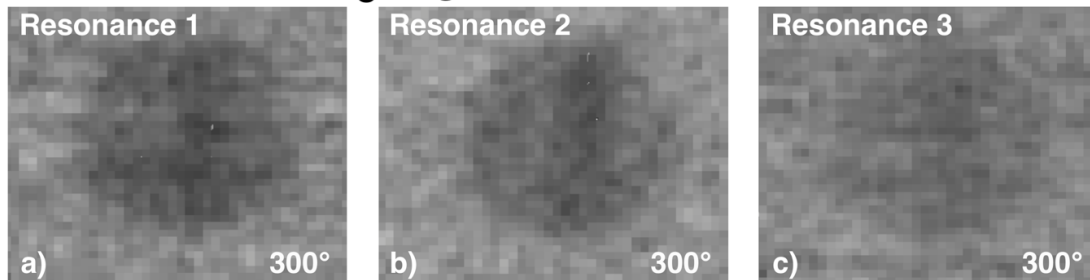


Figure 15: a) STXM-FMR images recorded with and without applied microwave excitation at the Co L₃ edge at 112.7 mT. The difference data is shown in the last column. The blue highlighted area shows the recorded STXM-FMR data with the first row corresponding to the last one. b) FMR induced X-ray transmission for the Co resonance and for an off-resonance $|B_{\text{Ext}}|$. Figure adapted from [48].

Figure 15 a) shows the 12 STXM-FMR images recorded with a time distance of 18 ps (@ 9.129 GHz) at the Co L_3 edge for resonance 3 at 112.7 mT. The data acquired with and without microwave excitation is displayed, as well as the microwave induced X-ray transmission in the fourth column. In [46] and [47] a set of procedures for background correction is presented. To preserve the information featured by the STXM-FMR data the images in Figure 15 and Figure 16 are adjusted to the same background color level [48].

For the microwave induced X-ray transmission at the Co resonance a clearly sinusoidal behavior of the magnetization oscillation is visible in Figure 15 b), with a relative phase shift of 90° to the off-resonance case recorded at an external magnetic field of 30 mT, at which Co is only driven by the applied microwave [48]. This corresponds to the general behavior of a resonance to its excitation [123]. Also, a difference of the signal amplitude of about 25 % can be observed between both signals. The complete measurement rows for both the Ni and the Co L_3 edge are displayed in appendix 7.3. Figure 16 displays the STXM-FMR measurement results for the three resonances for both X-ray absorption edges.

STXM-FMR on Ni L_3 edge



STXM-FMR on Co L_3 edge

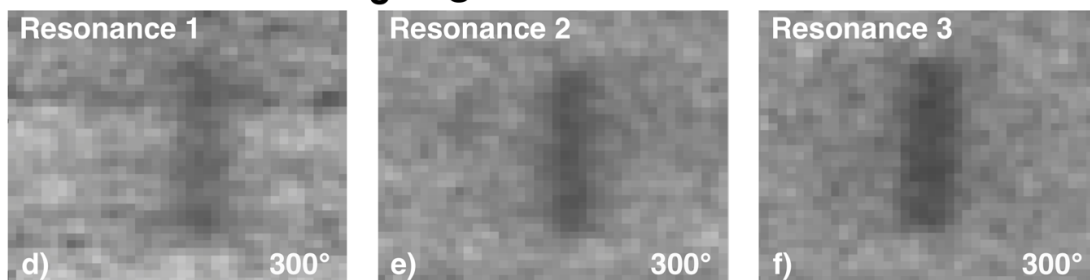


Figure 16: Results of the STXM-FMR measurements for the three resonances, for each resonance the scans at the Ni L_3 and the Co L_3 edge is displayed. Image taken from [48].

The images at the same relative phase of 300° (92 ps) are shown. The STXM-FMR image taken at the Py resonance at the Ni L_3 edge is shown in Figure 16 a). A strong contrast is visible within the Py disk, which indicates that the Py is in resonance at this value of the external field [48]. The measurement at the same magnetic field value at the Co L_3 edge (Figure 16 d)) shows no contrast within the Py disk and a weak contrast at the area of the Co stripe. This can be understood in the way that the magnetic moments of the Co are not fully orientated in the direction of the external field at the Py resonance field, so angular momentum is transferred from the Py to the Co, resulting in a weak collective precession of the magnetic moments of the Co stripe [48]. At this resonance field the line width of the conventional FMR spectrum has the highest value of 15 mT observed within the measurement (see chapter 4.1.2 and [48]), which is due to an intrinsic contribution to the damping of the Py disk, connected with a line distribution originating in the sample parts directly below and around the Co stripe[48].

Figure 16 b) and e) visualize the STXM-FMR data obtained at the external magnetic field value of the intermediate resonance. At both X-ray absorption edges a strong contrast can be observed within the Py disk, as well as in the Co stripe, displaying that both parts of the sample are in resonance [48]. This is also supported by the smallest observed FMR line width of 5 mT [48]. A more pronounced contrast is seen in Figure 16 b) at the area of the Co stripe due to a widened precession cone of the magnetic moments in the Py caused by the exchange coupling with Co [48]. This indicates that the origin of resonance 2 lies in the exchange coupled layers of the sample [48], with both magnetic constituents being in resonance reciprocally enhancing each other [48]. The influence of magnetic dipolar coupling will be shown later in this chapter.

In Figure 16 c) and f) the STXM-FMR images for both X-ray absorption edges at resonance 3 are depicted. At the Ni L_3 edge only a weak contrast within the Py disk can be detected, while a strong contrast within the Co stripe at the Co L_3 edge can be observed, indicating that the Co stripe is in resonance [48]. An angular momentum transfer from Co to Py is the reason for the weak contrast visible in Figure 16 c). The contrast is less intense as the magnetic moments of Py are aligned by the external field and therefore they are only slightly driven by Co [48]. The behavior of the FMR

line-width can be explained by the same origin as for the corresponding behavior at resonance 1 [48].

The contrast within the Co stripe shows a larger broadness and a higher intensity than the contrast within the Co stripe shown in Figure 16 e), see Figure 17. This can be explained by the complete excitation of the Co stripe at resonance 3, while the magnetic moments at the long edges of the Co stripe are not in resonance at the magnetic field value of the coupled resonance [48], due to the different orientation of the magnetization along the long sides of the stripe, as it can be seen in the result of micromagnetic simulations in Figure 18 [48]. As described in chapter 4.1.2, the resonance field for this edge mode is at 344 mT [48]. Investigations on edge modes in Py are reported e. g. in [33, 119-122].

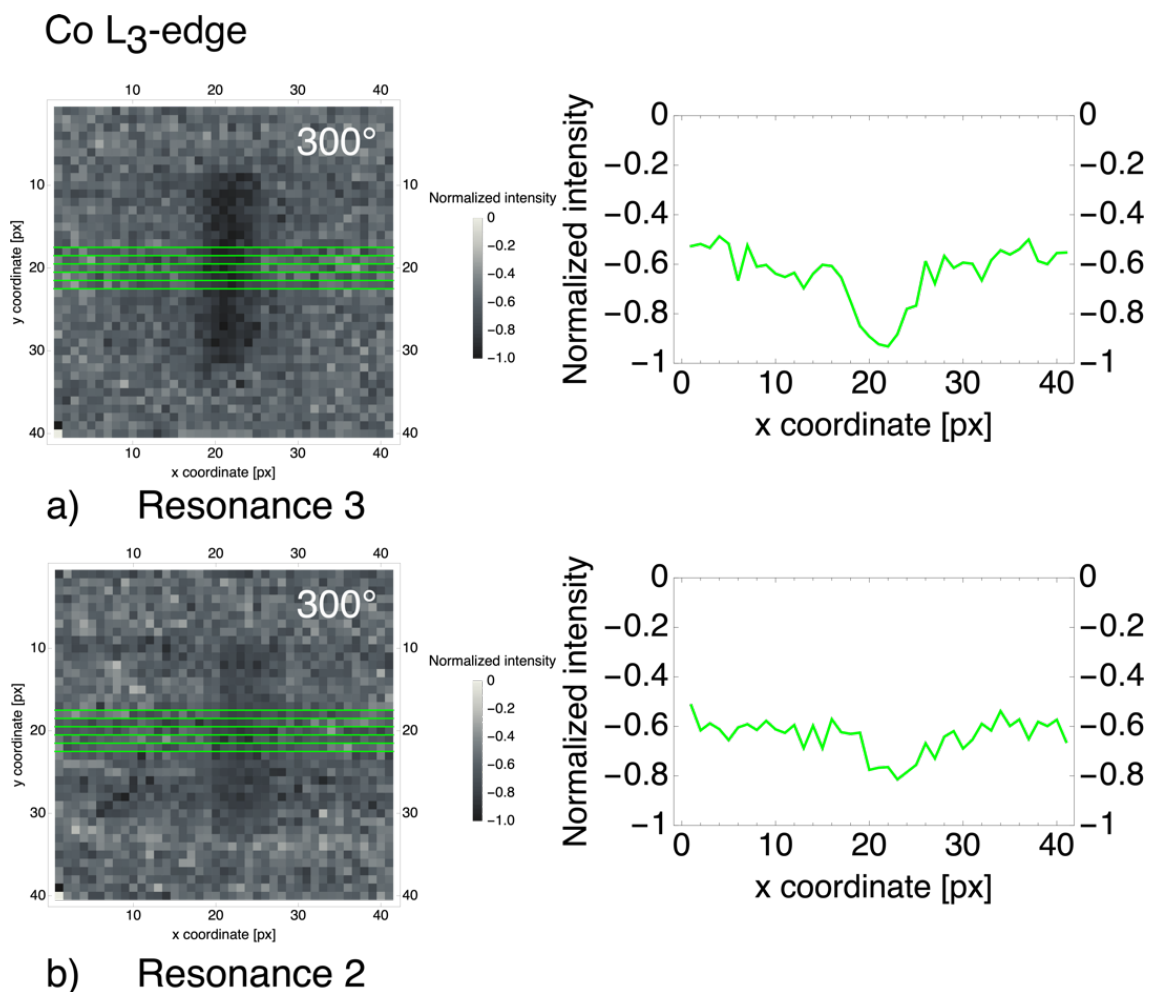


Figure 17: Line scans of the STXM-FMR images recorded at the Co L_3 edge for resonance 3 (a) and resonance 2 (b)). For comparison the images were normalized to the 0 to -1 range. The averaged intensity of the linescans is plotted to the right.

This interpretation is also supported by micromagnetic simulations using MuMax3 [124], which were performed for a single Co stripe (2048 nm x 512 nm x 32 nm) and a Py disk (2560 nm x 32 nm) / Co stripe (2048 nm x 512 nm x 32 nm) bilayer microstructure. The selected simulation parameters are for Py: $A_{\text{ex}} = 13 \cdot 10^{-12}$ J/m, $M_{\text{sat}} = 860 \cdot 10^3$ A/m and for Co $A_{\text{ex}} = 30 \cdot 10^{-12}$ J/m, $M_{\text{sat}} = 1420 \cdot 10^3$ A/m, both values of A_{ex} are taken from the OOMMF database [27], both values of M_{sat} are taken from [13]. In the simulations an energy minimization was processed (see chapter 3.5). The orientation of the magnetization is shown in Figure 18, for the simulation an external magnetic field of 85 mT, resembling the experimental value of the coupled resonance, was applied perpendicularly to the long sides of the stripe. Within the Py disk (Figure 18 a)) the magnetization is orientated parallelly along the direction of the external magnetic field with deviations at the position of the Co stripe, showing a rhomboid-shaped area with field parallel orientation of the magnetization confined by a differently orientated magnetization starting at the long sides of the stripe. The orientation of the magnetization within the disk corresponds to its orientation within the Co stripe, as shown in Figure 18 b), resembling the rhomboid-shaped area with field parallel magnetization alignment. The different orientation of the magnetization along the long sides of the Co stripe result in a higher resonance field of these sides (compare to the higher demagnetization field intensity in Figure 19), which is located at 344 mT in the conventional FMR measurements (Figure 14) [48].

Figure 19 a) shows the stray- /demagnetization field intensity of the Py disk, the dipolar coupling between the Co stripe and the Py disk is clearly visible at the position of the Co stripe (compare to the magnetization orientation in Figure 18). From the top edge to the lower disk edge a rhomboidally shaped area with a demagnetization field intensity of about 75 mT is visible confined by boundaries with demagnetization field values up to about 125 mT. This observation is corresponding to the orientation of the magnetization pictured in Figure 18. Outside this area, the demagnetization field intensity also is about 75 mT at the position of the stripe. The intensity decreases along the x-direction (Figure 11) to values slightly above 0 mT and increases while approaching the disk edges to values up to about 200 mT. The stray- / demagnetization field intensity of the Co stripe is depicted in Figure 19 b), showing the highest intensity along the long edges of the stripe with values up to 450 mT at

the centers of the long side edges. The observations made in Figure 19 clearly show the influence of magnetic dipolar coupling between the Py disk and the Co stripe.

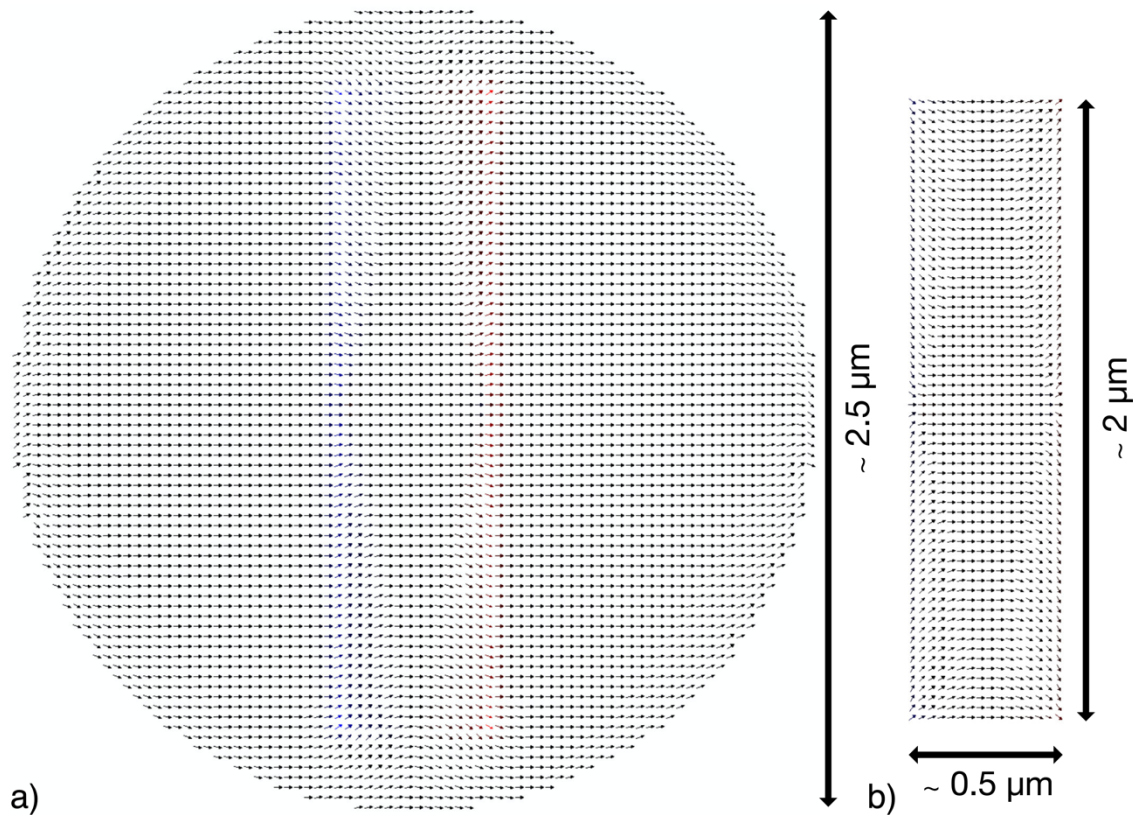


Figure 18: Two-dimensional representation of the magnetization for the simulated bilayer microstructure a) the Py disk, b) the Co stripe at $|B_{Ext}| = 85$ mT along the x -direction has been applied perpendicular to the long sides of the stripe.

The color code fit analysis (see chapter 3.4 and [103]) was applied to the STXM-FMR data, to reveal information on the phase and amplitude distribution not visible in Figure 16. At the field of resonance 1 (Py), showing data recorded at the Ni L_3 edge, Figure 20 a) depicts a homogenous distribution of the relative phase of about 90° and an amplitude distribution showing more pronounced pixels at the position of the Co stripe indicating a weak exchange coupled precession between the resonating Py disk and the weakly precessing Co [48].

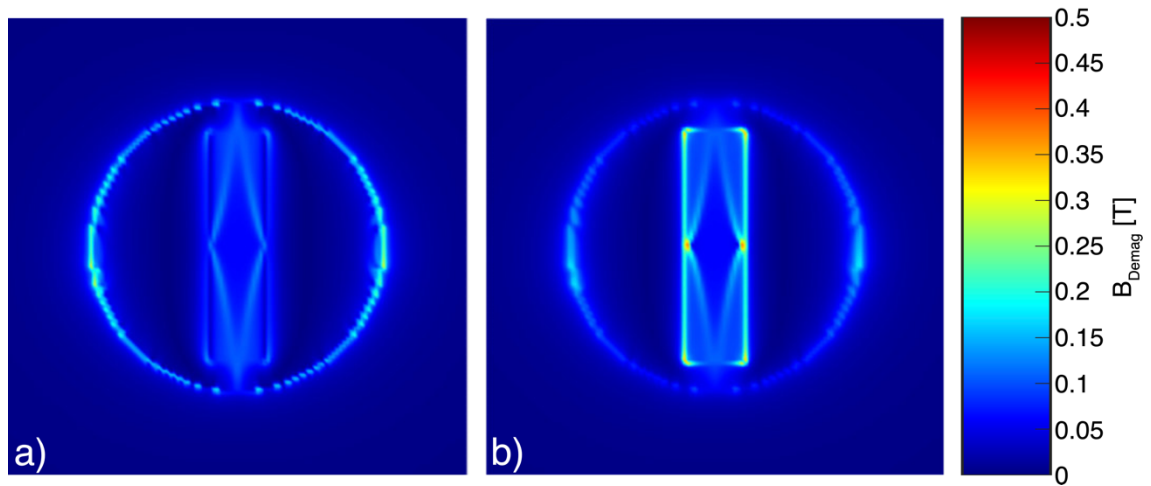


Figure 19: Simulated stray-/demagnetization field intensity viewed from the z -direction for a) the Py disk and b) the Co stripe. Figure adapted from [48].

At the Co L_3 edge (Figure 20 d)) only a weak excitation of the Co stripe can be observed displaying a weak, but homogeneous amplitude distribution and a relative phase of about 90° , with a deviation at the stripe center showing a relative phase between 60° and 90° , revealing an inhomogeneous excitation in this part of the stripe. This result confirms the assumption of a precession of the not-saturated Co magnetization, which is caused by an angular momentum hand-over from the Py disk, which results in a different phase within the Co at the yellow-colored parts of the stripe [48]. At the field of resonance 2 a homogenous distribution of the relative phase of about 90° is visible with pixels with higher brightness at the top and bottom location, where the edges of the Co stripe are situated on top (Figure 20 b)) [48].

Figure 20 e) shows a uniform relative phase of about 90° at the center of the Co stripe, while at the upper and lower edges a relative phase of about 60° can be seen, originating in the slightly different orientation of the magnetization with respect to the alignment along the direction of the external field, due to the stray field exiting and entering at these poles [48].

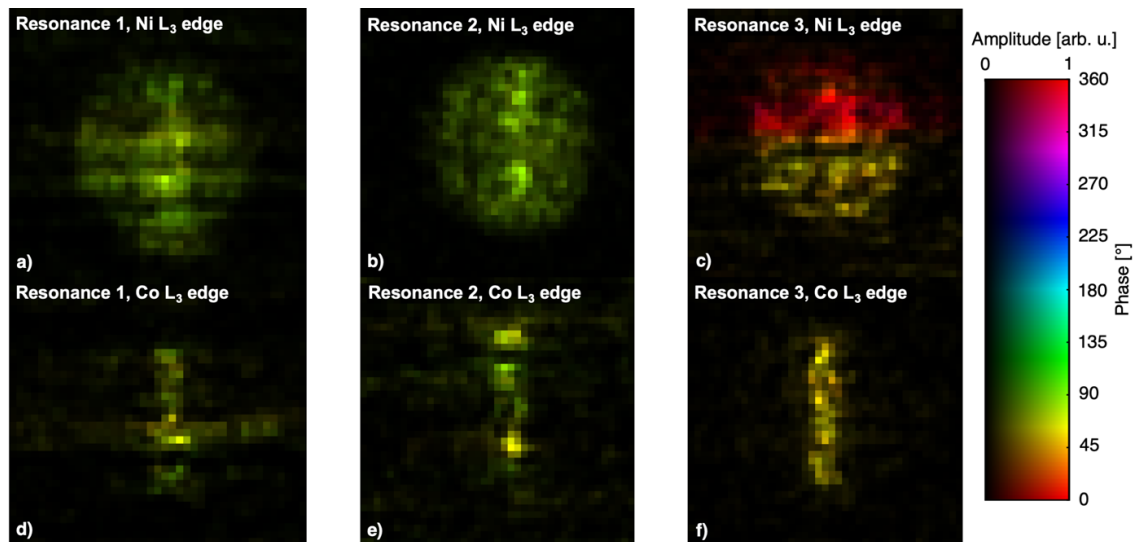


Figure 20: Results of the color code fit analysis for the STXM-FMR data of the Py/Co sample. b) and e) are taken from [48]. The color bar was adapted from B. Zingsem for [48]

The images presented in Figure 20 c) and f), which show the STXM-FMR data recorded at resonance 3 at the Ni L_3 and Co L_3 edges, have to be handled cautiously. Due to a phase shift in the microwave synchronization board within the measurement (see appendix: Figure 85), Figure 20 c) shows a relative phase divided into an upper part with a phase value of $0^\circ/360^\circ$ and a lower part with a phase value of about 60° . In between is a transition phase area with a value of about 45° . The transition between the phases is abrupt without a visible phase gradient, which supports the presence of the two relative phases due to the reported phase shift during the measurement. Therefore, no additional information to the grayscale STXM-FMR images shown in Figure 16 and in appendix 7.3 can be obtained from this image. Figure 20 f) shows the result of the color code fit analysis for the STXM-FMR measurement taken at the Co L_3 edge at resonance 3. The homogeneous phase distribution of about 60° , indicates a uniform excitation of the Co stripe. The relative phase value deviates from the observation made in Figure 15 b), which reveals a relative phase of about 90° . The origin of this deviation is unclear, but it can be concluded, that Figure 20 f) as well as Figure 16 f) show both a uniform excitation of the Co stripe, as it is expected for the Co main resonance.

In Figure 16 as well as in Figure 20 a weak oscillation at the Si_3N_4 membrane surrounding the sample is visible. In [46] this observation is attributed to an antenna-

like effect of the cabling of the avalanche photodiode, detecting standing waves originating in the used microwave radiation, which can result in additional detected counts. An additional possible, presumably larger, contribution to the background oscillation is attributed to stray field oscillations induced by the microwave, as it has been shown in the PhD thesis of B. Zingsem in the scope of Transmission Electron Microscopy detected magnetization dynamics and micromagnetic simulations [40] (not published as of July 2020).

By employing STXM-FMR it was possible to confirm that the resonances 1 and 3 originate in the Py disk and the Co stripe, respectively [48]. In addition, the excitation of the constituent, which is not in resonance at the respective external field value, due to an angular momentum transfer, could be shown, which cannot be extracted from the conventional FMR measurement [48]. While the general assignment of resonance 1 and 3 to the Py disk and the Co stripe is expectable, the origin of resonance 2 as a coupled resonance, at which both constituents resonate was only possible due to the STXM-FMR measurement. Furthermore, the color code fit analysis revealed an inhomogeneous excitation of the Co stripe at the stripe poles caused by the stray field [48]. Magnetic dipolar coupling could be identified as an additional component next to exchange coupling as the origin of the observed behavior of both sample parts at the investigated resonances [48].

4.2. Visualization of standing spin waves in different Py stripe arrangements

In chapter 4.1, angular momentum transfer and coupling phenomena in a Py/Co bilayer microstructure were investigated at the uniform resonances of each element. In addition, a dipolarly influenced exchange coupled resonance of both ferromagnetic constituents was detected, which deviates from the known observed behavior of equally sized ultrathin ferromagnetic films [48]. In the scope of spin wave based computing, e. g. [4, 6, 7, 125, 126], standing uniform and non-uniform spin wave modes in various Py stripe ensembles are visualized by STXM-FMR and the influence of the presence of a second stripe is investigated. The results in this chapter of the thesis have been published in part in [30].

Conventional FMR measurements in combination with micromagnetic simulations on a single Py stripe ($5.04 \mu\text{m} \cdot 0.59 \mu\text{m} \cdot 0.056 \mu\text{m}$) were done in [15], showing in the spectra a uniform resonance and four non-uniform modes, which were visualized by micromagnetic simulations. The external magnetic field was orientated in-plane perpendicularly towards the long stripe side [15]. With STXM-FMR it was possible to experimentally visualize these modes of a single Py stripe, albeit the STXM-FMR results are located at lower resonance fields, as the measurements were performed at a frequency of 9.446 GHz [30] with $\underline{B}_{\text{Ext}}$ orientated along the easy axis of the stripe in comparison to $f = 14.13 \text{ GHz}$ in [15] and $\underline{B}_{\text{Ext}}$ along the in-plane hard axis.

4.2.1. Sample overview

Three types of Py ($\text{Ni}_{80}\text{Fe}_{20}$) stripe samples have been produced employing two-step lift-off lithography (electron beam and optical) by S. Pile at the Johannes Kepler University in Linz, Austria. The samples consist of a single Py stripe with a length of $5 \mu\text{m}$, a width of $1 \mu\text{m}$ and a thickness of $0.03 \mu\text{m}$ and two arrangements of Py stripes each with the aforementioned dimensions in T- and L-shape geometries. In the first step the Py stripes were produced on a Si_3N_4 membrane with 200 nm thickness. The T- and L-shape arrangements are positioned with a $2 \mu\text{m}$ distance between the

stripes [30]. Each stripe has an oxidation protection layer of 5 nm Al on top [30]. In the second step the micro-resonator was applied with the resonator loop around the samples. A schematic overview of the samples geometries is shown in Figure 21.

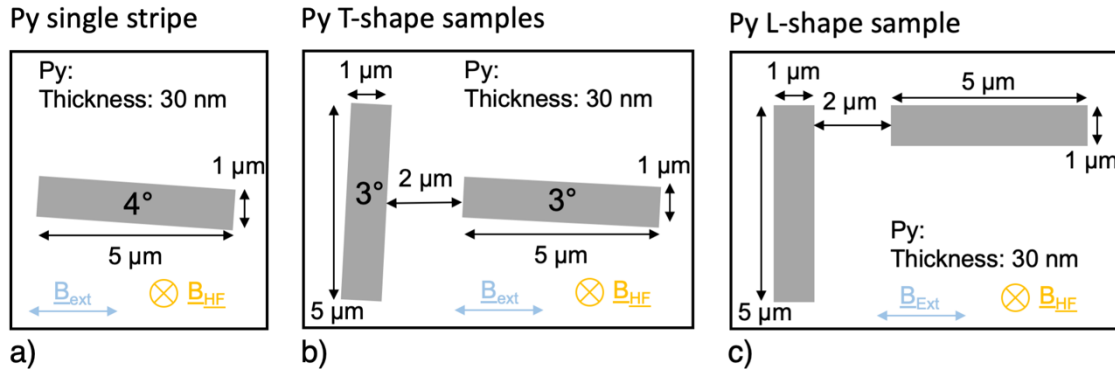


Figure 21: Schematic overview on the Py stripe sample geometries. In the micro-magnetic simulations the external field has been tilted correspondingly to the orientation of the sample in the experiment.

For the single Py stripe and the Py T-shaped stripe arrangement in-plane tilting angles of the samples with respect to $\underline{B}_{\text{Ext}}$ of about 4° and 3° are assumed. For the simulations, $\underline{B}_{\text{Ext}}$ was tilted in-plane with respect to the experimental sample orientation, as a turned sample in the simulation grid results in simulations artifacts.

The demagnetization factors for a single stripe are given in Table 2 using the coordinate system indicated in Figure 82. The shape anisotropy easy axis is directed along the stripes' long sides, resulting in the vertical Py stripe having $\underline{B}_{\text{Ext}}$ orientated perpendicular to its easy axis. As the result the resonance field of this stripe is at a higher value (123 mT, simulation) as the horizontal stripe (80 mT, simulation), as shown in Figure 23 [30].

Demagnetization factor	Horizontal stripe	Vertical stripe
N_1 eq. (A1)	0.046	0.009
N_2 eq. (A2)	0.945	0.945
N_3 eq. (A2)	0.009	0.046

Table 2: Demagnetization factors for the horizontal and vertical stripe calculated using equations (A1) to (A3).

4.2.2. Micromagnetic simulations of the Py stripe ensembles

The magnetization response excited at 9.446 GHz [30] was simulated using MuMax3 (see chapter 3.5 and [29]) for the above samples. The frequency corresponds to the excitation in the STXM-FMR measurements (chapter 4.2.3 to 4.2.6). The energy minimization method presented in [108] was used in addition to the MuMax3 build-in “relax()” function [29]. The simulation parameters are given in Table 3.

A_{ex} [J/m]	M_{sat} [A/m]	Cell size	Grid size
$13 \cdot 10^{-12}$	$7.2 \cdot 10^5$	$(32 \text{ nm})^3$	$264 \cdot 180 \cdot 1$

Table 3: Parameters for the micromagnetic simulations of the Py stripe arrangements excited at 9.446 GHz. The A_{ex} taken from the OOMMF database, OOMMF [27]. M_{sat} is obtained from magnetization measurements of Py samples at Johannes Kepler University Linz.

Due to the xy-dimensions of the stripe ensembles in the micrometer range, the cell size was selected larger than the exchange length of 6.3 nm, which was calculated using the parameters given in Table 3. The simulated FMR absorption spectra for the single stripe, the T-shape, and the L-shape stripe arrangements are presented for the tilting angles of the external magnetic field corresponding to the experimental geometry in Figure 22 and Figure 23. The resonances in the range of the STXM-FMR measurements are indicated.

For the single Py stripe the main resonance is located at 80 mT (Figure 22). For the stripe ensembles, two main resonances can be observed, at 80 mT the uniform resonance of the horizontal stripe can be found, while at 123 mT the uniform resonance of the vertical stripe is located [30]. The spectra for the T- and L-shape geometry (Figure 23) show no difference in resonance positions and number of resonances [30]. For all three stripe arrangements several spin wave modes can be seen, which will be visualized in part by means of STXM-FMR and micromagnetic simulations in chapters 4.2.4 to 4.2.6. As all simulations were performed at the same frequency of 9.446 GHz and an amplitude of 0.5 mT the resonance intensities can be compared, which is shown in Table 4. The highest deviations are between the Py single stripe

and both stripe ensembles, e. g. for the resonance at 80 mT the signal intensity of the single stripe is 48.2 % higher than for the T-shape arrangement and 49.1 % higher than the signal of the L-shape arrangement. The higher intensity of the signals of the single stripe is attributed to the missing stray-field influence by the 2nd stripe.

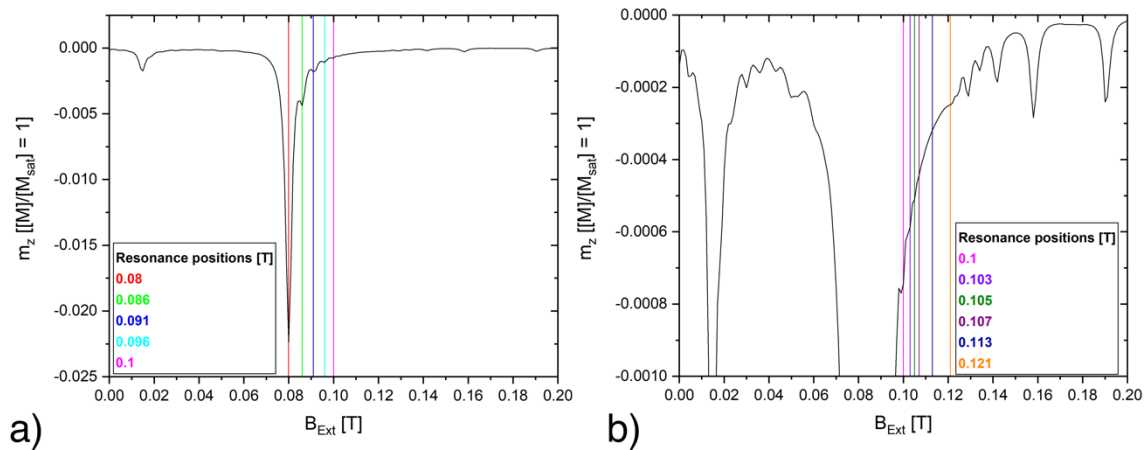


Figure 22: a) Simulated FMR spectrum for the single Py stripe simulated with a tilting angle of 4° (see Figure 21). b) Magnification of the simulated FMR spectrum for the single Py stripe simulated with a tilting angle of 4° (see Figure 21). The resonance positions in the range of the STXM-FMR measurements are indicated in the graph.

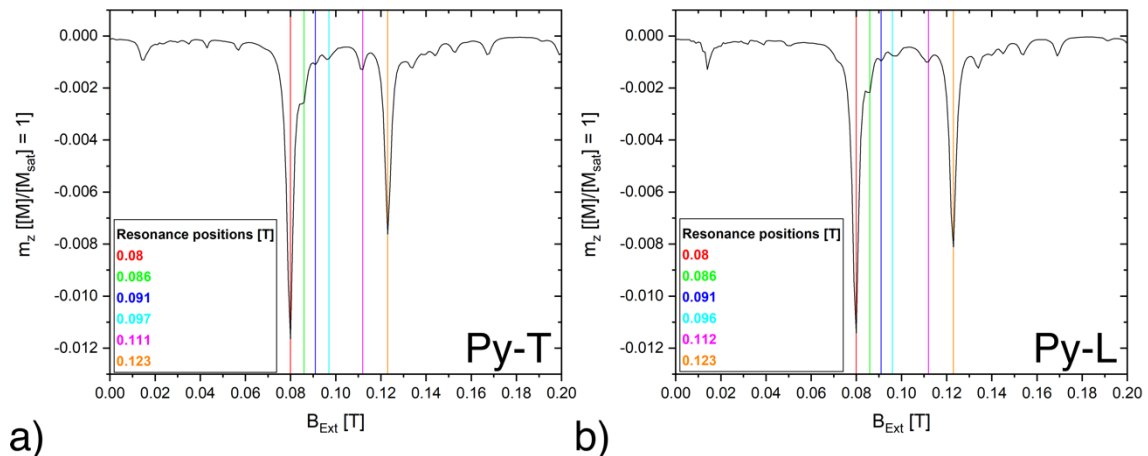


Figure 23: a) Simulated FMR spectrum for the T-shaped Py stripe arrangement simulated with a tilting angle of 3° (see Figure 21). b) Simulated FMR spectra for the L-shaped Py stripe arrangement. The external magnetic field is orientated along the horizontal stripe. The resonance positions in the range of the STXM-FMR measurements are indicated in the graph.

$ \mathbf{B}_{\text{Ext}} $	$I_{\text{Py-Str.}}$	$I_{\text{Py-T}}$	$I_{\text{Py-L}}$	Deviation $I_{\text{Py-Str.}} / I_{\text{Py-T}}$	Deviation $I_{\text{Py-Str.}} / I_{\text{Py-L}}$	Deviation $I_{\text{Py-T}} / I_{\text{Py-L}}$
[T]	[arb. u.]	[arb. u.]	[arb. u.]	[%]	[%]	[%]
0.08	-0.0224	-0.0116	-0.0114	48.2	49.1	1.7
0.086	-0.0044	-0.0026	-0.0021	40.9	52.3	19.2
0.091	-0.0018	-0.0011	-0.0010	38.9	44.4	9.1
0.096/ 0.097	-0.0011	-0.0009	-0.0007	18.2	36.4	22.2
0.1	-0.0007					
0.103	-0.0006					
0.105	-0.0005					
0.107	-0.0004					
0.111/ 0.112		-0.0013	-0.0010			23.1
0.113	-0.0003					
0.121	-0.0002					
0.123		-0.0076	-0.0081			-6.6

Table 4: Intensities of the simulated FMR signal for the Py single stripe, T- and L-shape geometry with deviations for corresponding spin wave modes.

To visualize the stray/demagnetization field intensity/distribution micromagnetic simulations performing an energy minimization at the resonance fields indicated in Figure 22 and Figure 23 were performed. All following visualizations are viewed from the z-direction (Figure 11).

The averaged demagnetization, exchange, Zeeman, and total energy densities for the single Py stripe, calculated by the micromagnetic simulation, are shown in Figure 24. As magneto crystalline anisotropy is not taken into account in the simulation, the corresponding energy density term [29] is not calculated and therefore it is not shown. The dominating energy contribution with respect to its absolute value is the Zeeman energy density, regarding the influence of the external magnetic field (Figure 24 c)). As a logical consequence, the absolute value for this energy density decreases with decreasing field strength.

The second-largest contribution is given by the demagnetization energy density shown in Figure 24 a). The demagnetization energy density increases with increasing $|\underline{B}_{\text{Ext}}|$ as it depends on the magnetization [29]. The exchange energy density (Figure 24 b)) is the smallest contribution to the total energy density, decreases with increasing $|\underline{B}_{\text{Ext}}|$.

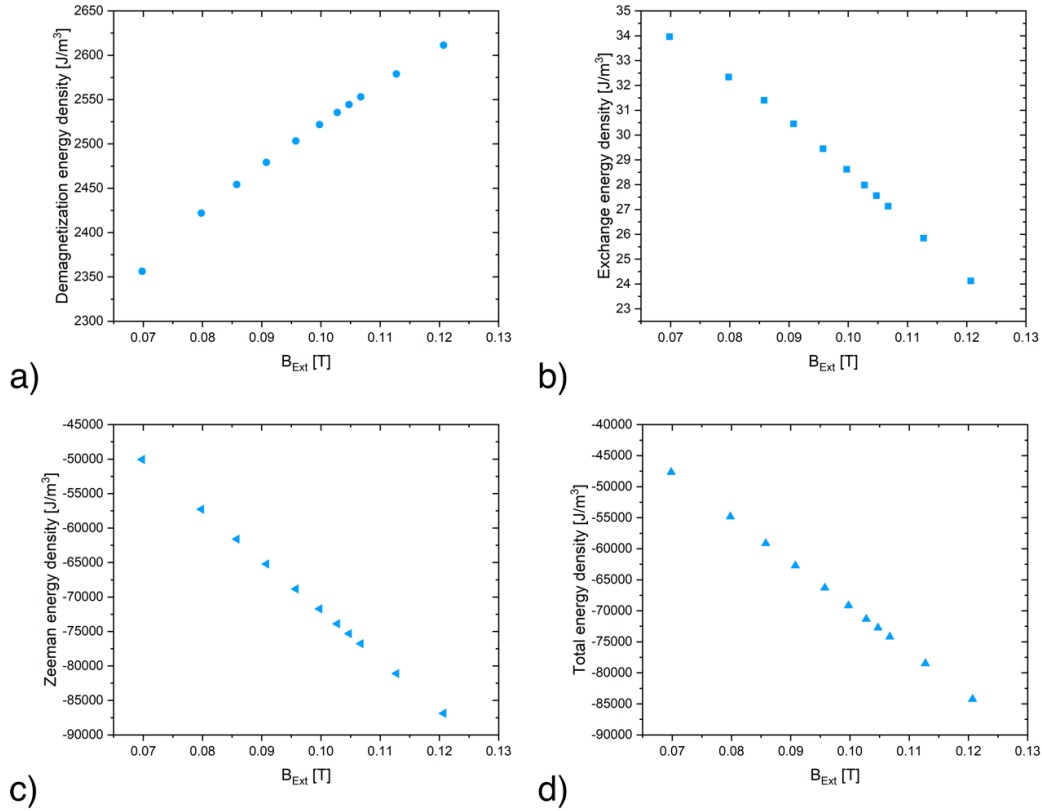


Figure 24: Averaged free energy densities for the single Py stripe for the different resonance fields.

As the selected cell size is above the exchange length of the sample material, the effect of exchange coupling and the resulting energy density cannot be taken as reliable values and are therefore given to show all contributions of the total energy density; its absolute value is increasing with increasing $|\underline{B}_{\text{Ext}}|$ due to the dominating contribution of the Zeeman energy density (Figure 24 d)).

Figure 25 visualizes the demagnetization and stray field intensity/distribution for the single Py stripe for $|\underline{B}_{\text{Ext}}| = 80$ mT. Figure 25 a) shows the highest intensity values up to about 180 mT along the short sides of the stripes, while along the long stripe sides and around the short stripe sides values of about 10 mT are visible. The stray field distribution shown in Figure 25 b) corresponds in general to the expected

distribution for a stripe dipole magnet, with distorted field lines due to the tilted angle of $\underline{B}_{\text{Ext}}$ of about 4° . As the stray- / demagnetization field intensity and distributions only slightly vary in intensity with increasing field, additional plots are not shown.

The stray- / demagnetization field intensity and distribution for the Py T-shape geometry are shown in Figure 25 c) and d) for $|\underline{B}_{\text{Ext}}| = 80 \text{ mT}$, which is orientated as pictured in Figure 21. Figure 25 c) shows an intensity of the stray- / demagnetization field of $< 10 \text{ mT}$ in wide areas of the simulated sample system. Within the vertical stripe, the demagnetization field decreases from about 180 mT at both long sides of the stripe to about 25 mT at the stripe center. Peak intensities up to 200 mT are visible at the upper and lower parts of the long sides of the stripe. Most parts of the horizontal stripes show the same intensity of $< 10 \text{ mT}$ as for the surrounding space, with increasing intensity of about 180 mT towards the short stripe edges. Peak intensities up to 200 mT are visible at the upper and lower parts of the short sides of the stripe. The stray field intensity decreases from the long side of the vertical stripe, which is orientated towards the horizontal stripe from about 180 mT directly at the stripe side to $< 10 \text{ mT}$ at the center between the stripes and increases towards the short side of the horizontal stripe again.

In Figure 25 d) the stray field distribution is shown. It clearly can be seen that in contrast to the stray field distribution shown for the single stripe in Figure 25 b), the stray field lines are distorted due to the presence of the 2nd Py stripe. Higher densities of stray field lines are symmetrically present at the top and the bottom of the long side of the vertical stripe and at the edges of the short sides of the horizontal stripe. Stray field lines enter and leave both stripes at the long sides in both cases, in contrary to the distribution of a single stripe with an external field perfectly aligned along the stripe exhibiting poles at the short edges, where the stray field leaves and enters the stripe.

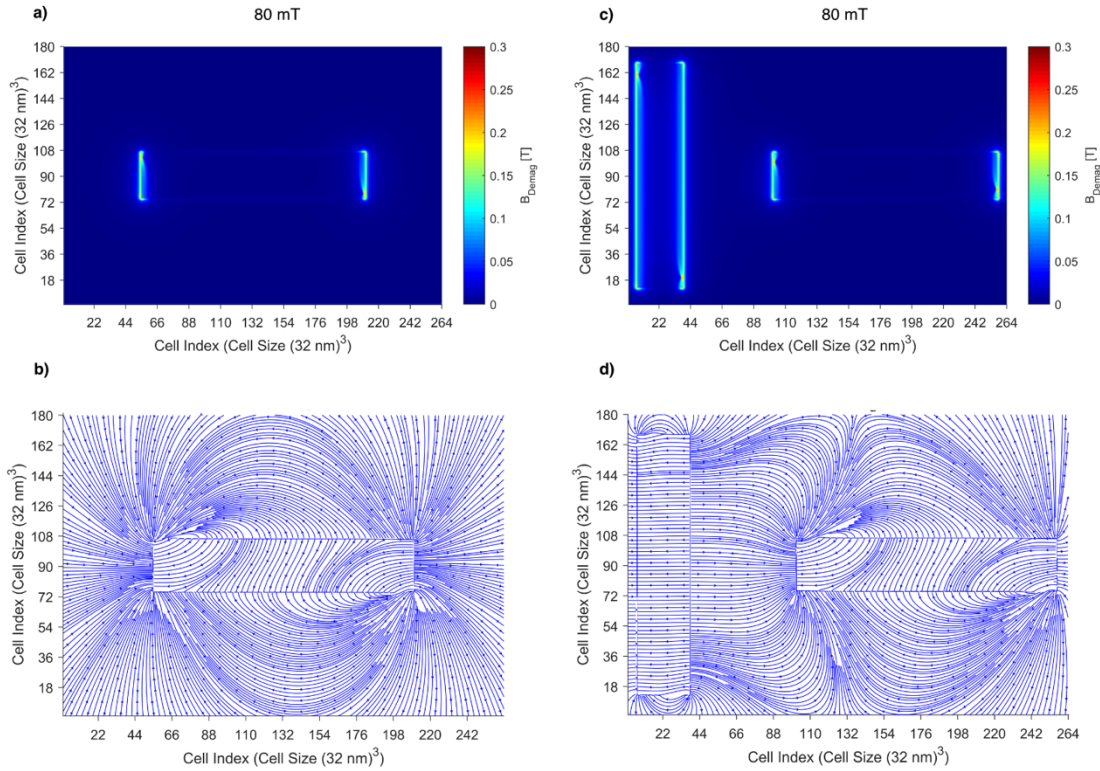


Figure 25: Stray- / demagnetization field intensity (a, c)) and distribution (b, d)) for the single Py stripe and the T-shape geometry with an external magnetic field of 80 mT.

The field lines of the demagnetization field within the vertical stripe are homogeneously oriented antiparallel to the orientation of $\underline{B}_{\text{Ext}}$ along the -x direction (see Figure 11 for the coordinate system), exhibiting curved field lines at the poles at the short stripe sides. The demagnetization field of the horizontal stripe exhibits a complex distribution caused by the tilted angle of $\underline{B}_{\text{Ext}}$ by 3°. As for the single stripe, the stray- and demagnetization field intensity and distribution vary only slightly with increasing $|\underline{B}_{\text{Ext}}|$.

The averaged free energy densities for the T-shaped Py stripe geometry are shown in Figure 26. As for the single Py stripe before the dominating energy contribution with respect to its absolute value is the Zeeman energy density for both stripes (Figure 26 e, f)), and the absolute value for this energy density increases with increasing field strength.

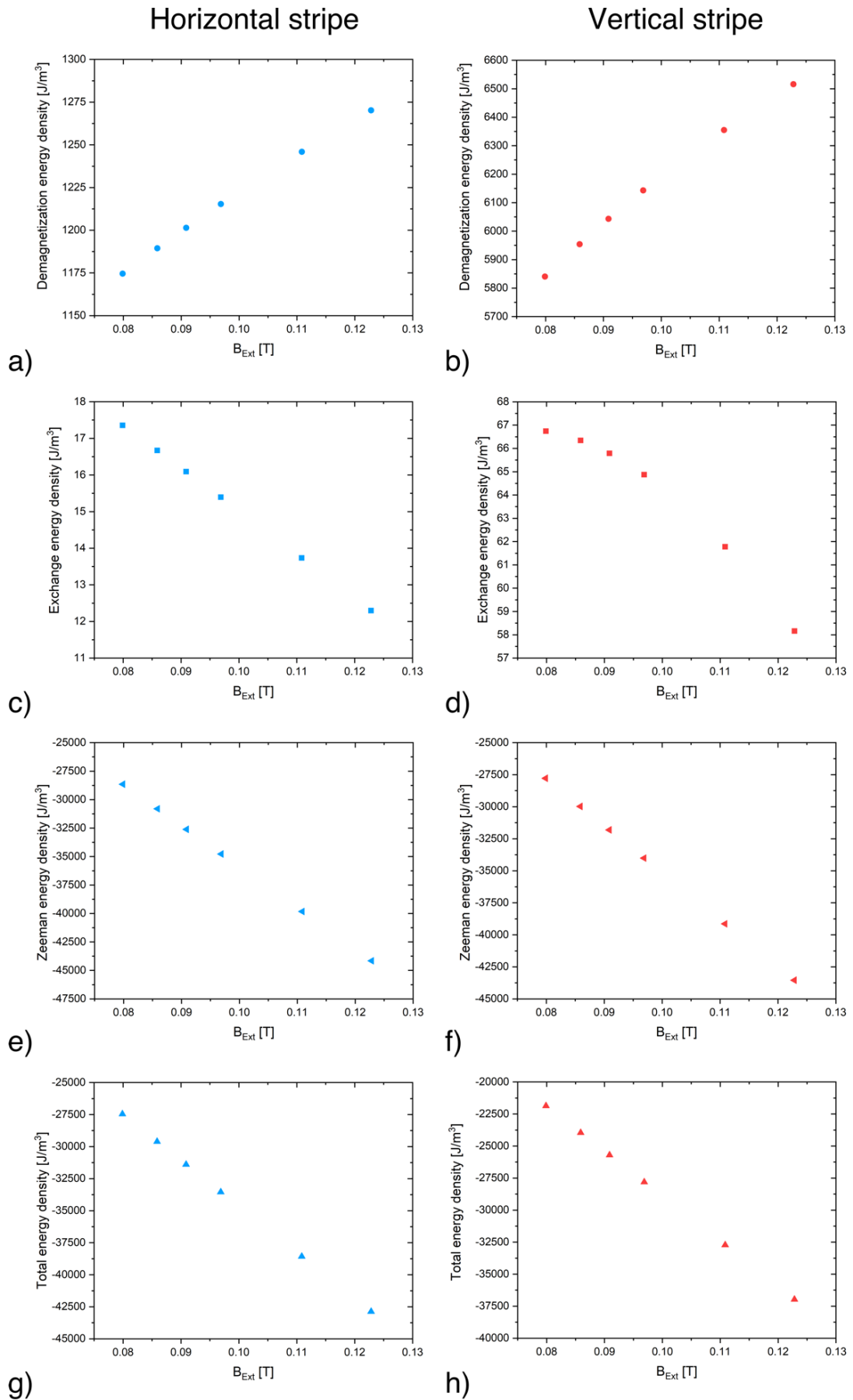


Figure 26: Averaged free energy densities for the horizontal and vertical Py stripe for the different resonance fields for the T-shaped sample geometry.

The second-largest contribution is given by the demagnetization energy density (Figure 26 a), b)), which is about 5.8 times lower for the horizontal stripe than for the vertical stripe. This shape anisotropy effect can be explained by the orientation of the horizontal stripe with its long easy axis orientated parallel to the $\underline{B}_{\text{Ext}}$.

The exchange energy density shown in Figure 26 c), d) is the smallest contribution, while for the horizontal stripe, a linear decrease with increasing $|\underline{B}_{\text{Ext}}|$ is visible, for the vertical stripe the data points show a curvature. As the selected cell size is above the exchange length the effect of exchange coupling and the resulting energy density cannot be taken as reliable values. The absolute value of the total energy density is increasing with increasing $|\underline{B}_{\text{Ext}}|$ due to the dominating contribution of the Zeeman energy density (Figure 26 g), h)).

The asymmetric L-shape stripe geometry causes an asymmetrically distributed stray field (Figure 27), showing asymmetrically located high field line densities at the upper and lower part of the long side of the vertical stripe (Figure 27 c), d)). High field line densities exist at the bottom edges of the horizontal stripe. In general, the demagnetization field lines are orientated antiparallely to the direction of $\underline{B}_{\text{Ext}}$ for both stripes with a distortion in the horizontal stripe caused by the vertical stripe. The parallel orientation of $\underline{B}_{\text{Ext}}$ to the horizontal stripe results in peak intensities located at the center of each short stripe side. The influence of the horizontal stripe on the vertical stripe causes an asymmetric position of the peak intensity at the side facing towards the horizontal stripe, while on the opposite stripe side it is located at the center, in contrast to the position near the upper and lower edges for the T-shape arrangement. The intensity values correspond to the observations in Figure 25 for the T-shaped ensemble.

The values and the behavior of the calculated energy densities deviate only slightly from the ones given in Figure 26 and show an equivalent development with changing $|\underline{B}_{\text{Ext}}|$. They are presented in the appendix in Figure 89.

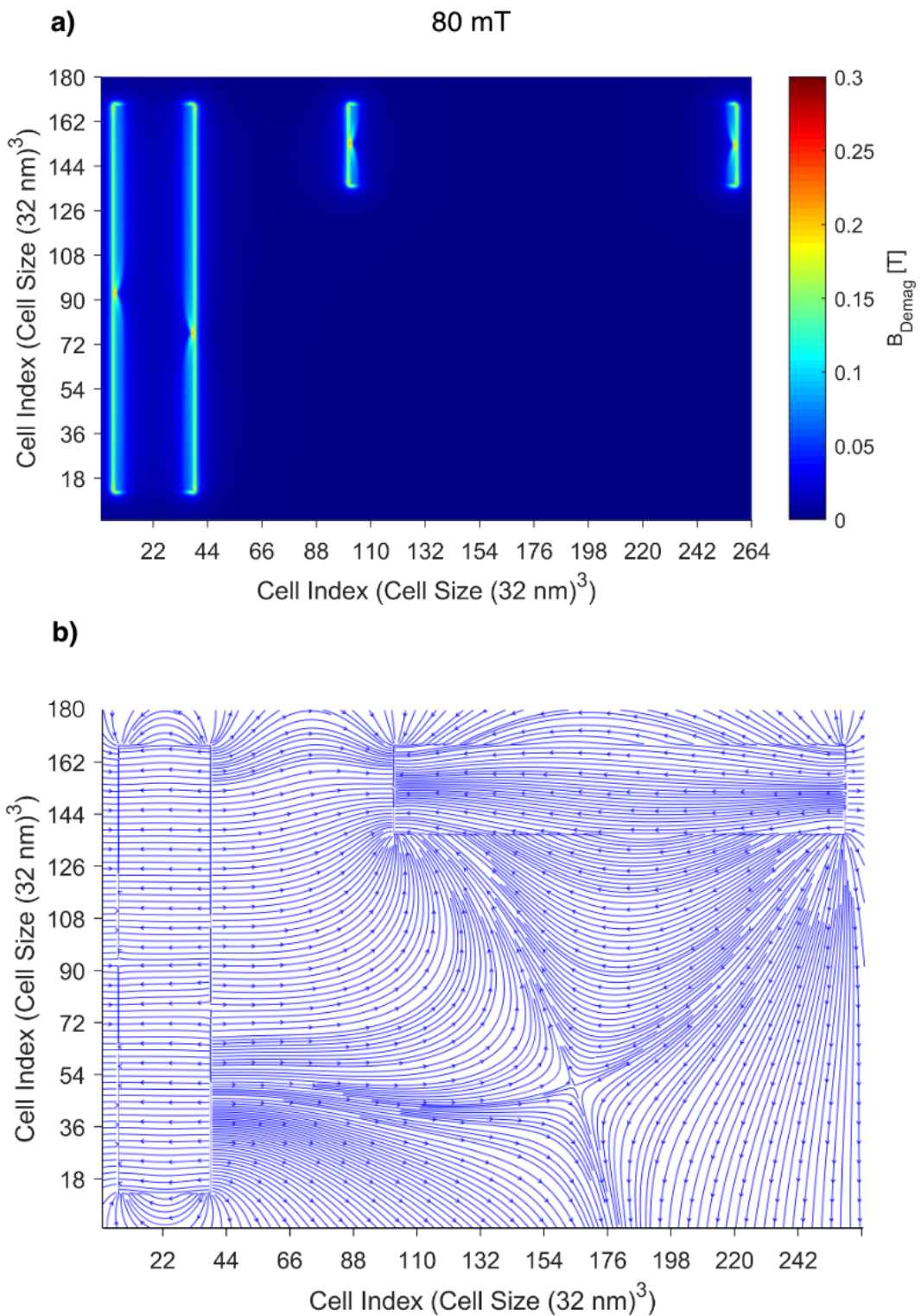


Figure 27: a) Stray- / demagnetization field intensity and b) distribution for the Py L-shape geometry with an external magnetic field of 80 mT.

The micromagnetic simulations reveal the distortion of the demagnetization- and stray field distribution due to an asymmetric stripe arrangement (L-shape sample)

and an in-plane tilted $\underline{B}_{\text{Ext}}$ (single Py stripe and T-shape sample). For each sample geometry, areas showing higher stray-field densities at the side edges of the stripes are visualized. The locations of these high-density field line areas are determined by the stripe arrangement. In the following, these results will be used to explain the observed properties of the measured spin wave modes. It will be explained that the here depicted influence of the stray field induces additional resonance conditions initiating so-called edge modes, see e. g. [119-122], which result in a directed oscillatory behavior of the observed spin waves in the experiments, as well as in the simulations.

4.2.3. STXM-FMR experiment introduction

The STXM-FMR measurements of the Py single stripe and the T, and L shape geometries were performed at the Ni L_3 edge [30] (865 eV) with a step size of 100 nm and a dwell time of 5000 ms. The microwave frequency was set to 9.446 GHz [30] with a power of 27 dBm (beamtime July 2018, T-shape geometry) and 29 dBm (beamtime November 2018, single stripe, T- and L-shape geometries). Selected datasets of measured spin wave modes are presented in this chapter, while additional datasets showing comparable spin wave modes are presented in appendix 7.5. For all STXM-FMR datasets the natural logarithm of the division of the data obtained with and without microwave excitation was taken, and a minimum-maximum normalization [127] was applied. One of the characteristics of a micro-resonator is the homogeneous distribution of the high-frequency magnetic field in the center area of the resonator loop, as it is demonstrated in e. g. [18] and [15]. By positioning the sample within the aforementioned area of the resonator loop, a uniform excitation of the sample is achieved.

The research of Kittel showed that standing spin waves [71] are the consequence of a uniform rf-excitation of a ferromagnetic sample [30, 72] (see also chapter 2.3). Taking into account the position of the Py stripe ensembles in the micro-resonator loop and the area of the homogeneous high-frequency magnetic field distribution [18], [15]; a uniform excitation of the samples can still be assumed. For each measured spin wave mode, the simulated m_z -component of the magnetization is shown as a two-dimensional representation for a tilting angle of $\underline{B}_{\text{Ext}}$ of 4° (singly Py stripe), of 3° (T-shape arrangement) and 0° , (L-shape arrangement). Due to technical issues concerning the Hall-probe measurements at both measurement beamtimes, the measured values of for $|\underline{B}_{\text{Ext}}|$ are not reliable and show deviations up to 20 mT. Measurements on the T-shape Py stripe geometry performed by A. Ney et al. [128] (reference to the unpublished dataset) at the MAXYMUS beamline [129] at the BESSY II synchrotron in Berlin were used to assign values of $|\underline{B}_{\text{Ext}}|$ to the corresponding spin wave modes. The assignment compares well to $|\underline{B}_{\text{Ext}}|$ obtained from the micromagnetic simulations. These unpublished measurements are going to be part of the PhD thesis of S. Pile and therefore are not presented as part of this thesis. In the following, the assigned values for $\underline{B}_{\text{Ext}}$ are stated with the Hall probe values

given in brackets. For the single Py stripe $|\underline{B}_{\text{Ext}}|$ corresponding to the micromagnetic simulation is given, with the Hall probe value given in brackets. All presented experimental visualizations have been blurred for better visibility.

4.2.4. Py single stripe

A close to uniform excitation within the single Py stripe imaged by STXM-FMR is shown in Figure 28. Subfigure a) presents the six recorded images of the magnetization cycle temporally separated by 18 ps.

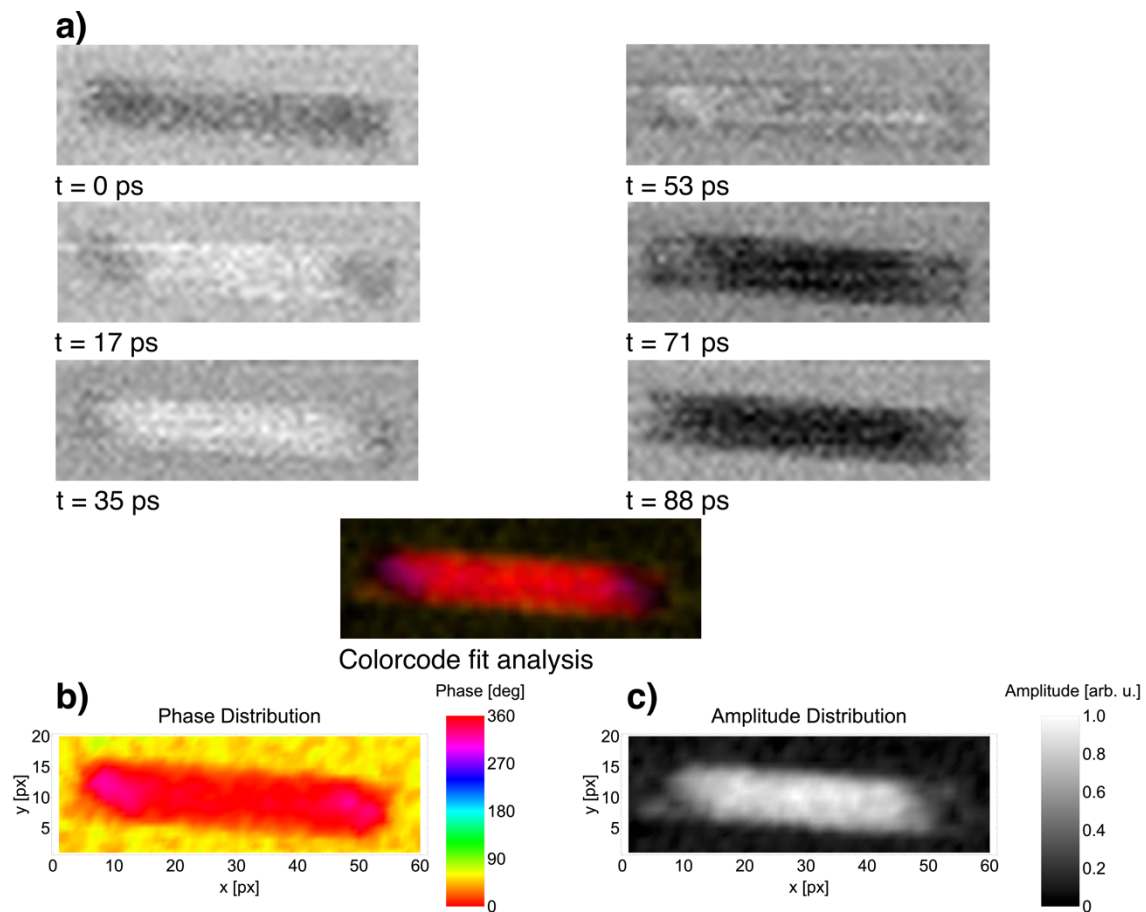


Figure 28: STXM-FMR data of the single Py stripe at a static bias field of 80 mT (100 mT) and a microwave power of 29 dBm. **a)** Microwave induced X-ray transmission for 6 timesteps with a time distance of about 18 ps. **b), c)** Distribution of the relative phase with respect to the timestep $t = 0$ and the normalized amplitude extracted out of the color-code fit analysis (chapter 3.4).

Black depicts a contrast below the average (grey), while white indicates the opposite. A mostly homogeneous contrast is visible within the stripe with slightly less intensity at both edges. The color code fit analysis (see chapter 3.4) reveals a close to uniform excitation with a phase relative to $t = 0$ ps of about 290° to $0^\circ/360^\circ$ in most areas of the stripe. At both stripe edges, a phase value of about 280° is visible (Figure 28 b)), which indicates the presence of a phase gradient of the magnetization between the stripe center and the edges, resulting in a close to uniform mode. For a uniform mode, a homogeneous phase distribution would be expected [71]. The normalized amplitude distribution shown in Figure 28 c) has its peak value at the stripe center showing a slight decrease towards both stripe edges. The origin of the different phase at the stripe edges is the result of the stray field distribution at the stripe edges, as pictured from micromagnetic simulations in Figure 25 a), b). It results in a directed oscillation of the spin wave from the center towards both stripe edges, a behavior unexpected for a standing wave, which would exhibit an alternating behavior of the anti-nodes without an oscillation to a certain direction. All investigated Py stripe samples presented in the current chapter 4.2 fulfill the boundary conditions for standing spin waves under a homogeneous excitation as described in [72-74].

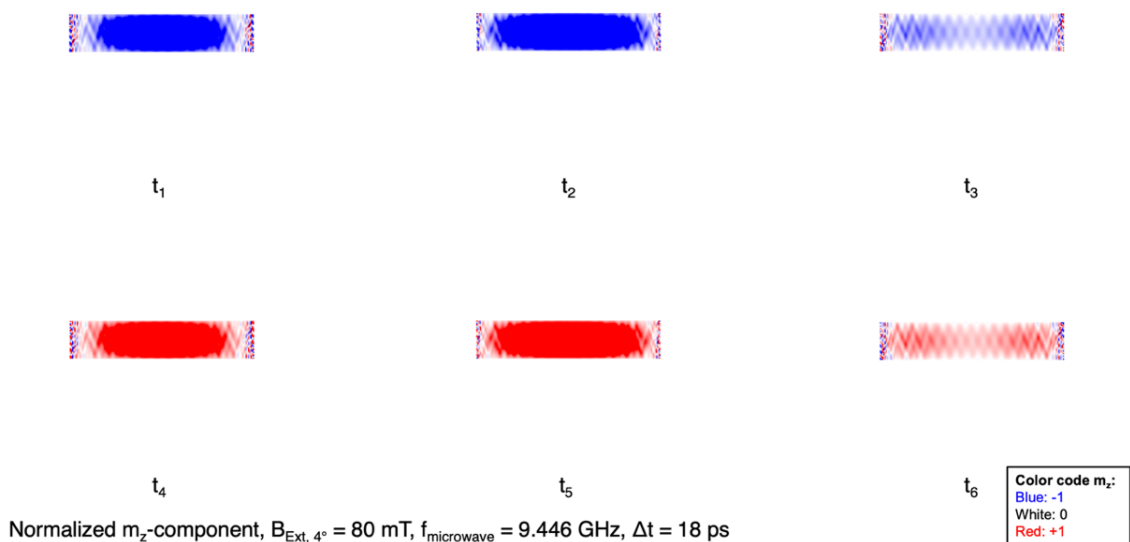


Figure 29: Two-dimensional representation of the simulated normalized m_z -component of the magnetization for $|\underline{B}_{Ext}| = 80$ mT. The external field is tilted by an angle of 4° (see Figure 21) to resemble the geometry of the experiment. Six images of the magnetization oscillation with a time distance of 18 ps are shown.

Due to the stray field influence located at the edges of the stripe, resonance conditions for the excitation of edge modes are fulfilled. This magnetic dipolar influence is described for Py stripes in [119-121] and for Py ellipses in [33]. The directed oscillatory behavior of such modes was demonstrated for Py dots in [122]. The manipulation of the localization of edge modes by the stray field of the tip of the used Ferromagnetic Resonance Force Microscope is described in [120]. In consequence this additional edge mode excitations lead to the presence of the observed phase gradient and the directed oscillatory behavior.

The weak coloring visible around the Py stripe indicates an oscillating background, which explained by the influence of the microwave radiation on the avalanche photo diode [46], as described in chapter 4.1.3. The oscillation of the simulated m_z component of the magnetization (for the color code see the inset of the figure) normalized to M_{sat} (Table 3) is shown for six time points in Figure 29 under an applied magnetic field tilted by 4° (Figure 21). A uniform excitation can be seen, corresponding to the experimental observations in Figure 28. The zig-zag patterns seen in the simulation result originates in the perfect stripe geometry without any roughness of the stripe sides and is regarded as a simulation artifact.

The modes observed in STXM-FMR and the micromagnetic simulations correspond to the observations on a single Py stripe at $|\underline{B}_{\text{Ext}}|$ of 252.5 mT (experiment) and 249.6 mT (simulation) in [15]. The difference in the resonance fields is due to the aforementioned orientation of $\underline{B}_{\text{Ext}}$ and the excitation at 14.13 GHz in [15] (chapter 4.2).

A resonant response only visible at the edges of the Py stripe is visualized in Figure 31 at a field below the uniform resonance mode at 80 mT. When taking into account an estimated field offset of about -20 mT, $|\underline{B}_{\text{Ext}}|$ of about 50 mT can be assumed. A magnification of the simulated FMR spectrum in Figure 22 shown in Figure 30 reveals the presence of a spin wave mode at 50 mT.

The STXM-FMR images in Figure 31 a) show a higher than average (grey) contrast at the long and short stripe edges with an average contrast in the stripe center. This reverts to a frame of lower-than-average contrast at timepoints 53 ps to 88 ps. The color code fit analysis reveals only a weak oscillatory behavior at the stripe center showing mostly dark and not saturated space, with a phase distribution of about 50° around the stripe center and a phase of about 40° at the four edges.

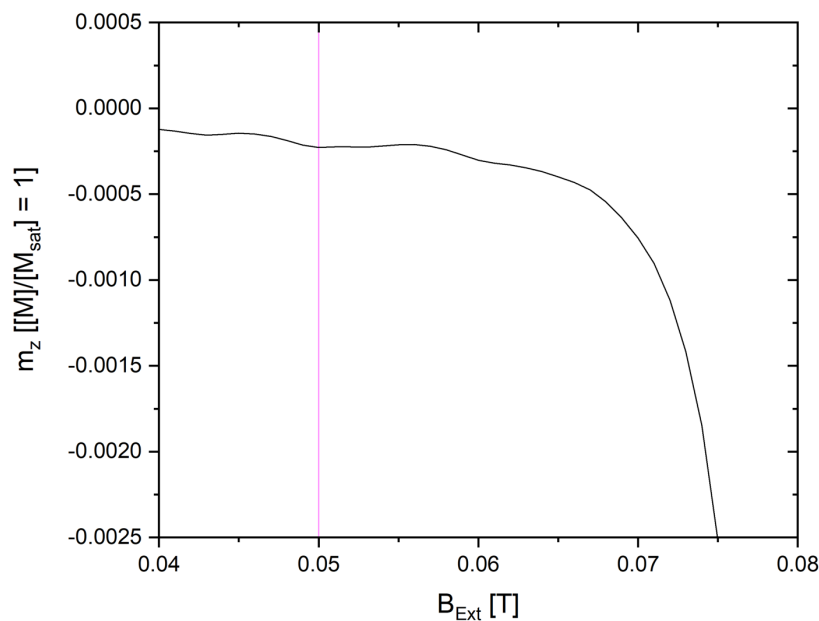


Figure 30: Magnification of the simulated FMR spectrum for the single Py stripe simulated with a tilting angle of 4° (see Figure 21). Indicated is the resonance at 50 mT.

At the stripe center, a phase of about $0^\circ/360^\circ$ to about 10° to 20° is visible, with a deviation at the left side of the stripe showing a phase of about 90° . This deviation is also visible in the STXM-FMR data, e. g. at time point $t = 71$ ps, showing a lower-than-average contrast at the left stripe side, corresponding to the observed relative phase of 90° at the same position.

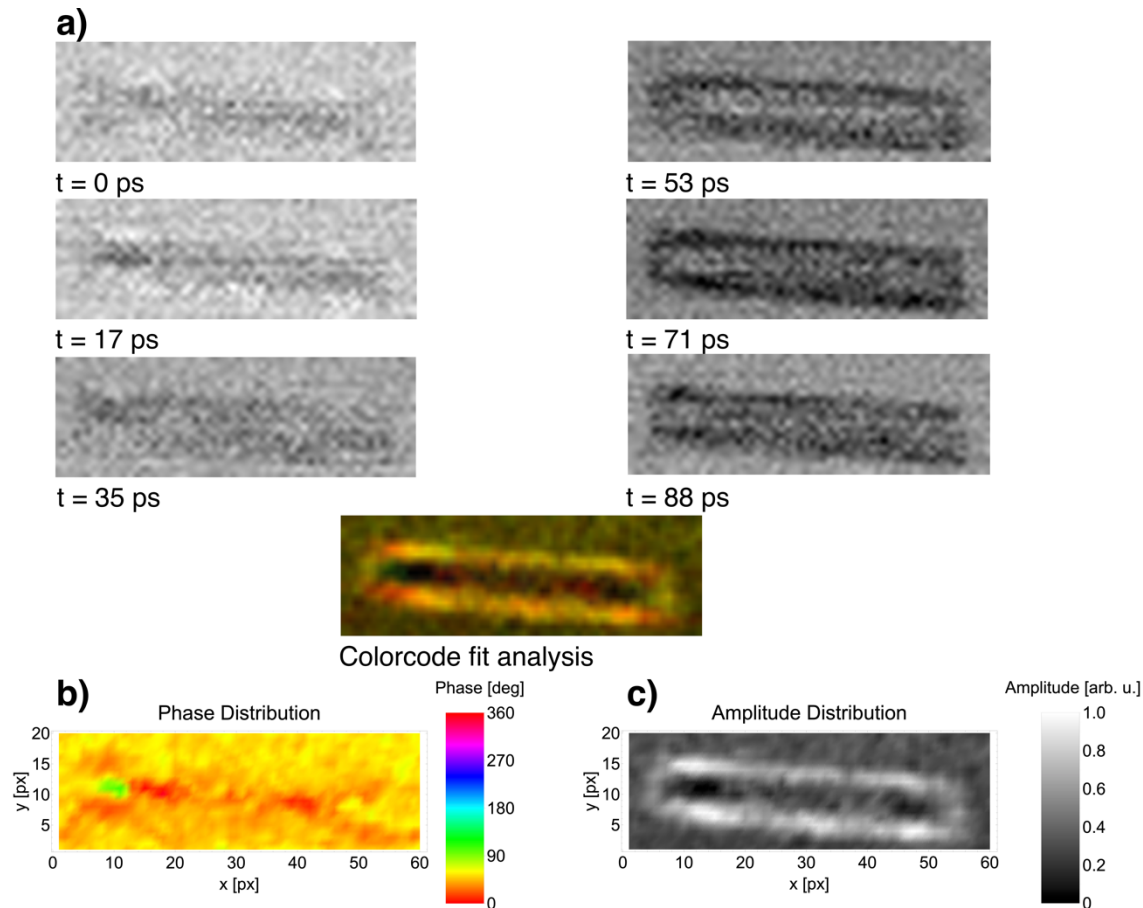


Figure 31: STXM-FMR data of the single Py stripe at a static bias field 70 mT (hall probe value) and a microwave power of 29 dBm. a) Microwave induced X-ray transmission for 6 timesteps with a time distance of about 18 ps. b), c) Distribution of the relative phase with respect to the timestep $t = 0$ and the normalized amplitude extracted out of the color-code fit analysis (chapter 3.4).

The amplitude distribution in Figure 31 c) shows a high amplitude around the stripe center with nearly no amplitude in the center itself. At the four stripe edges, the amplitude exhibits peak values. The observations point to an excitation of the Py stripe only at the edges, also shown by animating the STXM-FMR data shown in Figure 31 a). The phase gradient present at the stripe edges results in a directed oscillation from the long edge centers towards the outer sides of the stripe, as it was observed before. The origin of the phase gradient is attributed to an influence of the stray field, showing numerous stray field lines entering at the stripe center with a higher field line density at the long bottom side of the stripe (Figure 25 a), b). As stated before this leads to the additional excitation of edge modes, see e. g. [120] for the stray field induced localization of edge-modes.

Figure 32 shows the oscillation of the m_z -component of the magnetization normalized to M_{sat} (Table 3) for six timesteps of the simulation with a time distance of about 18 ps. The color code is shown in the inset of the figure. Two oscillating parts can be seen, an oscillating stripe center and an oscillating frame at all stripe edges. The magnitude of m_z is inverted between the center and the surrounding frame. The animation of the data shows that the oscillation of both parts is directed from the stripe center towards the outer stripe edges, resembling the experimental observations. While the experiment shows only a weak oscillation within the stripe center, the intensity of both oscillating parts in the simulation is equal. The zig-zag pattern seen in the simulated stripes is attributed to a simulation artifact due to the perfect geometry of the stripe, neglecting any roughness. A possible explanation for the different behavior of the stripe center between the experiment and the simulation is a deviation in the applied field, resulting in a pure edge excitation of the stripe, as the real value of $|\underline{B}_{\text{Ext}}|$ is not known due to the earlier mentioned lack of accuracy of the hall probe during the experiment. Nevertheless, the simulation confirms the directed oscillatory behavior of the frame surrounding the stripe center, and therefore, experiment and simulation are in good agreement.

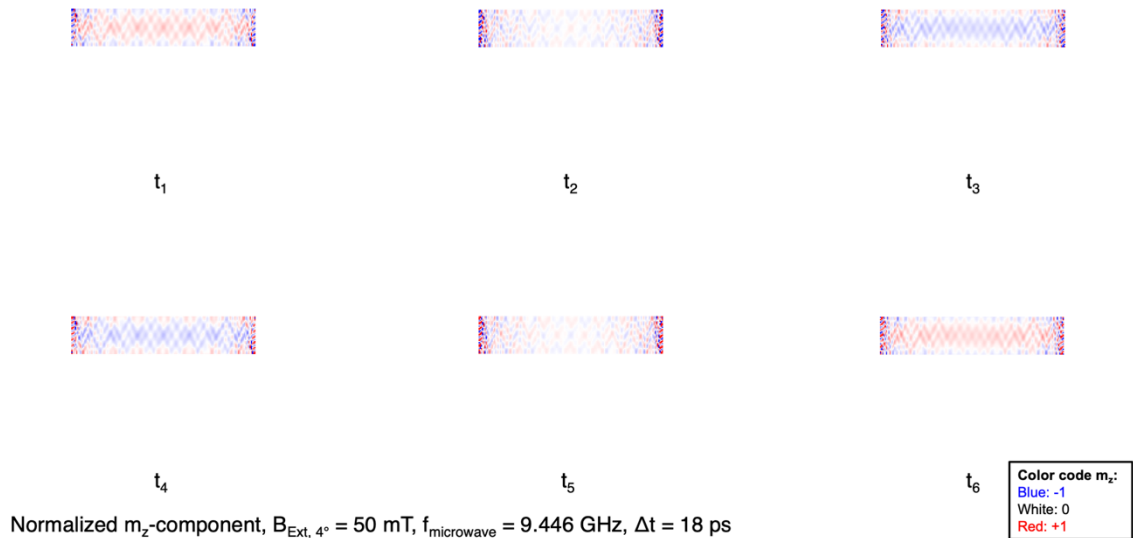


Figure 32: Two-dimensional representation of the simulated normalized m_z -component of the magnetization for $|\underline{B}_{\text{Ext}}| = 50 \text{ mT}$. The external field is tilted by an angle of 4° (see Figure 21) to resemble the geometry of the experiment. Six images of the magnetization oscillation with a time distance of 18 ps are shown.

An intermediate spin wave mode between a uniform excitation and a mode with three anti-nodes and two nodes (Figure 34) is shown in Figure 33 at

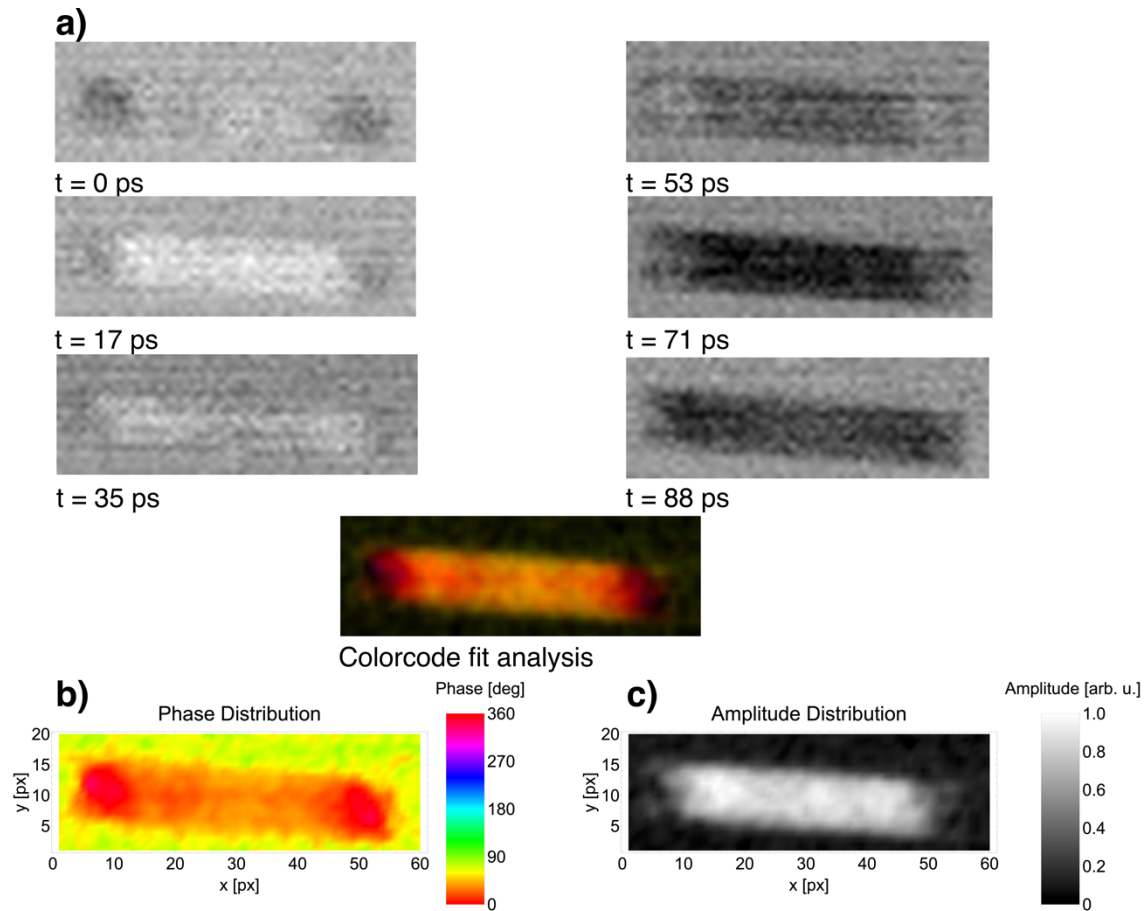


Figure 33: STXM-FMR data of the single Py stripe at a static bias field of about 83 mT (103 mT) and a microwave power of 29 dBm. a) Microwave induced X-ray transmission for 6 timesteps with a time distance of about 18 ps. b), c) Distribution of the relative phase with respect to the timestep $t = 0$ and the normalized amplitude extracted out of the color-code fit analysis (chapter 3.4).

The STXM-FMR contrast images in Figure 33 a) show a homogeneous contrast distribution in the stripe center with slightly weaker contrast at the stripe edges, which corresponds to the mostly homogeneous amplitude distribution within the stripe (Figure 33 c)) obtained from the color code fit analysis. The relative phase changes from about $0^\circ/360^\circ$ to 10° at the stripe edges to about 20° to 50° at the central stripe area. This larger phase gradient of the magnetization up to 50° due to the before stated stray field effects (Figure 25 a), b)), results in a more pronounced oscillatory

behavior directed from the stripe center towards the stripe edges than seen at ~ 80 mT.

Increasing $|\underline{B}_{\text{Ext}}|$ to about 91 mT results in a three anti-nodes and two nodes spin wave, corresponding to the mode shown as solid dark blue line in the absorption spectrum in Figure 22 a). The STXM-FMR images are shown in Figure 34.

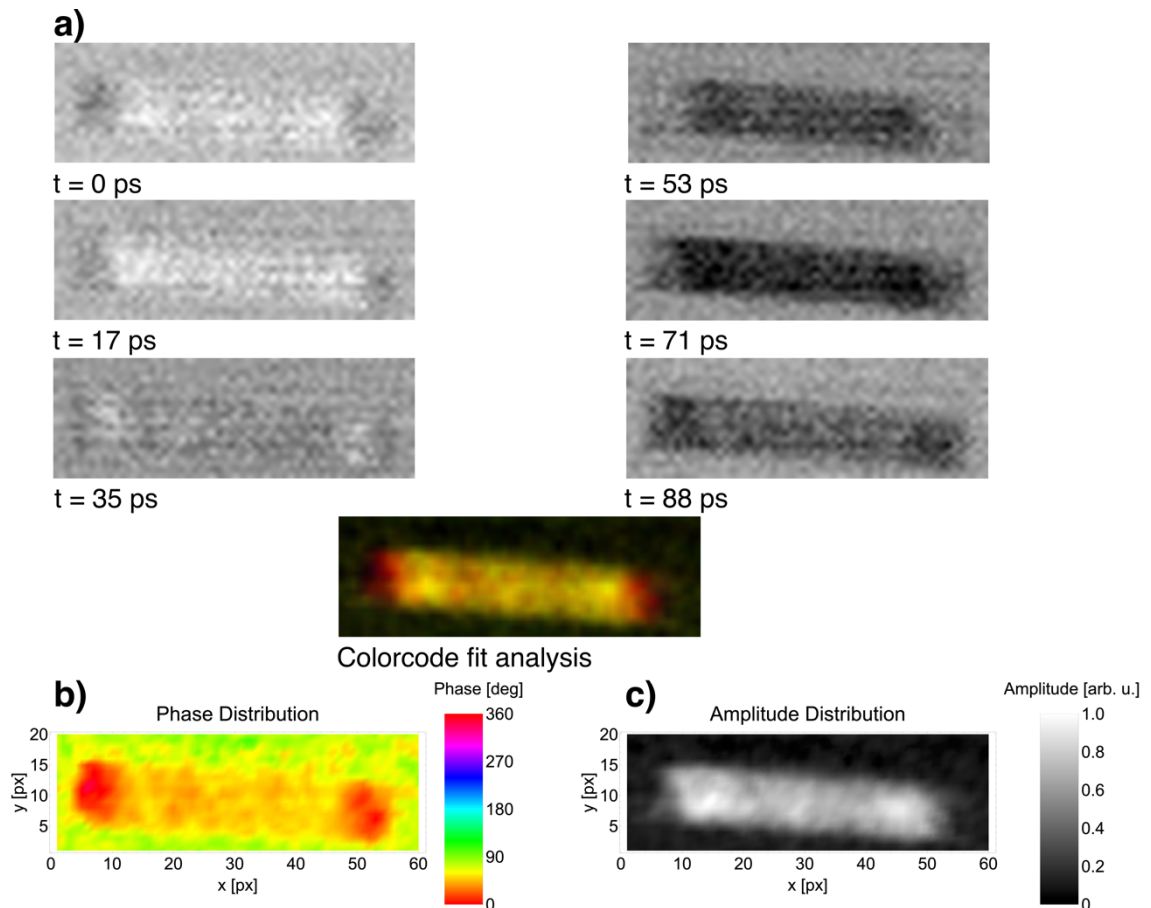


Figure 34: STXM-FMR data of the single Py stripe at a static bias field of about 91 mT (109 mT) and a microwave power of 29 dBm. a) Microwave induced X-ray transmission for 6 timesteps with a time distance of about 18 ps. b), c) Distribution of the relative phase with respect to the timestep $t = 0$ and the normalized amplitude extracted out of the color-code fit analysis (chapter 3.4).

The contrast images shown in subfigure a) reveal the node- antinode structure best at the time point $t = 88$ ps, a clearer image of the mode is given by the result of the color code fit analysis, which shows a higher amplitude for the three anti-nodes in contrast to the amplitude at the node positions. The relative phase has a distribution

within the stripe center between about 50° and 60° , while as for the mode observed before a relative phase of about 10° to 20° is present at both stripe edges.

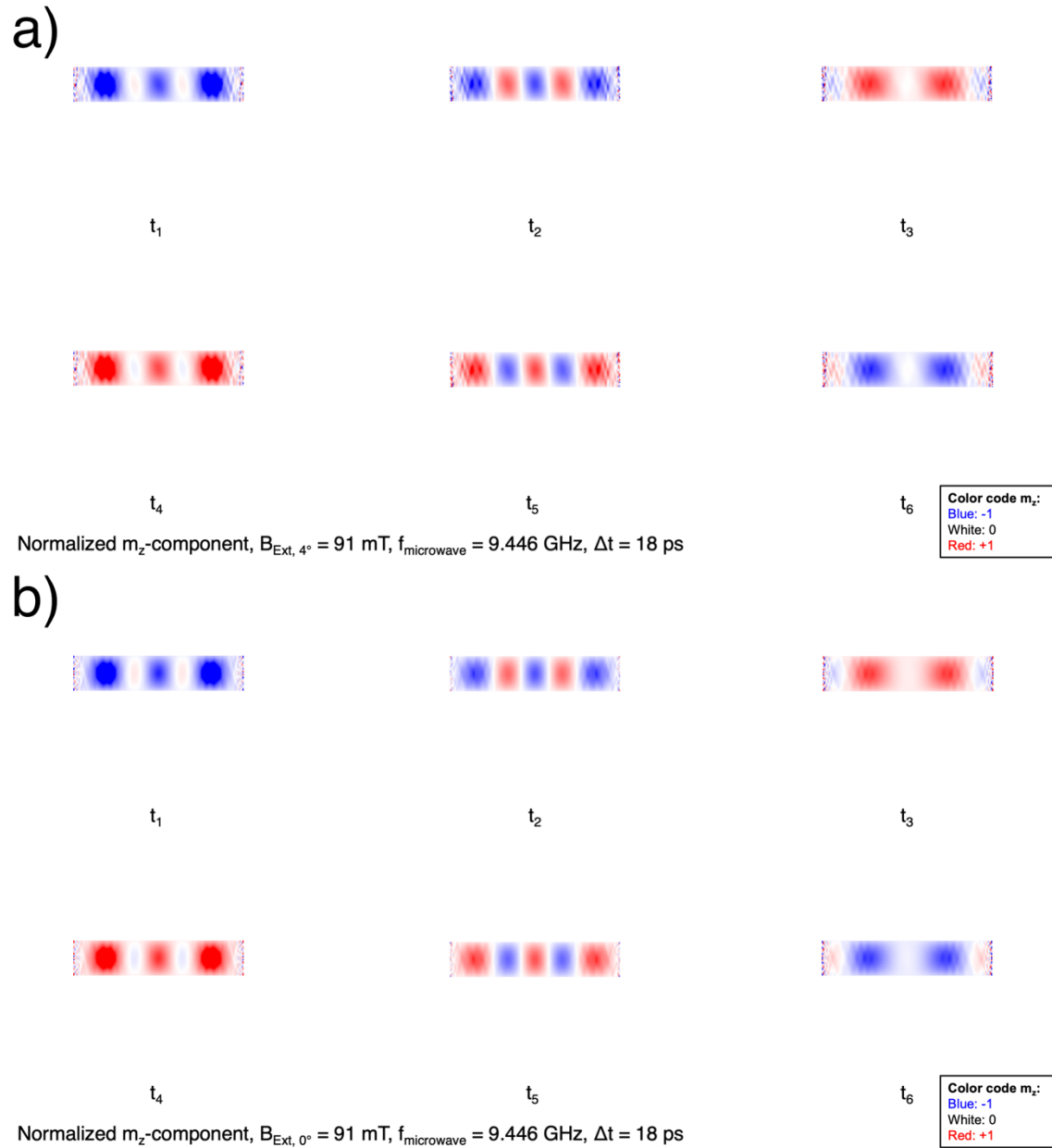


Figure 35: Simulated normalized m_z -component of the magnetization for $|B_{Ext}| = 91$ mT. **a)** B_{Ext} tilted by 4° (Figure 21), **b)** B_{Ext} aligned parallel to the long side of the stripe. Six images of the magnetization oscillation with a time distance of 18 ps are shown.

The resulting phase gradient of about 40° to 50° results in a directed oscillation of the spin wave towards both edges, which is resembled by the micromagnetic simulations shown in Figure 35 a) and b). The directed oscillatory behavior is attributed

to the influence of the stray field (simulation, see Figure 25 a), b)), resulting in edge mode excitations, see e. g. [120, 122]. The tilted external magnetic field results in a diagonal shape of the node- anti-node structure of the spin wave mode Figure 35 a). When applying $\underline{B}_{\text{Ext}}$ parallel to the long stripe side this effect on the shape of the nodes- anti-nodes is not visible anymore Figure 35 b). As the influence on the shape of the node- anti-nodes reoccurs in all simulations showing the same effect, only the simulations resembling the experiment are shown in the following.

A corresponding spin wave mode at 14.13 GHz was observed at $|\underline{B}_{\text{Ext}}|$ of 240 mT (experiment) and 237 mT (simulation) in [15].

Figure 36 shows a spin wave mode with three nodes and four anti-nodes.

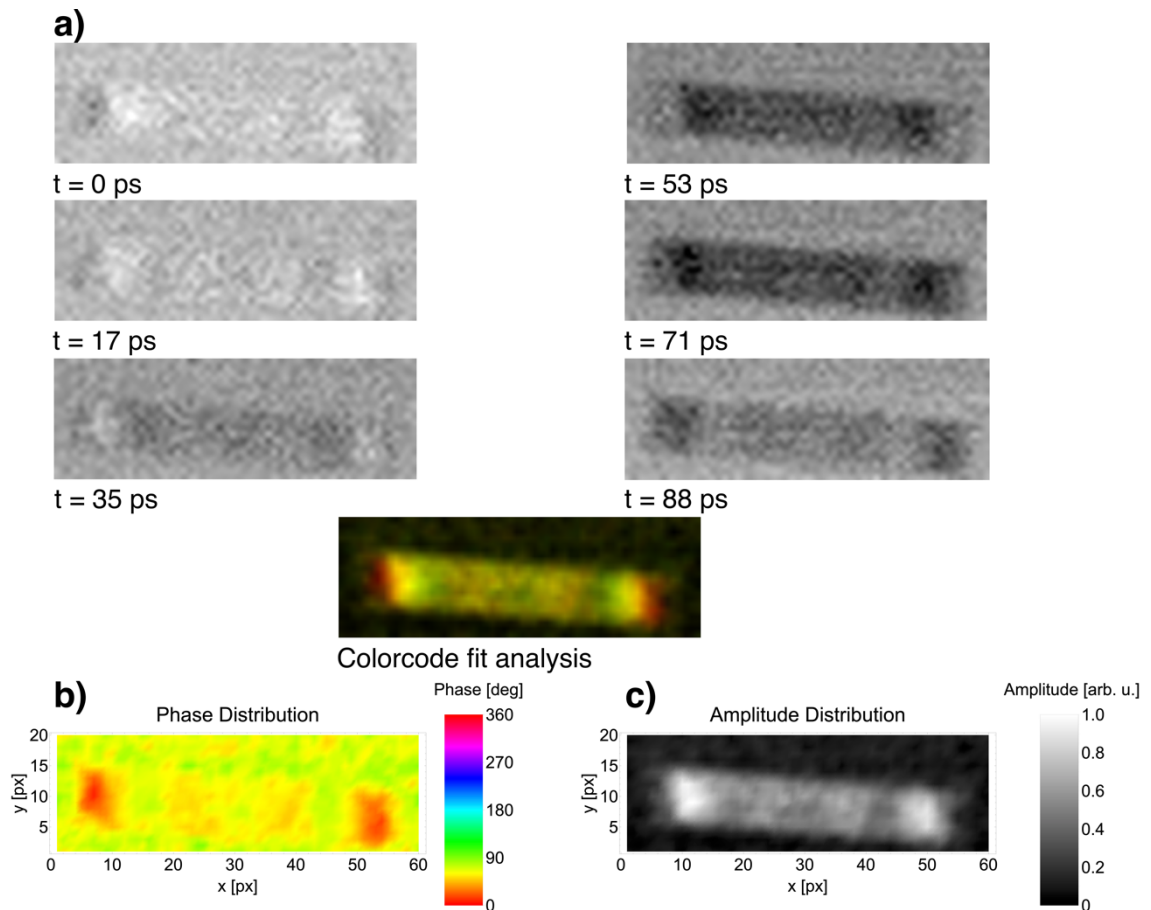


Figure 36: STXM-FMR data of the single Py stripe at a static bias field of about 96 mT (115 mT) and a microwave power of 29 dBm. a) Microwave induced X-ray transmission for 6 timesteps with a time distance of about 18 ps. b), c) Distribution of the relative phase with respect to the timestep $t = 0$ and the normalized amplitude extracted out of the color-code fit analysis (chapter 3.4).

The relative phase distribution obtained from the color code fit analysis in Figure 36 b) reveals a phase value of about 10° to 20° at the stripe edges, a value of about 50° to 60° at the two inner anti-nodes and a value of about 80° in between the anti-nodes. Influenced by the stray-field distribution (Figure 25 a), b)) and the excitation of edge modes, see e. g. [120, 122], the spin wave mode exhibits a directed oscillation from the stripe center towards the outer edges due to the presence of the phase gradient of about 80° between the stripe edges and the neighboring node and of about 30° to 50° between the nodes and the central anti-nodes. The amplitude distribution shows the highest amplitude values at the positions of the anti-nodes with peak amplitude values at the stripe edges. This behavior is also shown by the micromagnetic simulations presented in Figure 37. In [15] the here observed mode is located at $|\underline{B}_{\text{Ext}}|$ of 222 mT (experiment) and 219.6 mT (simulation).

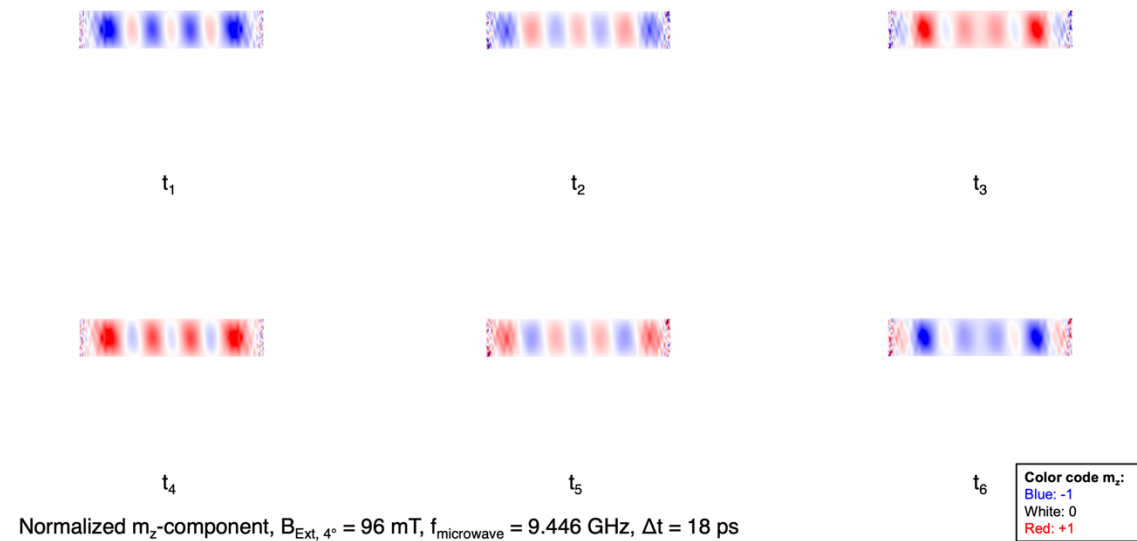


Figure 37: Two-dimensional representation of the simulated normalized m_z -component of the magnetization for $|\underline{B}_{\text{Ext}}| = 96$ mT. The external field is tilted by an angle of 4° (see Figure 21) to resemble the geometry of the experiment. Six images of the magnetization oscillation with a time distance of 18 ps are shown.

A four node – five anti-node spin wave is depicted in Figure 38. The peak amplitude values obtained from the color code fit analysis are located at the stripe edges, while lower amplitude values, but higher than the amplitude at the node locations, can be found at the left-sided positions of the inner anti-nodes, while on the right stripe size deviations in amplitude are nearly indistinguishable (Figure 38 c). The

distribution of the relative phase shows a phase gradient between the outer anti-nodes and the neighboring nodes from about $0^\circ/360^\circ$ to about 20° at the stripe edges to about 60° to about 80° at the nodes. Towards the inner anti-nodes the relative phase changes to about 45° to 50° , while between the inner anti-nodes and nodes the relative phase varies from about 45° to 50° to about 60° . As before the presence of these phase gradients cause an oscillation of the spin wave directed from the stripe center towards the outer sides, due to the influence of the stray-field, leading to an additional excitation of edge modes, see e. g. [120, 122].

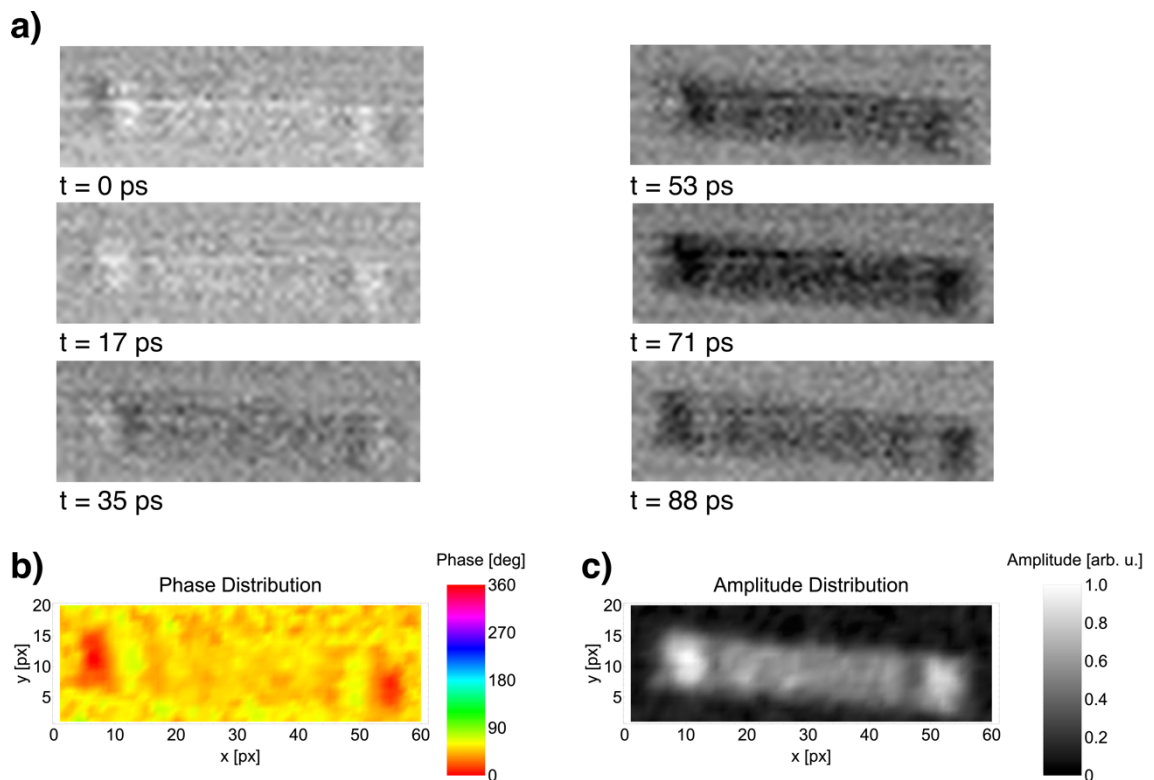


Figure 38; STXM-FMR data of the single Py stripe at a static bias field of about 100 mT (120 mT) and a microwave power of 29 dBm. a) Microwave induced X-ray transmission for 6 timesteps with a time distance of about 18 ps. b), c) Distribution of the relative phase with respect to the timestep $t = 0$ and the normalized amplitude extracted out of the color-code fit analysis (chapter 3.4).

The micromagnetic simulations, showing the normalized m_z -component of the magnetization for six time points of the simulation, correspond to the experimental observations Figure 39.

A close to uniform and non-uniform spin wave modes with three, four and six anti-nodes could be visualized for the single Py stripe by means of STXM-FMR. The analysis reveals a phase gradient of the magnetization causing an oscillatory behavior of the spin wave modes from the stripe center towards the stripe edges due to the influence of the stray- and demagnetization field distribution shown by micromagnetic simulations in Figure 25 a), b). The aforementioned observations are confirmed by the micromagnetic simulations showing six timesteps of the simulation for each spin wave mode. The simulations also reveal that the tilted \underline{B}_{Ext} causes a change in the shape of the nodes and anti-nodes of a spin-wave (see the comparison in Figure 35).

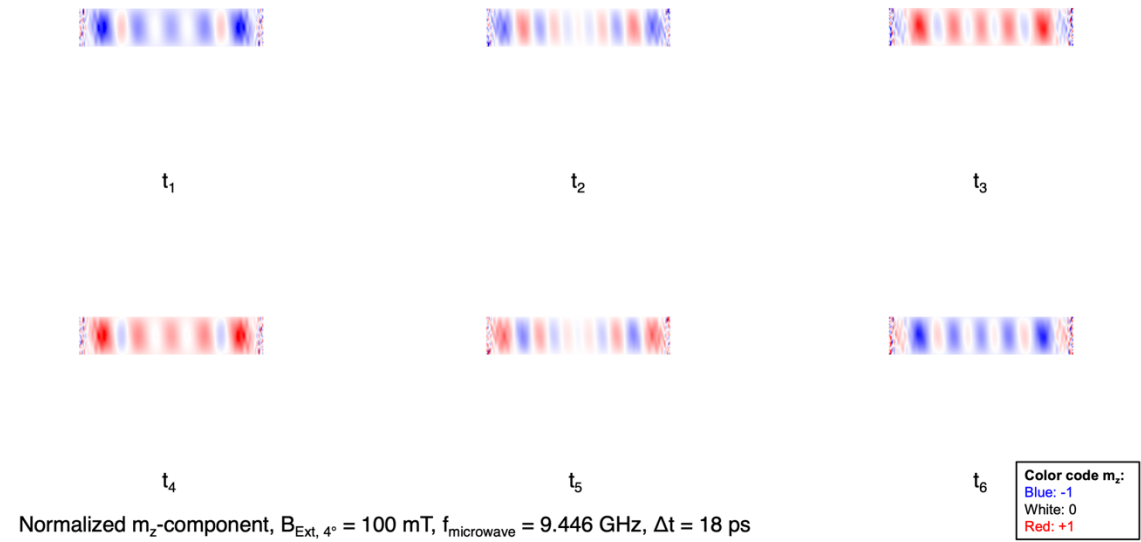


Figure 39: Two-dimensional representation of the simulated normalized m_z -component of the magnetization for $|B_{Ext}| = 100$ mT. The external field is tilted by an angle of 4° (see Figure 21) to resemble the geometry of the experiment. Six images of the magnetization oscillation with a time distance of 18 ps are shown.

The stray- and demagnetization field are regarded as the origin of the observed phase gradient and the resulting directed oscillation of the spin wave modes due to the additional excitation of edge modes, see e. g. [119-121]. In the next chapters the influence of a second stripe in a T- and L-shaped arrangement is shown (Figure 21).

4.2.5. Py T-shape stripe geometry

The STXM-FMR data measured at $|\underline{B}_{\text{Ext}}| \sim 98$ mT for the vertical Py stripe of the T-shape geometry is presented in Figure 40. Subfigure a) shows the recorded six images in time after taking the natural logarithm of the division of the data obtained with and without microwave excitation (see chapter 3.3). In the lower part of the images a phase jump caused by an error in the microwave synchronization board can be seen.

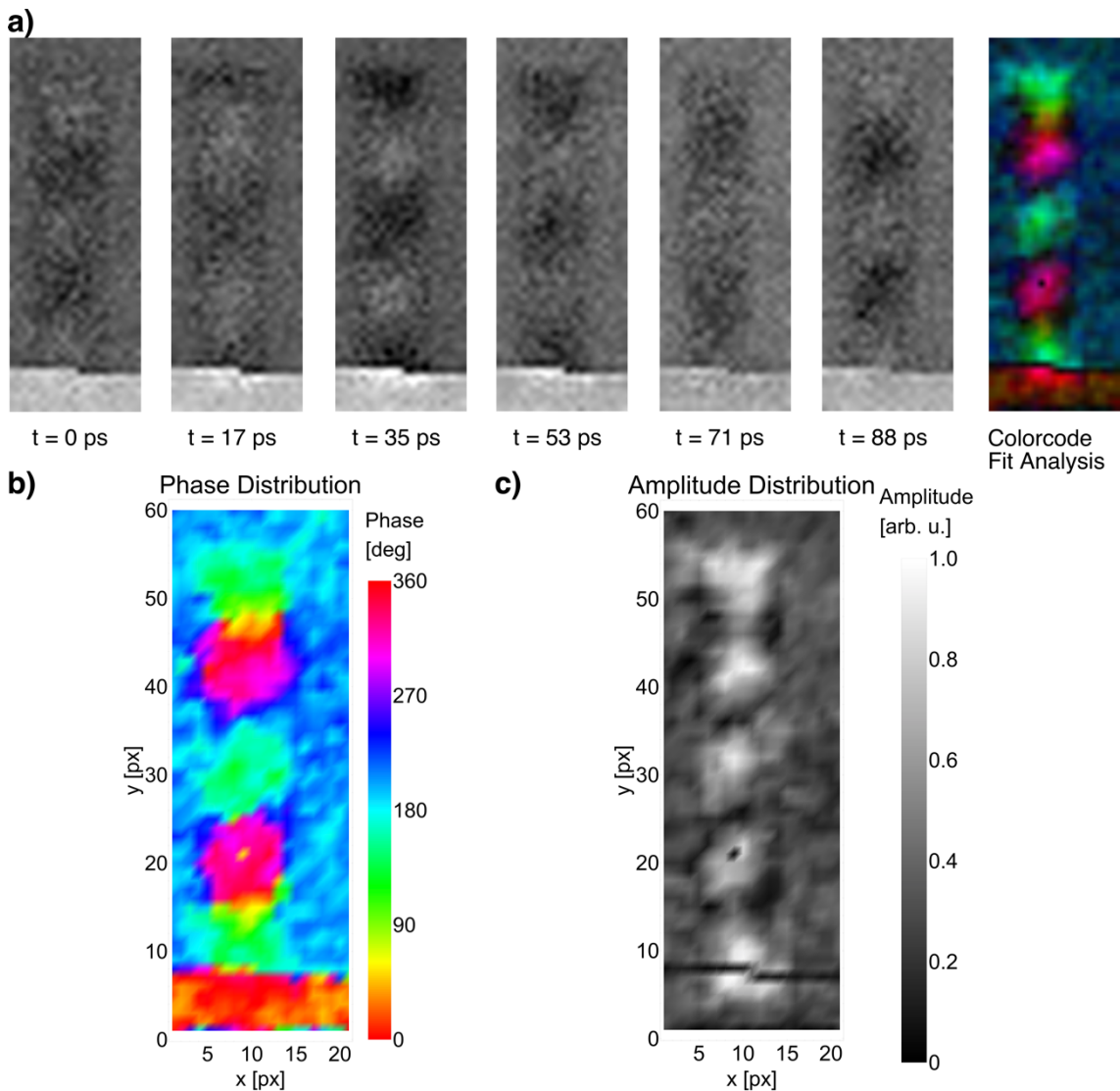


Figure 40: STXM-FMR data of the vertical Py stripe of the T-shape geometry at a static bias field of about 98 mT and a microwave power of 27 dBm. **a)** Microwave induced X-ray transmission for 6 timesteps with a time distance of about 18 ps. **b)**, **c)** Map of the relative phase with respect to the timestep $t = 0$ and the normalized amplitude extracted out of the color-code fit analysis (chapter 3.4). The measurement data is published in [30].

The black area (phase: (yellow)) visible in the result of the color code fit analysis and the amplitude distribution is attributed to an artifact of the measurement and/or the evaluation. A spin wave mode showing five anti-nodes and four nodes is detected (Figure 40). At the time point of $t = 0$ ps an absorption below the average is detected at the top of the stripe, alternating with a higher-than-average absorption in the following. With increasing time steps, the absorption behavior inverts at $t = 35$ ps to revert back to the initial state at $t = 88$ ps. As with the single Py stripe (chapter 4.2.4) the spin wave shows an oscillation direction from the upper and lower edges towards the stripe center. The color code fit analysis (subfigure b)) depicts a relative phase alternating between 135° and $0^\circ/360^\circ$, showing smooth phase transitions between the alternating anti-nodes. This indicates the presence of a phase gradient of the magnetization, which causes the oscillating behavior. The oscillating background is attributed as aforementioned to an influence of the microwave on the avalanche photodiode [46] and chapter 4.1.3. The amplitude distribution reveals a high amplitude at the positions of the anti-nodes, which corresponds to the behavior of a wave. As for the single Py stripe (chapter 4.2.4) the presence of the phase gradient can be explained by the influence of the stray field, here due to an influence on the vertical stripe by the horizontal stripe

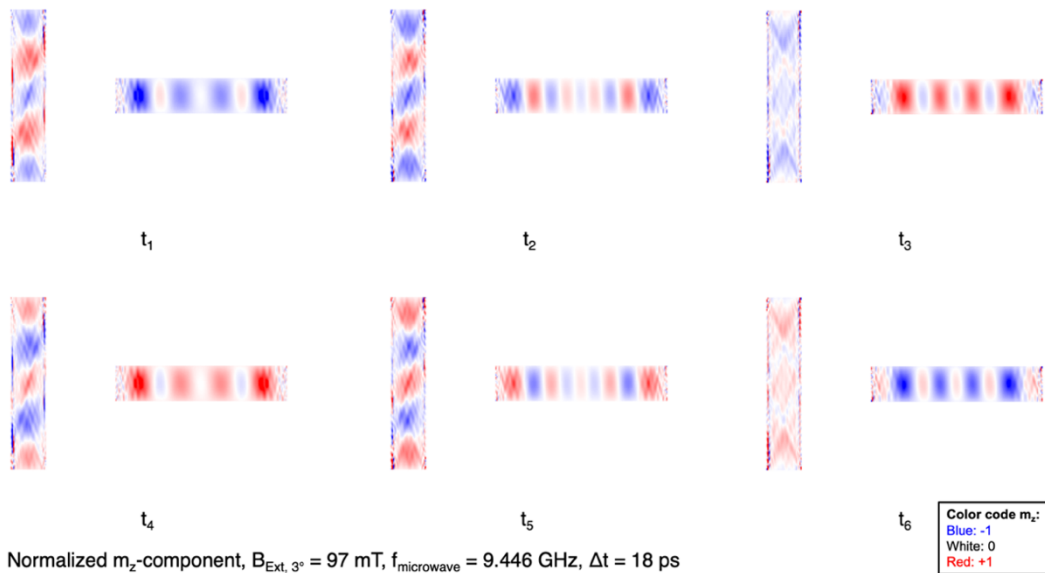


Figure 41: Two-dimensional representation of the simulated normalized m_z -component of the magnetization for $|\underline{B}_{Ext}| = 97$ mT. The external field is tilted by an angle of 3° (see Figure 21) to resemble the geometry of the experiment. Six images of the magnetization oscillation with a time distance of 18 ps are shown.

This is shown by the micromagnetic simulations depicting a higher stray field line density at the top and bottom stripe edges (see Figure 25 c), d)). This influence causes the aforementioned additional edge mode excitations (e. g. [120, 122]). See e. g. [120] for the stray field induced localization of edge modes.

The micromagnetic simulation performed at a simulated $|\underline{B}_{\text{Ext}}|$ of 97 mT (Figure 41) corresponds to the STXM-FMR data showing a spin wave with 5 anti-nodes and 4 nodes within the vertical stripe. The oblique shape of the anti-nodes, which is also observed in the STXM-FMR images (see Figure 40), is the result of the tilted $\underline{B}_{\text{Ext}}$. This is confirmed by the micromagnetic simulation performed with $\underline{B}_{\text{Ext}}$ oriented parallelly to the horizontal stripe (Figure 42), which does not show any oblique anti-nodes. As this behavior is present for all investigated spin wave modes, the simulations with the non-tilted fields are not shown in the following. The horizontal stripe showing nine anti-nodes and 8 nodes was not imaged by STXM-FMR at this $|\underline{B}_{\text{Ext}}|$. Animating the representations of the normalized m_z -component shows an oscillating behavior independent from the tilting angle, as in the experiment.

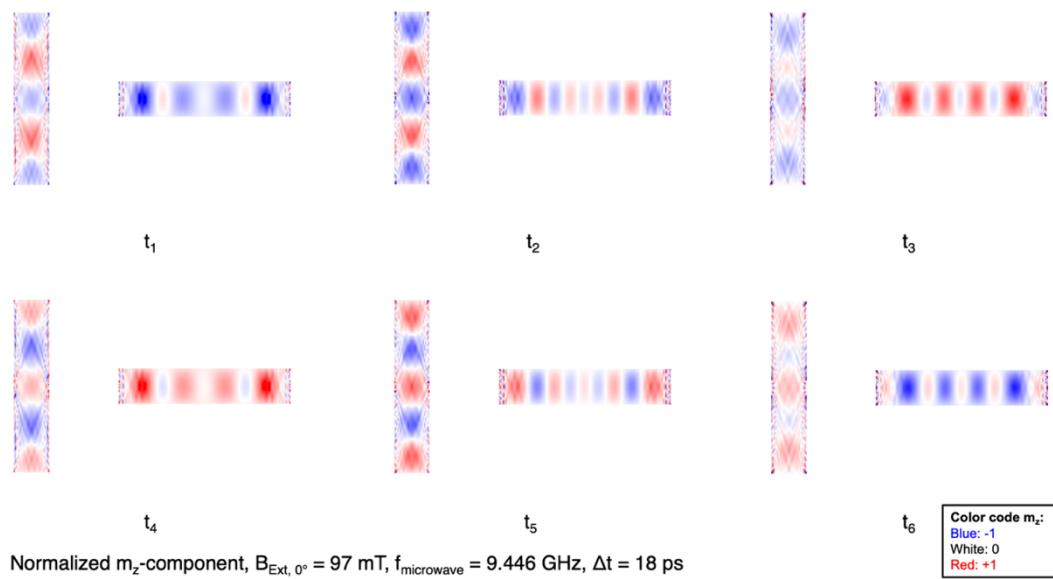


Figure 42: Two-dimensional representation of the simulated normalized m_z -component of the magnetization for $|\underline{B}_{\text{Ext}}| = 97$ mT. The external field is oriented parallel to the horizontal Py stripe. Six images of the magnetization oscillation with a time distance of 18 ps are shown.

Figure 43 visualizes the STXM-FMR measurement data for the vertical stripe at $|\underline{B}_{\text{Ext}}|$ of about 112 mT. A spin wave mode with three anti-nodes and two nodes is

revealed. The STXM-FMR contrast is alternating from higher-than-average values at $t = 0$ ps to lower-than-average values at $t = 35$ ps and reverts back to the initial anti-node configuration at $t = 88$ ps. An oscillation from the top and bottom stripe edges towards the center is revealed, as in the case before. The color code fit analyses (sub-figure b)) reveals a phase difference of about 280° (edges) to about 135° (center) with a transition phase area in between.

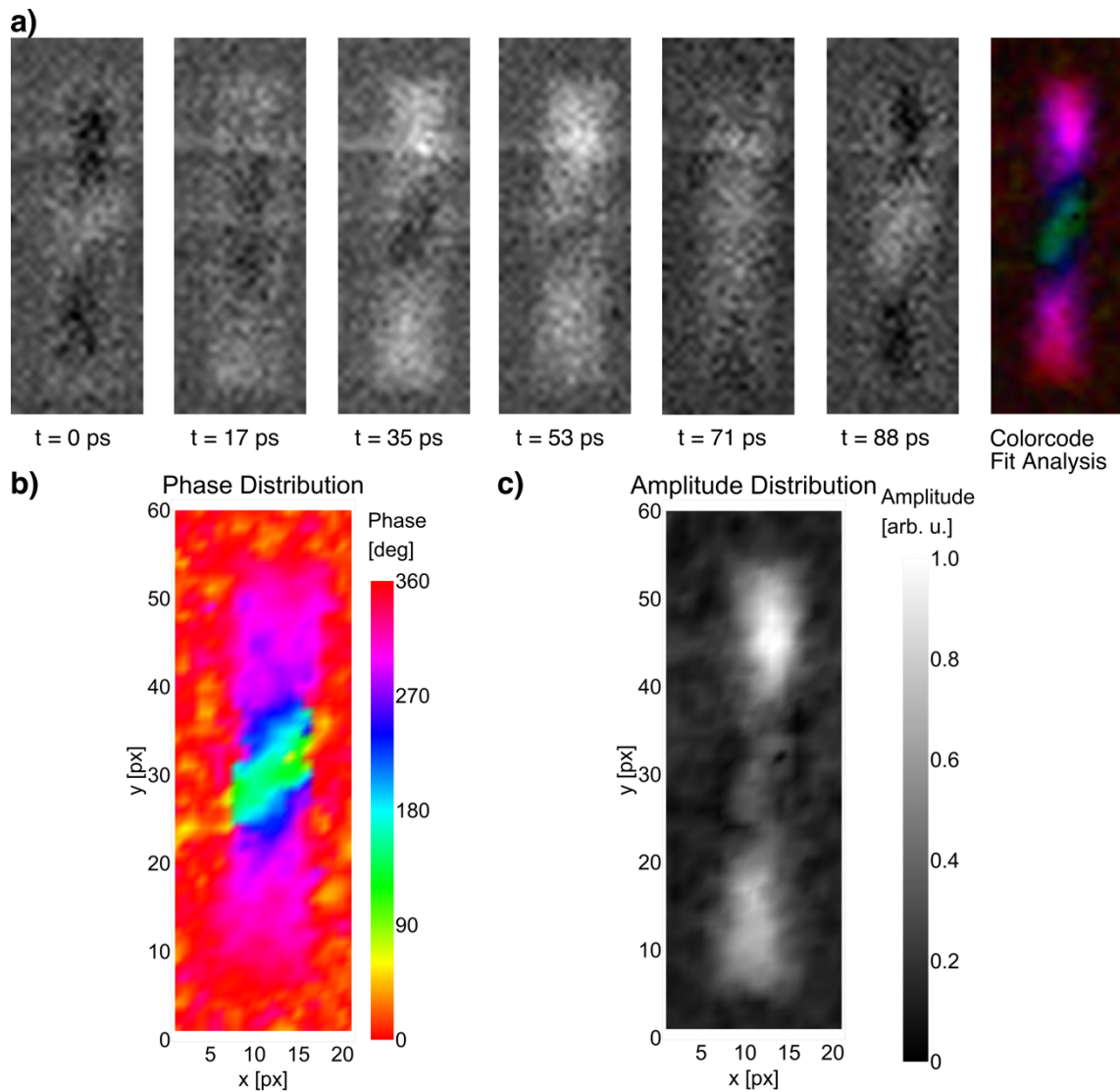


Figure 43: STXM-FMR data of the vertical Py stripe of the T-shape geometry at a static bias field of about 112 mT [128] (103 mT) and a microwave power of 27 dBm. a) Microwave induced X-ray transmission for 6 timesteps with a time distance of about 18 ps. b), c) Distribution of the relative phase and the normalized amplitude extracted out of the color-code fit analysis (chapter 3.4). The measurement data is published in [30].

This phase gradient, causing the directed oscillation, is attributed to the stray field distribution (simulation see Figure 25 c), d)) and the followed excitation of edge modes, see e. g. [120, 122]. The black (yellow) area in the phase and amplitude distribution (Figure 43) is explained as before as measurement/evaluation artifact. The amplitude distribution shows the highest amplitude at the top and the bottom anti-nodes and a weaker amplitude at the center anti-node.

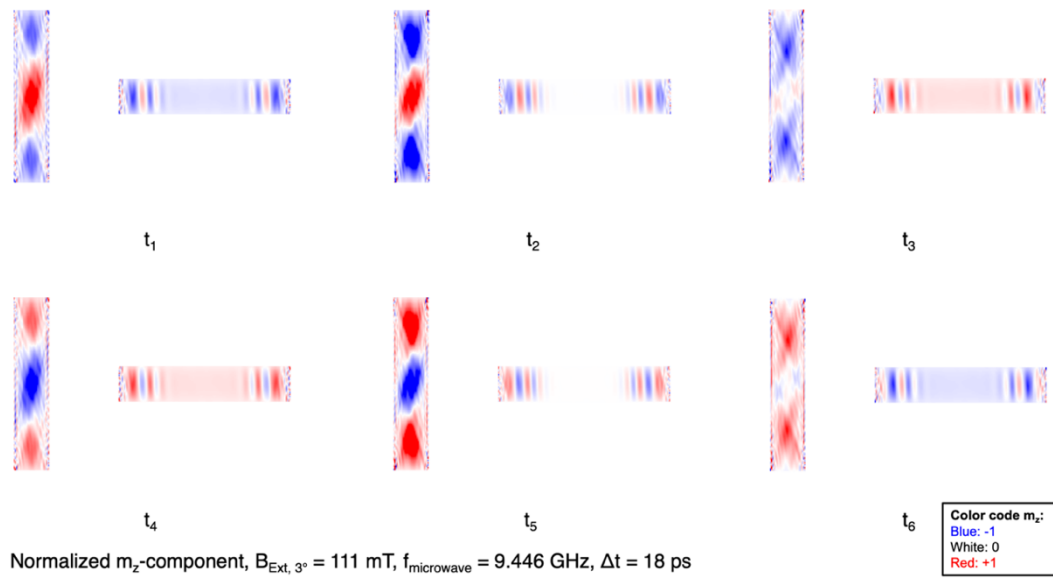


Figure 44: Two-dimensional representation of the simulated normalized m_z -component of the magnetization for $|\underline{B}_{Ext}| = 111$ mT. The external field is tilted by an angle of 3° (see Figure 21) to resemble the geometry of the experiment. Six images of the magnetization oscillation with a time distance of 18 ps are shown. The simulation data is published in part in [30].

The two-dimensional representations of the simulated normalized m_z -component of the magnetization shown in Figure 44 (\underline{B}_{Ext} tilted by 3°) depict the same spin wave mode with three anti-nodes and two nodes within the vertical stripe as in the experiment. The animation of the simulation data shows an oscillation of the spin wave towards the stripe center, corresponding to the measurement and its aforementioned explanations. The horizontal stripe shows spin wave modes only at the outer left and right edges of the stripe at this value of $|\underline{B}_{Ext}|$.

According to the micromagnetic FMR simulations, the uniform resonance mode of the vertical Py stripe is at $|\underline{B}_{Ext}| = 123$ mT (Figure 23 a)). Two STXM-FMR measurements performed at around $|\underline{B}_{Ext}|$ of the uniform mode are presented in Figure 45

and Figure 46. The STXM-FMR data is displayed for the scanned time steps in both cases in subfigure a). The contrast changes from the average value to a lower-than-average contrast, passes a higher-than-average contrast, and reverts back to the average contrast. Animating the STXM-FMR data of the measurement at $|\underline{B}_{\text{Ext}}|$ of about 126 mT reveals a pronounced oscillation from the stripe center towards the long sides of the stripe. By extracting the relative phase and the amplitude distribution out of the color code fit analyses, a phase gradient of the magnetization is revealed, showing a smooth transition from $0^\circ/360^\circ$ in the stripe center to 280° at the long sides of the stripe. The directed oscillatory behavior cannot be attributed to the influence of the stray field alone (simulation see Figure 25 c), d)), as the STXM-FMR measurement performed at $|\underline{B}_{\text{Ext}}|$ of about 122 mT shows a minimal phase gradient around a phase value of 250° to 260° (Figure 46) with a much weaker directed oscillation. The strength of the directed oscillation depends on the magnitude of the phase gradient of the magnetization. Setting a value of $|\underline{B}_{\text{Ext}}|$ aside to the resonance field results at least for the (close to) uniform excitation mode in a stronger phase gradient and an increasingly stronger oscillatory behavior of the mode with increasing deviation from the exact resonance field, see also [30, 130]. From this it can be concluded that the effective field $|\underline{B}_{\text{eff}}|$ fulfilling the resonance condition for edge modes, causing the phase gradient and the directed oscillatory behavior of the modes, is the result of the interplay between $|\underline{B}_{\text{Ext}}|$ and the stray field. For the dipolar influence on the excitation of edge modes and oscillating character see [119-121].

For both measurements, the amplitude distribution shows the highest amplitude in the stripe center, but the amplitude distribution of the data recorded at $|\underline{B}_{\text{Ext}}| \sim 126$ mT is homogeneous within the central stripe area, while at $|\underline{B}_{\text{Ext}}| \sim 122$ mT the area of a high amplitude is inhomogeneously distributed at the stripe center. No pronounced oscillation of the background is visible in both measurements. The directed oscillatory behavior is confirmed by the micromagnetic simulations (Figure 47).

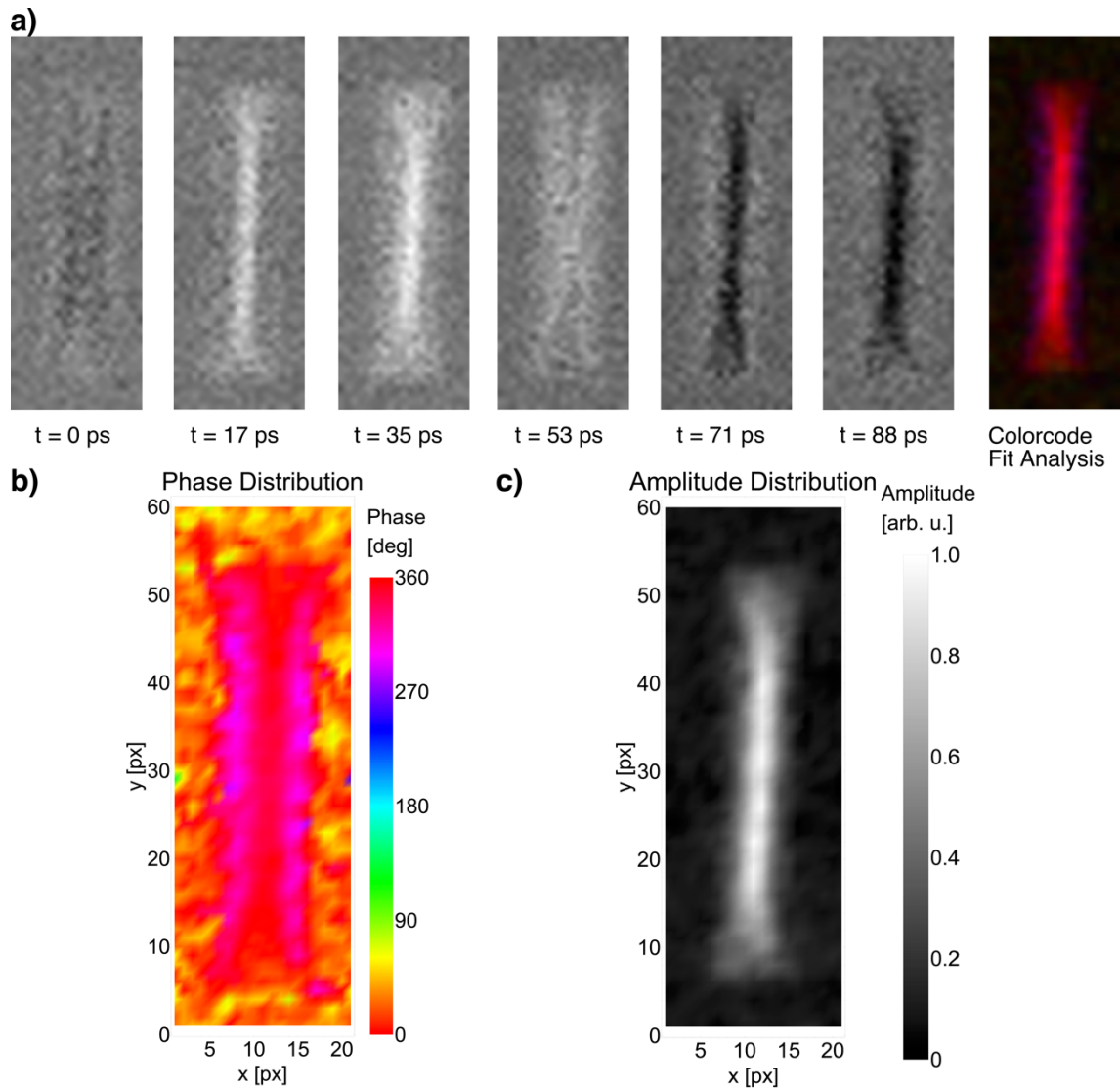


*Figure 45: STXM-FMR data of the vertical Py stripe of the T-shape geometry at a static bias field of about 126 mT [128] (113 mT) and a microwave power of 27 dBm. **a)** Microwave induced X-ray transmission for 6 timesteps with a time distance of about 18 ps. **b), c)** Distribution of the relative phase with respect to the timestep $t = 0$ and the normalized amplitude extracted out of the color-code fit analysis (chapter 3.4). The measurement data is published with a different analysis method in [30].*

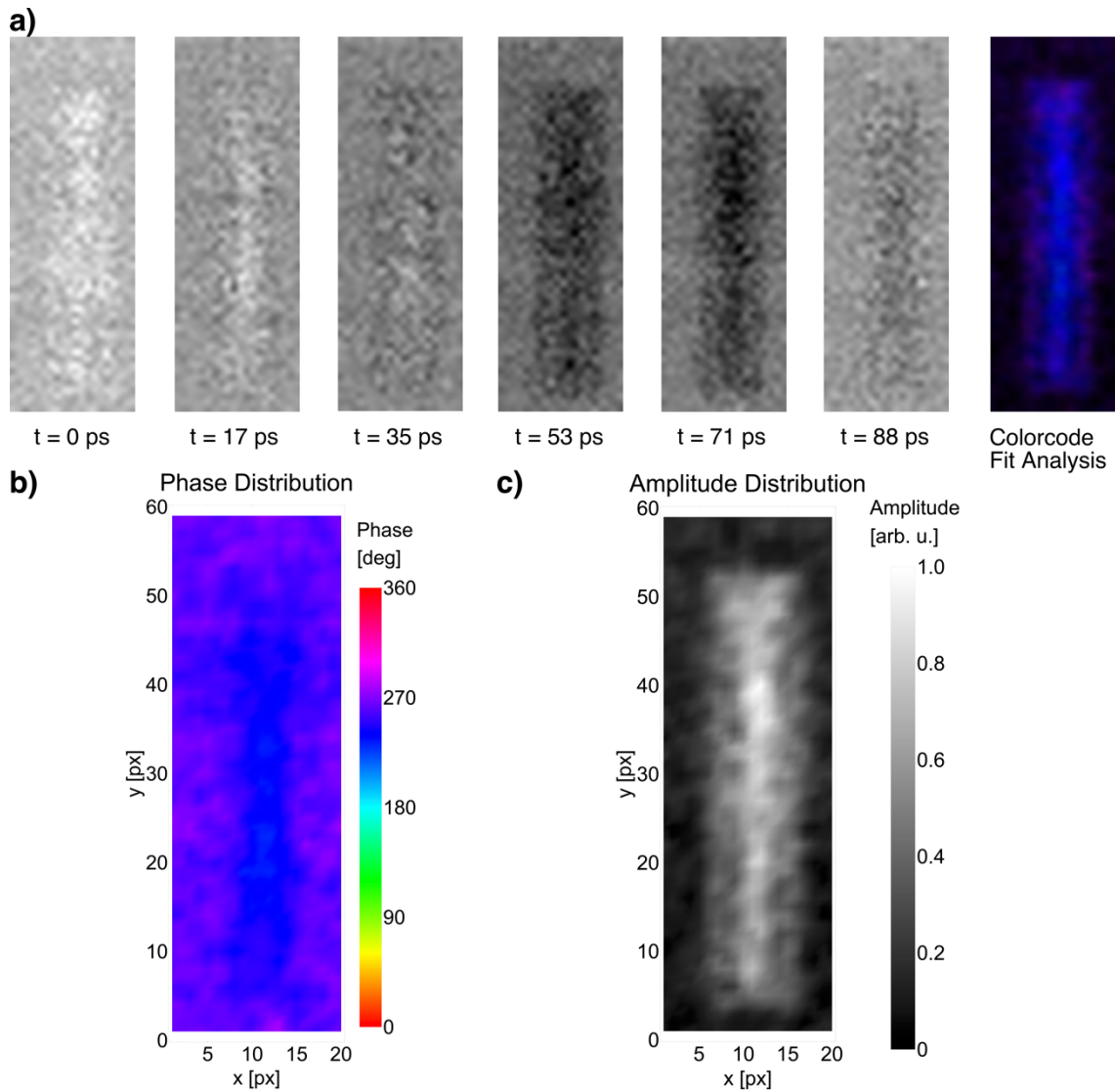


*Figure 46: STXM-FMR data of the vertical Py stripe of the T-shape geometry at a static bias field of about 122 mT and a microwave power of 29 dBm. **a)** Microwave induced X-ray transmission for 6 timesteps with a time distance of about 18 ps. **b)**, **c)** Distribution of the relative phase with respect to the timestep $t = 0$ and the normalized amplitude extracted out of the color-code fit analysis (chapter 3.4). The investigated sample is from a different batch than the T-shaped samples investigated before employing the same dimensions and fabrication process.*

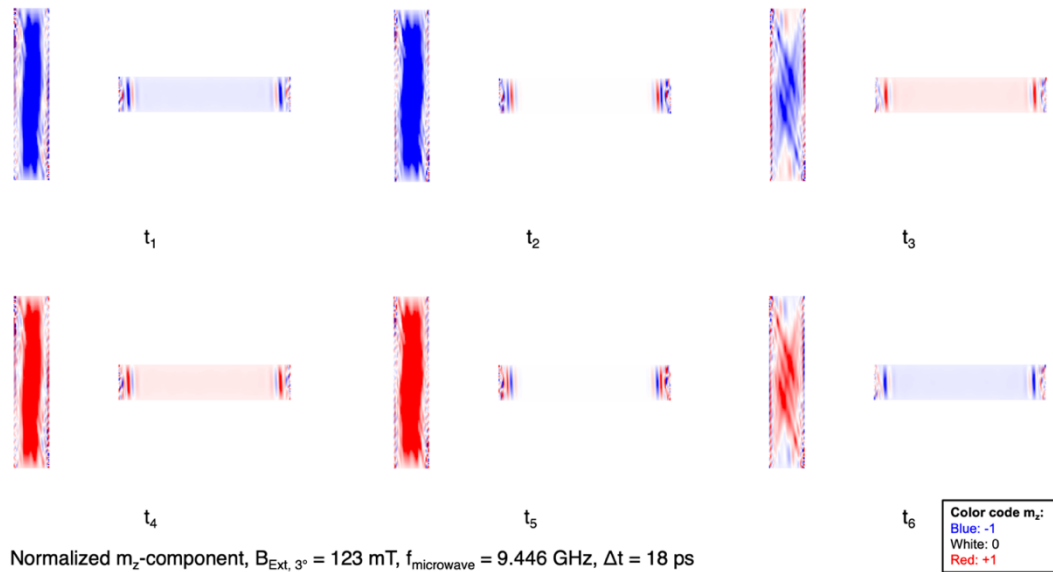


Figure 47: Two-dimensional representation of the simulated normalized m_z -component of the magnetization for $|\underline{B}_{\text{Ext}}| = 123 \text{ mT}$. The external field is tilted by an angle of 3° (see Figure 21) to resemble the geometry of the experiment. Six images of the magnetization oscillation with a time distance of 18 ps are shown. The simulation data is published in part in [30].

To scan the uniform mode of the horizontal stripe, STXM-FMR measurements were performed at $|\underline{B}_{\text{Ext}}| \sim 81 \text{ mT}$ (see Figure 23 a)). The animation of STXM-FMR data, presented in Figure 48, reveals a directed oscillation of the magnetization from the stripe center towards both short edges, as it was observed for the singly Py stripe (chapter 4.2.4), which is confirmed by the micromagnetic simulations shown in Figure 49 (tilting angle of 3°). A phase gradient of about 70° to 80° is visible in the visualization of the relative phase in Figure 48 b), which is attributed to the influence of the stray field distribution (simulation see Figure 25 c), d)), causing the excitation of additional edge modes, e. g. [120, 122]. See e. g. [120] for the stray field induced localized excitation of edge modes.

The amplitude distribution, shown in Figure 48 c) shows the highest amplitude in the stripe center, as it was seen for the single Py stripe in chapter 4.2.4.

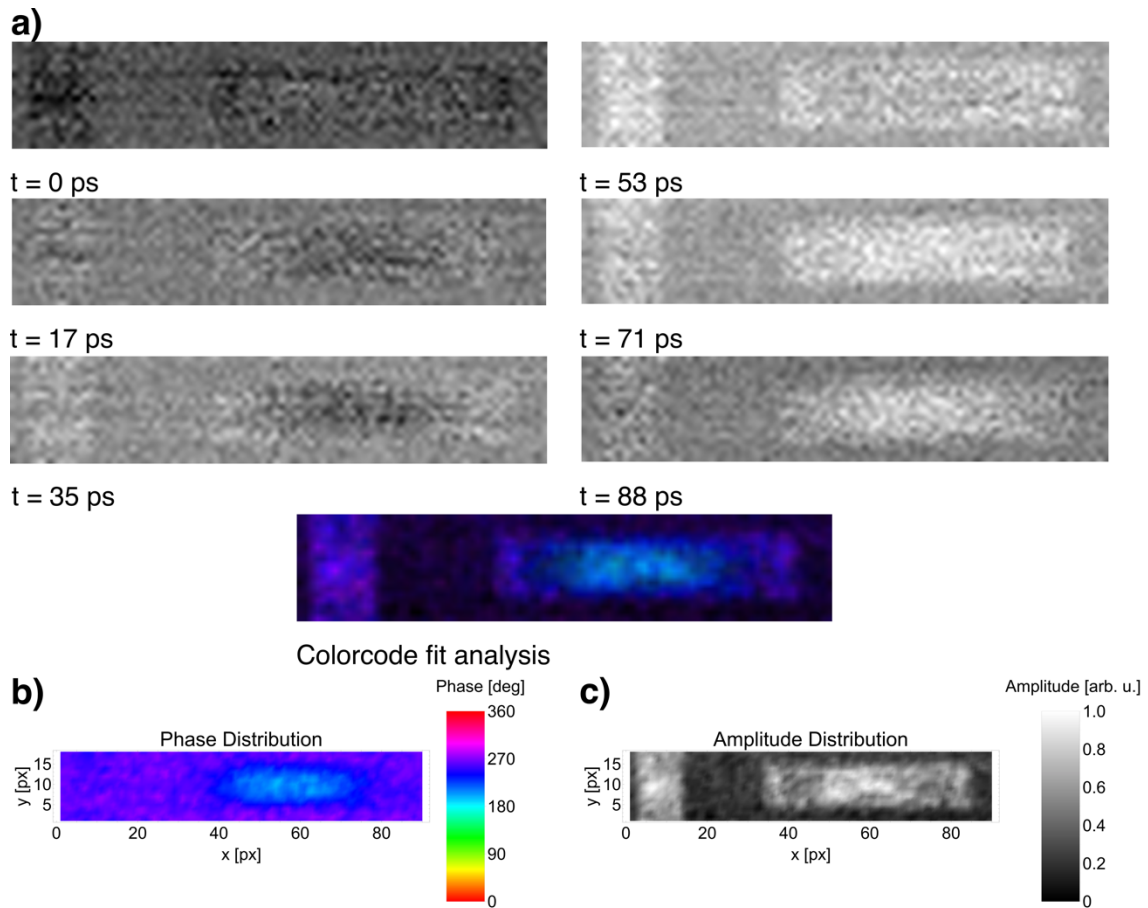


Figure 48: STXM-FMR data of the horizontal Py stripe of the T-shape geometry at a static bias field of about 81 mT and a microwave power of 29 dBm. a) Microwave induced X-ray transmission for 6 timesteps with a time distance of about 18 ps. b), c) Distribution of the relative phase with respect to the timestep $t = 0$ and the normalized amplitude extracted out of the color-code fit analysis (chapter 3.4). The investigated sample is from a different batch than the T-shaped samples investigated before employing the same dimensions and fabrication process.

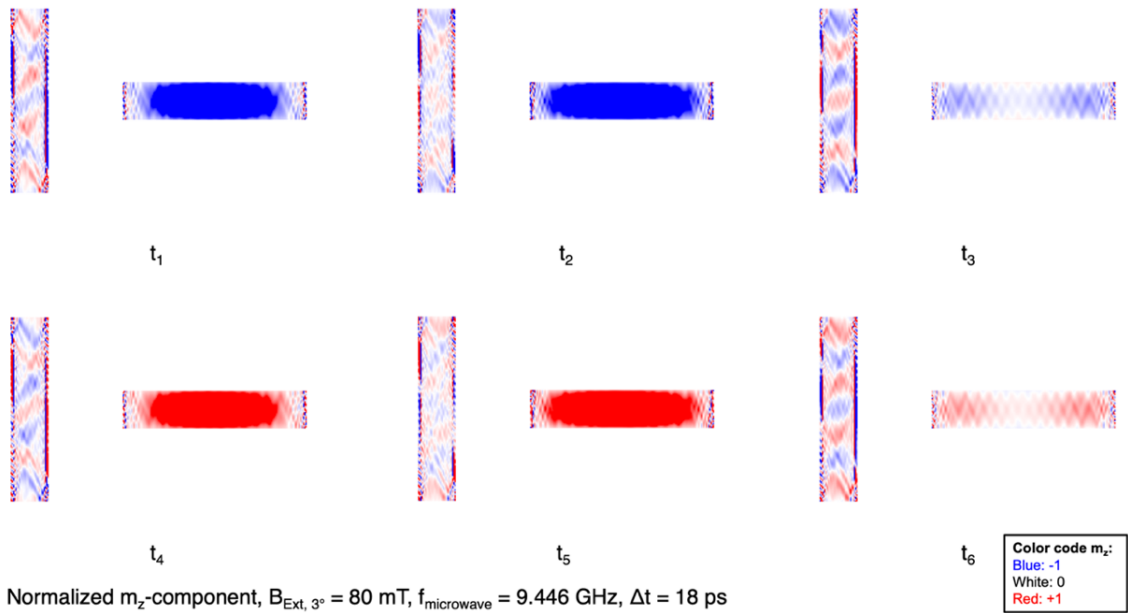


Figure 49: Two-dimensional representation of the simulated normalized m_z -component of the magnetization for $|B_{Ext}| = 80$ mT. The external field is tilted by an angle of 3° (see Figure 21) to resemble the geometry of the experiment. Six images of the magnetization oscillation with a time distance of 18 ps are shown.

The presence of the second stripe results in general in a symmetric distortion of the stray field (Figure 25 c), d)) with small deviations due to the tilted external magnetic field. High stray field line densities are located at the top and bottom part of the vertical Py stripe, which can be assumed to be positions, where the resonance conditions of edge modes are fulfilled, resulting in the directed oscillatory behavior, see e. g. [120, 122]. Due to the distance of $2 \mu\text{m}$ between the stripes, the stray field intensity between the stripes is in the < 10 mT range, resulting only in a weak influence on the respective Py stripe. Nevertheless, for the uniform mode of the vertical stripe (Figure 45, Figure 46), already slight differences in the resonance field were sufficient to influence the strength of the phase gradient of the magnetization and therefore the strength of the directed oscillation. In conclusion even a small influence of the stray field on the respective Py stripe can be regarded as sufficient in the interplay between the external field and the stray field to result in the excitation of edge modes causing the phase gradient and the directed oscillation. See [119-121] for investigations of edge modes in Py stripes. The directed oscillatory behavior of edge modes was shown in [122]. In the next chapter an asymmetric Py stripe arrangement is investigated.

4.2.6. Py L-shape stripe geometry

A spin wave mode with five anti-nodes and 4 nodes is imaged by STXM-FMR at $|\underline{B}_{\text{Ext}}|$ of about 97 mT (Figure 50). The color code fit analysis shows a strong phase gradient between 80° and $0^\circ/360^\circ$ with smooth transitions. In consequence, the analyses of the animated STXM-FMR measurement shows an oscillation direction of the mode from the top and bottom edge of the stripe to the center, comparable to the corresponding measurement for the T-shaped geometry (Figure 40).

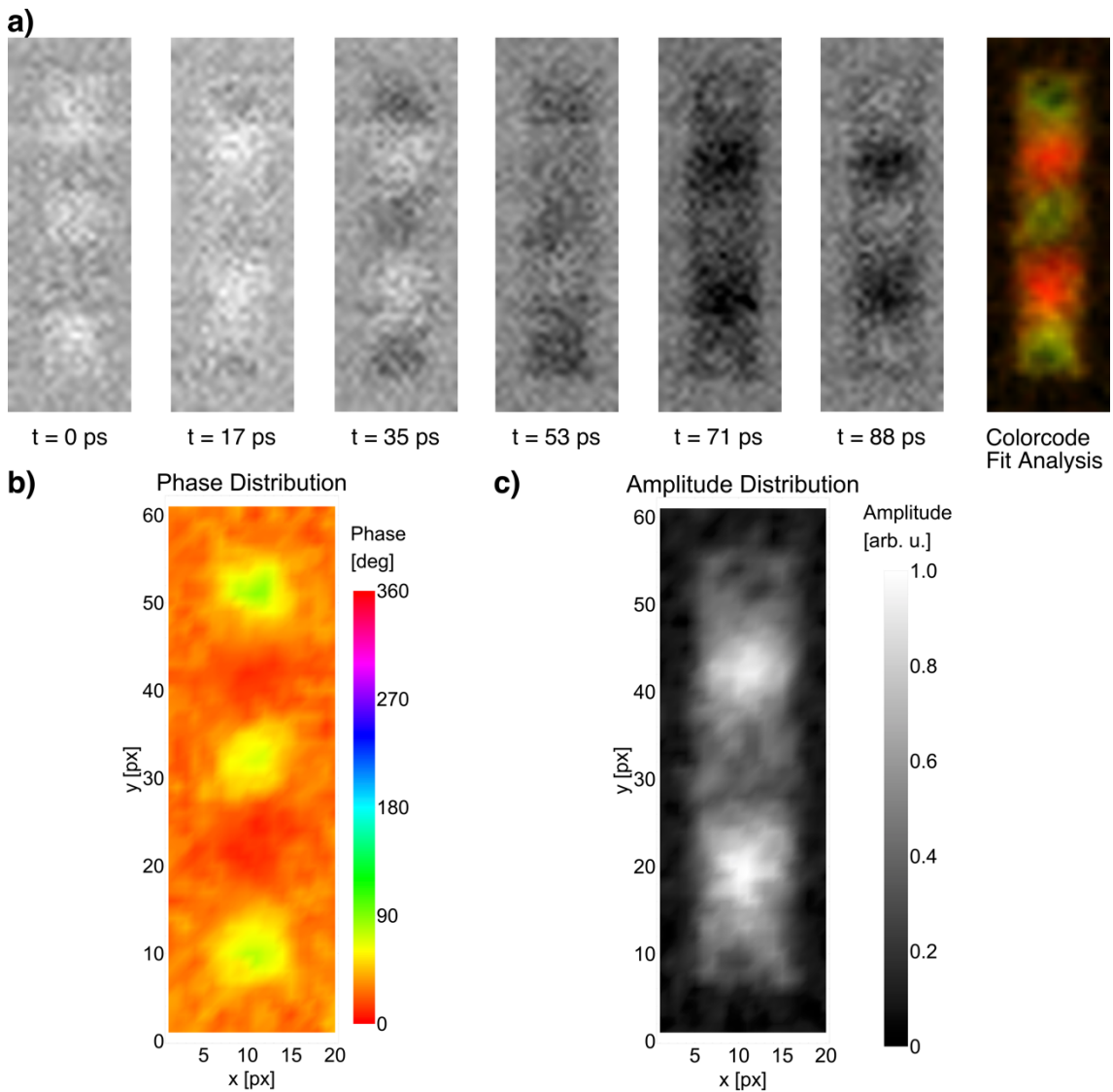


Figure 50: STXM-FMR data of the vertical Py stripe of the L-shape geometry at a static bias field of about 97 mT and a microwave power of 29 dBm. a) Microwave induced X-ray transmission for 6 timesteps with a time distance of about 18 ps. b), c) Distribution of the relative phase with respect to the timestep $t = 0$ and the normalized amplitude extracted out of the color-code fit analysis (chapter 3.4). The measurement data is published with a different analysis method in [30].

The amplitude distribution (Figure 50 c)) shows a peak amplitude at the two anti-nodes showing a relative phase $\sim 0^\circ/360^\circ$ and a lower amplitude at the other anti-nodes. The upper anti-node located at the height of the horizontal stripe shows the weakest amplitude.

The observations of the experiments are also confirmed by the micromagnetic simulations, depicted in Figure 51 (\underline{B}_{Ext} parallel to the horizontal stripe) and originate for the experiment, as well as for the simulation, in the stray field distribution of the stripe ensemble (Figure 27), causing additional edge mode excitations, see e. g. [120, 122] for investigations on edge modes and the dipolar influence on these modes.

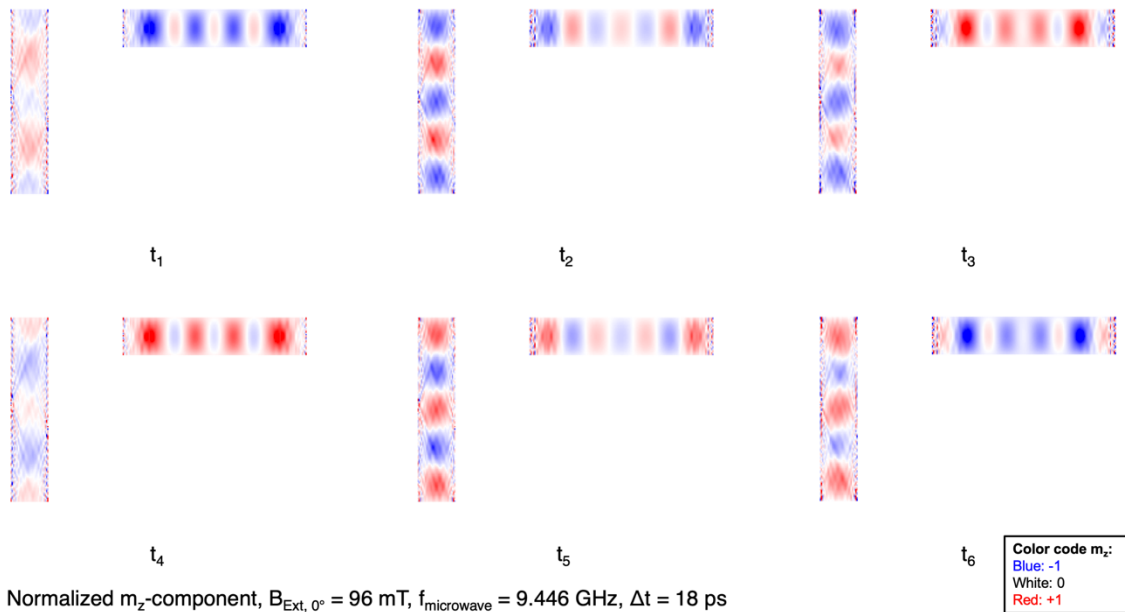


Figure 51: Two-dimensional representation of the simulated normalized m_z -component of the magnetization $|B_{Ext}| = 96$ mT. The external field is oriented parallel to the horizontal Py stripe. Six images of the magnetization oscillation with a time distance of 18 ps are shown. The simulation data is published in part in [30].

A three anti-node, two node spin wave was imaged at $|\underline{B}_{\text{Ext}}|$ of about 107 mT. The STXM-FMR data is shown in Figure 52.

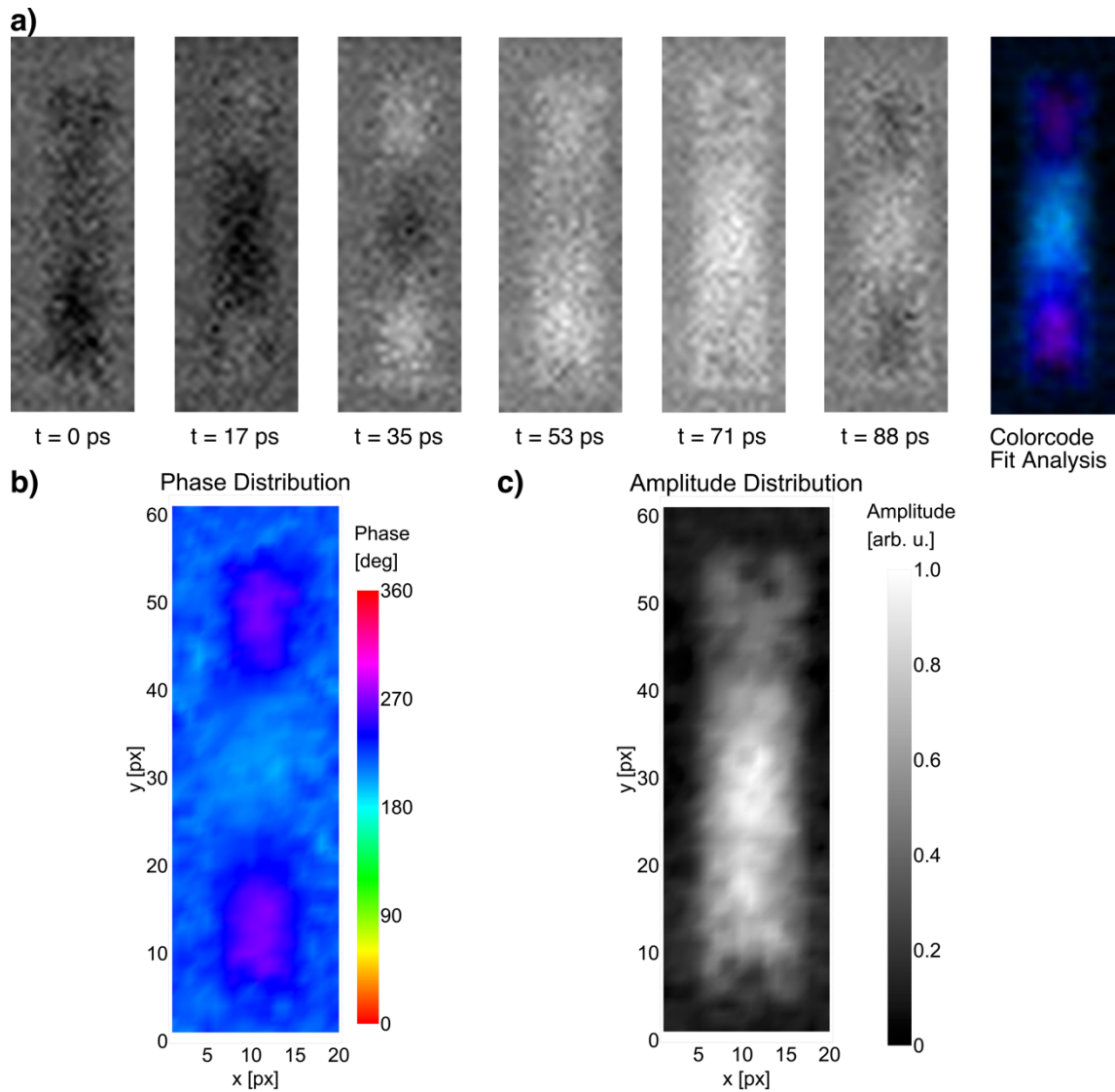


Figure 52: STXM-FMR data of the vertical Py stripe of the L-shape geometry at a static bias field of about 107 mT and a microwave power of 29 dBm. a) Microwave induced X-ray transmission for 6 timesteps with a time distance of about 18ps. b), c) Distribution of the relative phase with respect to the timestep $t = 0$ and the normalized amplitude extracted out of the color-code fit analysis (chapter 3.4). The data has been published with a different analysis in [30]

Animating the STXM-FMR images shown in subfigure a) reveals an oscillation of the mode from the upper and lower edges to the center, indicating the presence of a phase gradient of the magnetization. The color code fit analysis shows a relative phase from 280° at the outer anti-nodes to 200° at the center anti-node. The

amplitude distribution shows a high amplitude at all anti-nodes with the highest amplitude at the bottom and center anti-node. A slightly lower amplitude at the upper anti-node is located at the height of the horizontal stripe. The micromagnetic simulation, showing the spin wave mode corresponding to the experiment is performed at a simulated $|\underline{B}_{\text{Ext}}|$ of 112 mT. The deviation in the field is explained with the calibration of the Hall probe. The two-dimensional representation of the normalized m_z -component of the magnetization is shown in Figure 53 for $\underline{B}_{\text{Ext}}$ aligned parallelly to the horizontal stripe. The animation of the simulation data reveals the oscillation of the mode from the outer top and bottom edges of the stripe to the stripe center, which corresponds to the experimental observations. The horizontal stripe exhibits spin wave modes at the stripe edges, which were not imaged by STXM-FMR.

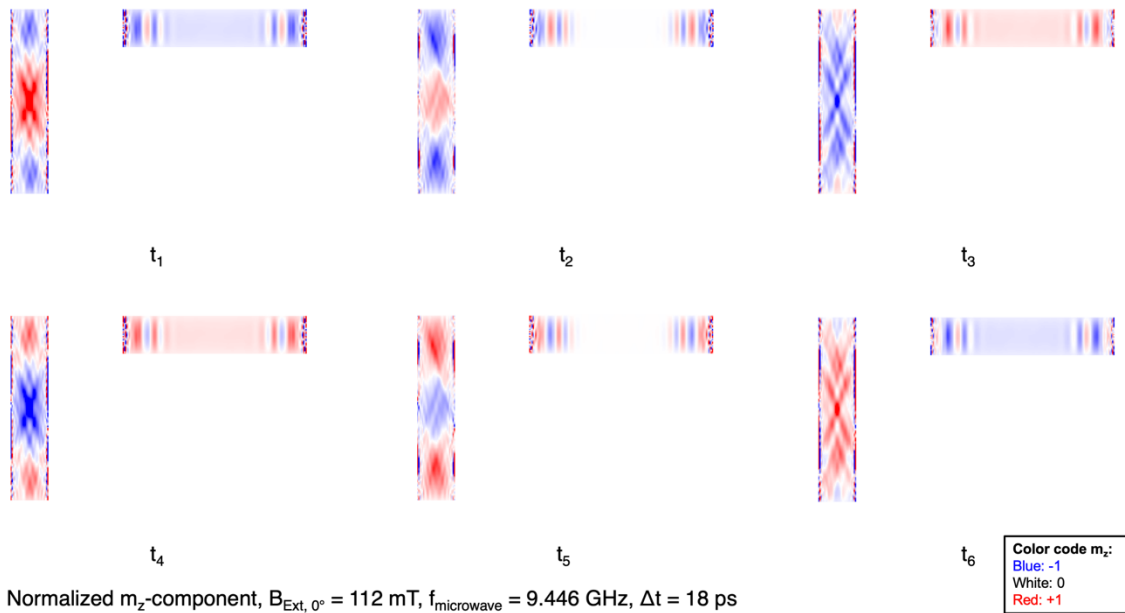


Figure 53: Two-dimensional representation of the simulated normalized m_z -component of the magnetization for $|\underline{B}_{\text{Ext}}| = 112 \text{ mT}$. The external field is oriented parallel to the horizontal Py stripe. Six images of the magnetization oscillation with a time distance of 18 ps are shown. The simulation data is published in part in [30].

A close to a uniform mode of the vertical Py stripe was imaged by STXM-FMR at a field of about 112 mT. The data is depicted in Figure 54. The animation of the images seen in subfigure a) reveals an oscillation of the mode from the center towards the long sides of the stripe as it has been observed for the T-shaped sample before (Figure 45 and Figure 46). The causative phase gradient can be seen in the plot of the

relative phase in subfigure b), showing a change of the phase from about 280° in the center to about 250° at the long sides of the stripe with a smooth transition. The amplitude distribution shows the highest amplitude at the stripe center. In contrast to the aforementioned STXM-FMR measurements of the L-shape geometry, the measurement data shows a slight tilt of the sample. The origin of the slight tilt of the sample in this measurement might be caused by a mechanical tilt of the sample holder.

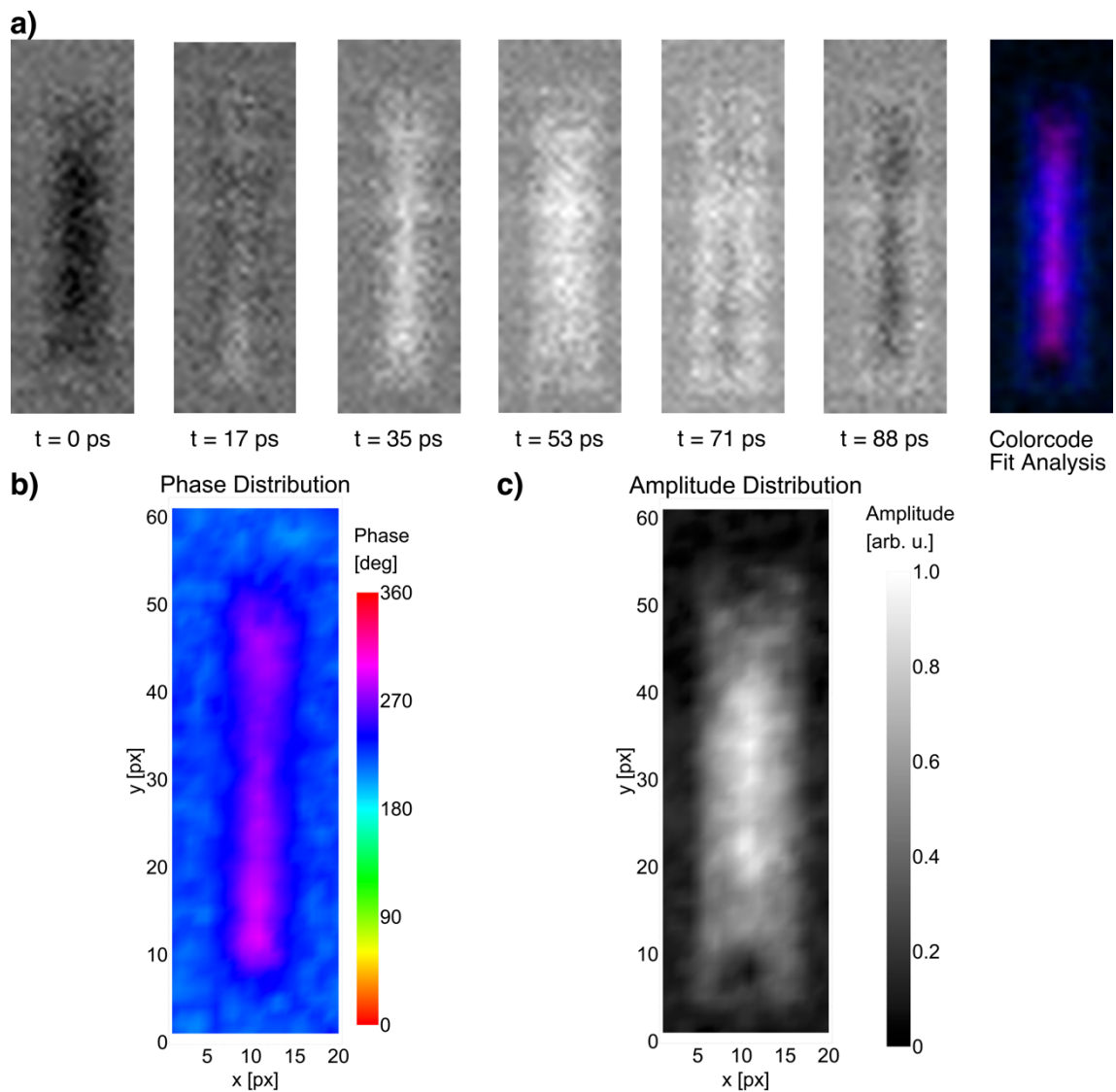


Figure 54: STXM-FMR data of the vertical Py stripe of the L-shape geometry at a static bias field of about 112 mT and a microwave power of 29 dBm. a) Microwave induced X-ray transmission for 6 timesteps with a time distance of about 18ps. b), c) Distribution of the relative phase with respect to the timestep $t = 0$ and the normalized amplitude extracted out of the color-code fit analysis (chapter 3.4).

The micromagnetic simulations of the uniform mode, shown in Figure 55 ($\underline{B}_{\text{Ext}}$ aligned parallelly to the horizontal stripe), show the same directed oscillatory behavior. As for the other Py stripe measurements before, the oscillatory behavior of the spin wave is attributed to the stray field distribution (Figure 27) causing additional edge mode excitations, e. g. [120, 122]. An influence of the strength of the applied external magnetic field with a possible offset to the exact resonance field, as it has been seen for the T-shaped stripe ensemble (Figure 45 and Figure 46), is a possible contribution to the magnitude of the phase gradient of the magnetization and the excitation of edge modes. As there is no additional dataset available for the L-shaped sample arrangement, this contribution cannot be elucidated.

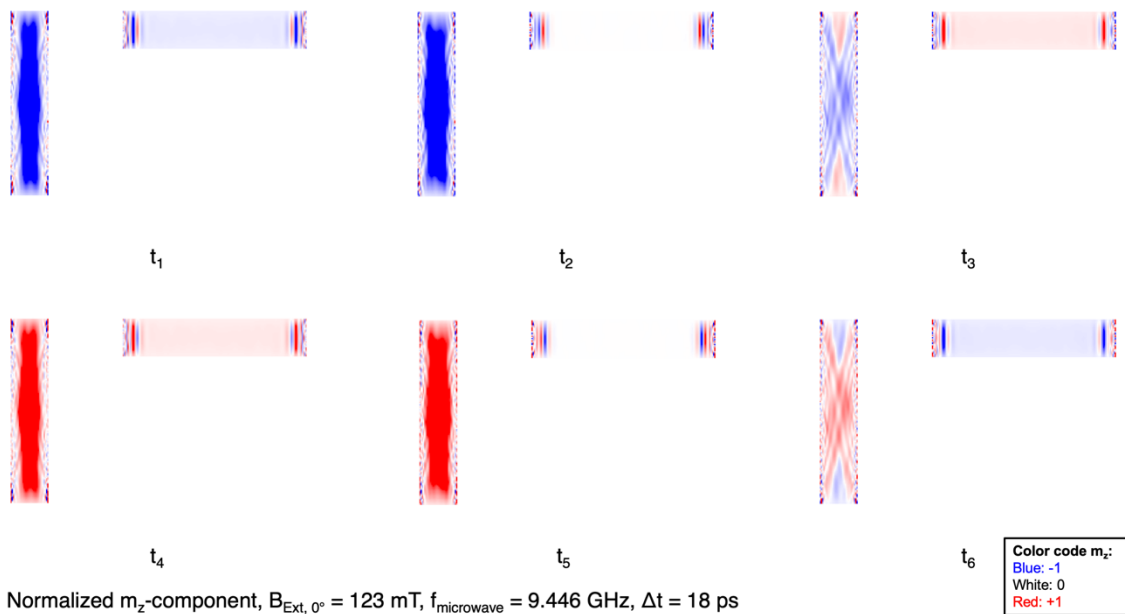


Figure 55: Two-dimensional representation of the simulated normalized m_z -component of the magnetization for $|\underline{B}_{\text{Ext}}| = 123 \text{ mT}$. The external field is oriented parallel to the horizontal Py stripe. Six images of the magnetization oscillation with a time distance of 18 ps are shown.

The horizontal Py stripe of the L-shaped sample geometry was imaged by STXM-FMR for three different $|\underline{B}_{\text{Ext}}|$. The results are visualized in Figure 56, Figure 58 and Figure 59. A close to uniform spin wave mode is shown in Figure 56. The animation of the data shown in Figure 56 a) reveals a weak directed oscillation of the mode from the center towards the short sides of the stripe, as it was observed for the corresponding mode in chapters 4.2.4 and 4.2.5. The color code fit analysis shows a change of the phase from about 225° (stripe center) to about 200° to 210° (outer

area of the stripe) with a smooth transition, indicating the presence of a phase gradient of the magnetization of about 15° to 25° . The amplitude distribution is mostly homogeneously distributed within the stripe with a slight decrease at both short stripe edges.

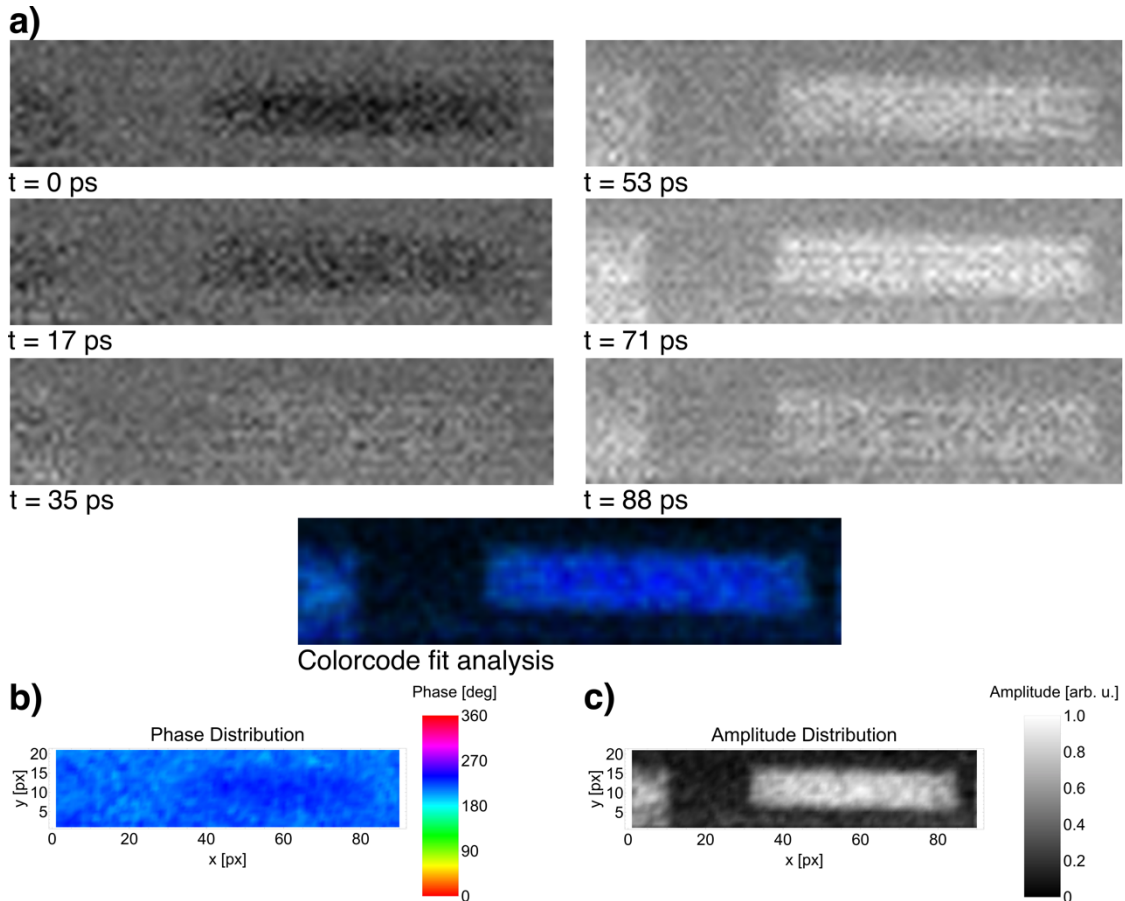


Figure 56: STXM-FMR data of the horizontal Py stripe of the L-shape geometry at a static bias field of about 74 mT and a microwave power of 29 dBm. a) Microwave induced X-ray transmission for 6 timesteps with a time distance of about 18ps. b), c) Distribution of the relative phase with respect to the timestep $t = 0$ and the normalized amplitude extracted out of the color-code fit analysis (chapter 3.4).

The directed oscillatory behavior of the spin wave mode is attributed to the stray field (simulation see Figure 27) induced excitation of edge modes (e. g. [120, 122]). Taking into account the observations for the close to a uniform mode of the T-shape geometry in Figure 45 and Figure 46, which showed a stronger phase gradient and therefore a stronger directed oscillation of the mode with $|B_{\text{Ext}}|$ deviating more from the assumed exact resonance field. It can be concluded that this measurement was

taken closely to the resonance field, as only a weak directed oscillatory behavior is seen.

The micromagnetic simulations shown in Figure 57 (not-tilted \underline{B}_{Ext}), resemble the experimental observations. The animation of the simulation data reveals a directed oscillation from the stripe center towards the stripe edges. The vertical stripe exhibits in the simulation a spin wave mode with seven anti-nodes and six nodes, which was not imaged by STXM-FMR.

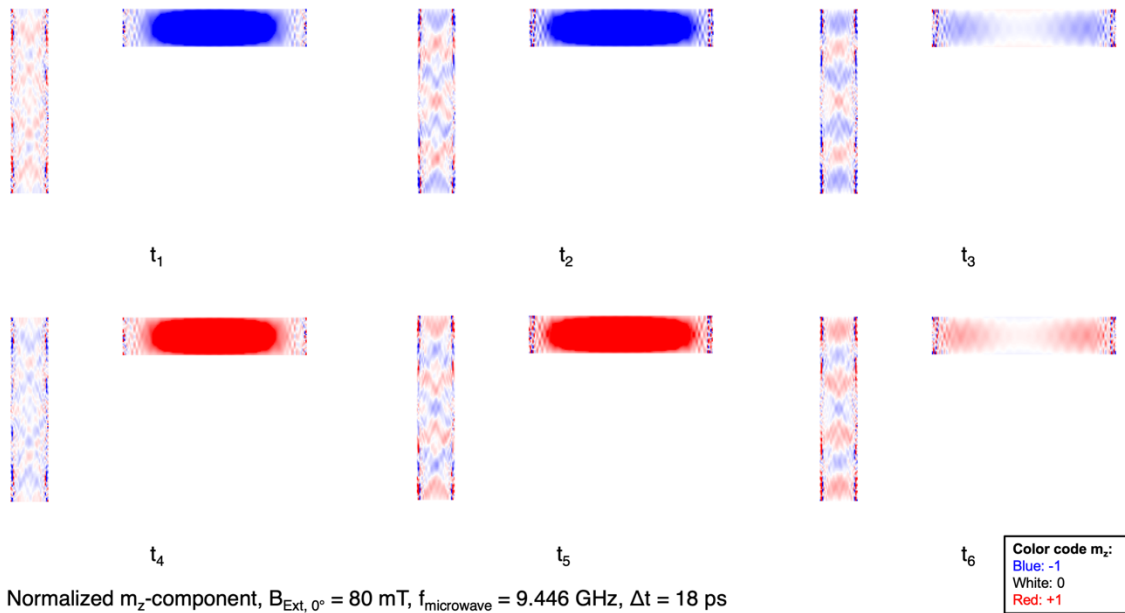


Figure 57: Two-dimensional representation of the simulated normalized m_z -component of the magnetization for $|B_{Ext}| = 80 \text{ mT}$. The external field is oriented parallel to the horizontal Py stripe. Six images of the magnetization oscillation with a time distance of 18 ps are shown.

Towards a spin wave mode showing two nodes and three anti-nodes (Figure 59) a measured intermediate mode is shown in Figure 58, comparable to the mode detected for the single Py stripe depicted in Figure 33. The animation of the data shown in Figure 58 a) reveals an oscillation direction of the mode from the center towards the short sides of the stripe. The color code fit analysis shows a phase gradient of the magnetization from about 135° (stripe center) to about 40° (outer area of the stripe) with a smooth transition, which is attributed to the influence of the stray field distribution (simulation see Figure 27), as for all other stripe ensembles, leading to additional edge mode excitations (e. g. [120, 122]). The amplitude distribution

shows the highest amplitude at the outer parts of the stripe and much lower amplitude at the stripe center. The visible oscillation of the background is attributed to the influence of the microwave on the avalanche photodiode [46], as described in chapter 4.1.3.

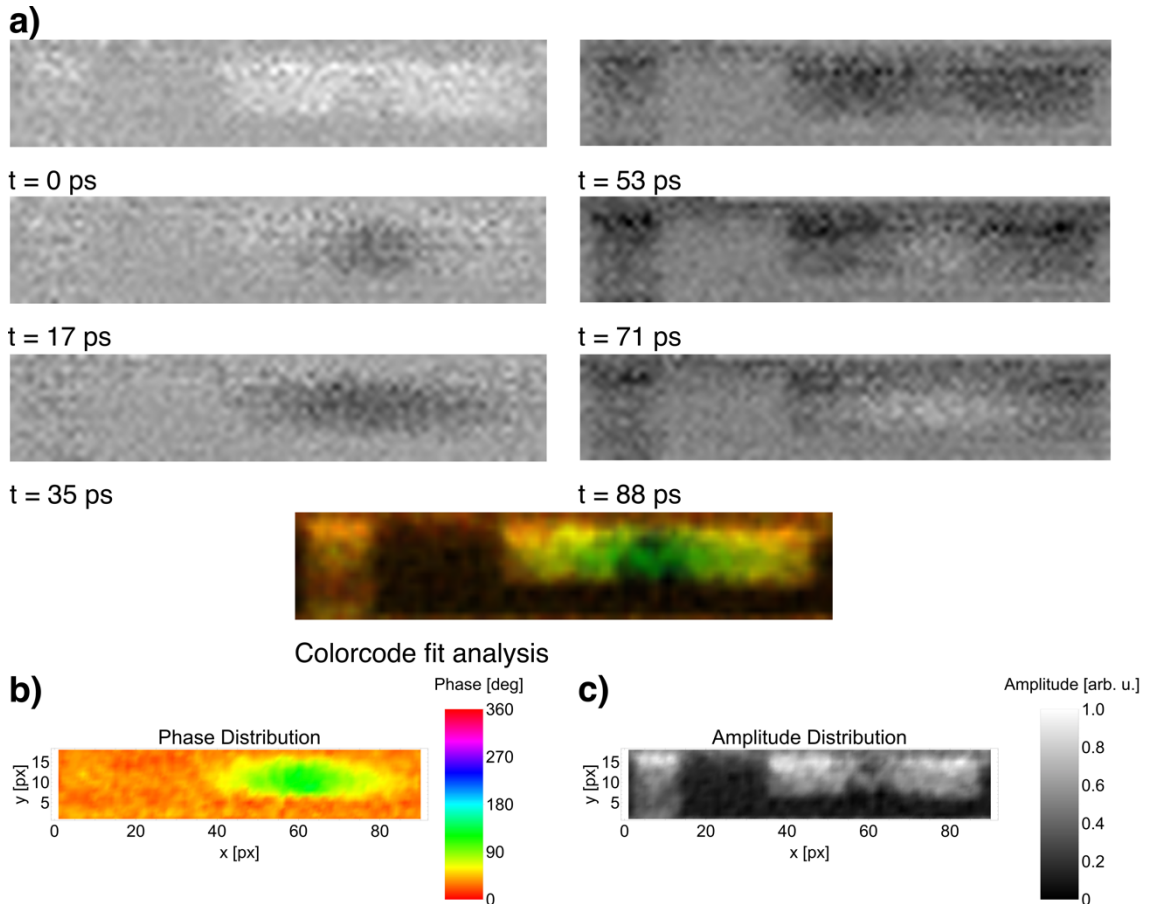


Figure 58: STXM-FMR data of the horizontal Py stripe of the L-shape geometry at a static bias field of about 81 mT and a microwave power of 29 dBm. a) Microwave induced X-ray transmission for 6 timesteps with a time distance of about 18ps. b), c) Distribution of the relative phase with respect to the timestep $t = 0$ and the normalized amplitude extracted out of the color-code fit analysis (chapter 3.4).

The STXM-FMR data showing a two-node and three anti-node spin wave mode is pictured in Figure 59. As for the horizontal stripes shown in chapters 4.2.4 to 4.2.5, a directed oscillation from the stripe center to the short sides of the stripe can be observed caused by the stray field influence (Figure 27) causing edge mode excitations [120, 122]. The phase distribution reveals a change of the relative phase from about 280° in the stripe center to about 135° at the stripe edges, indicating the phase

gradient of the magnetization causative for the directed oscillation. The phase distribution is inverted compared to the mode observed in the vertical stripe of the T-shape sample in Figure 43. The amplitude distribution shows the highest amplitude at the outer anti-nodes and a less intense amplitude at the center anti-node. The micromagnetic simulations shown in Figure 60 show the same spin wave mode as the experiment. The animation of the simulation data shows an oscillation direction of the mode from the center of the stripe towards the short stripe sides, which corresponds to the experimental observations. The simulated vertical stripe exhibits a spin wave mode with seven anti-nodes and six nodes. The background oscillations are attributed to the microwave radiation influencing the avalanche photodiode [46] (see chapter 4.1.3).

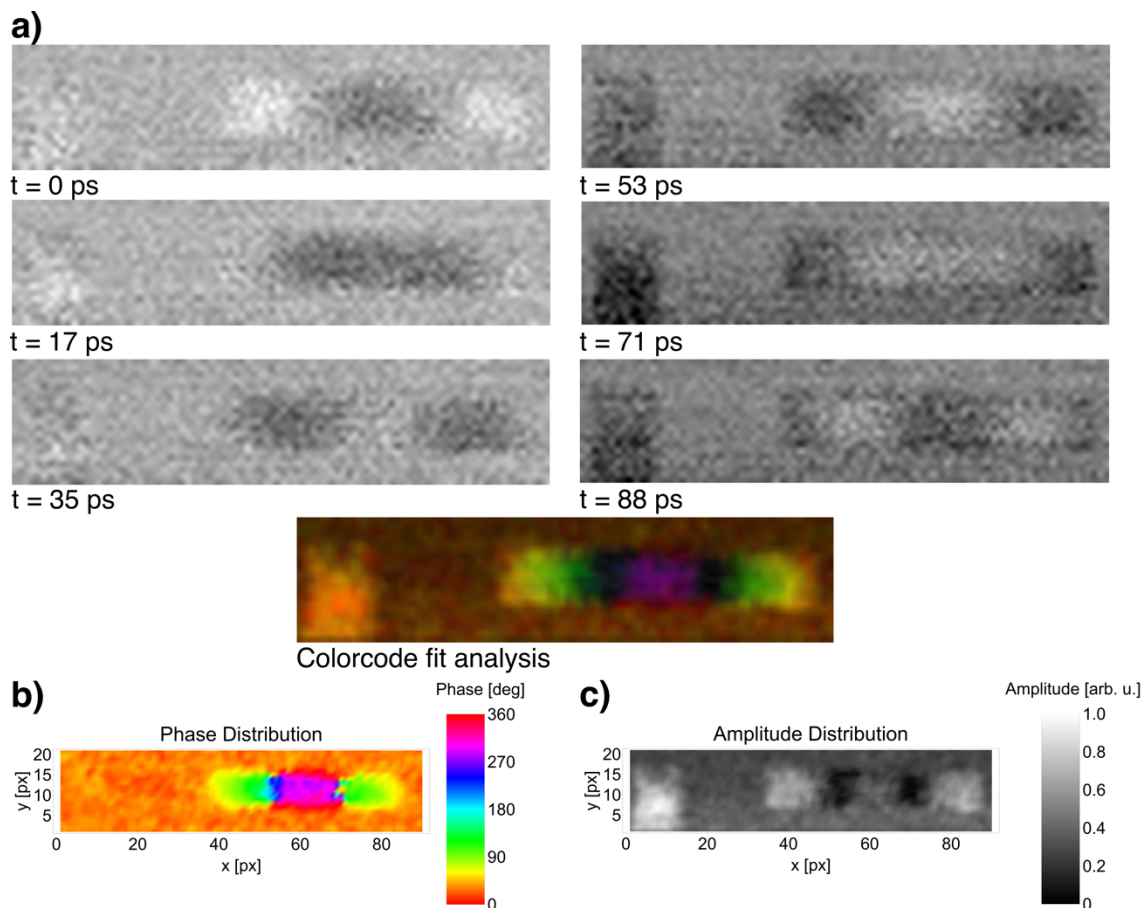


Figure 59: STXM-FMR data of the horizontal Py stripe of the L-shape geometry at a static bias field of about 87 mT and a microwave power of 29 dBm. a) Microwave induced X-ray transmission for 6 timesteps with a time distance of about 18ps. b), c) Distribution of the relative phase with respect to the timestep $t = 0$ and the normalized amplitude extracted out of the color-code fit analysis (chapter 3.4).

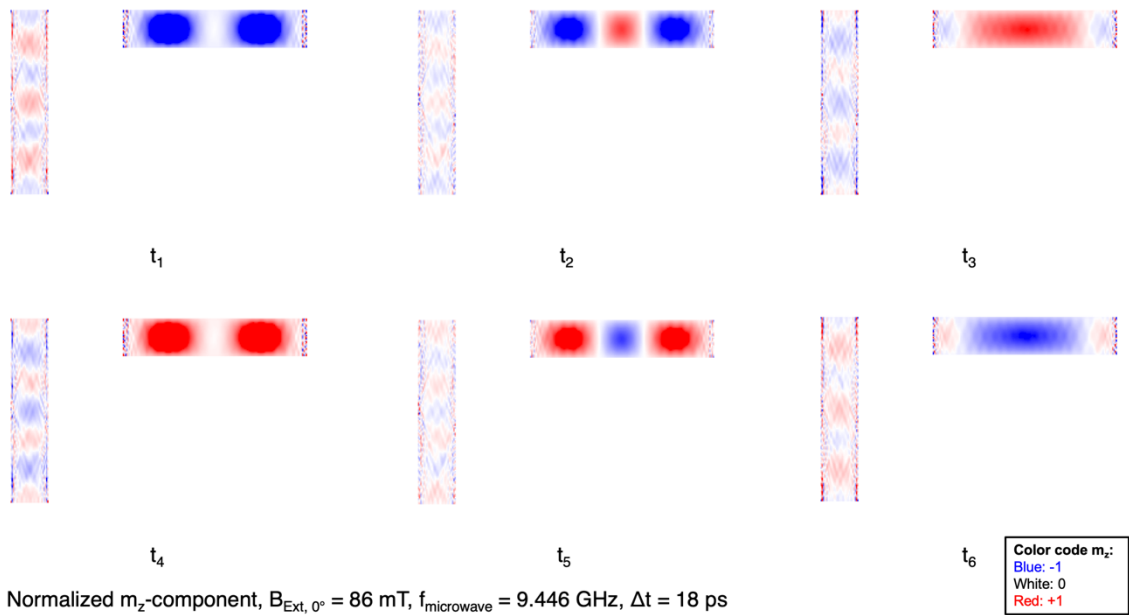


Figure 60: Two-dimensional representation of the simulated normalized m_z -component of the magnetization for $|B_{Ext}| = 86$ mT. The external field is oriented parallel to the horizontal Py stripe. Six images of the magnetization oscillation with a time distance of 18 ps are shown.

4.2.7. Summary

The STXM-FMR measurements revealed the magnetization dynamics in three different Py stripe geometries, a single Py stripe, a T-shaped, and an L-shaped Py stripe arrangement. Spin wave modes up to five nodes and six anti-nodes could be visualized, all showing a directed oscillatory behavior deviating from the expected behavior of a pure standing spin wave excited by a homogeneous microwave field [30, 71, 72]. The presence of a phase gradient of the magnetization is causative for the directed oscillation with its strength depending on the strength of the phase gradient. For the (close to) uniform mode of the vertical stripe of the T-shaped stripe arrangement the influence of the strength of $|\underline{B}_{\text{Ext}}|$ on the directed oscillation could be revealed, as the strength of the directed oscillation and correspondingly the strength of the phase gradient changes with a larger deviation from the exact resonance field of this mode (Figure 45, Figure 46). A tilted external magnetic field results in a different shape of the nodes and anti-nodes, but shows no visible influence on the directed oscillation in the micromagnetic simulations.

The spin wave modes and their directed oscillatory behavior is directly confirmed by these micromagnetic simulation. By taking into account the demagnetization- and stray field distribution obtained from the simulation, the directed oscillations in the experiments and the simulations can be attributed to the stray field influence on the Py stripes (Figure 25, Figure 27), resulting in the presence of additional resonance conditions for the corresponding stripe. In consequence, additional edge modes are excited, as they have been described in [119-121], resulting in the phase gradient and the observed directed oscillatory behavior. This stray field influence is present for all investigated spin wave modes, which can be observed in the simulated stray field distribution (Figure 25 b), d), Figure 27 b)). Therefore, all experimental results show a phase gradient and the resulting directed oscillating modes, with the strength of the latter depending on the strength of the phase gradient. At least for the uniform mode it is shown that the strength is, as aforementioned, also dependent on deviations from the exact resonance field of the corresponding mode (Figure 45, Figure 46), see also the explanations in [30, 130]. It can be assumed that this behavior is given for uniform and non-uniform spin waves, taking into account that the interplay between $|\underline{B}_{\text{Ext}}|$ and the stray field defines the effective field $|\underline{B}_{\text{eff}}|$,

at which the resonance condition for edge modes is fulfilled, resulting in the directed oscillatory behavior of the spin wave modes. In literature roughness effects affecting the spin wave behavior are reported, e. g. [131] [30]. As the here performed micro-magnetic simulations do not employ any sample imperfections or roughness, but nevertheless are resembling the experimental observations, the excitation of edge modes due to stray field effects is regarded as the source of the observed directed oscillatory behavior, albeit for the experiment's roughness effects cannot be neglected.

Slight deviations of comparable spin wave modes in the T- and L-shape geometries are attributed in [30] to the arrangement of the stripe ensemble. In the analysis here the spin wave modes show in general a similar behavior with respect to the number of nodes, anti-nodes and the directed oscillatory behavior, while the amplitude distributions and the simulated FMR absorption spectra for both geometries show slightly less amplitudes and intensities, respectively. This small effect is attributed to the large distance of 2 μm between the stripes, resulting in a weak stray field influence.

5. Magnetization dynamics of nanometer sized sample structures

5.1. Visualization of the magnetization dynamics of Yttrium Iron Garnet nanoparticles

The first measurements to demonstrate the nanometer scale spatial resolution of STXM-FMR were performed on Yttrium Iron Garnet (YIG) nanoparticles.

5.1.1. Sample overview

The nanoparticles with a diameter of ≥ 40 nm were produced by laser ablation and fragmentation of pressed powders [132]. A solution of particles and ethanol was put into a micro-resonator loop by Eppendorf micro-capillaries with a tip diameter of 4 μm attached to an Eppendorf PatchMan NP2 micro-manipulator. An SEM image of the sample is shown in Figure 61, depicting an agglomerate of YIG particles with the size of about 300 nm · 150 nm (size obtained from STXM measurements), pictured within the dotted yellow circle.

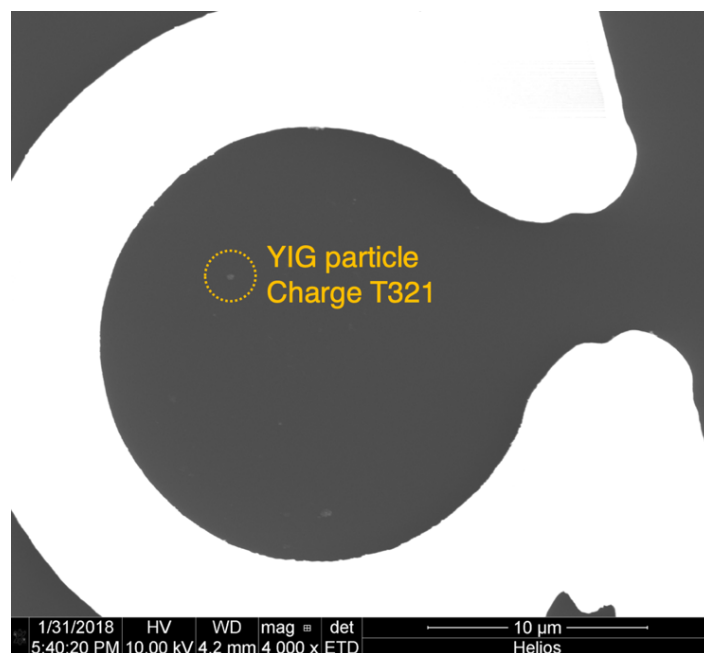


Figure 61: SEM image of the YIG nanoparticle sample positioned in the micro-resonator loop. The SEM image was taken by D. Spoddig.

The number of particles within this agglomerate can be estimated to about 30+ by taking into account the area of the agglomerate and the particle size, neglecting a stacking of particles.

5.1.2. Ferromagnetic Resonance measurement of the YIG sample

The sample was measured by FMR (see chapter 3.1) at a frequency of 8.15 GHz with a microwave power of 20 dBm at room temperature. The recorded FMR spectrum is shown in Figure 62. The error bar of $|B_{\text{Ext}}|$ is ± 0.5 mT. Three pronounced resonances can be seen, one at $|B_{\text{Ext}}|$ of 9 mT with a line width of 27 mT and one at 80 mT with a line width of 44 mT. At 2.2 mT the spectrum shows an additional signal with a line width of 0.5 mT, shown in the inset of Figure 62. The signal consists in total of 4 measurement points, so it cannot be clearly attributed to a resonance from the single measurement. As in [133] a similar signal at the top of the main resonance of investigated YIG nanoparticles (size 100 nm +) is visible, a third resonance in the spectrum in Figure 62 is probable, while no further explanation is given in [133].

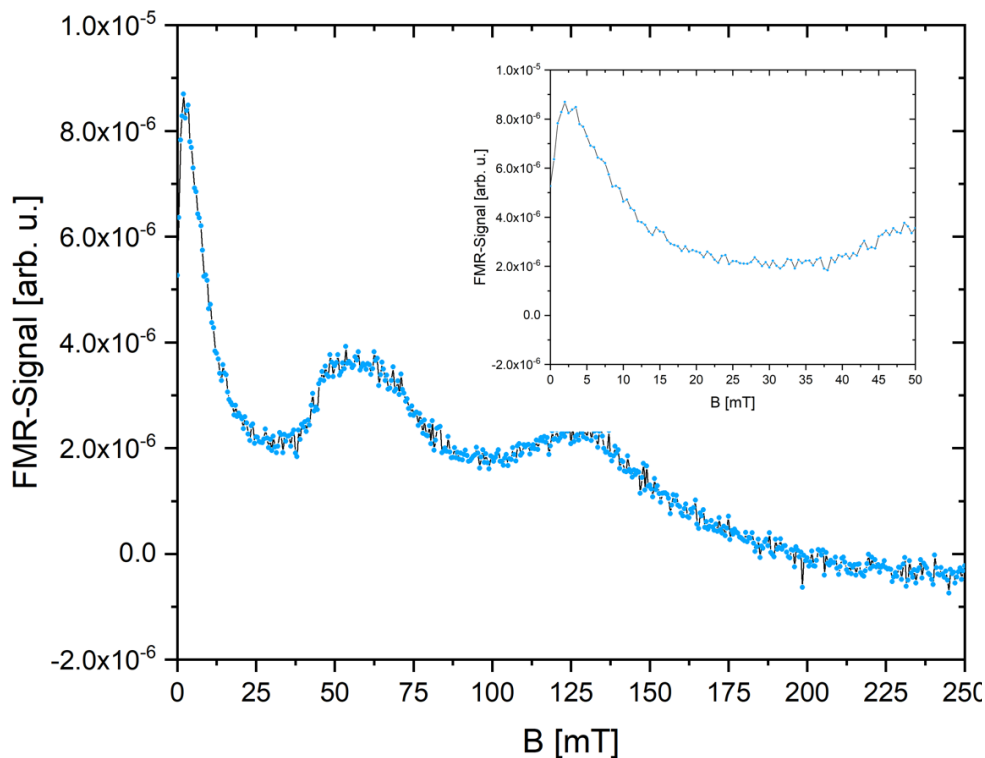


Figure 62: FMR spectrum of the YIG sample designated for STXM-FMR measurements. The measurement was performed at room temperature at 8.15 GHz. The inset shows a magnification for the field range from 0 mT to 50 mT.

It has to be noted, that a multitude of YIG particles is situated in the resonator loop, which all contribute to the FMR measurement, resulting in a broad FMR signal.

5.1.3. STXM-FMR measurements of the YIG sample

The STXM-FMR measurement was performed at the Fe L_3 absorption edge at an energy of 706.8 eV [134]. The images were recorded with a scan step size of 20 nm a focus of 50 nm and a dwell time for each single pixel of 5000 ms with a negative helicity of the X-ray photons. The excitation frequency was set to 6.748 GHz, which corresponds to the 14th harmonic + $1/(m=6)$ of the synchrotron frequency. The microwave power was set to 28 dBm. The external static magnetic field was set to 80 mT.

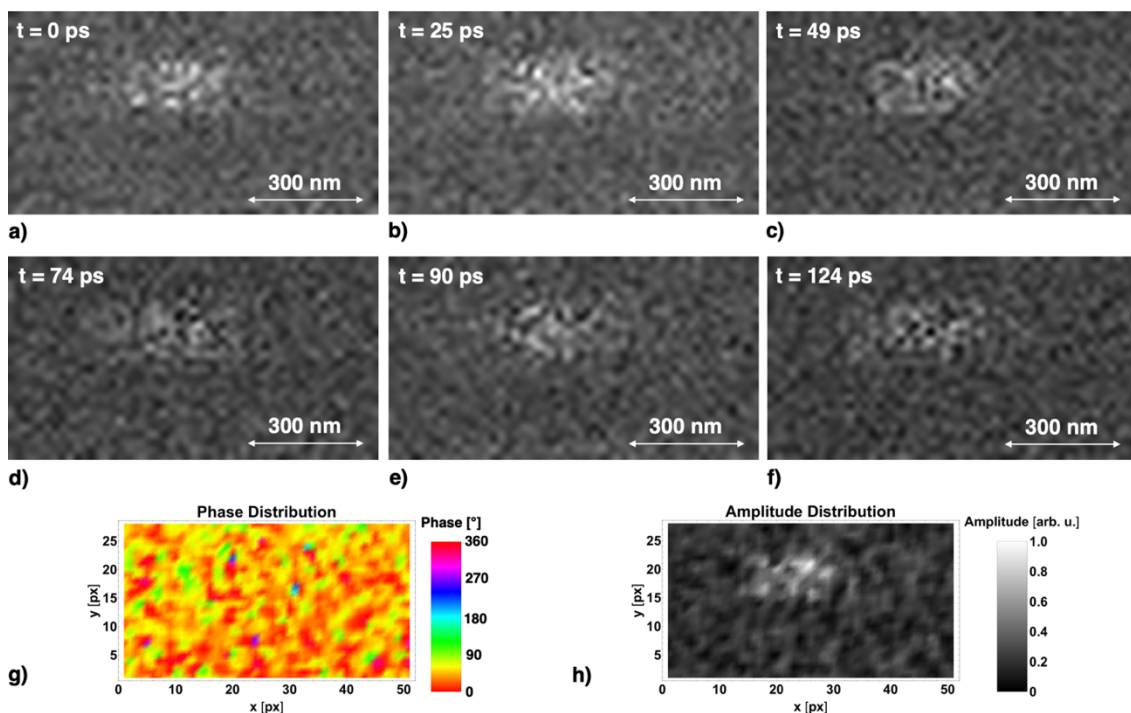


Figure 63: a) to f): STXM-FMR images after taking the natural logarithm of the division operation of the microwave on and microwave off images for the recorded time steps. A minimum-maximum normalization [127] was applied to the images. The images in a) to f) are blurred to enhance visibility. g) and e) Phase and normalized amplitude distribution extracted out of the color code fit analyses (see chapter 3.4 and [103] of the whole scan area).

The STXM-FMR data obtained from the YIG particle sample is shown in Figure 63. The subfigures a) to f) are indicating an oscillation with a non-uniform amplitude within the area of the YIG particle agglomerate. The distribution of the relative phase, which was extracted from the result of the color code fit analyses (see chapter 3.4 and [103]), shows an inhomogeneous distribution of the phase, which is not visible in the grayscale STXM-FMR data. The extracted amplitude distribution shows a pronounced amplitude at the location of the YIG particle agglomerate, which corresponds to the grayscale data presented in subfigures a) to f). Figure 64 shows an overlay of the amplitude distribution over the phase distribution. From this representation, it is probable that segments of multiple particles are resonating at the same phase, while other particle segments or single particles are resonating with a different phase.

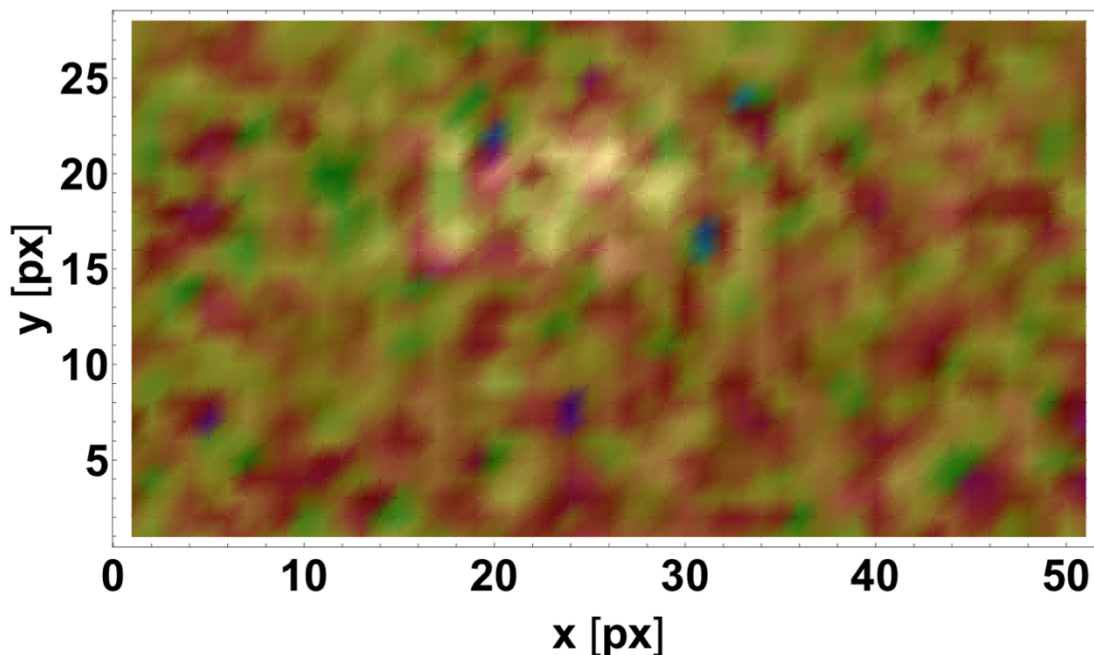


Figure 64: Overlay of the amplitude distribution (Figure 63 h) over the phase distribution (Figure 63 g).

For dipolarly coupled Fe_3O_4 nanoparticles with similar dimensions, a behavior of single particles or particle segments being in resonance with the same phase, while other particles / particle segments exhibit a resonance at a different phase, was shown in [11], using angular dependent FMR measurements and micromagnetic simulations. The aforementioned behavior results in so-called magnonic band gaps in the angular dependent spectra. The observed behavior of the YIG nanoparticles

here can probably be attributed to a similar effect assuming only dipolar coupling between the particles. To proof this angular dependent FMR measurements of the particle agglomerate would be necessary. Nevertheless, the measurement shows that the resonant response of particles on the nanoscale has successfully been detected by STXM-FMR.

5.2. STXM-FMR measurements of nanoparticle chains in bacteria *Magnetospirillum Magnetotacticum*

For future magnonic computing, the use of the nanoparticle chains inside of magnetotactic bacteria as magnonic logic devices has been suggested in [11]. By manipulating the bacteria DNA it is possible to alter the arrangement of the nanoparticles and by that alter the magnon dispersion of these particle ensembles to realize magnon based binary logic [11]. These investigations were performed employing conventional micro-resonator based FMR and micromagnetic simulations [11]. Here the first element-specific, spatially, and time-resolved visualizations of FMR of single chains magnetosome chains of magnetite (Fe_3O_4) nanoparticles inside a bacterium *Magnetospirillum Magnetotacticum* [135, 136] by STXM-FMR are presented.

5.2.1. *Magnetospirillum Magnetotacticum*

The bacterium *Magnetospirillum Magnetotacticum* [135, 136] has been described and specified as type strain MS-1 in [136]. An electron micrograph image of a cell of this bacterium is shown in Figure 65, revealing a chain of 19 magnetic nanoparticles (white spots) in the cell center.

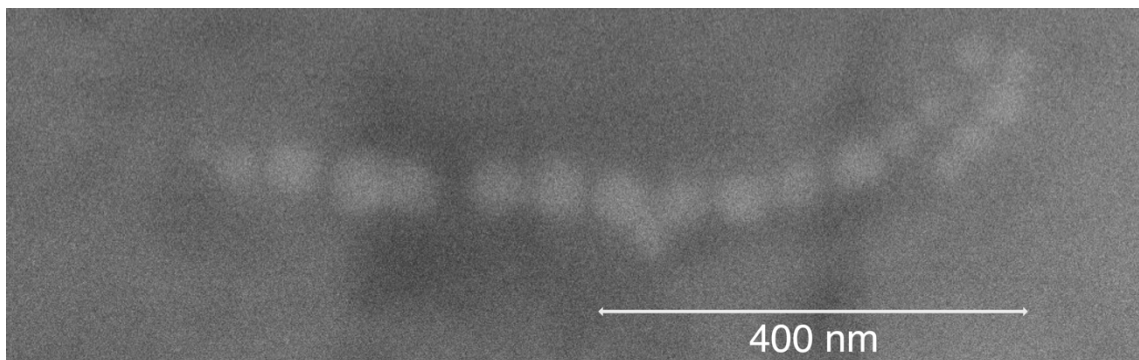


*Figure 65: SEM image of a magnetosome chain inside a bacterium *Magnetospirillum Magnetotacticum*, the chain is subject of investigation by means of STXM-FMR. The image was taken by D. Spoddig. For better visibility the contrast has been adjusted by +40 %.*

Magnetospirilla, like many other magnetotactic bacteria from the Alphaproteobacteria taxon, are capable of biomineralizing membrane-enclosed single-crystal Fe_3O_4

particles (magnetosomes) and aligning them in a chain along the cell axis [137-139]. In fully grown cells of MSR-1, the magnetosomes consistently have a particle size in the range of 40 nm to 50 nm [136].

Fe_3O_4 is cubic (space group $Fd\bar{3}m$ [137, 140]) above the Verwey transition at 122 K [140]. Above the isotropic point at 130 K [141], the $\langle 111 \rangle$ crystal axes (body diagonals) define the magnetic easy axes [141], which can be described by a negative first-order cubic magneto crystalline anisotropy constant. From single-crystal FMR measurements, K_4 was determined as $-1.1 \cdot 10^4 \text{ J/m}^3$ at room temperature [141]. From magnetization curves on a series of single-crystals with known stoichiometry, K_4 was determined as $-1.2 \cdot 10^4 \text{ J/m}^3$ for purely stoichiometric magnetite [142]. In [143] a value of $K_4 = -1.3 \cdot 10^4 \text{ J/m}^3$ is given. The second-order cubic anisotropy constant is with $K_6 = 3 \cdot 10^4 \text{ J/m}^3$ [143] much smaller in value than K_4 and therefore, it exhibits a higher relative error than the value of K_4 . A schematic overview of the Fe_3O_4 easy axis is pictured in Figure 66. In magnetotactic spirilla, each magnetite particle is arranged such that one of the $\langle 111 \rangle$ axes is aligned along the axis of the magnetosome chain [144]. The magnetosomes with the dimensions given before are in the single domain state [145], as the single domain limit is at $68 \pm 10 \text{ nm}$ [146]. These findings are supported by investigations in [147-149]. Micromagnetic simulations performed by the author in [85] also confirm the single domain size limit.

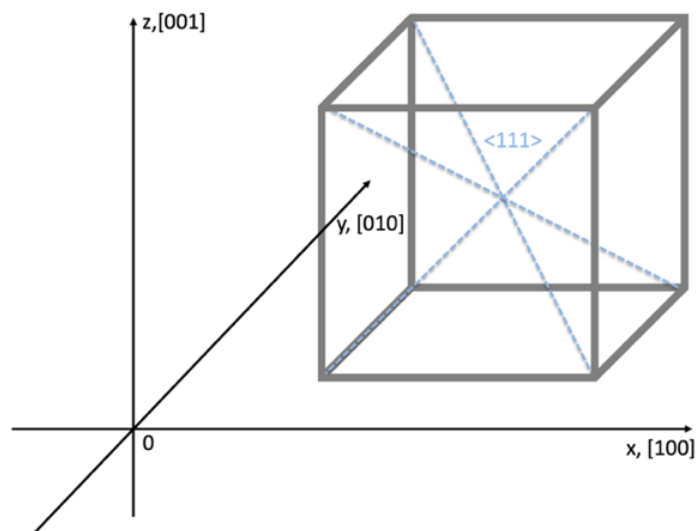


Figure 66: Schematic representation of the magnetic easy directions in a single Fe_3O_4 cube. Figure adapted from [85].

5.2.2. Sample preparation

The bacteria cells of *Magnetospirillum Magnetotacticum* strain MS-1 were purchased as actively growing culture in liquid medium from Leibniz Institute DSMZ-German Collection of Microorganisms and Cell Cultures GmbH, article number DSM 3856 [150]. After shipment, the bacteria culture was stored in a lab refrigerator at a temperature of about 278 K for 14 days, during which time the cell density in the storage tube increased. For sample preparation, a drop of cell suspension was transferred from the storage tube with a sterile syringe to a 15 ml Eppendorf tube and concentrated by centrifugation at 14000 rpm for a time of 30 minutes. From the resulting pellet, bacteria cells were suctioned into an Eppendorf microcapillary with 4 μm tip diameter, which was re-positioned over a micro-resonator with the aid of a micromanipulator Eppendorf PatchManNP2 mounted to an inverted light microscope Zeiss Type 471705-9901/09. The cells were dropped onto the loop of the micro-resonator with the aid of a microinjector Eppendorf CellTram Vario. For the control of the preparation an inverted light microscope Zeiss Axiovert 100 was used.

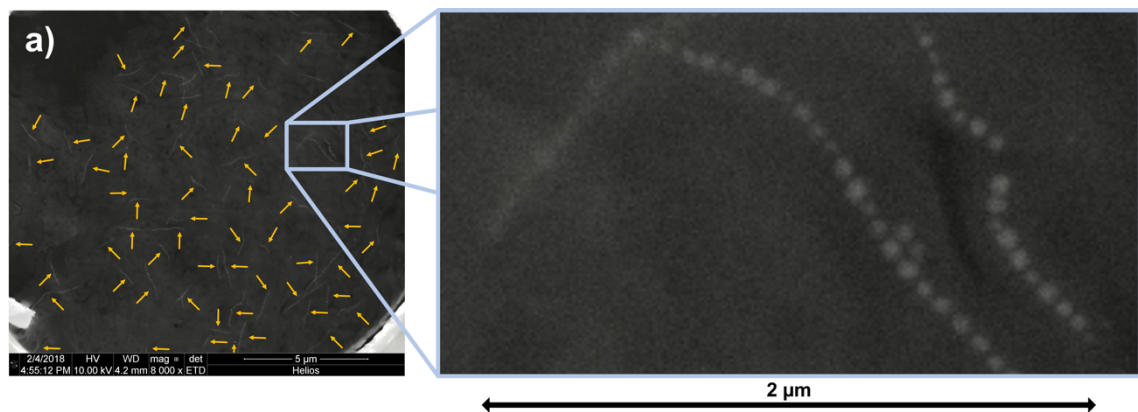


Figure 67: Scanning Electron Microscopy (SEM) images of the triple chain magnetosome ensemble for the STXM-FMR beamtime February 2018: a) Magnetosome chain distribution inside the micro-resonator loop. The chains enclosed in the blue square were measured by STXM-FMR. Other chains in the micro-resonator loop are marked by yellow arrows. b) Magnification of the magnetosome chain ensemble. The SEM images were taken by D. Spoddig.

Due to the adhesive force, the bacteria cultures remain at the position they were placed. Scanning electron microscopy, shown in Figure 67, was used to confirm that

the resonator loop contained a multitude of magnetosome chains in different orientations (Figure 67 a), so that at least a few of them would be aligned with the DC magnetic field of ≤ 200 mT available in the STXM-FMR and thus would meet the resonance condition in this field range. In conventional micro-resonator based FMR measurements, however, the resulting spectra of such a sample would contain the resonances of all magnetosome chains in the loop, making it impossible to assign resonances to a given magnetosome chain.

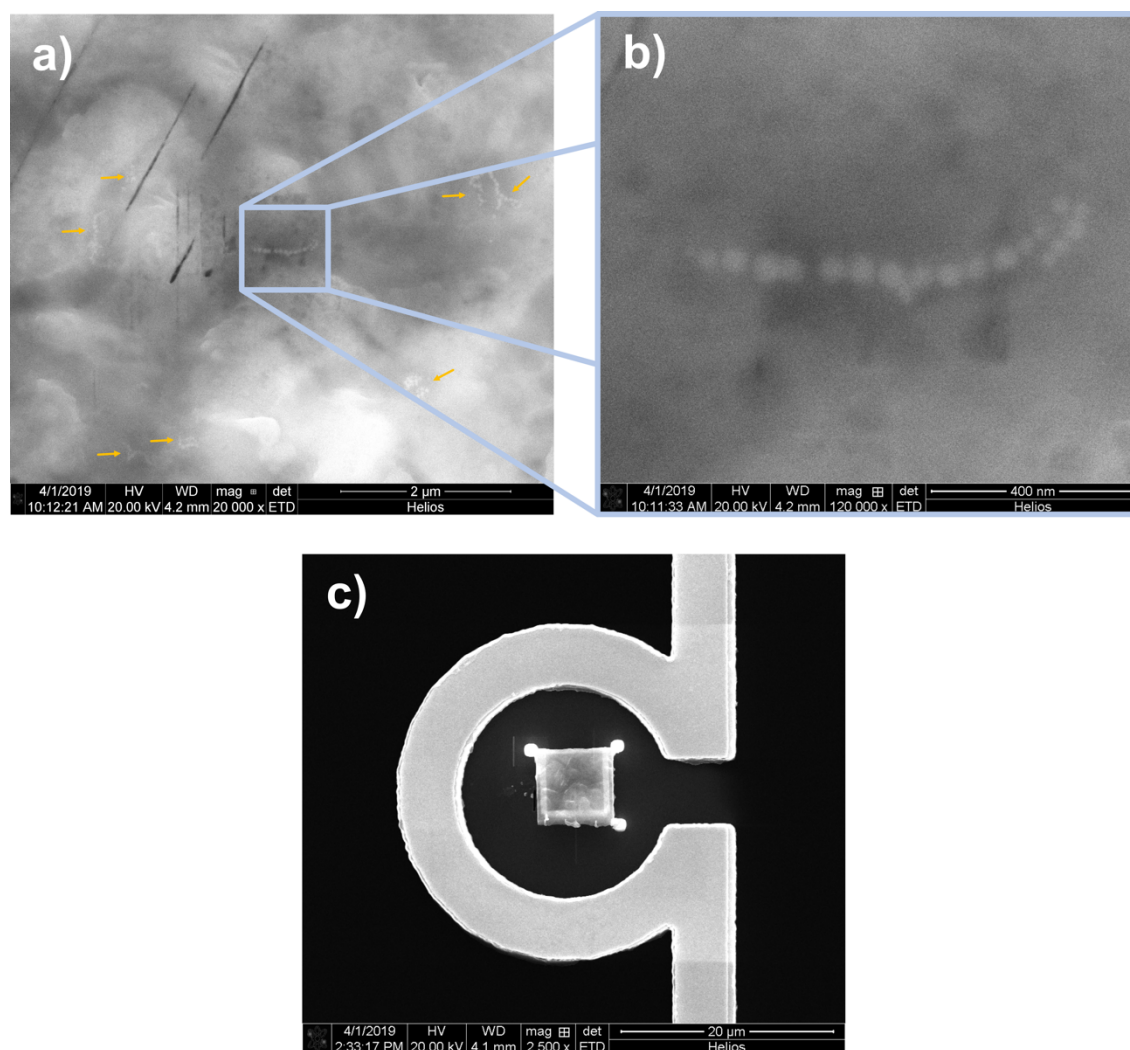


Figure 68: Scanning Electron Microscopy (SEM) images of the magnetosome chain preparation: a) TEM grid cutout showing the bi-segmented magnetosome chain for the STXM-FMR measurement inside the blue box. The diagonal black lines are carbon deposits. b)) Magnification of this particle chain. c) TEM grid cutout placed inside the micro-resonator loop, fixed with carbon at three corners of the cutout. The images were taken by D. Spoddig.

The three magnetosome chains selected for the STXM-FMR measurements in February 2018 are shown in Figure 67 b). For the STXM-FMR beamtime in April 2019, the samples were prepared in the following way. A drop of bacterial cells was first placed on onto Transmission Electron Microscopy (TEM) grids (Figure 68 a)), using the optical microscope setup and micromanipulator mentioned above following the same preprocessing method as for the sample described before. A segment of the TEM grid with several magnetosome chains was cut out by D. Spoddig (Figure 68 a), b)) using a focused ion beam (FIB, FEI Helios NanoLab 600 XL) and placed in the center of a micro-resonator loop on the Si_3N_4 membrane. The final STXM-FMR sample thus contained a magnetosome chain right in the center of the micro-resonator loop (Figure 68 c)).

5.2.3. STXM-FMR measurements of the triple chain magnetosome ensemble

A static characterization of the nanoparticle chains inside magnetotactic bacteria by soft X-ray ptychography are shown in [139]. Here we present in the two next chapters the characterization of the magnetization dynamics of such particle chains by means of STXM-FMR. The room temperature measurements were performed at a microwave frequency of 8.1766 GHz and a microwave power of nominal 40 dBm at $|\underline{B}_{\text{Ext}}| \sim 160$ mT. The pressure in the chamber was about $5 \cdot 10^{-7}$ Torr. An X-ray absorption spectrum (XAS) was performed at the Fe L_3 edge (706.8 eV [134]) from 703 eV to 715 eV to confirm the presence of Fe in the magnetosomes (Figure 69).

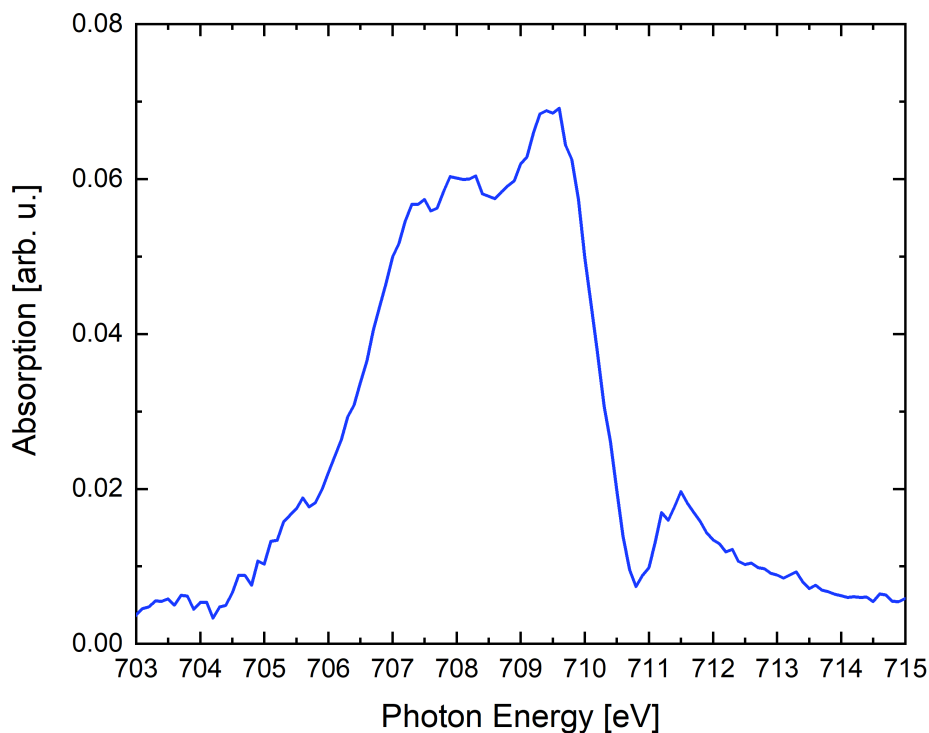


Figure 69: X-ray absorption spectrum around the energy of the Fe L_3 edge (708 eV). The spectrum was taken by H. Ohldag.

For STXM-FMR the X-ray energy was set to the center of the Fe L_3 absorption edge to 708 eV. Due to mechanical limitations of the setup a maximal focus of 50 nm could be reached.

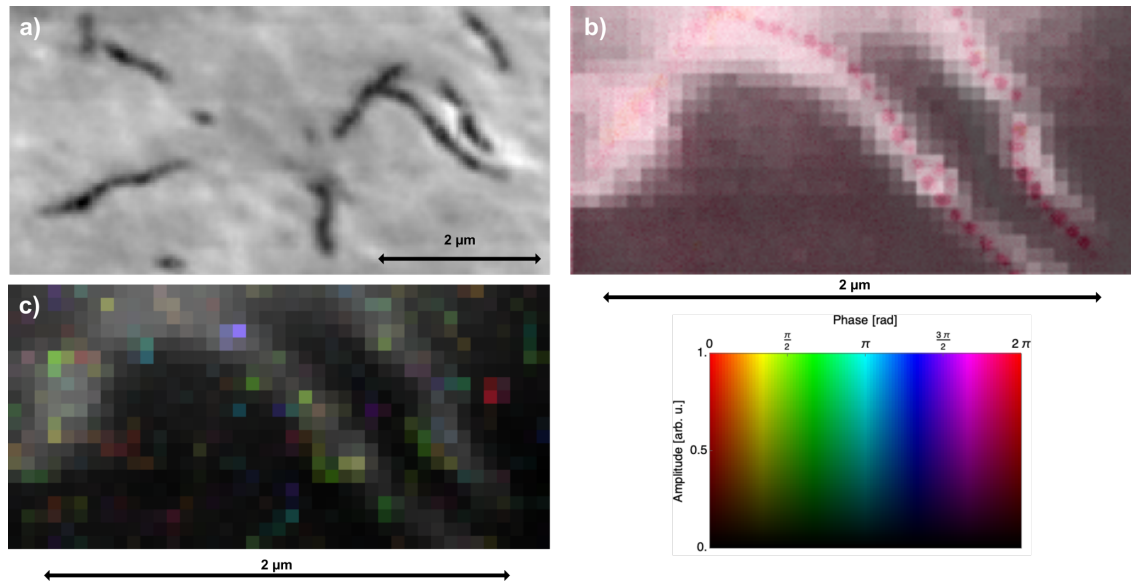


Figure 70: a) Grayscale STXM image of the magnetosome chain ensemble. The image has been taken by H. Ohldag. Darker colors represent areas with less transmission due to the magnetosome chains. b) Visualization of the investigated magnetosome chains in inverted colors with an overlay of the SEM image in Figure 67 b). The overlay has been created by B. Zingsem. c) Result of the color-code fit analysis, coding the relative phase as hue, the amplitude as brightness and the p-value as saturation.

The microwave induced X-ray transmission was analyzed by fitting a sinusoidal function to the time dependence of the absorption at each pixel (see chapter 3.4 and [103]). Each period was sampled with six timesteps, corresponding to six STXM-FMR images per 1/8.1766 GHz. The result of the analysis is shown in Figure 70 c). Several colored areas of single or small groups of pixels in the image are visible within the magnetosome chain and next to it. The brightest colored pixel ensembles can be observed at locations along the magnetosome chain, varying in the relative phase between $\pi/4$ and $(5\pi)/3$. This leads to the assumption that only small segments of the nanoparticle chain are in resonance. To clarify this assumption, the phase and amplitude information has been extracted from Figure 70 c) and is displayed in Figure 71.

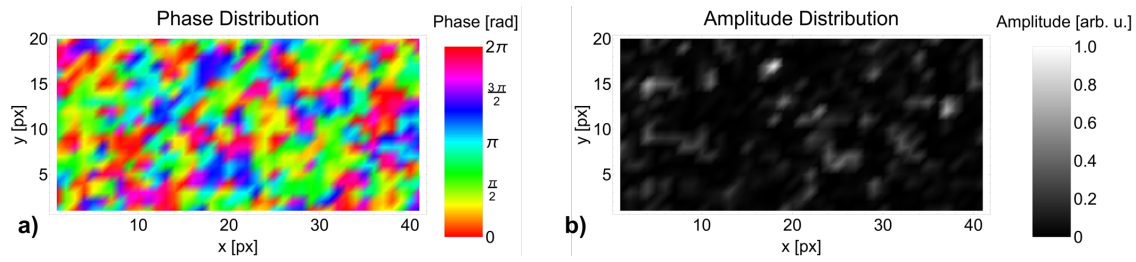


Figure 71: a) Phase and b) normalized amplitude distribution extracted from Figure 70 c).

An inhomogeneous phase distribution is found for the complete scanned area in Figure 71 a), which does not allow to assign distinct phase relations to the particle chain. The amplitude distribution shown in Figure 71 b) shows three coherent pixel ensembles indicating a high amplitude at the coordinates $(x=4, y=15)$, $(x=18, y=17)$ and $(x=38, y=13)$. While the pixels at the last set of coordinates are located at a position next to the magnetosome chain Figure 70 b), c), the first two sets of coordinates refer to locations of nanoparticles (Figure 70 b), c)). Further investigations of this sample were not possible, as the sample got lost during Transmission Electron Microscopy Measurements at the Forschungszentrum Jülich.

To proof the detection of resonant responses in magnetosome chains, a 2nd sample was prepared (see chapter 5.2.2) and investigated with STXM-FMR at the beamtime in April 2019. The findings are presented in the chapter 5.2.5.

5.2.4. Micromagnetic simulations of the triple chain magnetosome ensemble

Due to the huge amount of magnetosome chains within the micro-resonator loop (Figure 67 a)), which would result in an indistinguishable number of FMR signals in a conventional FMR measurement, a micromagnetic model of the magnetosome ensemble pictured in Figure 67 b) has been created in MuMax3 [29]. The dynamic simulation was performed at a frequency of 8.176 GHz, an amplitude of 0.5 mT, and an exchange stiffness $A_{\text{ex}} = 1.32 \cdot 10^{-11}$ J/m [151]. For energy minimization, the method presented in [108] was used next to the MuMax3 build-in “relax()” function [29]. A set of simulations was performed using the values for the saturation magnetization M_{sat} and magneto crystalline constant K_4 given in [141]. The simulation using $M_{\text{sat}} = 4.94 \cdot 10^5$ A/m and $K_4 = -0.63 \cdot 10^4$ J/m³ [141], while stated for a temperature of -100 °C, gave the simulation result closest to the experimental findings in the STXM-FMR. The static magnetic field was applied in-plane and orientated along the y-axis of the simulation grid (see chapter 3.5) to reflect the geometry of the experiment. Due to the immense amount of in total 52 simulated particles, the particle edge length had to be reduced to 32 nm, using a cell size of (8 nm)³, which is below the magnetic exchange length of 9.28 nm [106] for the selected parameters. The distance (edge to edge) between the magnetosomes is 8 nm. The simulation grid has the dimensions of 218x66x5 cells.

A two-dimensional representation of the simulated sample geometry is depicted in Figure 72 a). The simulated stray/demagnetization field intensity and distribution of the magnetosome chain ensemble is shown in Figure 72 b) and c). Values of $|\underline{B}_{\text{Demag}}|^{\ddagger} \sim 450$ mT are visible between the magnetosomes in Figure 72 b), pointing to a strong dipolar coupling between the particles. The distribution in Figure 72 c) also reveals that whole groups of magnetosomes are coupled by magnetic dipolar coupling, and the two neighboring chains are reciprocally weakly influenced by their stray fields. The simulated FMR absorption spectrum is shown in Figure 73. Two resonances at 157 mT and 164 mT can be identified, which are within the surroundings of the external magnetic field of about 160 mT used in the experiment.

[‡] The term $|\underline{B}_{\text{Demag}}|$ includes in MuMax3 the stray- and the demagnetization field [29].

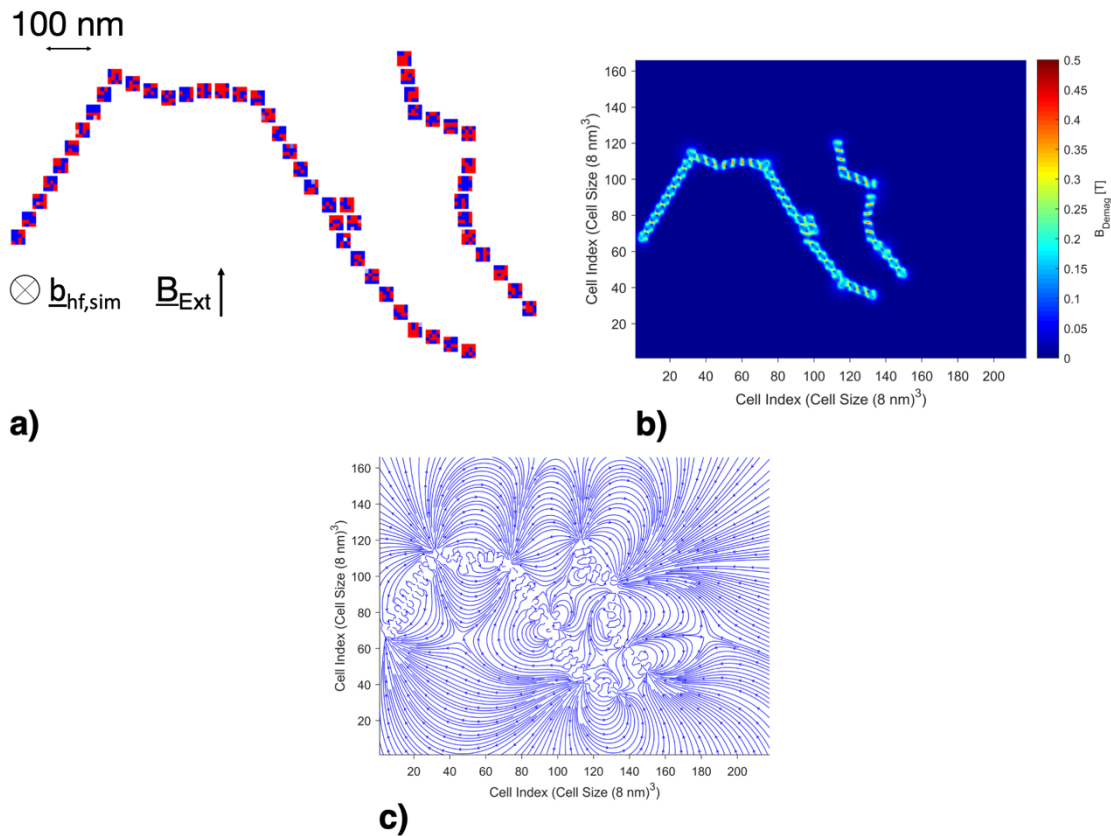


Figure 72: **a)** The simulated magnetosome chains, viewed from the $+z$ direction, shown in the state of a random start magnetization. Shown is the normalized m_z component: Blue $-m_z$, red $+m_z$. **b)** Stray- and demagnetization field intensity.[§] **c)** Stray field distribution. In all figures the cell layer in the particle center is shown.

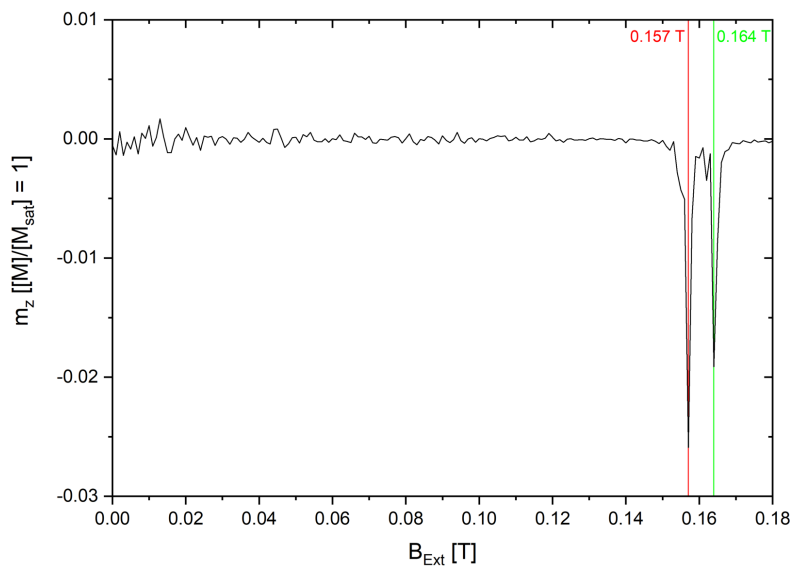


Figure 73: Simulated FMR spectrum of the triple magnetosome chain ensemble at 8.176 GHz and an amplitude of 0.5 mT.

[§] The term $|\underline{B}_{\text{Demag}}|$ includes in MuMax3 the stray- and the demagnetization field [29].

The normalized m_z -component of the magnetization is displayed in Figure 74 for a single time point of the simulation. The saturation of the colors indicates a weaker or stronger magnitude of the normalized m_z component of the magnetization corresponding to weaker and stronger color saturation. Except for five particles in the lower right chain, all particles show a weak red and blue coloring (blue: $-m_z$, red $+m_z$) pointing to an inhomogeneous excitation with the upper part of the particles having a positive magnitude of m_z , while the lower part of the particles shows a negative magnitude of m_z . The strong blue saturated particles in the lower right chain in Figure 74 a), b) and c) visualize the uniform resonance at 157 mT and its vicinity. Figure 74 d) to f) depicts the surroundings of the resonance at 164 mT (subfigure e) showing the upper four particles of the upper right chain uniformly in resonance concerning the magnitude and distribution of m_z , indicated by the homogeneous blue coloring.

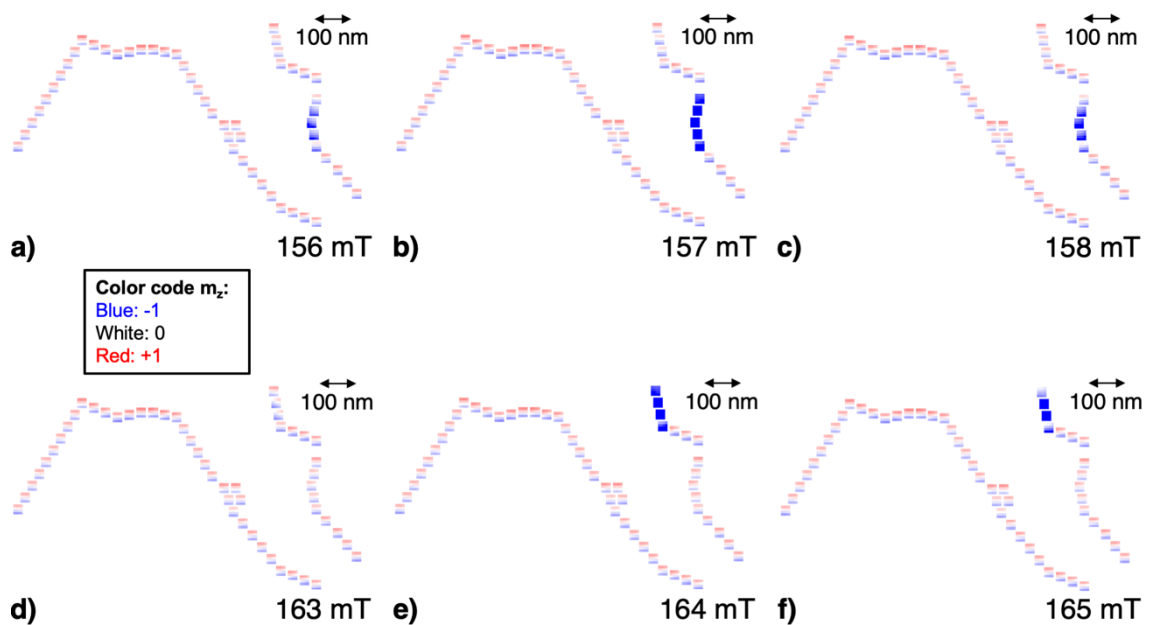


Figure 74: Two-dimensional representation of the simulated m_z -component of the magnetization for external magnetic bias field values of a): 156 mT, b): 157 mT, c) 158 mT, d) 163 mT, e) 164 mT and f) 165 mT. Shown is the center cell layer.

When comparing the experimental results (Figure 70, Figure 71) to the simulated m_z -component of the magnetization shown in Figure 74, the detection of a resonant response at the coordinates showing a high STXM-FMR amplitude seems to be

probable, while a clear assessment or identification of resonant responses in the magnetosome chains from the measurement data is difficult.

5.2.5. STXM-FMR measurements of a single bi-segmented magnetosome chain

The room temperature STXM-FMR measurements were performed at a microwave frequency of 6.748 GHz and a microwave power of about 25 dBm. The pressure in the chamber was about $5 \cdot 10^{-7}$ Torr. The X-ray energy was set to the Fe L₃ edge at nominal 708 eV with a focus of about 50 nm.

Figure 75 shows STXM-FMR images recorded with a step resolution of 25 nm and a dwell time of 5000 ms at an external field of 167 mT. All STXM-FMR images have been mirrored by 180° to reflect the SEM images, and a minimum-maximum normalization [127] was applied.

Figure 75 a) shows the STXM-FMR image of the bi-segmented magnetosome chain. The black contrast in the central area of the image represents the magnetosome chain. Due to the spatial resolution of 50 nm single magnetosomes cannot be distinguished due to a particle size of 40 nm to 50 nm, see chapter 5.2.1. An additional black contrast area is visible above the magnetosome chain, which is attributed to carbon deposition, as the SEM image in Figure 68 c) does not show evidence of magnetosomes at this position. An overlay with the SEM image Figure 68 c is shown in Figure 75 d). The alignment of the SEM image was orientated at the pronounced kink of the magnetosome chain, which is visible in the STXM-FMR images. To visualize and analyze the microwave induced X-ray transmission the color code fit analysis (see chapter 3.4), fitting a sinusoidal with relative frequency to each pixel in the row of six STXM images for the six timesteps was applied. The phase distribution is plotted in the range between 0 and 2π , while the amplitude is normalized between 0 to 1. The results are shown in Figure 76. A quite uniform relative phase is visible in Figure 76 a) between $(19\pi)/12$ and $(5\pi)/3$. This is confirmed by the phase distribution depicted in Figure 76 b), which is extracted from the color-code fit analyses. In the center of Figure 76 a) an area of contrast with brighter colored pixels is visible, following a curvature, which reflects the curvature of the magnetosome chain as it is depicted in Figure 68 c).

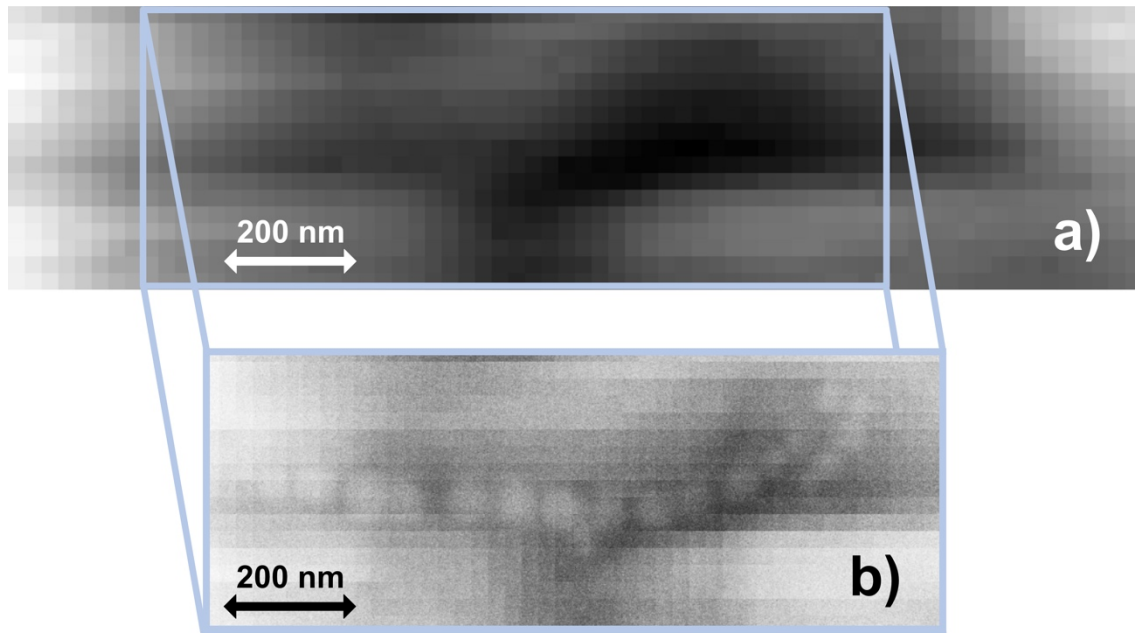


Figure 75: a) Grayscale STXM-FMR image of the investigated magnetosome chain. Darker colors represent areas with less transmission due to the sample and carbon on the sample surface. b) Cutout of image a) with an overlay of the SEM image, taken from Figure 68 c). The contrast has been adjusted for better visibility. The areas of dark contrast above and to the right of the depicted position of the magnetosome chain are attributed to deposited carbon, as the SEM image in Figure 68 c) shows no magnetosomes in these areas.

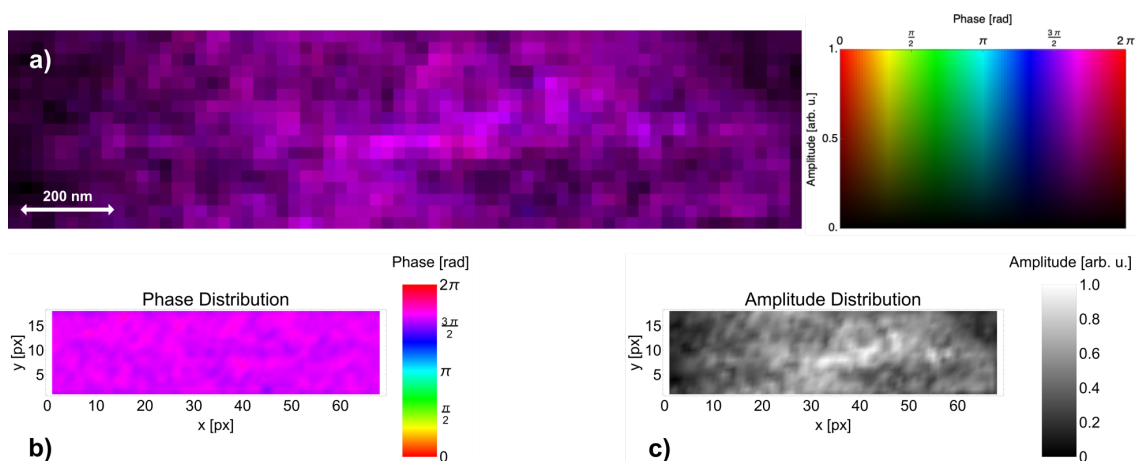


Figure 76: a) Result of the color-code fit analysis, coding the relative phase as hue, the amplitude as brightness and the p-value as saturation. b) Distribution of the relative phase extracted from image a). c) Normalized amplitude distribution extracted from image a).

By extracting the amplitude distribution out of the color-code analysis, which is shown in Figure 76 c), an area of non-uniform high amplitude following the curvature of the magnetosome chain is elucidated. An additional amplitude contribution visible in Figure 76 c) at $x = 56$ px and $y = 10$ px is not expected to originate from the investigated magnetosome chain. On the other hand, while at this position no particles are visible in the SEM images, one cannot exclude that particles are hidden by a large amount of biomass. A resonant response with uniform phase and non-uniform amplitude of the curved part of the magnetosome chain can be distinguished, while a much weaker excitation is assumed in the area of the detached four magnetosome chain segment. A verification of these results was done by creating a micromagnetic model of the sample (chapter 5.2.6).

5.2.6. Micromagnetic simulations of the single bi-segmented magnetosome chain

The 19 particle magnetosome chain was simulated using the following parameters $A_{\text{ex}} = 1.32 \cdot 10^{-11}$ J/m [151], $M_{\text{sat}} = 4.65 \cdot 10^5$ A/m and $K_4 = -1.0 \cdot 10^4$ J/m³** . The simulation grid consists of 200x80x12 cells, each with a cell size of (5 nm)³. Each simulated magnetosome has edge lengths of 50 nm, the distance between the particles is 10 nm. The high-frequency excitation was simulated at 6.748 GHz, which corresponds to the experimental value. The energy minimization was done with the method shown by [108] in combination with the MuMax3 build-in “relax()” function [29]. A three-dimensional representation of the simulated magnetosome chain in the random start configuration of the magnetization is depicted in Figure 77 a) together with visualizations of the simulated stray-/demagnetization field in Figure 77 b), c), d). For these visualizations a simulated external field of 169 mT was applied. As for the previous magnetosome chain (chapter 5.2.3 to 5.2.4), a high intensity of $|\underline{B}_{\text{Demag}}|^{\dagger\dagger}$ of up to about 450 mT can be seen between the neighboring nanoparticles, except between the upper edge particles in the right chain segment, which show an intensity of about 180 mT to 200mT. Between the chain segments an intensity of about 50 mT is visible. In combination with the stray field distribution

** Values for M_{sat} and K_4 : Personal communication with M. Winklhofer.

†† The term $|\underline{B}_{\text{Demag}}|$ includes in MuMax3 the stray- and the demagnetization field [29].

(subfigure c)) the of magnetic dipolar coupling between the single particles and the chain segments is elucidated.

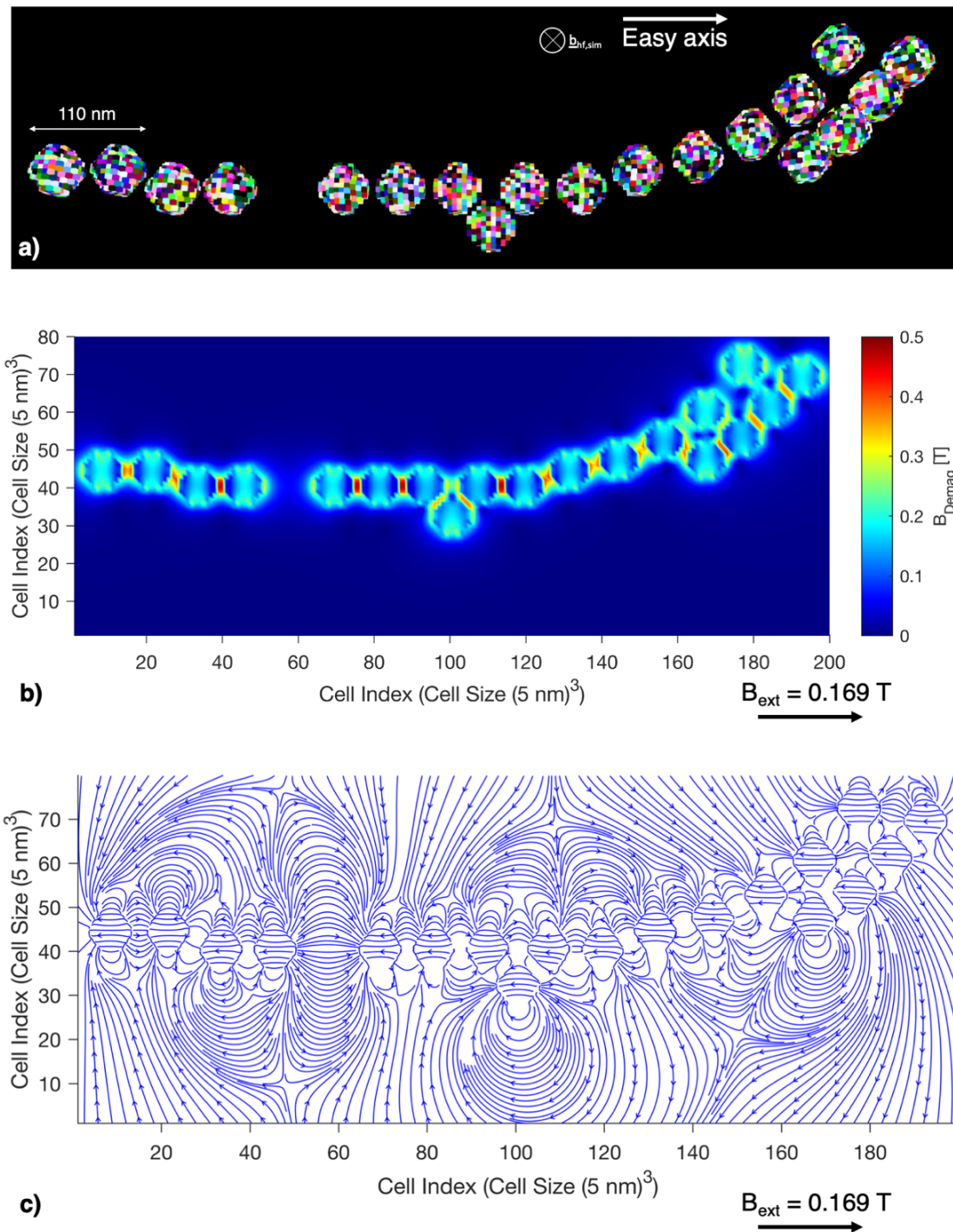


Figure 77: **a)** Three-dimensional representation of the simulated magnetosome chain for the beamtime in April 2019. Image was done in Muvier. The chain is imaged with the random start configuration of the magnetization. **b)** Plot of the stray- and demagnetization field strength. **c)** Stray field distribution. **b)** and **c)** are simulated with an applied $|B_{Ext}| = 169 \text{ mT}$ as indicated in the figure.

The simulated FMR absorption spectrum (m_z -component) pictured in Figure 78 shows several resonances above $|\underline{B}_{\text{Ext}}| = 160$ mT. The closest resonance peak to the experimental $|\underline{B}_{\text{Ext}}| \sim 167$ mT is at 169 mT.

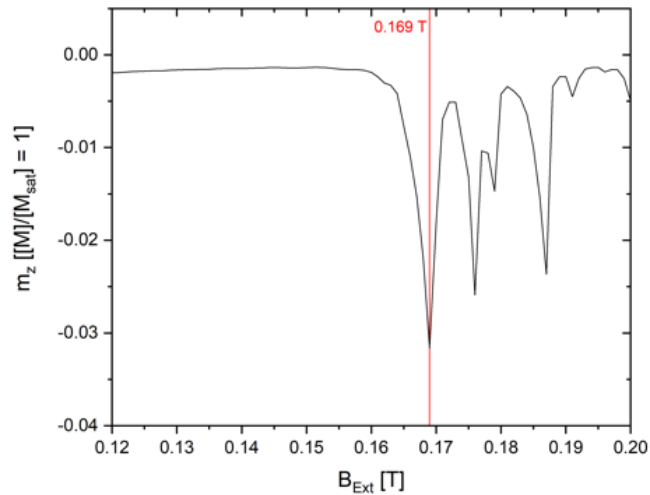


Figure 78: Simulated FMR absorption spectrum of the bi-segmented magnetosome chain. The resonance at 169 mT close to the experimentally observed resonance at 167 mT is indicated in red.

The magnitude of the normalized m_z -component of the magnetization is shown as two-dimensional visualization for six timesteps with a time distance of 24.7 ps for an external magnetic field of 166 mT in Figure 79 and for 169 mT in Figure 80. Shown is the lower cell layer, the oscillatory behavior of the other layers deviates only slightly from the shown data. As in the micromagnetic model all particles are of the same size, slight deviations between the experiment and the simulations are attributed to this difference, as particle size and positioning affect the strength of dipolar coupling and by that the resonant response. A pronounced resonant response can be seen in both figures within the curved segment of the magnetosome chain, while the 4-magnetosome segment exhibits a much weaker resonant response. In contrast to the simulation at 169 mT, which shows a non-uniform magnitude of the m_z -component, a dominantly uniform distribution of the m_z -magnitude is visible at 166 mT. The phase and amplitude analysis of the simulation data processed by M. Winklhofer gives the final confirmation of the experimental results. Both the experimental and the simulation results from this analysis are shown in Figure 81. The uniform phase distribution is in very good agreement between experiment and simulation with values between $(19\pi)/12$ and $(5\pi)/3$ (subfigures a) and c).

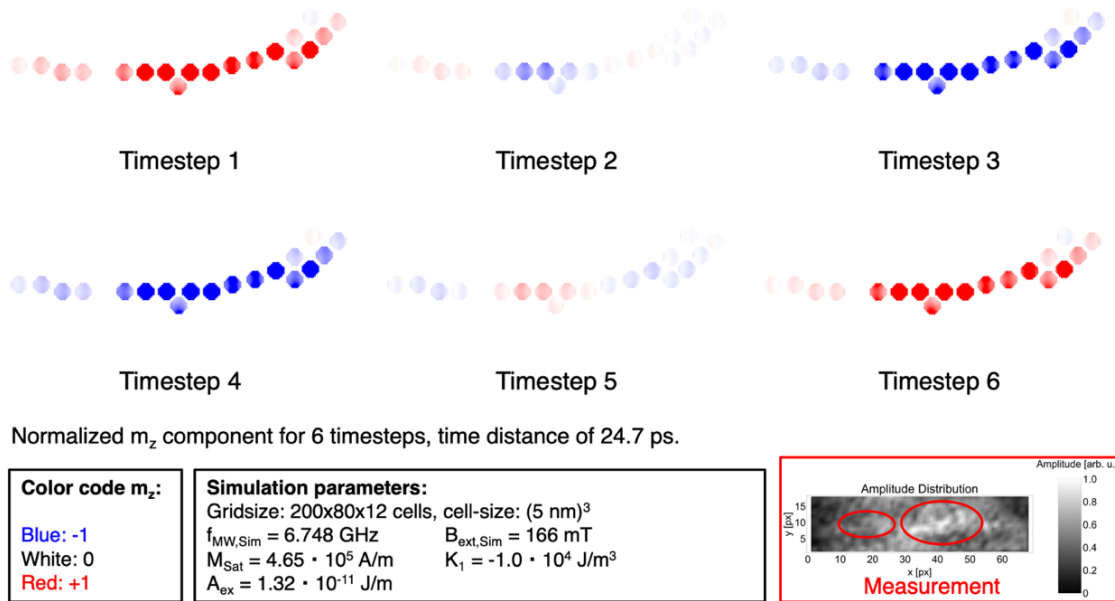


Figure 79: Micromagnetic simulation of the magnetosome chain investigated with STXM-FMR at the beamtime April 2019. The m_z -component of six timesteps of the simulation with a time distance of 24.7 ps are shown, simulated at $|B_{Ext}| = 166$ mT. The amplitude distribution of the STXM-FMR measurement is shown in the lower right corner, the areas showing a pronounced amplitude are circled in red.

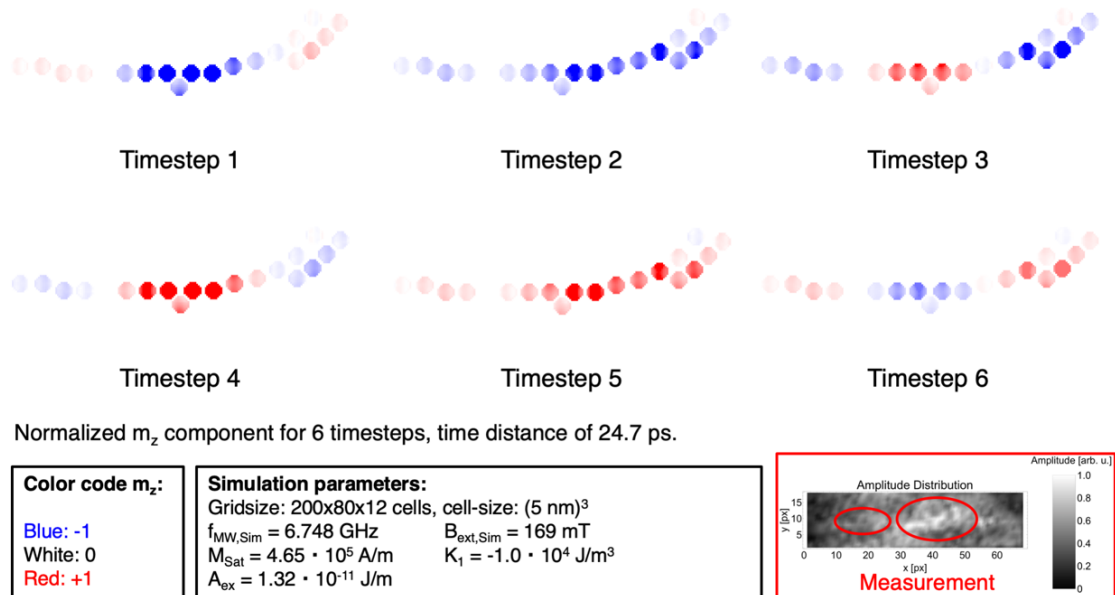


Figure 80: Micromagnetic simulation of the magnetosome chain investigated with STXM-FMR at the beamtime April 2019. The m_z -component of six timesteps of the simulation with a time distance of 24.7 ps are shown, simulated at $|B_{Ext}| = 169$ mT. The amplitude distribution of the STXM-FMR measurement is shown in the lower right corner, the areas showing a pronounced amplitude are circled in red.

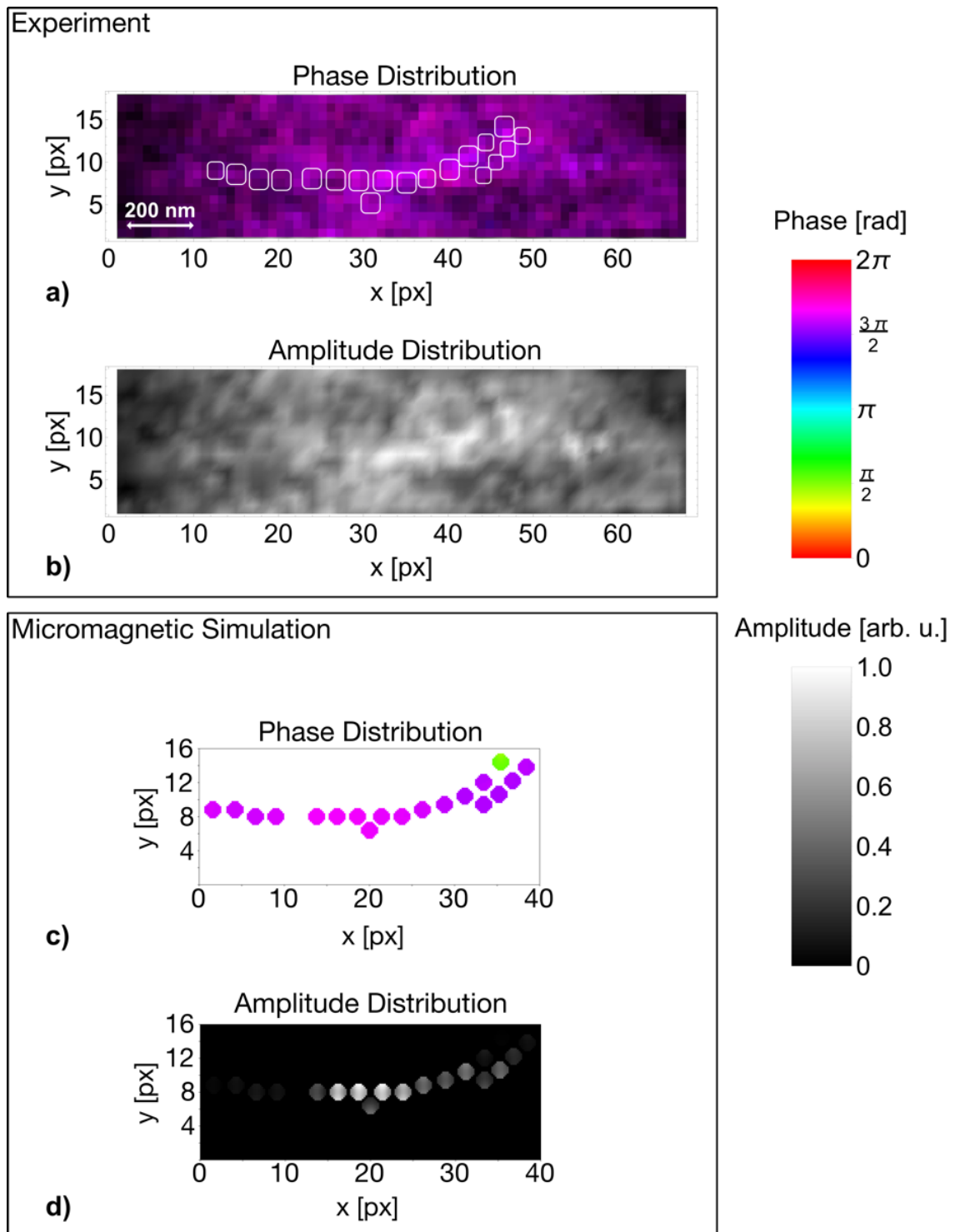


Figure 81: Phase and amplitude distribution from the STXM-FMR experiment at 167 mT (a, b)) and the micromagnetic simulation at 166 mT (c, d)). The phase- and amplitude analysis of the simulation data was processed by M. Winklhofer.

The pronounced non-uniform amplitude in the curved chain segment seen in the experimental data is resembled by the simulation, also showing only a very weak excitation of the four-particle segment of the chain as well. The single out of phase

oscillating particle (green) seen in Figure 81 c) is only weakly excited (low amplitude in Figure 81 d), and therefore it is not part of the uniform excitation. The phase analysis of the simulation at 169 mT (not shown) exhibits a non-uniform phase and amplitude distribution, which resembles the observations made for m_z in Figure 80.

By employing micromagnetic simulations, it was possible to confirm the validity of the STXM-FMR results of the single Fe_3O_4 magnetosome chain. While the simulation of the resonance at 169 mT exhibits a non-uniform response of the nanoparticle chain in phase, as well as in amplitude, the simulation at 166 mT confirms the experimental observations made at 167 mT, showing a resonant response with a uniform phase and a non-uniform amplitude distribution. The experimental and simulation results are in well agreement, showing the first element-specific, spatially, and time-resolved measurement FMR of a single nanometer sized magnetosome chain.

A manuscript meant for the publication in ACS Nanoletters is in preparation and shall be submitted end of July 2020.

6. Conclusion and outlook

The demands of current and future developments using magnetic materials for applications like biomedical treatment (e. g. [19-22, 152-158]), nano-mechanical machines (e. g. [23, 24, 159-161]) and magnonic computing (e. g. [2-8, 11]) require the element-specific, spatially and time-resolved measurement of the magnetization dynamics in micrometer and nanometer sized structures. I could show that Scanning Transmission X-ray Microscopy detected Ferromagnetic Resonance is a well suitable technique providing element-specific, spatially, and time-resolved measurements [44-46, 48] of FMR in periodic and non-periodic micro- and nanostructures. The used setup allows the measurement of STXM-FMR, as well as the measurement of conventional micro-resonator based FMR [44, 48]. It has been shown in this thesis that the combination of conventional (micro-resonator based) ferromagnetic resonance, micromagnetic simulations, and STXM-FMR is a complete set of techniques to understand the dynamic magnetic properties of the studied sample materials.

The element-specific detection of the magnetization dynamics is shown for the Py/Co disk/stripe bilayer microstructure (chapter 4.1). Three resonances, seen by conventional FMR (Figure 14), could be clearly assigned to the magnetic constituents of the sample [48]. The transfer of angular momentum from the Py in resonance to the Co stripe and vice versa from Co to Py at the respective main resonances could be shown [48]. Furthermore, it was possible to identify the third measured resonance as a coupled resonance of both sample parts [48]. The amplitude and phase evaluation method [103] allowed to reveal an inhomogeneous excitation of the Co stripe at the coupled resonance, an information not recognizable in conventional FMR and the grayscale STXM-FMR images. The STXM-FMR data for the coupled resonance at the Ni L_3 edge shows a stronger contrast (Figure 16) in the Py disk at the position of the Co stripe, which is attributed to an exchange coupling caused widening of the magnetization precession cone [48]. The results have been submitted to Physical Review Applied in July 2020.

The effect of magnetic dipolar coupling, the orientation, and strength of the external static magnetic bias field on spin wave modes in Py stripe ensembles is shown in

chapter 4.2. The STXM-FMR measurements on the single Py stripe and the T- and L-arranged stripe ensembles showed close to uniform and non-uniform spin wave modes with up to 4 nodes and 5 anti-nodes. The close to uniform and non-uniform modes depict a directed oscillatory behavior from the stripe center towards the left and right stripe edges for the single and the horizontal Py stripes. For the non-uniform modes in the vertical stripe, a directed oscillation is seen from the top and bottom edges towards the stripe center. The close to uniform modes in the vertical stripes show a directed oscillation from the stripe center towards the long stripe sides. The micromagnetic simulations performed for the sample geometries confirm the experimental observations. This behavior is unexpected as the investigated samples are homogeneously excited by the microwave and fulfill the boundary conditions for standing spin waves [72-74]. The origin of the directed oscillatory behavior lies in the influence of the stray field on the single stripe as well as on the stripe ensembles. The stray field distribution at the stripe edges results in the fulfillment of the resonance condition of additional modes excited at these stripe edges, see e. g. [119-121], which causes a phase gradient of the magnetization and the connected directed oscillatory behavior. The phase gradient could be visualized due to the use of the amplitude and phase analysis [103]. At least for the close to uniform modes a larger deviation of the external magnetic field from the resonance field of the mode results in a stronger phase gradient and a stronger directed oscillation, a behavior, which is expected as well for the non-uniform modes, but has not been studied by STXM-FMR. In conclusion the interplay of the external magnetic field and the stray field governs the excitation of edge modes, and therefore controls the strength of the phase gradient and the observed directed oscillation of the spin wave modes. A tilted static magnetic bias field results in a distortion of the demagnetization and stray field distribution and alters the shape of the nodes and anti-nodes of the observed spin waves, which could be shown by micromagnetic simulations employing different tilting angles of $\underline{B}_{\text{Ext}}$.

The transition from investigations on the micrometer scale to the nanometer scale was done with the STXM-FMR measurements of an Yttrium Iron Garnet nanoparticle agglomerate and Fe_3O_4 nanoparticle chains within magnetotactic bacteria *Magnetospirillum Magnetotacticum* in chapter 5. The YIG nanoparticle agglomerate consists of particles with the size ≥ 40 nm [132] and has the total dimensions of

300 nm x 150 nm. The STXM-FMR measurements and the amplitude phase analysis (chapter 5.1.3) show a non-uniform amplitude distribution, while the distribution of the relative phase indicates that parts consisting of multiple particles show a resonant response having the same phase, while other particle ensembles and single particles show a resonant response with a different phase. A similar behavior was observed for Fe₃O₄ nanoparticles resulting in magnonic band gaps in the angular dependent FMR spectra [11].

For the first time FMR of a single Fe₃O₄ magnetosome chain with particles having a diameter of about 50 nm was element-specifically and spatially resolved detected. While single particles could not be distinguished due to the limit in spatial resolution, it was possible to visualize the resonant response of the parts of the bi-segmented magnetosome chain by employing the amplitude phase evaluation (Figure 76). The mostly uniform distribution of the relative phase indicates a resonant response uniform in phase, with the amplitude distribution showing a non-uniform high amplitude area following the distribution of the magnetosome chain. Micro-magnetic simulations resembling the sample confirm the experimental observations in phase, as well as in amplitude, proving the STXM-FMR measurement result. A manuscript meant for the publication in ACS Nanoletters is in preparation and shall be submitted end of July 2020. In conclusion STXM-FMR is a well-suited technique for the research of the dynamic magnetic behavior of nanoparticles, as they are suggested for biomedical (e. g. [19-22, 152-158]), nano-mechanical (e. g. [23, 24, 159-161]) and magnonic applications (e. g. [9-11]).

The STXM-FMR setup at SLAC National Accelerator Laboratory was disassembled in July 2019 by H. Ohldag and the author, as the STXM technique is discontinued at the laboratory. This paves the way for an upgraded setup, which overcomes the current limitations of the old setup concerning spatial resolution, number of recorded time steps, strength of the static external magnetic bias field, possible measurement temperatures, and conventional FMR characterization. A new setup is planned by H. Ohldag, K. Ollefs, R. Meckenstock, H. Wende, M. Farle, and the author at the Advanced Lightsource synchrotron (ALS) at Lawrence Berkeley National Laboratory at Berkeley, CA, United States. The current STXM technique at the ALS offers a spatial resolution of down to 10 nm [162]. Next to an upgraded microwave synchronization and

data storage, allowing to record more channels than at the recent setup, a quadrupole magnet shall be implemented allowing fields up to 1 T. A sample cooling solution employing sapphire based heat pipes should allow to reduce the sample temperature from room temperature by several 10 K. The implementation of a Vector Network Analyzer and a field modulation is planned to optimize the conventional FMR measurements.

With these enhancements of the STXM-FMR technique, the element-specific investigation of the dynamic magnetic response of single sub 20 nm sized samples shall be achieved.

7. Appendix

7.1. Equations to calculate the demagnetization factors for rectangular ferromagnetic samples

Aharoni derived the following analytical expression (equation A3) for the demagnetization factors of rectangular ferromagnetic prisms in [65]. The presented equations are using the assignment of the side lengths as shown in Figure 82.

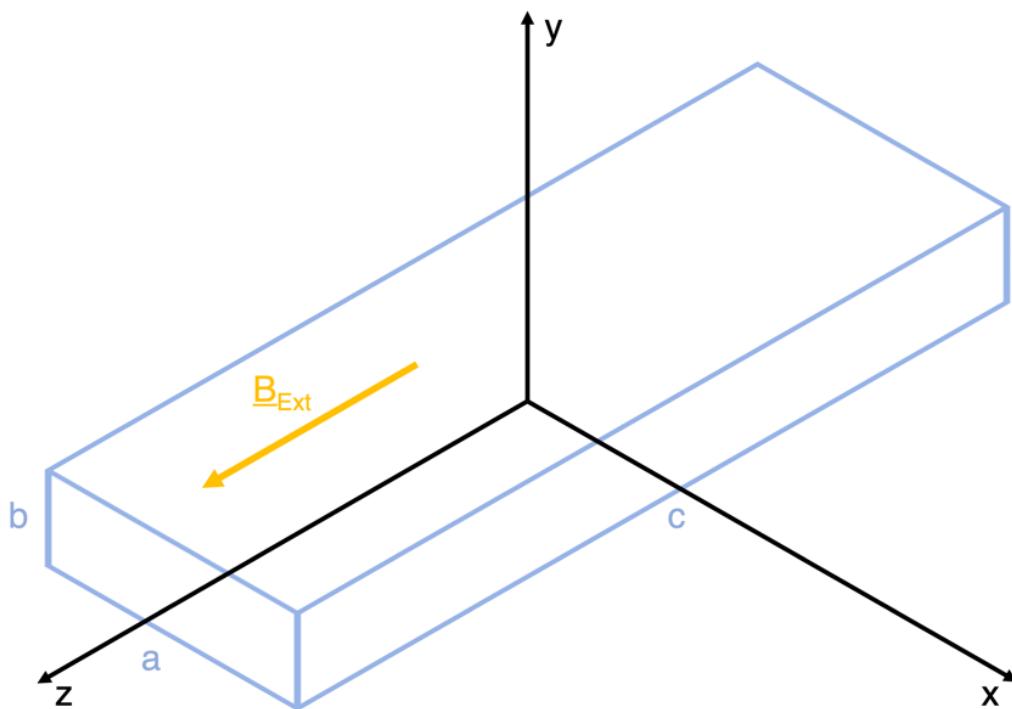


Figure 82: Definition of the side edges of the rectangular shaped body for the equations of the demagnetization factors. Figure redrawn and adapted from [65].

With these equations the demagnetization factors for stripe like sample shapes, as investigated in this thesis (Co and Py stripes) in chapters 4.1 and 4.2, are calculated. Results for $N_{1,2,3}$ using these equations are given in the corresponding chapters.

$$\begin{aligned}
 N_1 = & \frac{1}{\pi} \left(\frac{c^2 - a^2}{2 a c} \ln \left(\frac{\sqrt{a^2 + b^2 + c^2} - b}{\sqrt{a^2 + b^2 + c^2} + b} \right) + \frac{b^2 - a^2}{2 a b} \ln \left(\frac{\sqrt{a^2 + b^2 + c^2} - c}{\sqrt{a^2 + b^2 + c^2} + c} \right) \right. \\
 & + \frac{c}{2 a} \ln \left(\frac{\sqrt{b^2 + c^2} + b}{\sqrt{b^2 + c^2} - b} \right) + \frac{b}{2 a} \ln \left(\frac{\sqrt{b^2 + c^2} + c}{\sqrt{b^2 + c^2} - c} \right) \\
 & + \frac{a}{2 b} \ln \left(\frac{\sqrt{a^2 + c^2} - c}{\sqrt{a^2 + c^2} + c} \right) + \frac{a}{2 c} \ln \left(\frac{\sqrt{a^2 + b^2} - b}{\sqrt{a^2 + b^2} + b} \right) \\
 & + \tan^{-1} \left(\frac{b c}{a \sqrt{a^2 + b^2 + c^2}} \right) + \frac{b^3 + c^3 - 2 a^3}{3 a b c} \\
 & + \frac{b^2 + c^2 - 2 a^2}{3 a b c} \sqrt{a^2 + b^2 + c^2} + \frac{a}{b c} \left(\sqrt{a^2 + b^2} + \sqrt{a^2 + c^2} \right) \\
 & \left. - \frac{(b^2 + c^2)^{\frac{3}{2}} + (a^2 + c^2)^{\frac{3}{2}} + (a^2 + b^2)^{\frac{3}{2}}}{3 a b c} \right)
 \end{aligned}$$

Equation (A1): Demagnetization factor N_1 derived from equation (A3) [65].

$$\begin{aligned}
 N_2 = & \frac{1}{\pi} \left(\frac{a^2 - b^2}{2 a b} \ln \left(\frac{\sqrt{a^2 + b^2 + c^2} - c}{\sqrt{a^2 + b^2 + c^2} + c} \right) + \frac{c^2 - b^2}{2 b c} \ln \left(\frac{\sqrt{a^2 + b^2 + c^2} - a}{\sqrt{a^2 + b^2 + c^2} + a} \right) \right. \\
 & + \frac{a}{2 b} \ln \left(\frac{\sqrt{a^2 + c^2} + c}{\sqrt{a^2 + c^2} - c} \right) + \frac{c}{2 b} \ln \left(\frac{\sqrt{a^2 + c^2} + a}{\sqrt{a^2 + c^2} - a} \right) \\
 & + \frac{b}{2 c} \ln \left(\frac{\sqrt{a^2 + b^2} - a}{\sqrt{a^2 + b^2} + a} \right) + \frac{b}{2 a} \ln \left(\frac{\sqrt{b^2 + c^2} - c}{\sqrt{b^2 + c^2} + c} \right) \\
 & + \tan^{-1} \left(\frac{a c}{b \sqrt{a^2 + b^2 + c^2}} \right) + \frac{c^3 + a^3 - 2 b^3}{3 a b c} \\
 & + \frac{c^2 + a^2 - 2 b^2}{3 a b c} \sqrt{a^2 + b^2 + c^2} + \frac{b}{a c} \left(\sqrt{b^2 + c^2} + \sqrt{a^2 + b^2} \right) \\
 & \left. - \frac{(a^2 + c^2)^{\frac{3}{2}} + (a^2 + b^2)^{\frac{3}{2}} + (b^2 + c^2)^{\frac{3}{2}}}{3 a b c} \right)
 \end{aligned}$$

Equation (A2): Demagnetization factor N_2 derived from equation (A3) [65].

$$\begin{aligned}
 N_3 = \frac{1}{\pi} & \left(\frac{b^2 - c^2}{2 b c} \ln \left(\frac{\sqrt{a^2 + b^2 + c^2} - a}{\sqrt{a^2 + b^2 + c^2} + a} \right) + \frac{a^2 - c^2}{2 a c} \ln \left(\frac{\sqrt{a^2 + b^2 + c^2} - b}{\sqrt{a^2 + b^2 + c^2} + b} \right) \right. \\
 & + \frac{b}{2 c} \ln \left(\frac{\sqrt{a^2 + b^2} + a}{\sqrt{a^2 + b^2} - a} \right) + \frac{a}{2 c} \ln \left(\frac{\sqrt{a^2 + b^2} + b}{\sqrt{a^2 + b^2} - b} \right) \\
 & + \frac{a}{2 a} \ln \left(\frac{\sqrt{b^2 + c^2} - b}{\sqrt{b^2 + c^2} + b} \right) + \frac{c}{2 b} \ln \left(\frac{\sqrt{a^2 + c^2} - a}{\sqrt{a^2 + c^2} + a} \right) \\
 & + \tan^{-1} \left(\frac{a b}{c \sqrt{a^2 + b^2 + c^2}} \right) + \frac{a^3 + b^3 - 2 c^3}{3 a b c} \\
 & + \frac{a^2 + b^2 - 2 c^2}{3 a b c} \sqrt{a^2 + b^2 + c^2} + \frac{c}{a b} \left(\sqrt{a^2 + c^2} + \sqrt{b^2 + b^2} \right) \\
 & \left. - \frac{(a^2 + b^2)^{\frac{3}{2}} + (b^2 + c^2)^{\frac{3}{2}} + (a^2 + c^2)^{\frac{3}{2}}}{3 a b c} \right)
 \end{aligned}$$

Equation (A3): Equation for the demagnetization factor N_3 [65].

7.2. Tabular overview on other spatially- and/or time resolved magnetization detection methods

Method	Lateral resolution	Depth of information	Time resolution	Element selective
SthM-FMR	30 nm [113]	100 nm – 1 μ m [113]	-	No
SthEM-FMR	< 20 nm dep. on stability of STM [113]	1 μ m – 500 μ m [113]	-	No
PM-FMR	< 500 nm dep. on laser focus [113]	Dep. on MW penetration [113]	-	No
BLS	Scanning BLS: ~ 250 nm @ $\lambda_{\text{Laser}} = 532$ nm [32], BLS + near field optics: < 55 nm @ $\lambda_{\text{Laser}} = 532$ nm [33]	Dep. on excitation [113]	1 ns – 2 ns [31]	No
MOKE	< 300 nm dep. on laser focus, < 50 nm with near field optics (SNOM) [113]	50 nm [113], < 20 nm [163]	ps to fs [113], dep. on length of light pulse [164]	No
MRFM	25 nm (1D) [165]	nm [165]	TR-MRFM: Seconds [166]	
NF-FMR	> 1 μ m [113]	Integral [113]	-	No
SEMPA	≥ 3 nm [34]	< 1nm [34], < 0.5 nm [163]	TR-SEMPA: 700 ps [34]	No [163]
SPLEEM	10 nm to 20 nm [35]	< 1 nm [163]	TR-SPLEEM: seconds [36]	No [163]
X-PEEM	Down to 20 nm [42], with UV excitation: < 10 nm [42]	~ 100 nm [42]	> 1 ns [167], sub-ns [168], 50 ps – 200 ps [169], ~ 10 ps [41]	Yes (XMCD)
SP-STM	< 1 nm [163], [170]	< 0.2 nm [163]	With all-electronic pump probe scheme: ns [171], [172]	No
Lorentz microscopy	0.1 nm [173]	Transmission, < 100 nm [163]	Detection of MHz excitation in [37] (Ultrafast Lorentz microscopy), 700 fs (Femtosecond Lorentz microscopy with < 100 nm spatial resolution) [38]	Yes*
EMCD	< 0.2 nm [174]	Transmission [174]	-	Yes**
DFMR	≤ 1 nm [43]	Diffraction [43]	ps [43]	Yes [43]
STXM	≥ 10 nm [162], dep. on X-ray focus	Transmission [162]	-	Yes (XMCD)
STXM-FMR	as STXM, dep. on X-ray focus	Transmission [44]	< 20 ps [44], [45]	Yes (XMCD)
Scanning thermal Microscopy detected FMR (SthM-FMR) Scanning thermoelastic Microscopy detected FMR, Photothermally Modulated FMR (PM-FMR) Brillouin Light Scattering (BLS) Magneto-optical Kerr-Effect (MOKE) Magnetic Resonance Force Microscopy (MRFM) Near Field FMR (NF-FMR) Scanning Electron Microscope with Polarization Analysis (SEMPA) Spin Polarized Low-Energy Electron Microscopy (SPLEEM) X-ray excited Photoemission electron microscopy (X-PEEM) Spin Polarized Scanning Tunneling Microscopy (SP-STM) Electron Energy-loss Magnetic chiral Dichroism (EMCD) X-ray Diffractive Ferromagnetic Resonance (DFMR) *Energy Filtered Transmission Electron Microscopy [173] ** Electron Energy Loss Spectroscopy (EELS) [174]				

Table 5: Overview of several experimental techniques to detect the magnetization with respect to element specificity, spatial and time resolution.

7.3. Complete dataset of the presented STXM-FMR measurements

In the following the complete dataset of the STXM-FMR measurement presented in chapter 4.1.3 is shown. The subfigures correspond to the time point / relative phase value given in Table 6. In chapter 4.1.3 and [48] the timepoint 92 ps is shown. The data treatment is the same as described in chapter 4.1.3.

Subfigure	Timepoint [ps]	Relative phase [°]
a)	18	60
b)	37	120
c)	55	180
d)	74	240
e)	92	300
f)	110	360

Table 6: Correspondence table to assign timepoints and relative phase to subfigures.

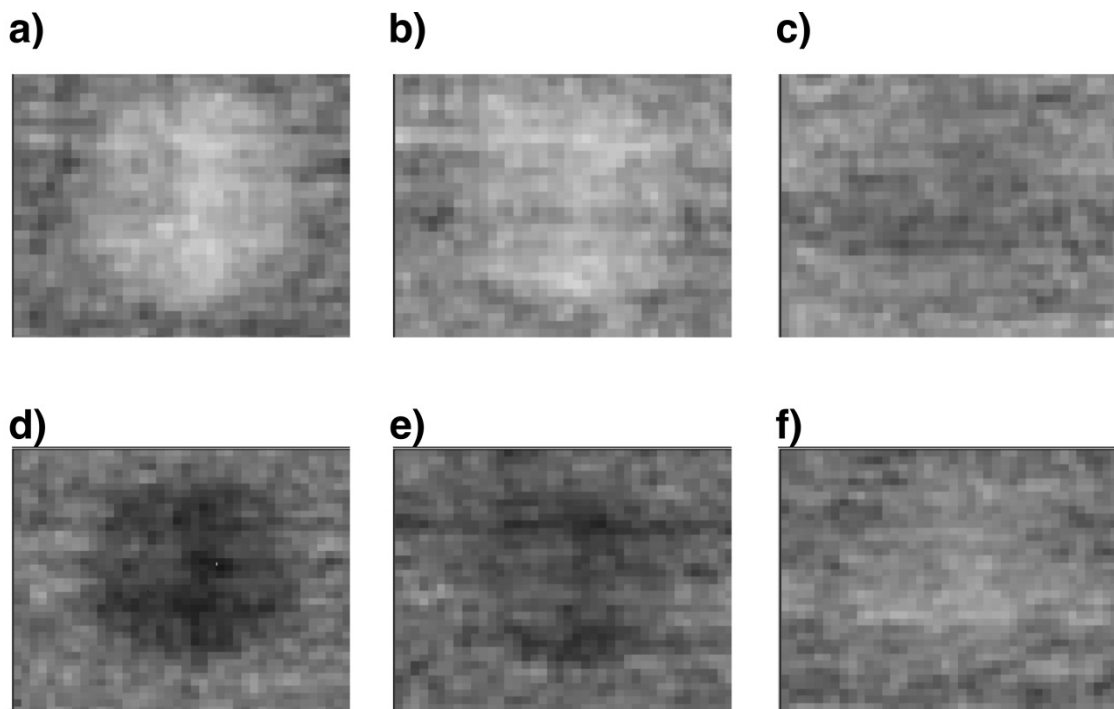


Figure 83: STXM-FMR of the Py resonance measured at the Ni L_3 .

Figure 83 shows the recorded microwave cycle at the resonance of the Py disk at 58.3 mT measured at the Ni L_3 edge. A homogeneous oscillation of the magnetization

is visible starting in subfigures a) and b) with higher than average (grey) STXM-FMR contrast, showing a close to average contrast in subfigure c) and lower than average contrast in subfigures d) and e). A close to average contrast in subfigure f) concludes the recorded dataset. The STXM-FMR images clearly show an excitation of the whole Py disk with a widely homogeneous contrast distribution (chapter 4.1.3 and [48]).

The coupled resonance (84.9 mT) is pictured at the Ni L_3 edge in the dataset presented in Figure 84. The overall behavior of the magnetization oscillation corresponds to the observations made for Figure 83, but at the position of the Co stripe stronger contrast is visible for the higher than average contrast images, as well as for the lower than average contrast images, indicating a widened precession cone in the Py due to the exchange coupling with the Co (chapter 4.1.3 and [48]). As described in chapter 4.1.3, both sample parts are in resonance (chapter 4.1.3 and [48]).

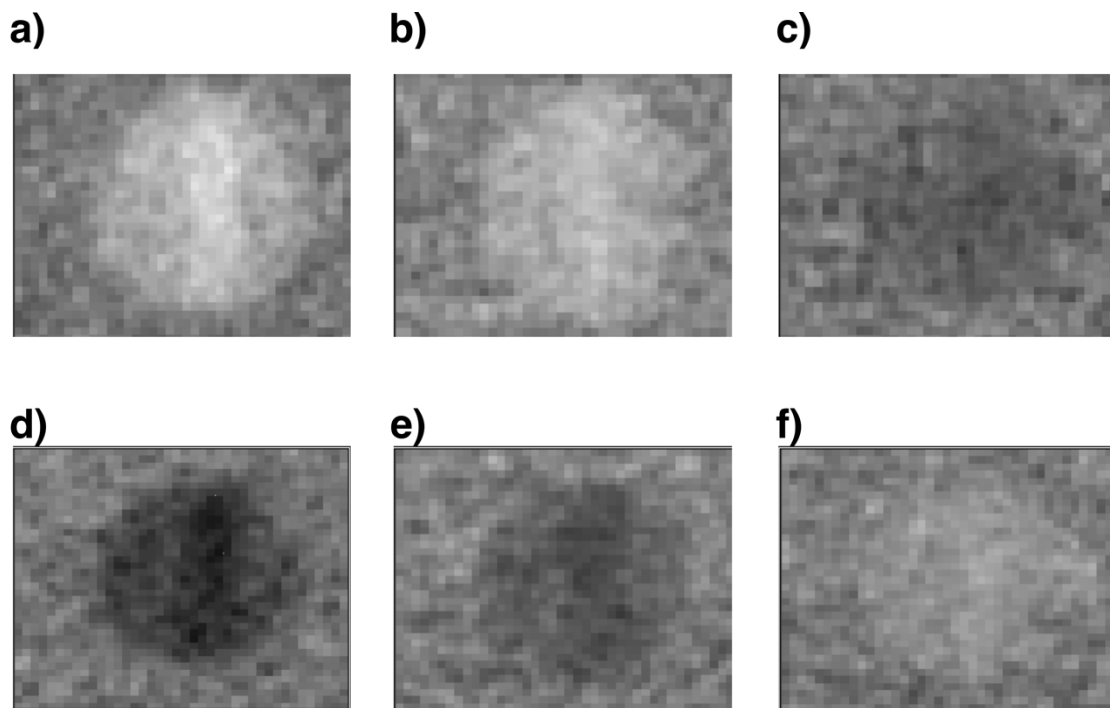


Figure 84: STXM-FMR of the coupled resonance measured at the Ni L_3 .

The STXM-FMR images recorded at the Ni L_3 edge at the field of the Co resonance (112.7 mT) are depicted in Figure 85. Only a weak oscillation in the area of the Py disk is visible, indicating driven Py magnetic moments by an angular momentum transfer from the Co in resonance (chapter 4.1.3 and [48]). The broad rectangular

area in the images results from a phase shift of the microwave synchronization board during the measurement.

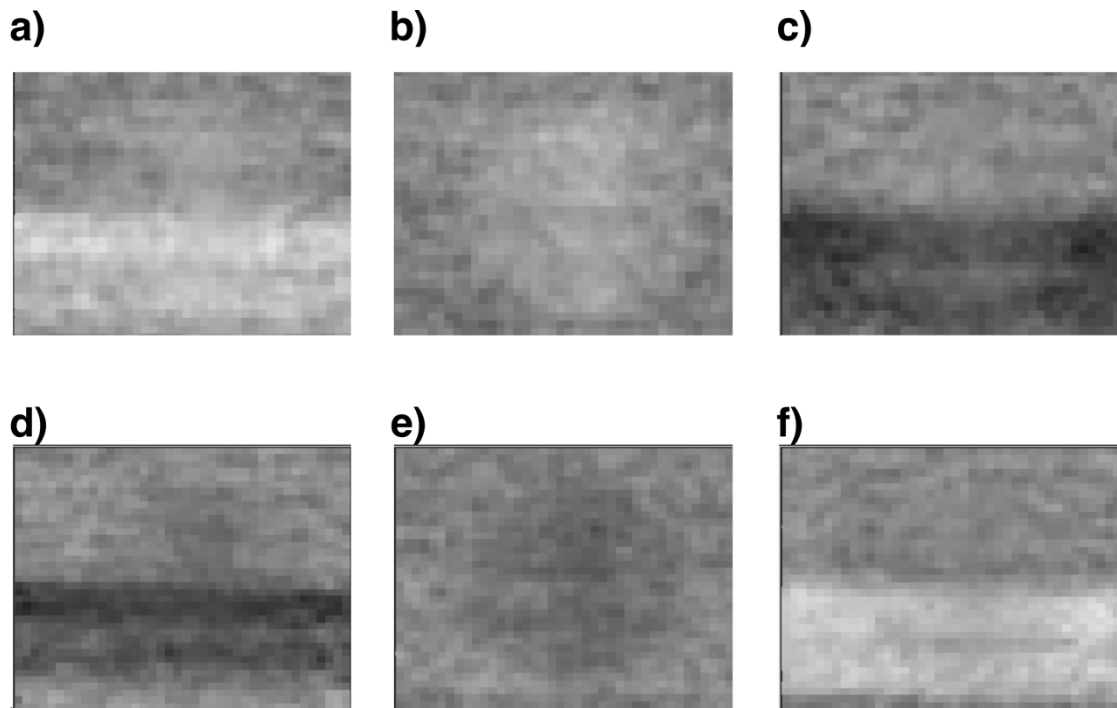


Figure 85: STXM-FMR of the Co resonance measured at the Ni L_3 .

In Figure 86 recorded at the Co L_3 edge, the Co stripe shows only a weak contrast during the magnetization oscillation at the Py resonance field due to an angular momentum transfer from the Py in resonance to the Co (chapter 4.1.3 and [48]). At the coupled resonance (Figure 87) a strong contrast is visible at the Co stripe with a slightly narrower contrast width than for the Co resonance (Figure 88) caused by the magnetic moments at the long stripe sides being not in resonance at this magnetic field value (chapter 4.1.3 and [48]). The Co resonance is imaged in Figure 88 showing a homogeneous contrast distribution at the Co stripe, indicating the uniform resonance mode of the Co stripe (chapter 4.1.3 and [48]).

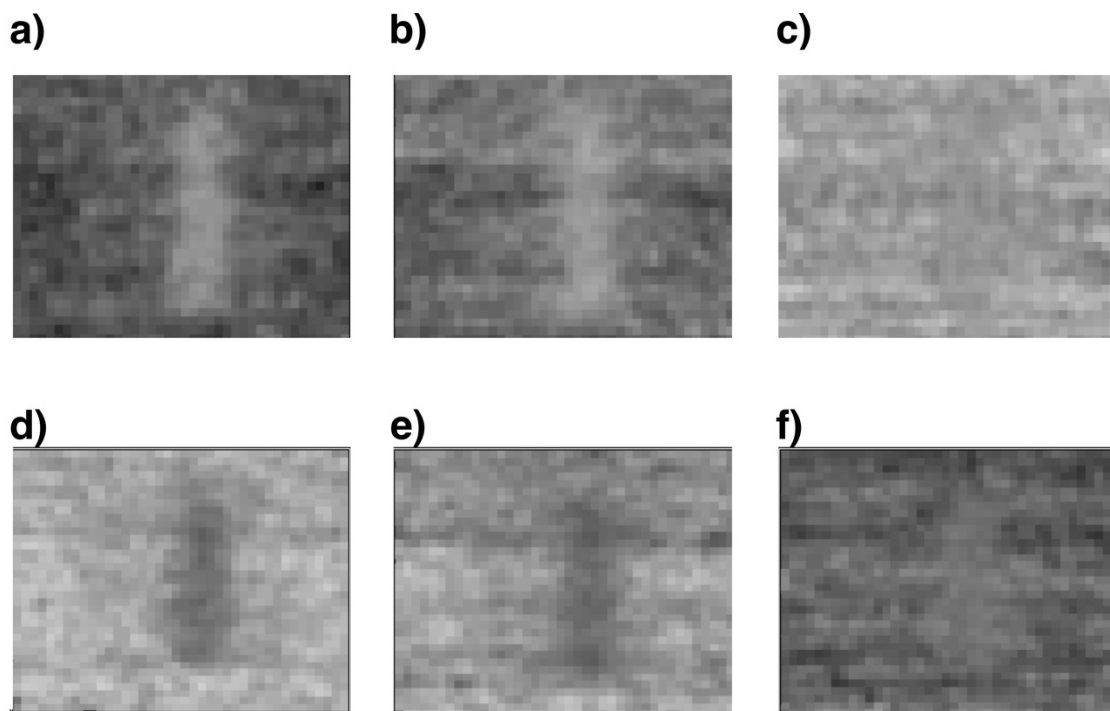


Figure 86: STXM-FMR of the Py resonance measured at the Co L_3 edge.

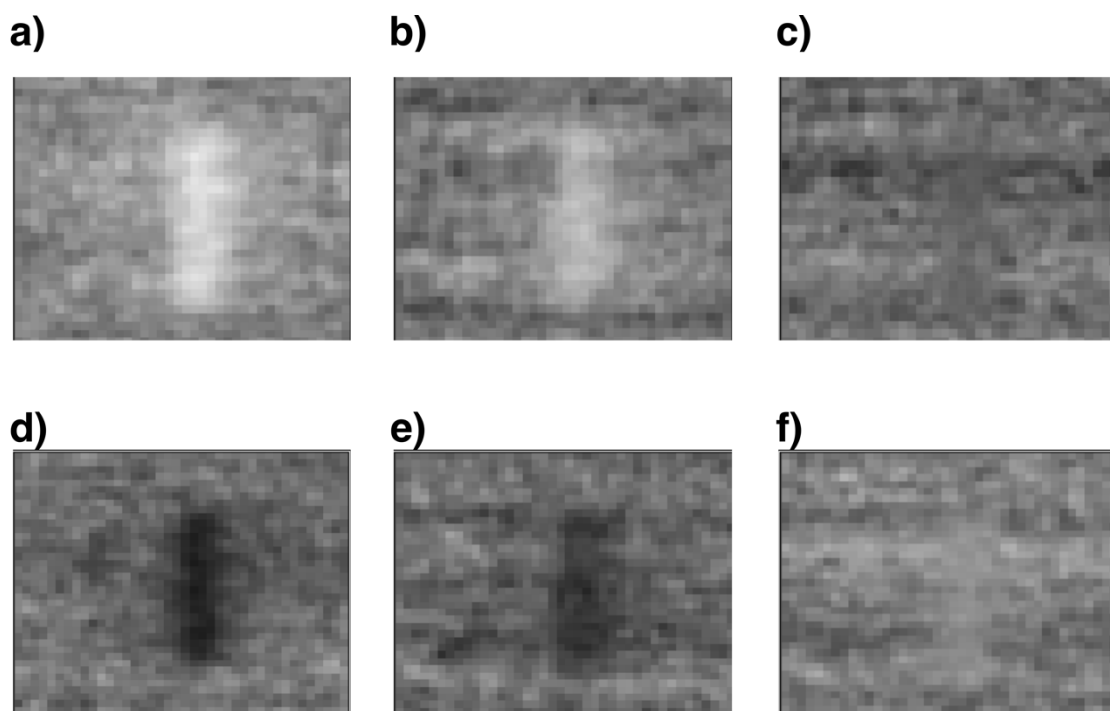


Figure 87: STXM-FMR of the coupled resonance measured at the Co L_3 edge.

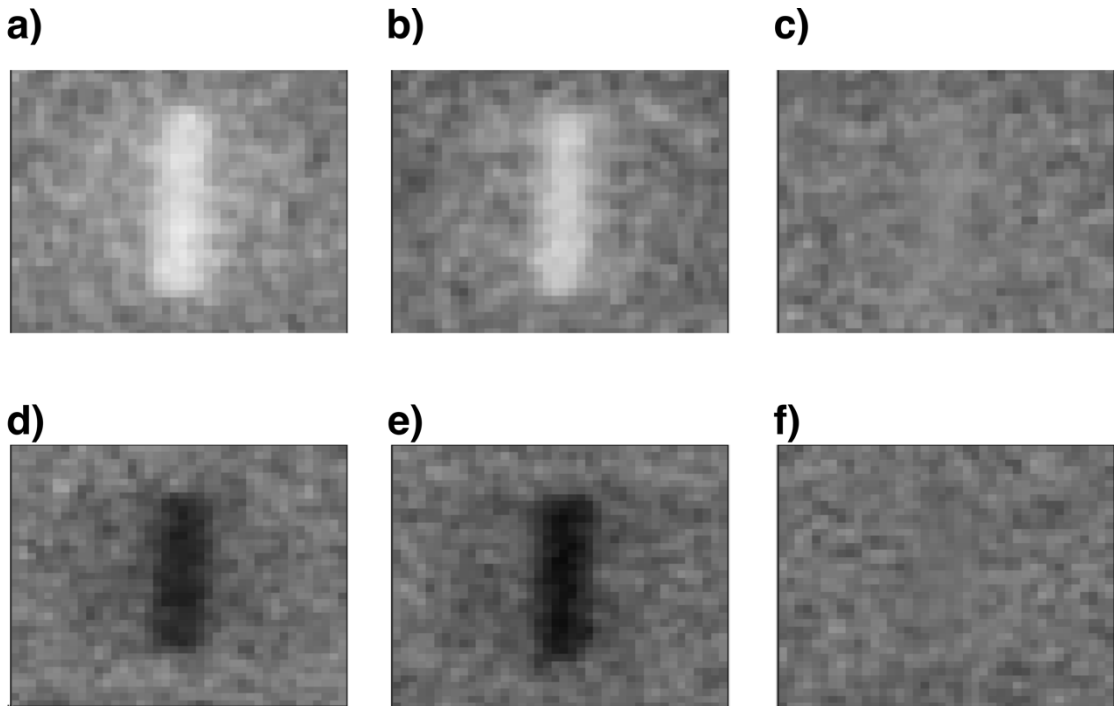


Figure 88: STXM-FMR of the Co resonance measured at the Co L_3 .

7.4. Micromagnetic simulations of the Py stripe arrangements

7.4.1. Averaged free energy densities of the L-shaped Py stripe arrangement

Figure 89 shows the averaged free energy densities for the L-shaped Py stripe geometry. As for the single Py stripe and the T-shape stripe arrangement the dominating energy contribution with respect to its absolute value is the Zeeman energy density for both stripes (Figure 89 e), f)), which is increasing with increasing field strength. The second-largest contribution is given by the demagnetization energy density (Figure 89 a), b)), which is about 5.3 times higher for the vertical stripe than for the horizontal stripe due to shape anisotropy. The exchange energy density shown in Figure 89 c), d) is the smallest contribution, while for the horizontal stripe, a linear decrease with increasing $|\underline{B}_{\text{Ext}}|$ is visible, for the vertical stripe the data points show a curvature. As the selected cell size is above the exchange length the effect of exchange coupling and the resulting energy density cannot be taken as reliable. The absolute value of the total energy density is increasing with increasing $|\underline{B}_{\text{Ext}}|$ due to the dominating contribution of the Zeeman energy density (Figure 89 g), h)).

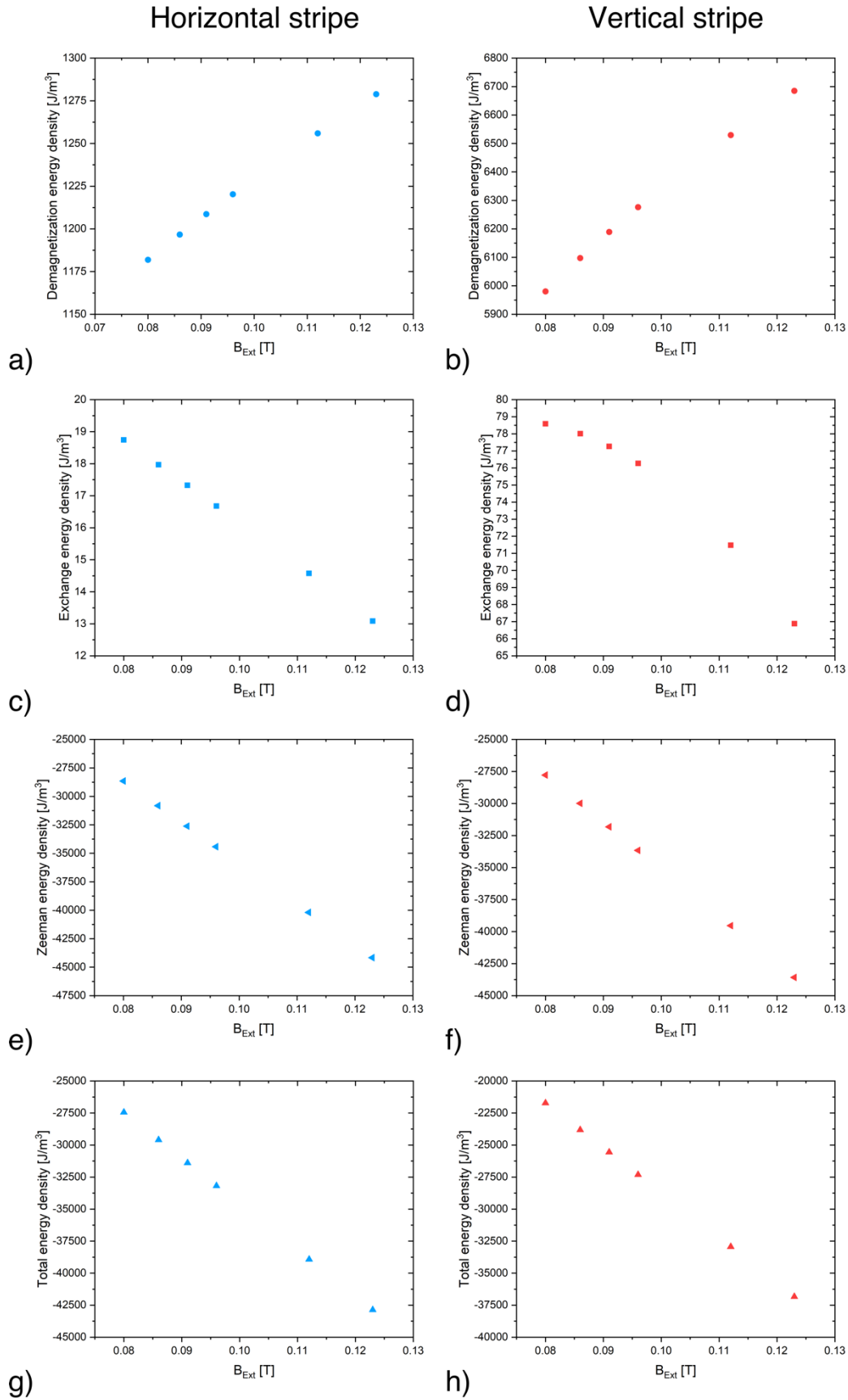


Figure 89: Averaged free energy densities for the horizontal and vertical Py stripe for the different resonance fields for the L-shaped sample geometry.

7.5. STXM-FMR images of the Py stripe arrangements

In the following additional STXM-FMR results for the three Py stripe sample systems, the single stripe, the T- and the L-shaped arrangements are shown. The sample geometries are shown in Figure 21. The natural logarithm of the division of microwave on and off data was taken, applying a minimum-maximum normalization [127] afterward.

7.5.1. Single Py stripe

Assuming an offset of the applied magnetic field of about 20 mT for the STXM-FMR measurements of the single stripe, Figure 90 to Figure 92 show resonances close to the uniform mode (80 mT, see the simulated spectrum in Figure 22 a)) at about 71 mT, 74 mT, and 77 mT. Animating the datasets reveal a directed oscillation from the stripe center towards the stripe edges due to a phase gradient of the magnetization from about 280° at the stripe center to about $0^\circ/360^\circ$ at the stripe sides, shown in the subfigures b). The presence of the phase gradient is attributed to the influence of the stray field (simulation see Figure 25 a), b)), resulting in additional resonance conditions to excite edge modes in the stripe, see e. g. [119-121].

While Figure 90 shows a non-uniform amplitude distribution in subfigure c), Figure 91 shows an area of homogeneous amplitude distribution at the stripe center with low amplitude areas towards both stripe edges with high amplitude spots directly at the edges. The diagonal shape of the high contrast area is caused by the $|\underline{B}_{\text{Ext}}|$ tilted by 4° , corresponding to the experimental geometry (Figure 21). The area of high contrast gets bigger with increasing $|\underline{B}_{\text{Ext}}|$, as visible in Figure 92.

A strong oscillation of the background can be seen, which is attributed to an influence of the microwave on the avalanche photodiode [46], as described in chapter 4.1.3.

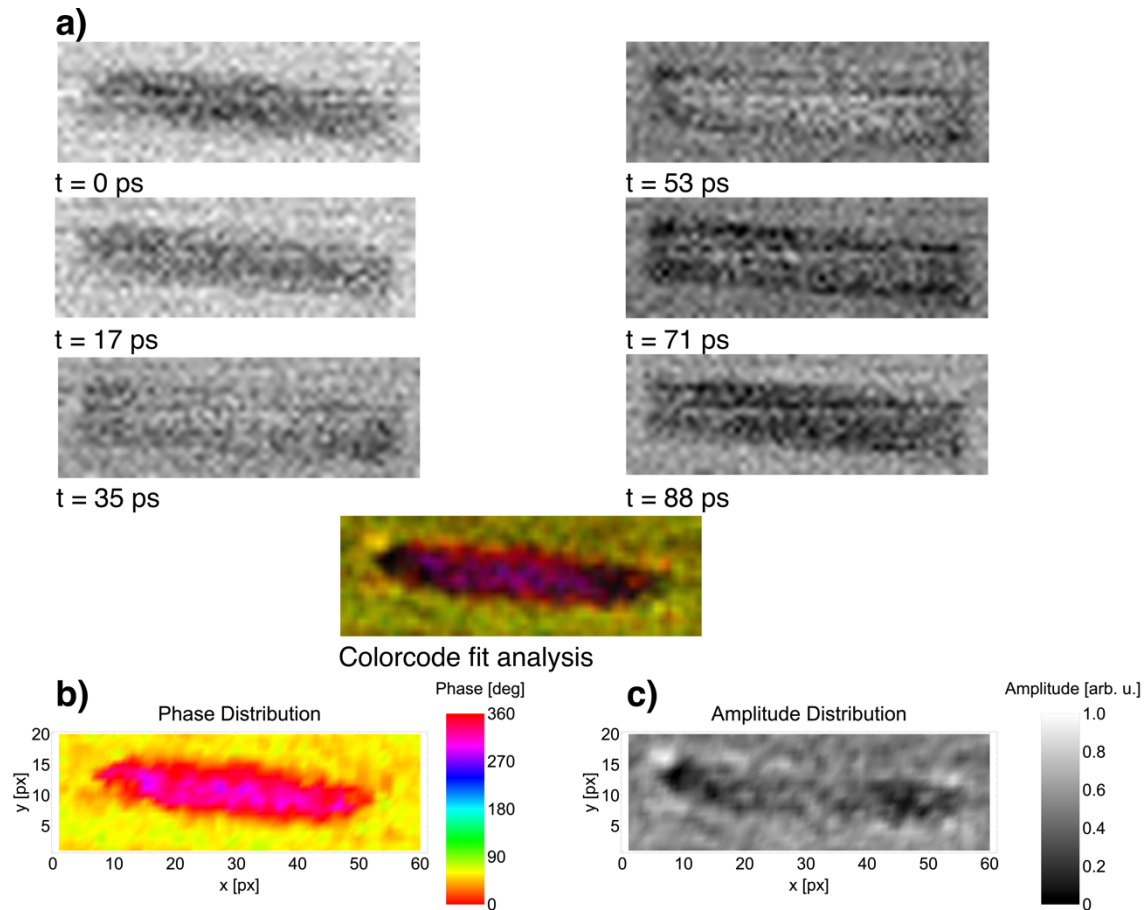
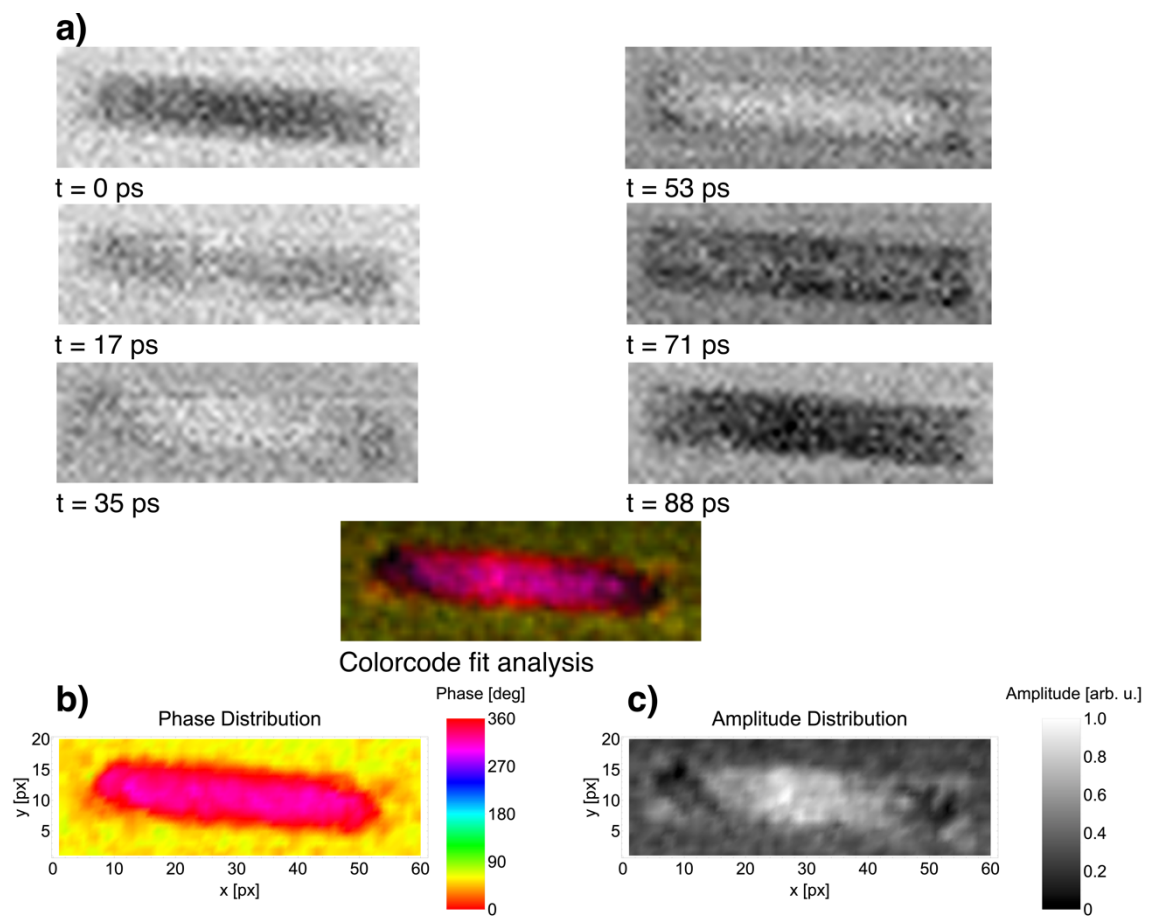


Figure 90: STXM-FMR data of the single Py stripe at a static bias field about 71 mT (91 mT) and a microwave power of 29 dBm. a) Microwave induced X-ray transmission for 6 timesteps with a time distance of about 18 ps. b), c) Distribution of the relative phase with respect to the timestep $t = 0$ and the normalized amplitude extracted out of the color-code fit analysis (chapter 3.4).

The areas of different relative phase decrease and shift towards the stripe edges (Figure 92) with increasing field while approaching the field value of the uniform mode.

Figure 93 shows a spin wave mode close to the mode pictured in Figure 34 showing two nodes and three anti-nodes. The relative phase changes from about $0^\circ/360^\circ$ to 10° at the stripe edges to about 20° to 50° at the central stripe area. Due to the phase gradient a directed oscillation of the spin wave mode from the center towards the stripe edges can be observed by animating the STXM-FMR images shown in Figure 93 a). As before the directed oscillatory behavior is attributed to the influence of the stray field (simulation, see Figure 25 a), b)).



*Figure 91: STXM-FMR data of the single Py stripe at a static bias field 74 mT (94 mT) and a microwave power of 29 dBm. **a)** Microwave induced X-ray transmission for 6 timesteps with a time distance of about 18 ps. **b), c)** Distribution of the relative phase with respect to the timestep $t = 0$ and the normalized amplitude extracted out of the color-code fit analysis (chapter 3.4).*

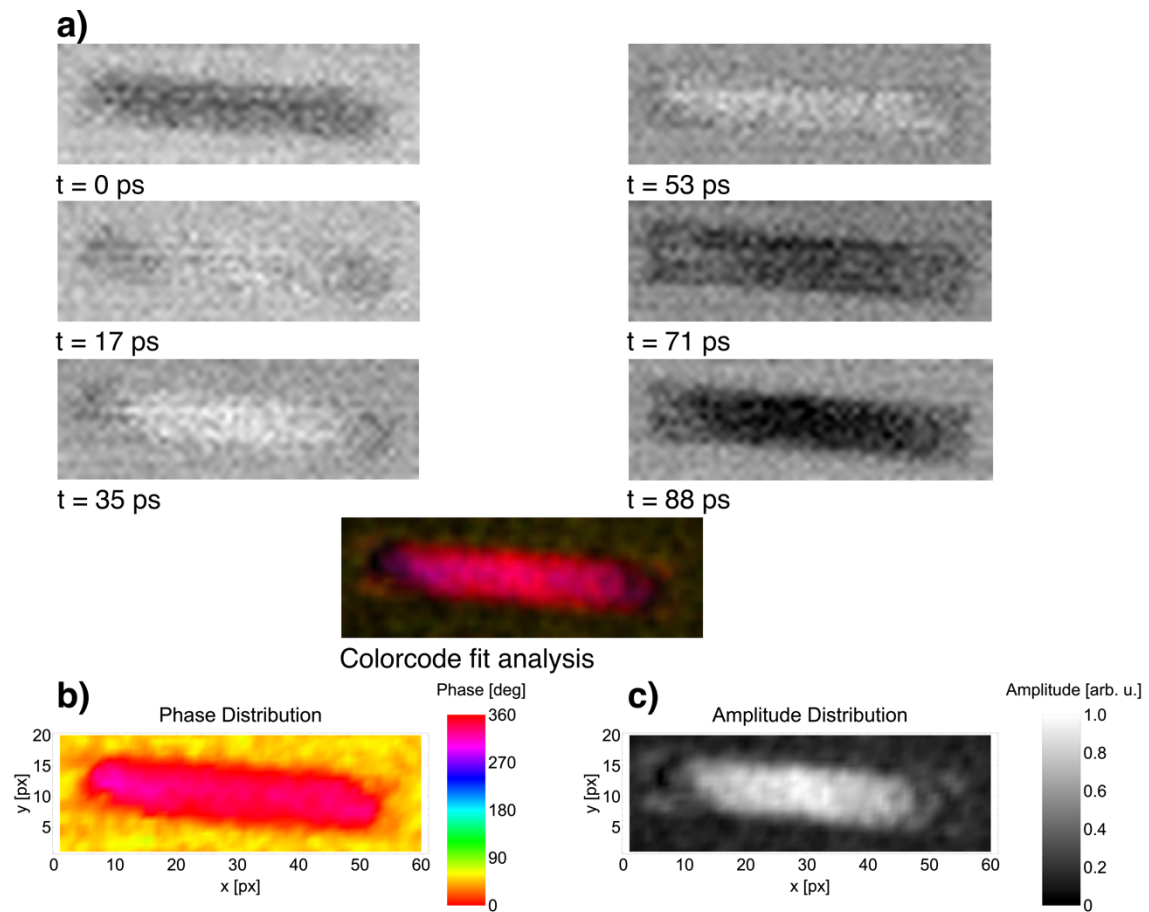
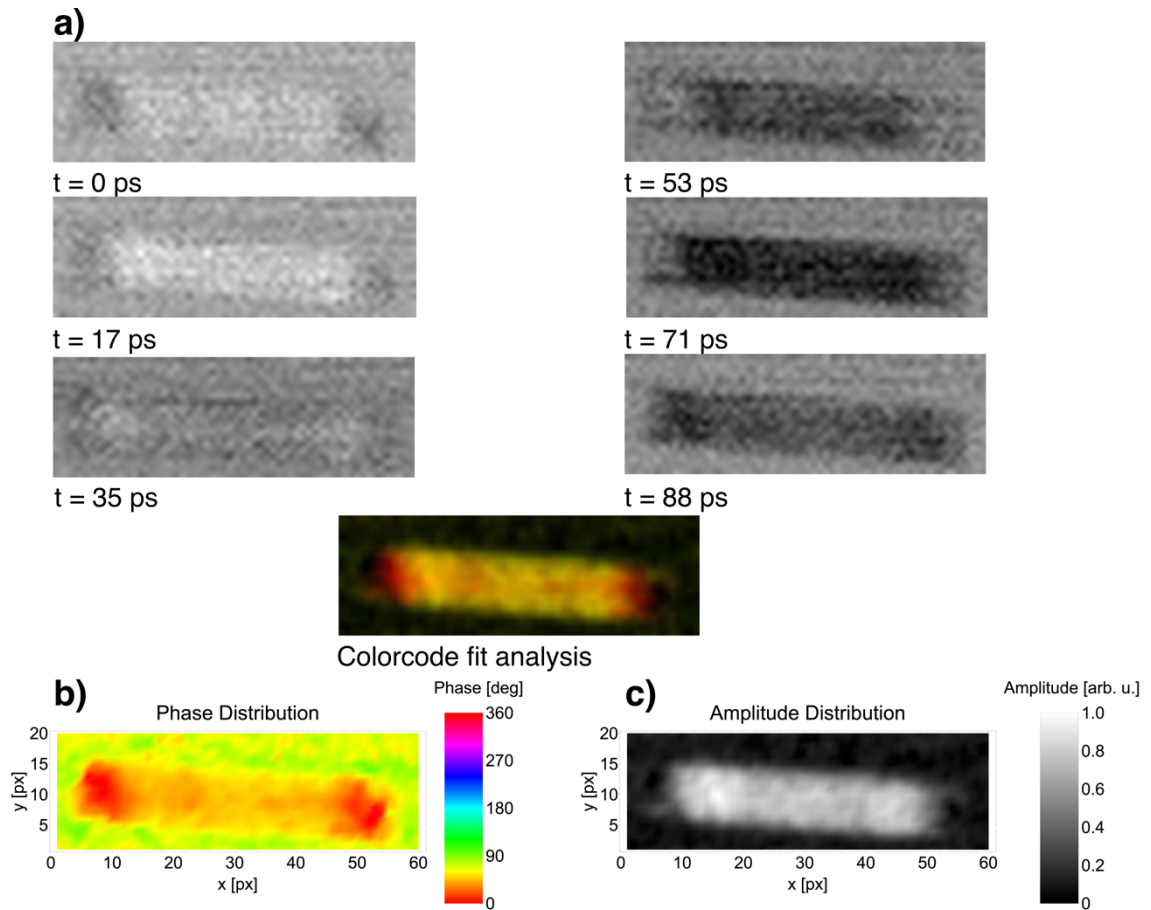


Figure 92: STXM-FMR data of the single Py stripe at a static bias field of about 77 mT (97 mT) and a microwave power of 29 dBm. a) Microwave induced X-ray transmission for 6 timesteps with a time distance of about 18 ps. b), c) Distribution of the relative phase with respect to the timestep $t = 0$ and the normalized amplitude extracted out of the color-code fit analysis (chapter 3.4).



*Figure 93: STXM-FMR data of the single Py stripe at a static bias field of about 86 mT (106 mT) and a microwave power of 29 dBm. **a)** Microwave induced X-ray transmission for 6 timesteps with a time distance of about 18 ps. **b), c)** Distribution of the relative phase with respect to the timestep $t = 0$ and the normalized amplitude extracted out of the color-code fit analysis (chapter 3.4).*

7.5.2. T-shaped sample geometry

Figure 94 shows the STXM-FMR data of a spin wave mode of the vertical stripe of the T-shaped stripe arrangement in between the two nodes, three anti-nodes mode depicted in Figure 43 and the close to uniform modes presented in Figure 45 and Figure 46. The distribution of the relative phase shows a broad area of a uniform phase of about 260° with a slight deviation towards 135° .

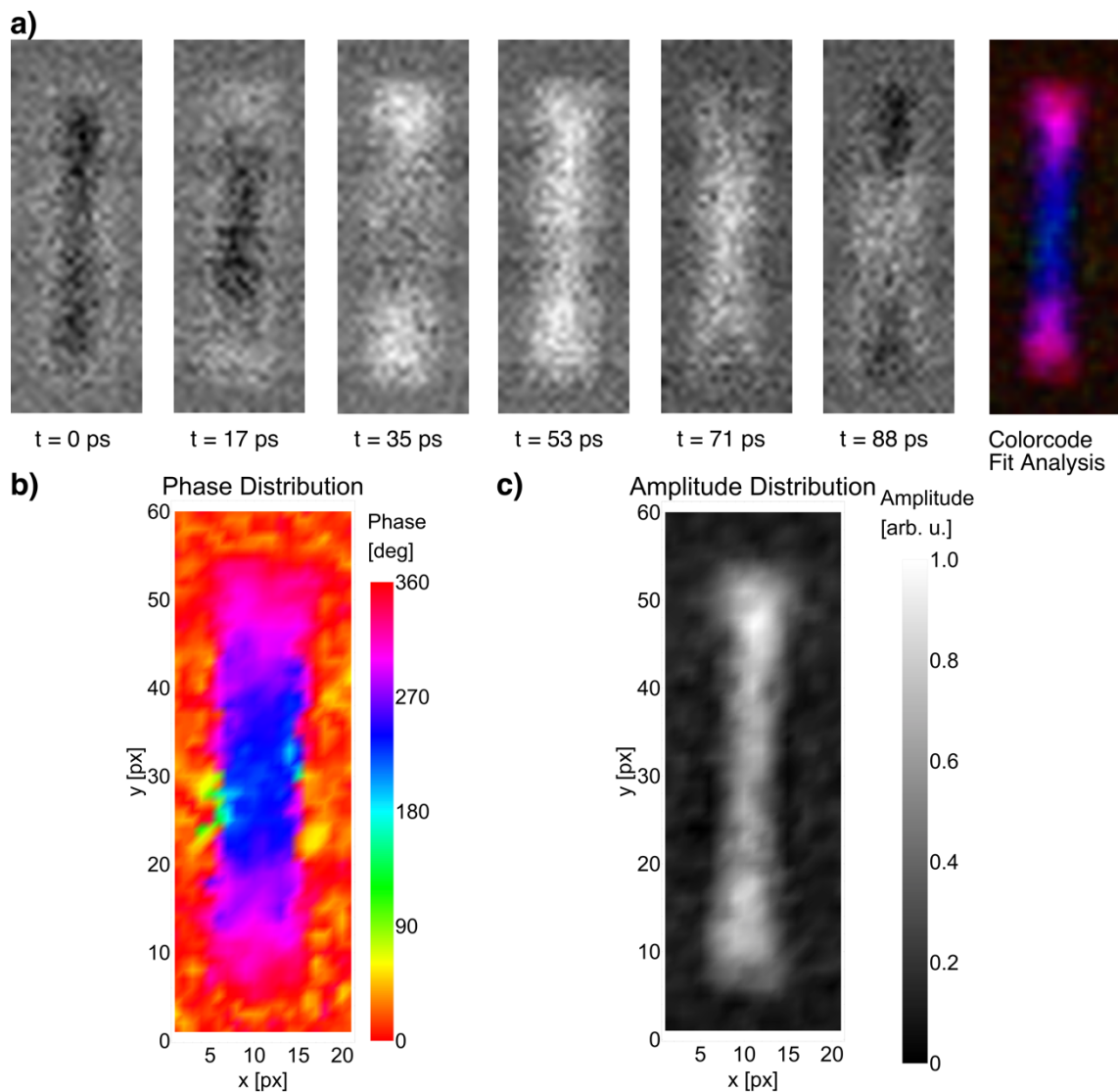


Figure 94: STXM-FMR data of the vertical Py stripe of the T-shape geometry at a static bias field of 107 mT and a microwave power of 27 dBm. **a)** Microwave induced X-ray transmission for 6 timesteps with a time distance of about 18 ps. **b), c)** Distribution of the relative phase with respect to the timestep $t = 0$ and the normalized amplitude extracted out of the color-code fit analysis (chapter 3.4).

On both the lower and upper edge of this phase area, a smooth transition to a phase of about 280° takes place, indicating a phase gradient of the magnetization. The normalized amplitude distribution shows a homogeneous high amplitude over the stripe with peak values at both stripe edges.

Animating the STXM-FMR data (Figure 94 a)) shows an oscillation of the spin wave directed from the stripe edges to the center due to the phase gradient, as it has been observed in chapter 4.2.5. The presence of the phase gradient is, as aforementioned, attributed to the influence of the stray field on the stripe.

7.5.3. L-shaped sample geometry

Additional STXM-FMR measurements showing a two node – three anti-node spin wave in Figure 95 and a single node and two anti-node spin wave in Figure 96 are presented in this chapter. Animating the STXM-FMR images presented in both subfigures a) reveals a directed oscillation from the upper and lower stripe edges towards the stripe center, caused by the phase gradients visible in both subfigures b).

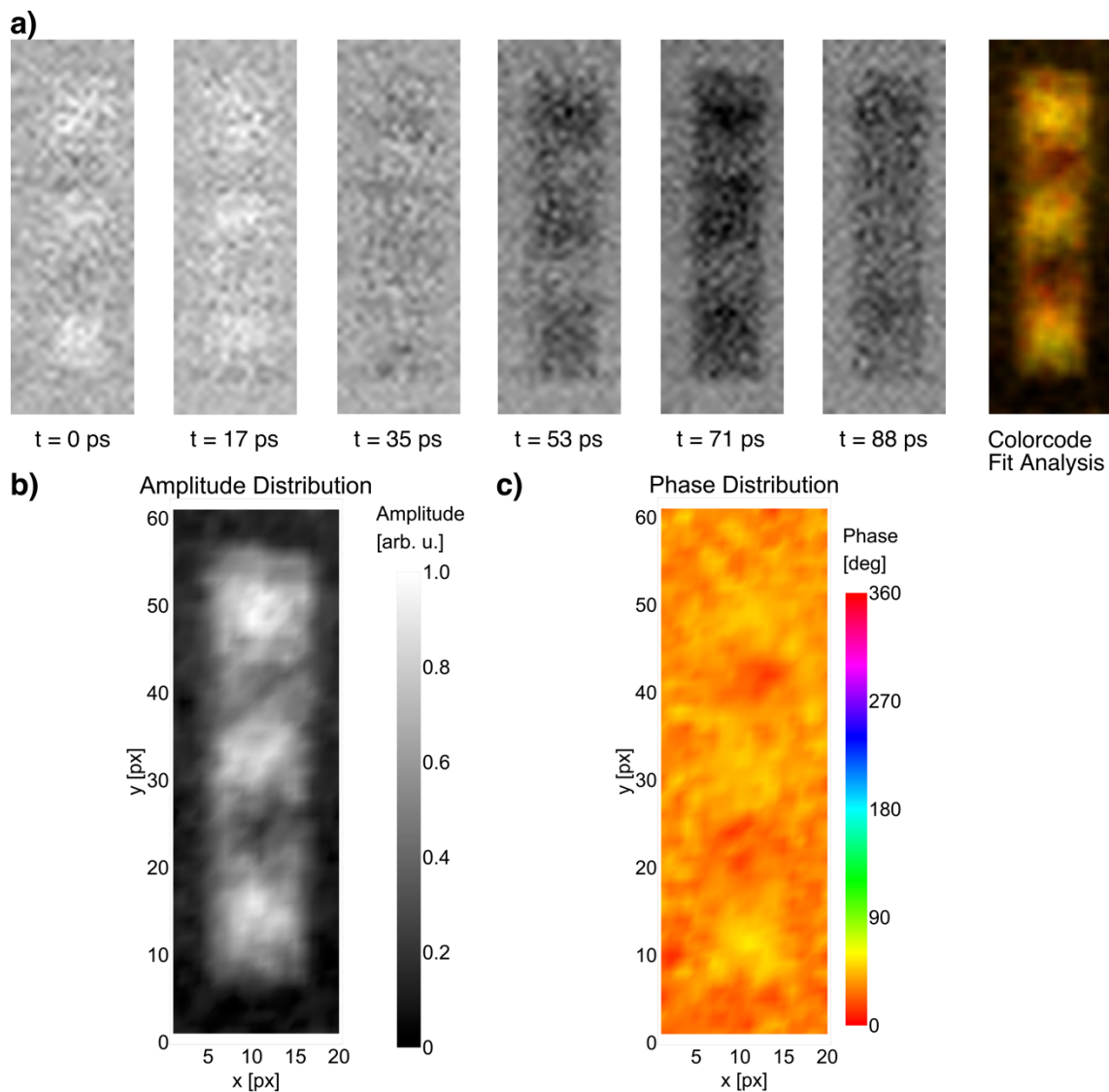


Figure 95: STXM-FMR data of the vertical Py stripe of the L-shape geometry at a static bias field of 92 mT and a microwave power of 29 dBm. a) Microwave induced X-ray transmission for 6 timesteps with a time distance of about 18 ps. b), c) Distribution of the relative phase with respect to the timestep $t = 0$ and the normalized amplitude extracted out of the color-code fit analysis (chapter 3.4).

Figure 95 b) shows a gradient of the phase relative to the time point $t = 0$ ps of about 45° to about $0^\circ/360^\circ$ to 20° , with an area showing a phase of about 60° . The amplitude distribution shows the highest amplitude at the anti-nodes (subfigure c)). Figure 96 b) shows a relative phase of about 60° degrees at the anti-nodes with a value of about 90° at the center of the lower anti-node and a phase of about $0^\circ/360^\circ$ to 20° at the nodes.

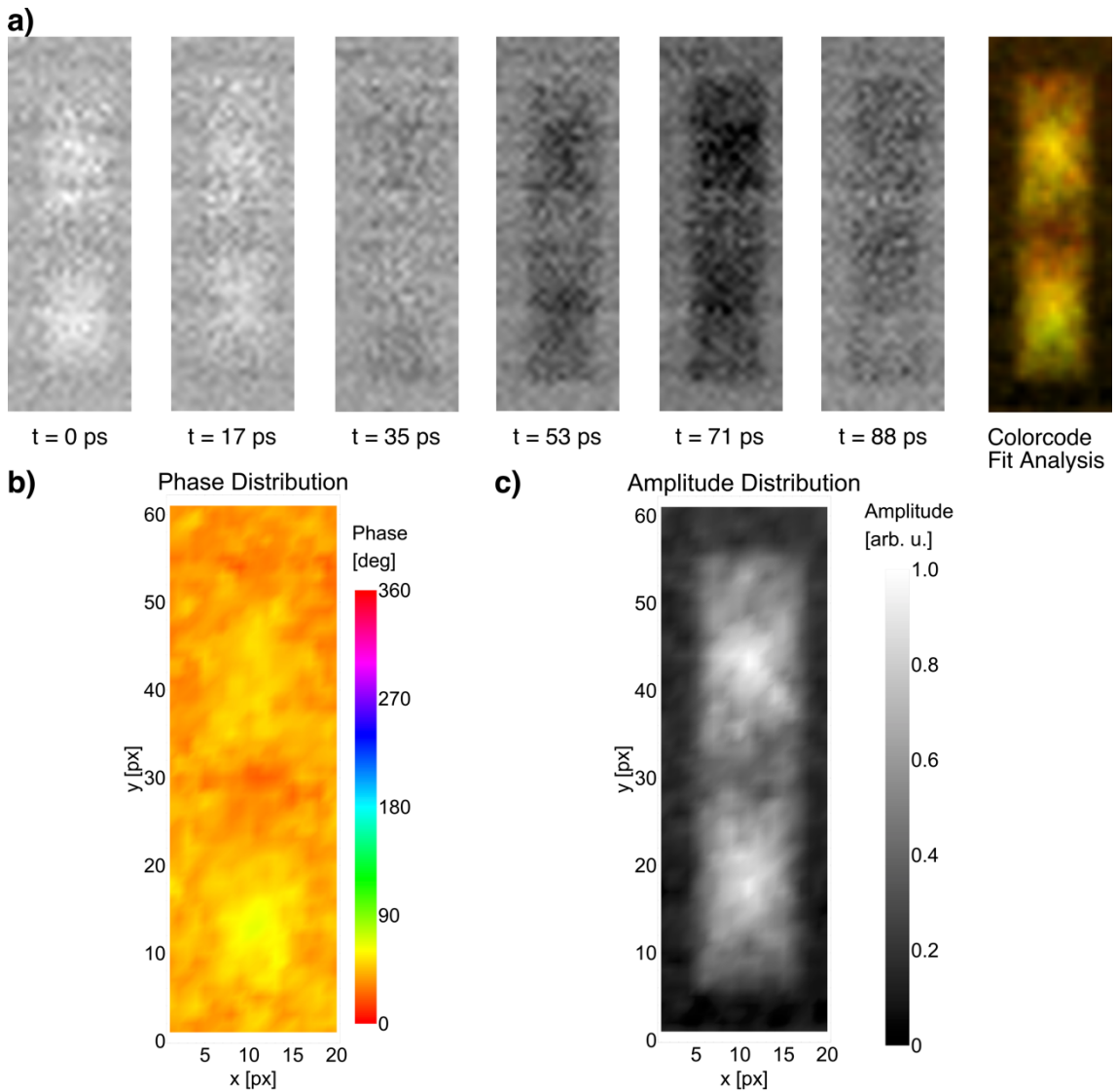


Figure 96: STXM-FMR data of the vertical Py stripe of the L-shape geometry at a static bias field of 102 mT and a microwave power of 29 dBm. a) Microwave induced X-ray transmission for 6 timesteps with a time distance of about 18 ps. b), c) Distribution of the relative phase with respect to the timestep $t = 0$ and the normalized amplitude extracted out of the color-code fit analysis (chapter 3.4).

As before the different phase value of the lower anti-node is attributed to the stray field influence of the horizontal Py stripe. The directed oscillatory behavior for both

spin wave modes is attributed to the influence of the stray field distribution, as described in chapter 4.2.

8. List of figures

- Figure 1: Coordinate system and angular dependencies of the magnetization used in this work. The in-plane rotation angle of the magnetization M is denoted as ϕ , while the out-of-plane rotation angle is denoted as θ . Figure redrawn from [56].5
- Figure 2: Visualization of the minimization of the stray field and the formation of magnetic domains. Figure adapted and redrawn from [57].7
- Figure 3: Schematic representation of X-ray absorption edges. As the experiments in this thesis are performed at the L_3 edge, the L edges are highlighted in the figure. Figure adapted from [77]. 15
- Figure 4: Schematic representation of excitations at the L_2 and L_3 edge. The “-“ sign denotes the odd parity of the term symbols. Figure redrawn and adapted from [79]. 17
- Figure 5: Schematic representation of the ferromagnetic resonance spectrometer used for the conventional FMR measurements. For cavity based FMR measurements the micro-resonator is replaced by a resonant cavity. Figure adapted from [85]... 19
- Figure 6: Schematic visualization of the transverse and longitudinal XMCD geometries for X-ray detected magnetic resonance. Figure redrawn and adapted from [92]. 21
- Figure 7: Schematic representation of the STXM-FMR setup at the Stanford Synchrotron Radiation Lightsource at SLAC National Accelerator Laboratory. The electromagnet is not shown for better visibility. Figure adapted from [48]. 24
- Figure 8: **a)** Schematic representation of a strip-line micro-resonator, allowing measurements in reflection and transmission geometries. **b)** Example picture of the sample holder with the attached semi-rigid cable to deliver the microwave power to the sample. 25
- Figure 9: STXM-FMR at the Co L_3 edge of a Py/Co disk-stripe bilayer microstructure. The blue rectangular marks the recorded dataset. The first row is the same dataset

as the last one to show a complete magnetization oscillation. 1st column: Timepoints and the recorded phase relative to the time $t = 0$. The 2nd and 3rd columns: STXM-FMR data recorded with microwave on (MW on) and off (MW off). 4th column: Difference of column 3 and 2 (MW off – MW on). This dataset is analyzed in detail in chapter 4.1. Image adapted from [48]..... 27

Figure 10: Color code fit analysis. a): Image i) STXM-FMR image of a Py stripe (see chapter 4.2). Images ii), iii) and iv): Extracted relative phase, fit accuracy and amplitude. Image v): Combination of the images ii) to iv). b): Example fit of the red marked square in a) i). c): Color code to visualize i) to v) in a). Figure taken from [103]..... 29

Figure 11: Coordination system and cell indexing of MuMax3. Figure adapted from [85]..... 30

Figure 12: Color wheel indicating the in-plane orientation of the simulated magnetization. Out-of-plane magnetization orientations are colored black for the +z direction and white for the -z direction. Intermediate out-of-plane components are using a color mixture of the in-plane and out-of-plane colors. The color wheel was created using the software WheelMasks by Roger Tallada and enhanced using Adobe Photoshop CC 2015. Figure taken from [85]..... 32

Figure 13: **a)** SEM image of the Py/Co multilayer sample on a Si₃N₄ membrane, indicating the sample dimensions. **b)** SEM image of the stripline micro resonator, **c)** magnification of the membrane area of the micro resonator. **d)** STXM image of the resonator loop including the sample. **e)** STXM image of the sample with a spatial resolution of 35 nm and a step-size of 100 nm. SEM images were taken by D. Spoddig and C. Schöppner. Image adapted from [48]..... 34

Figure 14: Conventional FMR spectra of the Py/Co multilayer sample. FMR-spectrum up to 400 mT, showing the main resonance modes as 1 (Py), 2 (coupled resonance), 3 (Co) and 4 (Co, edge resonance mode). Image taken from [48]..... 35

Figure 15: a) STXM-FMR images recorded with and without applied microwave excitation at the Co L₃ edge at 112.7 mT. The difference data is shown in the last column. The blue highlighted area shows the recorded STXM-FMR data with the first

row corresponding to the last one. b) FMR induced X-ray transmission for the Co resonance and for an off-resonance $|B_{\text{Ext}}|$. Figure adapted from [48]. 37

Figure 16: Results of the STXM-FMR measurements for the three resonances, for each resonance the scans at the Ni L_3 and the Co L_3 edge is displayed. Image taken from [48]. 38

Figure 17: Line scans of the STXM-FMR images recorded at the Co L_3 edge for resonance 3 (a)) and resonance 2 (b)). For comparison the images were normalized to the 0 to -1 range. The averaged intensity of the linescans is plotted to the right. 40

Figure 18: Two-dimensional representation of the magnetization for the simulated bilayer microstructure a) the Py disk, b) the Co stripe at $|B_{\text{Ext}}| = 85$ mT along the x-direction has been applied perpendicular to the long sides of the stripe. 42

Figure 19: Simulated stray-/demagnetization field intensity viewed from the z-direction for a) the Py disk and b) the Co stripe. Figure adapted from [48]. 43

Figure 20: Results of the color code fit analysis for the STXM-FMR data of the Py/Co sample. b) and e) are taken from [48]. The color bar was adapted from B. Zingsem for [48] 44

Figure 21: Schematic overview on the Py stripe sample geometries. In the micromagnetic simulations the external field has been tilted correspondingly to the orientation of the sample in the experiment..... 48

Figure 22: a) Simulated FMR spectrum for the single Py stripe simulated with a tilting angle of 4° (see Figure 21). b) Magnification of the simulated FMR spectrum for the single Py stripe simulated with a tilting angle of 4° (see Figure 21). The resonance positions in the range of the STXM-FMR measurements are indicated in the graph. 50

Figure 23: a) Simulated FMR spectrum for the T-shaped Py stripe arrangement simulated with a tilting angle of 3° (see Figure 21). b) Simulated FMR spectra for the L-shaped Py stripe arrangement. The external magnetic field is orientated along the

horizontal stripe. The resonance positions in the range of the STXM-FMR measurements are indicated in the graph..... 50

Figure 24: Averaged free energy densities for the single Py stripe for the different resonance fields..... 52

Figure 25: Stray- / demagnetization field intensity (a, c)) and distribution (b, d)) for the single Py stripe and the T-shape geometry with an external magnetic field of 80 mT..... 54

Figure 26: Averaged free energy densities for the horizontal and vertical Py stripe for the different resonance fields for the T-shaped sample geometry..... 55

Figure 27: a) Stray- / demagnetization field intensity and b) distribution for the Py L-shape geometry with an external magnetic field of 80 mT..... 57

Figure 28: STXM-FMR data of the single Py stripe at a static bias field of 80 mT (100 mT) and a microwave power of 29 dBm. **a)** Microwave induced X-ray transmission for 6 timesteps with a time distance of about 18 ps. **b), c)** Distribution of the relative phase with respect to the timestep $t = 0$ and the normalized amplitude extracted out of the color-code fit analysis (chapter 3.4). 60

Figure 29: Two-dimensional representation of the simulated normalized m_z -component of the magnetization for $|B_{Ext}| = 80$ mT. The external field is tilted by an angle of 4° (see Figure 21) to resemble the geometry of the experiment. Six images of the magnetization oscillation with a time distance of 18 ps are shown..... 61

Figure 30: Magnification of the simulated FMR spectrum for the single Py stripe simulated with a tilting angle of 4° (see Figure 21). Indicated is the resonance at 50 mT..... 63

Figure 31: STXM-FMR data of the single Py stripe at a static bias field 70 mT (hall probe value) and a microwave power of 29 dBm. **a)** Microwave induced X-ray transmission for 6 timesteps with a time distance of about 18 ps. **b), c)** Distribution of the relative phase with respect to the timestep $t = 0$ and the normalized amplitude extracted out of the color-code fit analysis (chapter 3.4). 64

Figure 32: Two-dimensional representation of the simulated normalized m_z -component of the magnetization for $|B_{\text{Ext}}| = 50$ mT. The external field is tilted by an angle of 4° (see Figure 21) to resemble the geometry of the experiment. Six images of the magnetization oscillation with a time distance of 18 ps are shown. 65

Figure 33: STXM-FMR data of the single Py stripe at a static bias field of about 83 mT (103 mT) and a microwave power of 29 dBm. **a)** Microwave induced X-ray transmission for 6 timesteps with a time distance of about 18 ps. **b), c)** Distribution of the relative phase with respect to the timestep $t = 0$ and the normalized amplitude extracted out of the color-code fit analysis (chapter 3.4). 66

Figure 34: STXM-FMR data of the single Py stripe at a static bias field of about 91 mT (109 mT) and a microwave power of 29 dBm. **a)** Microwave induced X-ray transmission for 6 timesteps with a time distance of about 18 ps. **b), c)** Distribution of the relative phase with respect to the timestep $t = 0$ and the normalized amplitude extracted out of the color-code fit analysis (chapter 3.4). 67

Figure 35: Simulated normalized m_z -component of the magnetization for $|B_{\text{Ext}}| = 91$ mT. **a)** B_{Ext} tilted by 4° (Figure 21), **b)** B_{Ext} aligned parallel to the long side of the stripe. Six images of the magnetization oscillation with a time distance of 18 ps are shown. 68

Figure 36: STXM-FMR data of the single Py stripe at a static bias field of about 96 mT (115 mT) and a microwave power of 29 dBm. **a)** Microwave induced X-ray transmission for 6 timesteps with a time distance of about 18 ps. **b), c)** Distribution of the relative phase with respect to the timestep $t = 0$ and the normalized amplitude extracted out of the color-code fit analysis (chapter 3.4). 69

Figure 37: Two-dimensional representation of the simulated normalized m_z -component of the magnetization for $|B_{\text{Ext}}| = 96$ mT. The external field is tilted by an angle of 4° (see Figure 21) to resemble the geometry of the experiment. Six images of the magnetization oscillation with a time distance of 18 ps are shown. 70

Figure 38; STXM-FMR data of the single Py stripe at a static bias field of about 100 mT (120 mT) and a microwave power of 29 dBm. **a)** Microwave induced X-ray transmission for 6 timesteps with a time distance of about 18 ps. **b), c)** Distribution

of the relative phase with respect to the timestep $t = 0$ and the normalized amplitude extracted out of the color-code fit analysis (chapter 3.4). 71

Figure 39: Two-dimensional representation of the simulated normalized m_z -component of the magnetization for $|B_{\text{Ext}}| = 100$ mT. The external field is tilted by an angle of 4° (see Figure 21) to resemble the geometry of the experiment. Six images of the magnetization oscillation with a time distance of 18 ps are shown. 72

Figure 40: STXM-FMR data of the vertical Py stripe of the T-shape geometry at a static bias field of about 98 mT and a microwave power of 27 dBm. **a)** Microwave induced X-ray transmission for 6 timesteps with a time distance of about 18 ps. **b)**, **c)** Map of the relative phase with respect to the timestep $t = 0$ and the normalized amplitude extracted out of the color-code fit analysis (chapter 3.4). The measurement data is published in [30]. 73

Figure 41: Two-dimensional representation of the simulated normalized m_z -component of the magnetization for $|B_{\text{Ext}}| = 97$ mT. The external field is tilted by an angle of 3° (see Figure 21) to resemble the geometry of the experiment. Six images of the magnetization oscillation with a time distance of 18 ps are shown..... 74

Figure 42: Two-dimensional representation of the simulated normalized m_z -component of the magnetization for $|B_{\text{Ext}}| = 97$ mT. The external field is oriented parallel to the horizontal Py stripe. Six images of the magnetization oscillation with a time distance of 18 ps are shown..... 75

Figure 43: STXM-FMR data of the vertical Py stripe of the T-shape geometry at a static bias field of about 112 mT [128] (103 mT) and a microwave power of 27 dBm. **a)** Microwave induced X-ray transmission for 6 timesteps with a time distance of about 18 ps. **b)**, **c)** Distribution of the relative phase and the normalized amplitude extracted out of the color-code fit analysis (chapter 3.4). The measurement data is published in [30]...... 76

Figure 44: Two-dimensional representation of the simulated normalized m_z -component of the magnetization for $|B_{\text{Ext}}| = 111$ mT. The external field is tilted by an angle of 3° (see Figure 21) to resemble the geometry of the experiment. Six

images of the magnetization oscillation with a time distance of 18 ps are shown. The simulation data is published in part in [30]. 77

Figure 45: STXM-FMR data of the vertical Py stripe of the T-shape geometry at a static bias field of about 126 mT [128] (113 mT) and a microwave power of 27 dBm. **a)** Microwave induced X-ray transmission for 6 timesteps with a time distance of about 18 ps. **b), c)** Distribution of the relative phase with respect to the timestep $t = 0$ and the normalized amplitude extracted out of the color-code fit analysis (chapter 3.4). The measurement data is published with a different analysis method in [30]. 79

Figure 46: STXM-FMR data of the vertical Py stripe of the T-shape geometry at a static bias field of about 122 mT and a microwave power of 29 dBm. **a)** Microwave induced X-ray transmission for 6 timesteps with a time distance of about 18 ps. **b), c)** Distribution of the relative phase with respect to the timestep $t = 0$ and the normalized amplitude extracted out of the color-code fit analysis (chapter 3.4). The investigated sample is from a different batch than the T-shaped samples investigated before employing the same dimensions and fabrication process. 80

Figure 47: Two-dimensional representation of the simulated normalized m_z -component of the magnetization for $|B_{Ext}| = 123$ mT. The external field is tilted by an angle of 3° (see Figure 21) to resemble the geometry of the experiment. Six images of the magnetization oscillation with a time distance of 18 ps are shown. The simulation data is published in part in [30]. 81

Figure 48: STXM-FMR data of the horizontal Py stripe of the T-shape geometry at a static bias field of about 81 mT and a microwave power of 29 dBm. **a)** Microwave induced X-ray transmission for 6 timesteps with a time distance of about 18 ps. **b), c)** Distribution of the relative phase with respect to the timestep $t = 0$ and the normalized amplitude extracted out of the color-code fit analysis (chapter 3.4). The investigated sample is from a different batch than the T-shaped samples investigated before employing the same dimensions and fabrication process. 82

Figure 49: Two-dimensional representation of the simulated normalized m_z -component of the magnetization for $|B_{Ext}| = 80$ mT. The external field is tilted by an

angle of 3° (see Figure 21) to resemble the geometry of the experiment. Six images of the magnetization oscillation with a time distance of 18 ps are shown..... 83

Figure 50: STXM-FMR data of the vertical Py stripe of the L-shape geometry at a static bias field of about 97 mT and a microwave power of 29 dBm. **a)** Microwave induced X-ray transmission for 6 timesteps with a time distance of about 18 ps. **b)**, **c)** Distribution of the relative phase with respect to the timestep $t = 0$ and the normalized amplitude extracted out of the color-code fit analysis (chapter 3.4). The measurement data is published with a different analysis method in [30]..... 85

Figure 51: Two-dimensional representation of the simulated normalized m_z -component of the magnetization $|B_{\text{Ext}}| = 96$ mT. The external field is oriented parallel to the horizontal Py stripe. Six images of the magnetization oscillation with a time distance of 18 ps are shown. The simulation data is published in part in [30]. 86

Figure 52: STXM-FMR data of the vertical Py stripe of the L-shape geometry at a static bias field of about 107 mT and a microwave power of 29 dBm. **a)** Microwave induced X-ray transmission for 6 timesteps with a time distance of about 18ps. **b)**, **c)** Distribution of the relative phase with respect to the timestep $t = 0$ and the normalized amplitude extracted out of the color-code fit analysis (chapter 3.4). The data has been published with a different analysis in [30] 87

Figure 53: Two-dimensional representation of the simulated normalized m_z -component of the magnetization for $|B_{\text{Ext}}| = 112$ mT. The external field is oriented parallel to the horizontal Py stripe. Six images of the magnetization oscillation with a time distance of 18 ps are shown. The simulation data is published in part in [30]. 88

Figure 54: STXM-FMR data of the vertical Py stripe of the L-shape geometry at a static bias field of about 112 mT and a microwave power of 29 dBm. **a)** Microwave induced X-ray transmission for 6 timesteps with a time distance of about 18ps. **b)**, **c)** Distribution of the relative phase with respect to the timestep $t = 0$ and the normalized amplitude extracted out of the color-code fit analysis (chapter 3.4)... 89

Figure 55: Two-dimensional representation of the simulated normalized m_z -component of the magnetization for $|B_{\text{Ext}}| = 123$ mT. The external field is oriented parallel to the horizontal Py stripe. Six images of the magnetization oscillation with a time distance of 18 ps are shown. 90

Figure 56: STXM-FMR data of the horizontal Py stripe of the L-shape geometry at a static bias field of about 74 mT and a microwave power of 29 dBm. **a)** Microwave induced X-ray transmission for 6 timesteps with a time distance of about 18ps. **b)**, **c)** Distribution of the relative phase with respect to the timestep $t = 0$ and the normalized amplitude extracted out of the color-code fit analysis (chapter 3.4)... 91

Figure 57: Two-dimensional representation of the simulated normalized m_z -component of the magnetization for $|B_{\text{Ext}}| = 80$ mT. The external field is oriented parallel to the horizontal Py stripe. Six images of the magnetization oscillation with a time distance of 18 ps are shown. 92

Figure 58: STXM-FMR data of the horizontal Py stripe of the L-shape geometry at a static bias field of about 81 mT and a microwave power of 29 dBm. **a)** Microwave induced X-ray transmission for 6 timesteps with a time distance of about 18ps. **b)**, **c)** Distribution of the relative phase with respect to the timestep $t = 0$ and the normalized amplitude extracted out of the color-code fit analysis (chapter 3.4)... 93

Figure 59: STXM-FMR data of the horizontal Py stripe of the L-shape geometry at a static bias field of about 87 mT and a microwave power of 29 dBm. **a)** Microwave induced X-ray transmission for 6 timesteps with a time distance of about 18ps. **b)**, **c)** Distribution of the relative phase with respect to the timestep $t = 0$ and the normalized amplitude extracted out of the color-code fit analysis (chapter 3.4)... 94

Figure 60: Two-dimensional representation of the simulated normalized m_z -component of the magnetization for $|B_{\text{Ext}}| = 86$ mT. The external field is oriented parallel to the horizontal Py stripe. Six images of the magnetization oscillation with a time distance of 18 ps are shown. 95

Figure 61: SEM image of the YIG nanoparticle sample positioned in the micro-resonator loop. The SEM image was taken by D. Spoddig..... 99

Figure 62: FMR spectrum of the YIG sample designated for STXM-FMR measurements. The measurement was performed at room temperature at 8.15 GHz. The inset shows a magnification for the field range from 0 mT to 50 mT..... 100

Figure 63: a) to f): STXM-FMR images after taking the natural logarithm of the division operation of the microwave on and microwave off images for the recorded time steps. A minimum-maximum normalization [127] was applied to the images. The images in a) to f) are blurred to enhance visibility. g) and e) Phase and normalized amplitude distribution extracted out of the color code fit analyses (see chapter 3.4 and [103] of the whole scan area. 101

Figure 64: Overlay of the amplitude distribution (Figure 63 h)) over the phase distribution (Figure 63 g)). 102

Figure 65: SEM image of a magnetosome chain inside a bacterium *Magnetospirillum Magnetotacticum*, the chain is subject of investigation by means of STXM-FMR. The image was taken by D. Spoddig. For better visibility the contrast has been adjusted by +40 %..... 105

Figure 66: Schematic representation of the magnetic easy directions in a single Fe_3O_4 cube. Figure adapted from [85]. 106

Figure 67: Scanning Electron Microcopy (SEM) images of the triple chain magnetosome ensemble for the STXM-FMR beamtime February 2018: a) Magnetosome chain distribution inside the micro-resonator loop. The chains enclosed in the blue square were measured by STXM-FMR. Other chains in the micro-resonator loop are marked by yellow arrows. b) Magnification of the magnetosome chain ensemble. The SEM images were taken by D. Spoddig..... 107

Figure 68: Scanning Electron Microcopy (SEM) images of the magnetosome chain preparation: a) TEM grid cutout showing the bi-segmented magnetosome chain for the STXM-FMR measurement inside the blue box. The diagonal black lines are carbon deposits. b)) Magnification of this particle chain. c) TEM grid cutout placed inside the micro-resonator loop, fixed with carbon at three corners of the cutout. The images were taken by D. Spoddig..... 108

Figure 69: X-ray absorption spectrum around the energy of the Fe L₃ edge (708 eV). The spectrum was taken by H. Ohldag..... 110

Figure 70: a) Grayscale STXM image of the magnetosome chain ensemble. The image has been taken by H. Ohldag. Darker colors represent areas with less transmission due to the magnetosome chains. b) Visualization of the investigated magnetosome chains in inverted colors with an overlay of the SEM image in Figure 67 b). The overlay has been created by B. Zingsem. c) Result of the color-code fit analysis, coding the relative phase as hue, the amplitude as brightness and the p-value as saturation. 111

Figure 71: a) Phase and b) normalized amplitude distribution extracted from Figure 70 c). 112

Figure 72: **a)** The simulated magnetosome chains, viewed from the +z direction, shown in the state of a random start magnetization. Shown is the normalized m_z component: Blue $-m_z$, red $+m_z$. **b)** Stray- and demagnetization field intensity. **c)** Stray field distribution. In all figures the cell layer in the particle center is shown. 114

Figure 73: Simulated FMR spectrum of the triple magnetosome chain ensemble at 8.176 GHz and an amplitude of 0.5 mT..... 114

Figure 74: Two-dimensional representation of the simulated m_z -component of the magnetization for external magnetic bias field values of **a)**: 156 mT, **b)**: 157 mT, **c)** 158 mT, **d)** 163 mT, **e)** 164 mT and **f)** 165 mT. Shown is the center cell layer..... 115

Figure 75: a) Grayscale STXM-FMR image of the investigated magnetosome chain. Darker colors represent areas with less transmission due to the sample and carbon on the sample surface. b) Cutout of image a) with an overlay of the SEM image, taken from Figure 68 c). The contrast has been adjusted for better visibility. The areas of dark contrast above and to the right of the depicted position of the magnetosome chain are attributed to deposited carbon, as the SEM image in Figure 68 c) shows no magnetosomes in these areas..... 118

Figure 76: a) Result of the color-code fit analysis, coding the relative phase as hue, the amplitude as brightness and the p-value as saturation. b) Distribution of the

relative phase extracted from image a). c) Normalized amplitude distribution extracted from image a).....118

Figure 77: **a)** Three-dimensional representation of the simulated magnetosome chain for the beamtime in April 2019. Image was done in Muvview. The chain is imaged with the random start configuration of the magnetization. **b)** Plot of the stray- and demagnetization field strength. **c)** Stray field distribution. **b)** and **c)** are simulated with an applied $|B_{Ext}| = 169$ mT as indicated in the figure.....120

Figure 78: Simulated FMR absorption spectrum of the bi-segmented magnetosome chain. The resonance at 169 mT close to the experimentally observed resonance at 167 mT is indicated in red.121

Figure 79: Micromagnetic simulation of the magnetosome chain investigated with STXM-FMR at the beamtime April 2019. The m_z -component of six timesteps of the simulation with a time distance of 24.7 ps are shown, simulated at $|B_{Ext}| = 166$ mT. The amplitude distribution of the STXM-FMR measurement is shown in the lower right corner, the areas showing a pronounced amplitude are circled in red.122

Figure 80: Micromagnetic simulation of the magnetosome chain investigated with STXM-FMR at the beamtime April 2019. The m_z -component of six timesteps of the simulation with a time distance of 24.7 ps are shown, simulated at $|B_{Ext}| = 169$ mT. The amplitude distribution of the STXM-FMR measurement is shown in the lower right corner, the areas showing a pronounced amplitude are circled in red.122

Figure 81: Phase and amplitude distribution from the STXM-FMR experiment at 167 mT (a, b)) and the micromagnetic simulation at 166 mT (c, d)). The phase- and amplitude analysis of the simulation data was processed by M. Winklhofer. 123

Figure 82: Definition of the side edges of the rectangular shaped body for the equations of the demagnetization factors. Figure redrawn and adapted from [65].129

Figure 83: STXM-FMR of the Py resonance measured at the Ni L₃.135

Figure 84: STXM-FMR of the coupled resonance measured at the Ni L₃.136

Figure 85: STXM-FMR of the Co resonance measured at the Ni L₃.137

Figure 86: STXM-FMR of the Py resonance measured at the Co L₃ edge..... 138

Figure 87: STXM-FMR of the coupled resonance measured at the Co L₃ edge..... 138

Figure 88: STXM-FMR of the Co resonance measured at the Co L₃..... 139

Figure 89: Averaged free energy densities for the horizontal and vertical Py stripe for the different resonance fields for the L-shaped sample geometry..... 140

Figure 90: STXM-FMR data of the single Py stripe at a static bias field about 71 mT (91 mT) and a microwave power of 29 dBm. **a)** Microwave induced X-ray transmission for 6 timesteps with a time distance of about 18 ps. **b), c)** Distribution of the relative phase with respect to the timestep $t = 0$ and the normalized amplitude extracted out of the color-code fit analysis (chapter 3.4)..... 142

Figure 91: STXM-FMR data of the single Py stripe at a static bias field 74 mT (94 mT) and a microwave power of 29 dBm. **a)** Microwave induced X-ray transmission for 6 timesteps with a time distance of about 18 ps. **b), c)** Distribution of the relative phase with respect to the timestep $t = 0$ and the normalized amplitude extracted out of the color-code fit analysis (chapter 3.4)..... 143

Figure 92: STXM-FMR data of the single Py stripe at a static bias field of about 77 mT (97 mT) and a microwave power of 29 dBm. **a)** Microwave induced X-ray transmission for 6 timesteps with a time distance of about 18 ps. **b), c)** Distribution of the relative phase with respect to the timestep $t = 0$ and the normalized amplitude extracted out of the color-code fit analysis (chapter 3.4)..... 144

Figure 93: STXM-FMR data of the single Py stripe at a static bias field of about 86 mT (106 mT) and a microwave power of 29 dBm. **a)** Microwave induced X-ray transmission for 6 timesteps with a time distance of about 18 ps. **b), c)** Distribution of the relative phase with respect to the timestep $t = 0$ and the normalized amplitude extracted out of the color-code fit analysis (chapter 3.4)..... 145

Figure 94: STXM-FMR data of the vertical Py stripe of the T-shape geometry at a static bias field of 107 mT and a microwave power of 27 dBm. **a)** Microwave induced X-ray transmission for 6 timesteps with a time distance of about 18 ps. **b), c)**

Distribution of the relative phase with respect to the timestep $t = 0$ and the normalized amplitude extracted out of the color-code fit analysis (chapter 3.4).146

Figure 95: STXM-FMR data of the vertical Py stripe of the L-shape geometry at a static bias field of 92 mT and a microwave power of 29 dBm. **a)** Microwave induced X-ray transmission for 6 timesteps with a time distance of about 18 ps. **b), c)** Distribution of the relative phase with respect to the timestep $t = 0$ and the normalized amplitude extracted out of the color-code fit analysis (chapter 3.4).148

Figure 96: STXM-FMR data of the vertical Py stripe of the L-shape geometry at a static bias field of 102 mT and a microwave power of 29 dBm. **a)** Microwave induced X-ray transmission for 6 timesteps with a time distance of about 18 ps. **b), c)** Distribution of the relative phase with respect to the timestep $t = 0$ and the normalized amplitude extracted out of the color-code fit analysis (chapter 3.4).149

9. List of tables

Table 1: Available Runge-Kutta methods within MuMax3 [29, 85].	31
Table 2: Demagnetization factors for the horizontal and vertical stripe calculated using equations (A1) to (A3).	48
Table 3: Parameters for the micromagnetic simulations of the Py stripe arrangements excited at 9.446 GHz. The A_{ex} taken from the OOMMF database, OOMMF [27]. M_{sat} is obtained from magnetization measurements of Py samples at Johannes Kepler University Linz.	49
Table 4: Intensities of the simulated FMR signal for the Py single stripe, T- and L-shape geometry with deviations for corresponding spin wave modes.	51
Table 5: Overview of several experimental techniques to detect the magnetization with respect to element specificity, spatial and time resolution.	133
Table 6: Correspondence table to assign timepoints and relative phase to subfigures.	135

10. List of references

1. P.J. Denning and T.G. Lewis, *Exponential laws of computing growth*. Communications of the ACM, 2016. **60**(1): p. 54-65.
2. S.A. Wolf, D.D. Awschalom, R.A. Buhrman, J.M. Daughton, S. von Molnár, M.L. Roukes, A.Y. Chtchelkanova, and D.M. Treger, *Spintronics: A Spin-Based Electronics Vision for the Future*. Science, 2001. **294**(5546): p. 1488-1495.
3. I. Žutić, J. Fabian, and S. Das Sarma, *Spintronics: Fundamentals and applications*. Reviews of Modern Physics, 2004. **76**(2): p. 323-410.
4. V.V. Kruglyak, S.O. Demokritov, and D. Grundler, *Magnonics*. Journal of Physics D: Applied Physics, 2010. **43**(26).
5. A. Hoffmann and S.D. Bader, *Opportunities at the Frontiers of Spintronics*. Physical Review Applied, 2015. **4**(4): p. 047001-1-047001-18.
6. A.V. Chumak, A.A. Serga, and B. Hillebrands, *Magnon transistor for all-magnon data processing*. Nature Communications, 2014. **5**: p. 4700.
7. A.V. Chumak, A.A. Serga, and B. Hillebrands, *Magnonic crystals for data processing*. Journal of Physics D: Applied Physics, 2017. **50**: p. 244001.
8. M. Vogel, R. Aßmann, P. Pirro, A.V. Chumak, B. Hillebrands, and G. von Freymann, *Control of Spin-Wave Propagation using Magnetisation Gradients*. Scientific Reports, 2018. **8**: p. 11099.
9. R.P. Cowburn and M.E. Welland, *Room Temperature Magnetic Quantum Cellular Automata*. Science, 2000. **287**(5457): p. 1466-1468.

10. P. Wadhwa and M.B.A. Jalil, *Magnetic soliton-based logic with fan-out and crossover functions*. Applied Physics Letters, 2004. **85**(12): p. 2367-2369.
11. B. Zingsem, T. Feggeler, A. Terwey, S. Ghaisari, D. Spoddig, D. Faivre, R. Meckenstock, M. Farle, and M. Winklhofer, *Biologically encoded magnonics*. Nature Communications, 2019. **10**: p. 4345.
12. S. Foner, *The vibrating sample magnetometer: Experiences of a volunteer (invited)*. Journal of Applied Physics, 1996. **79**(8): p. 4740-4745.
13. D. Jiles, *Introduction to Magnetism and Magnetic Materials*. 3 ed. 2016, Boca Raton: CRC Press Taylor and Francis Group.
14. S.V. Vonsovskii, *The Phenomenon of Resonant Absorption of a High-Frequency Magnetic Field in Ferromagnetic Substances*. 1966, Oxford, London, Edinburgh, New York, Toronto, Paris, Frankfurt: Pergamon Press.
15. A. Banholzer, R. Narkowicz, C. Hassel, R. Meckenstock, S. Stienen, O. Posth, D. Suter, M. Farle, and J. Lindner, *Visualization of spin dynamics in single nanosized magnetic elements*. Nanotechnology, 2011. **22**(29): p. 295713.
16. C. Schoeppner, K. Wagner, S. Stienen, R. Meckenstock, M. Farle, R. Narkowicz, D. Suter, and J. Lindner, *Angular dependent ferromagnetic resonance analysis in a single micron sized cobalt stripe*. Journal of Applied Physics, 2014. **116**(3): p. 033913-1-033913-6.
17. R. Narkowicz, D. Suter, and I. Niemeyer, *Scaling of sensitivity and efficiency in planar microresonators for electron spin resonance*. Review of Scientific Instruments, 2008. **79**(8): p. 084702-1-084702-8.
18. R. Narkowicz, D. Suter, and R. Stonies, *Planar microresonators for EPR experiments*. Journal of Magnetic Resonance, 2005. **175**: p. 275-284.

19. J. Xie and S. Jon, *Magnetic Nanoparticle-Based Theranostics*. *Theranostics*, 2012. **2**(1): p. 122-124.
20. A.J. Cole, V.C. Yang, and A.E. David, *Cancer theranostics: the rise of targeted magnetic nanoparticles*. *Trends in Biotechnology*, 2011. **29**(7): p. 323-332.
21. A. Singh and S.K. Sahoo, *Magnetic nanoparticles: a novel platform for cancer theranostics*. *Drug Discovery Today*, 2014. **19**(4): p. 474-481.
22. M. Angelakeris, *Magnetic nanoparticles: A multifunctional vehicle for modern theranostics*. *Biochimica et Biophysica Acta - General Subjects*, 2017. **1861**(6): p. 1642-1651.
23. B. Jang, E. Gutman, N. Stucki, B.F. Seitz, P.D. Wendel-García, T. Newton, J. Pokki, O. Ergeneman, S. Pané, Y. Or, and B.J. Nelson, *Undulatory Locomotion of Magnetic Multilink Nanoswimmers*. *Nano Letters*, 2015. **15**: p. 4829-4833.
24. T. Li, J. Li, H. Zhang, X. Chang, W. Song, Y. Hu, G. Shao, E. Sandraz, G. Zhang, L. Li, and J. Wang, *Magnetically Propelled Fish-Like Nanoswimmers*. *Small*, 2016. **12**(44): p. 6098-6105.
25. W.F. Brown, *Micromagnetics : Successor to domain theory ?* *J. Phys. Radium*, 1959. **20** (2-3): p. 101-104.
26. W.F. Brown, *Micromagnetics*. *Interscience Tracts on Physics and Astronomy*, ed. R.E. Marshak. 1963, New York, London: Interscience Publishers.
27. M.J. Donahue and D.G. Porter, *OOMMF User's Guide, Version 1.0*, in *Interagency Report NISTIR 6376*. 1999: Gaithersburg, MD.

28. R.W. Chantrell, J. Fidler, T. Schrefl, and M.A. Wongsam, *Micromagnetics: Finite Element Approach*, in *Encyclopedia of Materials: Science and Technology*, K.H.J. Buschow, et al., Editors. 2001, Elsevier Science Ltd. p. 5651-5661.
29. A. Vansteenkiste, J. Leliaert, M. Dvornik, M. Helsen, F. Garcia-Sanchez, and B. Van Waeyenberge, *The design and verification of MuMax3*. AIP Advances, 2014. **4**(10): p. 107133-1-107133-22.
30. S. Pile, T. Feggeler, T. Schaffers, R. Meckenstock, M. Buchner, D. Spoddig, B. Zingsem, V. Ney, M. Farle, H. Wende, H. Ohldag, A. Ney, and K. Ollefs, *Non-standing spin-waves in confined micrometer-sized ferromagnetic structures under uniform excitation*. Applied Physics Letters, 2020. **116**(7): p. 072401-1-072401-5.
31. S.O. Demokritov, B. Hillebrands, and A.N. Slavin, *Brillouin Light Scattering Studies Of Confined Spin Waves: Linear And Nonlinear Confinement*. Physics Reports, 2001. **348**: p. 441-489.
32. T. Sebastian, K. Schultheiss, B. Obry, B. Hillebrands, and H. Schultheiss, *Micro-focused Brillouin light scattering: imaging spin waves at the nanoscale*. Frontiers in Physics, 2015. **3**: p. 1-23.
33. J. Jersch, V.E. Demidov, H. Fuchs, K. Rott, P. Krzysteczko, J. Münchenberger, G. Reiss, and S.O. Demokritov, *Mapping of localized spin-wave excitations by near-field Brillouin light scattering*. Applied Physics Letters, 2010. **97**(15): p. 152502-1-152502-3.
34. R. Frömter, F. Klodt, S. Rößler, A. Frauen, P. Staeck, D.R. Cavicchia, L. Bocklage, V. Röbisch, E. Quandt, and H.P. Oepen, *Time-resolved scanning electron microscopy with polarization analysis*. Applied Physics Letters, 2016. **108**(14): p. 142401-1-142401-5.

35. T. Duden and E. Bauer, *Spin-polarized low energy electron microscopy of ferromagnetic layers*. Journal of Electron Microscopy, 1998. **47**(5): p. 379-385.
36. H. Pinkvos, H. Poppa, E. Bauer, and G.-M. Kim, *A Time-Resolved SPLEEM Study of Magnetic Microstructure in Ultrathin Co Films on W(110)*, in *Magnetism and Structure in Systems of Reduced Dimension*, R.F.C. Farrow, et al., Editors. 1993, Springer: New York.
37. M. Möller, J.H. Gaida, S. Schäfer, and C. Ropers, *Few-nm tracking of current-driven magnetic vortex orbits using ultrafast Lorentz microscopy*. Communications Physics, 2020. **3**(1).
38. N. Rubiano da Silva, M. Möller, A. Feist, H. Ulrichs, C. Ropers, and S. Schäfer, *Nanoscale Mapping of Ultrafast Magnetization Dynamics with Femtosecond Lorentz Microscopy*. Physical Review X, 2018. **8**(3): p. 031052-1-031052-7.
39. ITU, *Nomenclature of the frequency and wavelength bands used in telecommunications, Recommendation ITU-R V.431-8*, in *V Series Vocabulary and related subjects*. 2015: Genf. p. 1-3.
40. B. Zingsem, *Pico-second spin dynamics in nano-structures: Towards nanometer spatial resolution by Transmission electron microscopy*, in *Faculty of Physics*. 2020, University of Duisburg-Essen: Duisburg.
41. C.M. Schneider, A. Krasnyuk, S.A. Nepijko, A. Oelsner, and G. Schönhense, *Accessing fast magnetization dynamics by XPEEM: Status and perspectives*. Journal of Magnetism and Magnetic Materials, 2006. **304**(1): p. 6-9.
42. A. Scholl, *Applications of photoemission electron microscopy (PEEM) in magnetism research*. Current Opinion in Solid State and Materials Science, 2003. **7**(1): p. 59-66.

43. D.M. Burn, S. Zhang, K. Zhai, Y. Chai, Y. Sun, G. van der Laan, and T. Hesjedal, *Mode-Resolved Detection of Magnetization Dynamics Using X-ray Diffractive Ferromagnetic Resonance*. Nano Lett, 2020. **20**(1): p. 345-352.
44. S. Bonetti, R. Kukreja, Z. Chen, D. Spoddig, K. Ollefs, C. Schöppner, R. Meckenstock, A. Ney, J. Pinto, R. Houanche, J. Frisch, J. Stöhr, H.A. Dürr, and H. Ohldag, *Microwave soft x-ray microscopy for nanoscale magnetization dynamics in the 5–10 GHz frequency range*. Review of Scientific Instruments, 2015. **86**(9): p. 093703-1-093703-9.
45. T. Schaffers, R. Meckenstock, D. Spoddig, T. Feggeler, K. Ollefs, C. Schöppner, S. Bonetti, H. Ohldag, M. Farle, and A. Ney, *The combination of micro-resonators with spatially resolved ferromagnetic resonance*. Review of Scientific Instruments, 2017. **88**(9): p. 093703-1-093703-10.
46. T. Schaffers, T. Feggeler, S. Pile, R. Meckenstock, M. Buchner, D. Spoddig, V. Ney, M. Farle, H. Wende, S. Wintz, M. Weigand, H. Ohldag, K. Ollefs, and A. Ney, *Extracting the Dynamic Magnetic Contrast in Time-Resolved X-ray Transmission Microscopy*. Nanomaterials (Basel), 2019. **9**(7): p. 1-13.
47. T. Schaffers, *Magnetization dynamic in prototype microstructures investigated with ultimate time and space resolution and element selectivity*, in *Institute for semiconductor and solid state physics*. 2019, Johannes Kepler Universität: Linz.
48. T. Feggeler, R. Meckenstock, D. Spoddig, C. Schöppner, B.W. Zingsem, T. Schaffers, H. Ohldag, H. Wende, M. Farle, A. Ney, and K. Ollefs, *Direct visualization of dynamic magnetic coupling in a Co/Py bilayer with picosecond and nanometer resolution*. arXiv:1905.06772 [cond-mat.mes-hall], submitted to Physical Review Applied in July 2020., 2020.

49. J. Ben Youssef and A. Layadi, *Ferromagnetic resonance study of Permalloy/Cu/Co/NiO spin valve system*. Journal of Applied Physics, 2010. **108**(5): p. 053913-1-053913-6.
50. R. Salikhov, R. Abrudan, F. Brüssing, K. Gross, C. Luo, K. Westerholt, H. Zabel, F. Radu, and I.A. Garifullin, *Configurational dependence of the magnetization dynamics in spin valve systems: Influence of spin pumping and domain wall induced coupling*. Physical Review B, 2012. **86**(14): p. 144422-1-144422-6.
51. A. Layadi, *A theoretical investigation of Ferromagnetic Resonance Linewidth and damping constants in coupled trilayer and spin valve systems*. AIP Advances, 2015. **5**(5): p. 057113-1-057113-12.
52. F. Scheibel, B. Zingsem, T. Feggeler, R. Meckenstock, D. Spoddig, M. Farle, and M. Acet, *Magnetic anisotropy of single-crystal antiperovskite Mn₃GaC studied by ferromagnetic resonance and dynamic magnetic-response simulations*. Physical Review Materials, 2019. **3**(5): p. 054403-1-054403-5.
53. G. Woltersdorf, O. Mosendz, B. Heinrich, and C.H. Back, *Magnetization dynamics due to pure spin currents in magnetic double layers*. Physical Review Letters, 2007. **99**(24): p. 246603-1-246603-4.
54. A.A. Baker, A.I. Figueroa, L.J. Collins-McIntyre, G. van der Laan, and T. Hesjedal, *Spin pumping in Ferromagnet-Topological Insulator-Ferromagnet Heterostructures*. Scientific Reports, 2015. **5**: p. 7907.
55. F. Schwabl, *Quantenmechanik (QM I) Eine Einführung*. 7 ed. 2007, Berlin, Heidelberg, New York: Springer.
56. M. Getzlaff, *Fundamentals of Magnetism*. 2008, Berlin, Heidelberg, New York: Springer.
57. R. Gross and A. Marx, *Festkörperphysik*. 1 ed. 2012, München: Oldenbourg.

58. W. Nolting, *Quantentheorie des Magnetismus Teil 1 Grundlagen*. 1986, Wiesbaden: Springer.
59. F. Schwabl, *Statistische Mechanik*. 3 ed. 2006, Springer, Berlin, Heidelberg, NewYork: Springer.
60. W. Nolting, *Grundkurs Theoretische Physik 5/2 Quantenmechanik - Methoden und Anwendungen*. 7 ed. 2012, Heidelberg, Dordrecht, London, New York: Springer.
61. I. Dzyaloshinsky, *A thermodynamic theory of "weak" ferromagnetism of antiferromagnetics*. Journal of Physics and Chemistry of Solids, 1958. **4**(4): p. 241-255.
62. T. Moriya, *Anisotropic Superexchange Interaction and Weak Ferromagnetism*. Physical Review, 1960. **120**(1): p. 91-98.
63. K.-H. Hellwege, *Einführung in die Festkörperphysik*. 1976, Berlin, Heidelberg, New York: Springer.
64. D.C. Cronemeyer, *Demagnetization factors for general ellipsoids*. Journal of Applied Physics, 1991. **70**(6): p. 2911-2914.
65. A. Aharoni, *Demagnetizing factors for rectangular ferromagnetic prisms*. Journal of Applied Physics, 1998. **83**(6): p. 3432-3434.
66. A. Hubert and R. Schäfer, *Magnetic Domains The Analysis of Magnetic Microstructures*. 1998, Berlin, Heidelberg: Springer.
67. M. Farle, *Ferromagnetic resonance of ultrathin metallic layers*. Reports on Progress in Physics, 1998. **61**: p. 755-826.

68. T.L. Gilbert, *A Phenomenological Theory of Damping in Ferromagnetic Materials*. IEEE Transactions on Magnetics, 2004. **40**(6): p. 3443-3449.
69. L. Landau and E. Lifshits, *ON THE THEORY OF THE DISPERSION OF MAGNETIC PERMEABILITY IN FERROMAGNETIC BODIES*. Ukrainian Journal of Physics (Reprint from Phys. Zeitsch. der Sow. 8, pp. 153–169 (1935)), 2008. **53**: p. 14-22.
70. J.D. Jackson, *Classical Electrodynamics*. 1999, Hoboken, NJ: John Wiley & Sons.
71. D.D. Stancil and A. Prabhakar, *Spin Waves Theory and Applications*. 2009, New York: Springer.
72. C. Kittel, *Excitation of Spin Waves in a Ferromagnet by a Uniform rf Field*. Physical Review, 1958. **110**(6): p. 1295-1297.
73. J.W. Hartwell, *Standing spin waves in ferromagnetic thin films*. Proceedings of the IEEE, 1968. **56**(1): p. 23-31.
74. M.H. Seavey and P.E. Tannenwald, *Direct Observation of Spin-Wave Resonance*. Physical Review Letters, 1958. **1**(5): p. 168-169.
75. K.Y. Guslienko, S.O. Demokritov, B. Hillebrands, and A.N. Slavin, *Effective dipolar boundary conditions for dynamic magnetization in thin magnetic stripes*. Physical Review B, 2002. **66**(13): p. 132402-1-132402-4.
76. J. Stöhr and H.C. Siegmann, *Magnetism From Fundamentals to Nanoscale Dynamics*. Springer Series in solid-state sciences, ed. M. Cardona, et al. 2006, Berlin, Heidelberg: Springer.

77. J. Kowalska and S. DeBeer, *The role of X-ray spectroscopy in understanding the geometric and electronic structure of nitrogenase*. *Biochimica et Biophysica Acta*, 2015. **1853**(6): p. 1406-1415.
78. J.J. Rehr and R.C. Albers, *Theoretical approaches to x-ray absorption fine structure*. *Reviews of Modern Physics*, 2000. **72**(3): p. 621-654.
79. A. Rogalev, K. Ollefs, and F. Wilhelm, *X-Ray Magnetic Circular Dichroism*, in *X-Ray Absorption and X-Ray Emission Spectroscopy Theory and Applications*, J.A. Van Bokhoven and C. Lamberti, Editors. 2016, John Wiley & Sons: Chichester.
80. J. Stöhr, *Exploring the microscopic origin of magnetic anisotropies with X-ray magnetic circular dichroism (XMCD) spectroscopy*. *Journal of Magnetism and Magnetic Materials*, 1999. **200**: p. 470-497.
81. G. Schütz, W. Wagner, W. Wilhelm, P. Kienle, R. Zeller, R. Frahm, and G. Materlik, *Absorption of circularly polarized x rays in iron*. *Physical Review Letters*, 1987. **58**(7): p. 737-740.
82. A. Vansteenkiste, B. Van de Wiele, L. Dupré, B. Van Waeyenberge, and D. De Zutter, *Implementation of a finite-difference micromagnetic model on GPU hardware*. *International Journal of Numerical Modelling: Electronic Networks, Devices and Fields*, 2013. **26**: p. 366-375.
83. B. Van de Wiele, A. Vansteenkiste, M. Kammerer, B. Van Waeyenberge, L. Dupré, and D. De Zutter, *Micromagnetic Simulations on GPU, A Case Study: Vortex Core Switching by High-Frequency Magnetic Fields*. *IEEE Transactions on Magnetics*, 2012. **48**(6): p. 2068-2072.
84. A. Vansteenkiste and B. Van de Wiele, *MuMax: A new high-performance micromagnetic simulation tool*. *Journal of Magnetism and Magnetic Materials*, 2011. **323**: p. 2585-2591.

85. T. Feggeler, *Micromagnetic simulation for the static and dynamic characterization of nano particles*, in *Faculty of Physik*. 2016, University of Duisburg-Essen: Duisburg (not published).
86. Lake Shore Cryotronics, *User's Manual Model 425 Gaussmeter, Rev 1.0*. 2010.
87. S. Villa, P. Riani, F. Locardi, and F. Canepa, *Functionalization of Fe₃O₄ NPs by Silanization: Use of Amine (APTES) and Thiol (MPTMS) Silanes and Their Physical Characterization*. *Materials* (Basel), 2016. **9**: p. 1-14.
88. J. Jiang and R.T. Weber, *ELEXSYS E 500 User's Manual: Basic Operations*. 2001, Bruker BioSpin Corporation: Billerica, MA.
89. J.A. Weil and J.R. Bolton, *Electron Paramagnetic Resonance*. 2 ed. 2007, Hoboken, NJ: John Wiley & Sons.
90. P. Höfer, *Basic Experimental Methods in Continuous Wave Electron Paramagnetic Resonance*, in *ELECTRON PARAMAGNETIC RESONANCE A Practitioner's Toolkit*, M. Brustolon and E. Giamello, Editors. 2009, John Wiley & Sons: Hoboken, NJ.
91. J. Poole, Charles P., *Electron Spin Resonance A Comprehensive Treatise on Experimental Techniques*. 1983, New York, Chichester, Brisbane, Toronto, Singapore: John Wiley & Sons.
92. J. Goulon, A. Rogalev, F. Wilhelm, N. Jaouen, C. Goulon-Ginet, and C. Brouder, *X-ray detected ferromagnetic resonance in thin films*. *The European Physical Journal B*, 2006. **53**: p. 169-184.
93. J. Goulon, A. Rogalev, G. Goujon, F. Wilhelm, J. Ben Youssef, C. Gros, J.M. Barbe, and R. Guillard, *X-Ray Detected Magnetic Resonance: A Unique Probe of the Precession Dynamics of Orbital Magnetization Component*. *International Journal of Molecular Sciences*, 2011. **12**(12): p. 8797-8835.

94. W.E. Bailey, L. Cheng, D.J. Keavney, C.C. Kao, E. Vescovo, and D.A. Arena, *Precessional dynamics of elemental moments in a ferromagnetic alloy*. Physical Review B, 2004. **70**(17): p. 172403-1-172403-4.
95. G. Boero, S. Rusponi, P. Bencok, R.S. Popovic, H. Brune, and P. Gambardella, *X-ray ferromagnetic resonance spectroscopy*. Applied Physics Letters, 2005. **87**(15): p. 152503-1-152503-3.
96. K. Ollefs, R. Meckenstock, D. Spoddig, F.M. Römer, C. Hassel, C. Schöppner, V. Ney, M. Farle, and A. Ney, *Toward broad-band x-ray detected ferromagnetic resonance in longitudinal geometry*. Journal of Applied Physics, 2015. **117**(22): p. 223906-1-223906-10.
97. G. Boero, S. Rusponi, J. Kavich, A. Lodi Rizzini, C. Piamonteze, F. Nolting, C. Tieg, J.U. Thiele, and P. Gambardella, *Longitudinal detection of ferromagnetic resonance using x-ray transmission measurements*. Review of Scientific Instruments, 2009. **80**(12): p. 123902-1-123902-11.
98. C. Cheng and W.E. Bailey, *Sub-micron mapping of GHz magnetic susceptibility using scanning transmission x-ray microscopy*. Applied Physics Letters, 2012. **101**(18): p. 182407-1-182407-4.
99. M.K. Marcham, L.R. Shelford, S.A. Cavill, P.S. Keatley, W. Yu, P. Shafer, A. Neudert, J.R. Childress, J.A. Katine, E. Arenholz, N.D. Telling, G. van der Laan, and R.J. Hicken, *Phase-resolved x-ray ferromagnetic resonance measurements of spin pumping in spin valve structures*. Physical Review B, 2013. **87**(18): p. 180403-1-180403-4.
100. A. Puzic, B. Van Waeyenberge, K.W. Chou, P. Fischer, H. Stoll, G. Schütz, T. Tyliczszak, K. Rott, H. Brückl, G. Reiss, I. Neudecker, T. Haug, M. Buess, and C.H. Back, *Spatially resolved ferromagnetic resonance: Imaging of ferromagnetic eigenmodes*. Journal of Applied Physics, 2005. **97**(10): p. 10E704-1-10E704-3.

101. S. Bonetti, R. Kukreja, Z. Chen, F. Macià, J.M. Hernández, A. Eklund, D. Backes, J. Frisch, J. Katine, G. Malm, S. Urazhdin, A.D. Kent, J. Stöhr, H. Ohldag, and H.A. Dürr, *Direct observation and imaging of a spin-wave soliton with p-like symmetry*. Nature Communications, 2015. **6**(1): p. 8889.
102. Anritsu, *RF/Microwave Signal Generators MG3690B RF/Microwave Signal Generator, 0.1 Hz to 70 GHz/325 GHz, Technical Data Sheet No. 11410-00344, Rev. K*. 2011.
103. B. Zingsem, T. Feggeler, R. Meckenstock, T. Schaffers, S. Pile, H. Ohldag, M. Farle, H. Wende, A. Ney, and K. Ollefs, *Evaluation protocol for revealing magnonic contrast in STXM-FMR measurements*. arXiv:1901.10595 [cond-mat.str-el], 2019.
104. MuMax3. *mumax3 GPU-accelerated micromagnetism*. 2020 [cited 2020 /06/21]; Available from: <http://mumax.github.io>.
105. NVIDIA Corporation. *High Performance Computing*. 2020 [cited 2020 /06/21]; Available from: <https://developer.nvidia.com/hpc>.
106. G.S. Abo, Y.-K. Hong, J. Park, J. Lee, W. Lee, and B.-C. Choi, *Definition of Magnetic Exchange Length*. IEEE Transactions on Magnetics, 2013. **49**(8): p. 4937-4939.
107. C. Andreas, S. Gliga, and R. Hertel, *Numerical micromagnetism of strong inhomogeneities*. Journal of Magnetism and Magnetic Materials, 2014. **362**: p. 7-13.
108. L. Exl, S. Bance, F. Reichel, T. Schrefl, H.P. Stimming, and N.J. Mauser, *LaBonte's method revisited: An effective steepest descent method for micromagnetic energy minimization*. Journal of Applied Physics, 2014. **115**: p. 17D118-1-17D118-3.

109. P.J. Davis and I. Polonsky, *Numerical Interpolation, Differentiation, and Integration*, in *Handbook of Mathematical Functions with Formulas, Graphs, and Mathematical Tables*, M. Abramowitz and I.A. Stegun, Editors. 1965, Dover Publications: New York.
110. G.E. Rowlands, *Muview2 3D Visualization of Micromagnetic Data from OOMMF and Mumax*. 2014.
111. B. Heinrich, S.T. Purcell, J.R. Dutcher, K.B. Urquhart, J.F. Cochran, and A.S. Arrott, *Structural and magnetic properties of ultrathin Ni/Fe bilayers grown epitaxially on Ag(001)*. *Phys Rev B Condens Matter*, 1988. **38**(18): p. 12879-12896.
112. O. Posth, N. Reckers, R. Meckenstock, G. Dumpich, and J. Lindner, *Study of spin transfer torque in serially connected pillars by means of ferromagnetic resonance*. *Journal of Physics D: Applied Physics*, 2009. **42**(3): p. 035003.
113. R. Meckenstock, *Invited Review Article: Microwave spectroscopy based on scanning thermal microscopy: Resolution in the nanometer range*. *Review of Scientific Instruments*, 2008. **79**(4): p. 041101-1-041101-29.
114. P.E. Mijnders, S. Sahrakorpi, M. Lindroos, and A. Bansil, *Angle-resolved photoemission spectra, electronic structure, and spin-dependent scattering in Ni_{1-x}Fe_x Permalloys*. *Physical Review B*, 2002. **65**(7): p. 075106-1-075106-8.
115. R.J. Wakelin and E.L. Yates, *A Study of the Order-Disorder Transformation in Iron-Nickel Alloys in the Region FeNi₃*. *Proceedings of the Physical Society. Section B*, 1953. **66**: p. 221-240.
116. M.N. Shetty, *Materials Science and Engineering : Problems with Solutions*. 2016: Prentice Hall India Pvt., Limited.

117. C.L. Chien, *Magnetic Characterization of Materials*, in *Magnetic Interactions and Spin Transport*, A.Y. Chtchelkanova, S. Wolf, and Y. Izerda, Editors. 2003, Springer: New York.
118. R. Meckenstock, I. Barsukov, O. Posth, J. Lindner, A. Butko, and D. Spoddig, *Locally resolved ferromagnetic resonance in Co stripes*. Applied Physics Letters, 2007. **91**(14): p. 142507-1-142507-3.
119. C. Bayer, S.O. Demokritov, B. Hillebrands, and A.N. Slavin, *Spin-wave wells with multiple states created in small magnetic elements*. Applied Physics Letters, 2003. **82**(4): p. 607-609.
120. H.-J. Chia, F. Guo, L.M. Belova, and R.D. McMichael, *Two-dimensional spectroscopic imaging of individual ferromagnetic nanostripes*. Physical Review B, 2012. **86**(18): p. 184406-1-184406-7.
121. G.R. Aranda, G.N. Kakazei, J. González, and K.Y. Guslienko, *Ferromagnetic resonance micromagnetic studies in patterned permalloy thin films and stripes*. Journal of Applied Physics, 2014. **116**: p. 093908-1-093908-10.
122. A. Lara, V. Metlushko, and F.G. Aliev, *Observation of propagating edge spin waves modes*. Journal of Applied Physics, 2013. **114**: p. 213905-1-213905-5.
123. H.J. Pain, *The physics of vibrations and waves*. 6 ed. 2005, Chichester: John Wiley & Sons.
124. Y. Au, M. Dvornik, T. Davison, E. Ahmad, P.S. Keatley, A. Vansteenkiste, B. Van Waeyenberge, and V.V. Kruglyak, *Direct Excitation of Propagating Spin Waves by Focused Ultrashort Optical Pulses*. Physical Review Letters, 2013. **110**(9): p. 097201-1-097201-5.
125. N. Kumar and A. Prabhakar, *Spin Wave Dispersion in Striped Magnonic Waveguide*. IEEE Transactions on Magnetics, 2013. **49**(3): p. 1024-1028.

126. A.V. Chumak, V.I. Vasyuchka, A.A. Serga, and B. Hillebrands, *Magnon spintronics*. Nature Physics, 2015. **11**: p. 453-461.
127. K.L. Priddy and P.E. Keller, *Artificial neural networks : an introduction*. Tutorial Texts in Optical Engineering. Vol. TT68. 2005, Bellingham, WA: SPIE—The International Society for Optical Engineering (The Society of Photo-Optical Instrumentation Engineers).
128. S. Pile and A. Ney, *Sabbatical beamtime 01/04/2019*. 2019, Johannes Kepler University: Linz.
129. M. Weigand, *Realization of a new Magnetic Scanning X-ray Microscope and Investigation of Landau Structures under Pulsed Field Excitation*. 1 ed. 2015, Göttingen: Cuvillier.
130. Z. Zhang, M. Vogel, J. Holanda, J. Ding, M.B. Jungfleisch, Y. Li, J.E. Pearson, R. Divan, W. Zhang, A. Hoffmann, Y. Nie, and V. Novosad, *Controlled interconversion of quantized spin wave modes via local magnetic fields*. Physical Review B, 2019. **100**(1): p. 014429-1-014429-10.
131. Z. Duan, I.N. Krivorotov, R.E. Arias, N. Reckers, S. Stienen, and J. Lindner, *Spin wave eigenmodes in transversely magnetized thin film ferromagnetic wires*. Physical Review B, 2015. **92**(10): p. 104424-1-104424-10.
132. T. Schmitz, U. Wiedwald, C. Dubs, and B. Gökce, *Ultrasmall Yttrium Iron Garnet Nanoparticles with High Coercivity at Low Temperature Synthesized by Laser Ablation and Fragmentation of Pressed Powders*. ChemPhysChem, 2017. **18**: p. 1-9.
133. A. Mergen and A. Qureshi, *Characterization of YIG nanopowders by mechanochemical synthesis*. Journal of Alloys and Compounds, 2009. **478**: p. 741-744.

134. A.C. Thompson, J. Kirz, D.T. Attwood, E.M. Gullikson, M.R. Howells, J.B. Kortright, Y. Liu, A.L. Robinson, J.H. Underwood, K.-J. Kim, I. Lindau, P. Pianetta, H. Winick, G.P. Williams, and J.H. Scofield, *X-Ray Data Booklet*. 3 ed. 2009, Berkeley, CA: Lawrence Berkeley National Laboratory University of California.
135. K.H. Schleifer, D. Schüler, S. Spring, M. Weizenegger, R. Amann, W. Ludwig, and M. Köhler, *The Genus Magnetospirillum gen. nov. Description of Magnetospirillum gryphiswaldense sp. nov. and Transfer of Aquaspirillum magnetotacticum to Magnetospirillum magnetotacticum comb. nov.* Systematic and Applied Microbiology, 1991. **14**(4): p. 379-385.
136. D. Maratea and R. Blakemore, *Aquaspirillum magnetotacticum sp. nov., a Magnetic Spirillum*. International Journal of Systematic Bacteriology, 1981. **31**(4): p. 452-455.
137. M. Posfai, C.T. Lefèvre, D. Trubitsyn, D.A. Bazylinski, and R.B. Frankel, *Phylogenetic significance of composition and crystal morphology of magnetosome minerals*. Frontiers in Microbiology, 2013. **4**(344): p. 1-15.
138. R.B. Frankel, R. Blakemore, and R.S. Wolfe, *Magnetite in Freshwater Magnetotactic Bacteria*. Science, 1979. **203**: p. 1355-1356.
139. X. Zhu, A.P. Hitchcock, D.A. Bazylinski, P. Denes, J. Joseph, U. Lins, S. Marchesini, H.W. Shiu, T. Tyliczszak, and D.A. Shapiro, *Measuring spectroscopy and magnetism of extracted and intracellular magnetosomes using soft X-ray ptychography*. Proceedings of the National Academy of Sciences, 2016. **113**(51): p. E8219-E8227.
140. G.K. Rozenberg, M.P. Pasternak, W.M. Xu, Y. Amiel, M. Hanfland, M. Amboage, R.D. Taylor, and R. Jeanloz, *Origin of the Verwey transition in magnetite*. Physical Review Letters, 2006. **96**(4): p. 045705-1-045705-4.

141. L.R. Bickford, *Ferromagnetic Resonance Absorption in Magnetite Single Crystals*. Physical Review, 1950. **78**(4): p. 449-457.
142. Z. Kaçkol and J.M. Honig, *Influence of deviations from ideal stoichiometry on the anisotropy parameters of magnetite $Fe_{3(1-\delta)}O_4$* . Physical Review B, 1989. **40**(13): p. 9090-9097.
143. E. Lima, A.L. Brandl, A.D. Arelaro, and G.F. Goya, *Spin disorder and magnetic anisotropy in Fe_3O_4 nanoparticles*. Journal of Applied Physics, 2006. **99**(8): p. 083908-1- 083908-10.
144. A. Körnig, M. Winklhofer, J. Baumgartner, T.P. Gonzalez, P. Fratzl, and D. Faivre, *Magnetite Crystal Orientation in Magnetosome Chains*. Advanced Functional Materials, 2014. **24**: p. 3926-3932.
145. A. Fischer, M. Schmitz, B. Aichmayer, P. Fratzl, and D. Faivre, *Structural purity of magnetite nanoparticles in magnetotactic bacteria*. Journal of the Royal Society Interface, 2011. **8**(60): p. 1011-1018.
146. K. Fabian, A. Kirchner, W. Williams, F. Heider, T. Leibl, and A. Huber, *Three-dimensional micromagnetic calculations for magnetite using FFT*. Geophysical Journal International, 1996. **124**: p. 89-104.
147. A.R. Muxworthy and W. Williams, *Critical single-domain/multidomain grain sizes in noninteracting and interacting elongated magnetite particles: Implications for magnetosomes*. Journal of Geophysical Research, 2006. **111**(B12S12): p. 1-7.
148. A. Witt, K. Fabian, and U. Bleil, *Three-dimensional micromagnetic calculations for naturally shaped magnetite: Octahedra and magnetosomes*. Earth and Planetary Science Letters, 2005. **233**(3-4): p. 311-324.

149. A.R. Muxworthy, D.J. Dunlop, and W. Williams, *High-temperature magnetic stability of small magnetite particles*. Journal of Geophysical Research, 2003. **108**(B5, 2281): p. 18-1 - 18-9.
150. DSMZ. *Magnetospirillum magnetotacticum DSM 3856*. 2019 [cited 2019 10/17/2019]; Available from: <https://www.dsmz.de/collection/catalogue/details/culture/DSM-3856>.
151. H.-C. Wu, S.K. Arora, O.N. Mryasov, and I.V. Shvets, *Antiferromagnetic interlayer exchange coupling between Fe₃O₄ layers across a nonmagnetic MgO dielectric layer*. Applied Physics Letters, 2008. **92**(18): p. 182502-1-182502-3.
152. M.P. Melancon, A. Elliott, X. Ji, A. Shetty, Z. Yang, M. Tian, B. Taylor, R.J. Stafford, and C. Li, *Theranostics with Multifunctional Magnetic Gold Nanoshells: Photothermal Therapy and T2* Magnetic Resonance Imaging*. Investigative Radiology, 2011. **46**(2): p. 132-140.
153. Y. Cohen and S.Y. Shoushan, *Magnetic nanoparticles-based diagnostics and theranostics*. Current Opinion in Biotechnology, 2013. **24**(4): p. 672-681.
154. K. Hayashi, M. Nakamura, W. Sakamoto, T. Yogo, H. Miki, S. Ozaki, M. Abe, T. Matsumoto, and K. Ishimura, *Superparamagnetic Nanoparticle Clusters for Cancer Theranostics Combining Magnetic Resonance Imaging and Hyperthermia Treatment*. Theranostics, 2013. **3**(6): p. 366-376.
155. O.L. Gobbo, K. Sjaastad, M.W. Radomski, Y. Volkov, and A. Prina-Mello, *Magnetic Nanoparticles in Cancer Theranostics*. Theranostics, 2015. **5**(11): p. 1249-1263.
156. S. Same, A. Aghanejad, S.A. Nakhjavani, J. Barar, and Y. Omid, *Radiolabeled theranostics: magnetic and gold nanoparticles*. Bioimpacts, 2016. **6**(3): p. 169-181.

157. M.V. Efremova, Y.A. Nalench, E. Myrovali, A.S. Garanina, I.S. Grebennikov, P.K. Gifer, M.A. Abakumov, M. Spasova, M. Angelakeris, A.G. Savchenko, M. Farle, N.L. Klyachko, A.G. Majouga, and U. Wiedwald, *Size-selected Fe₃O₄-Au hybrid nanoparticles for improved magnetism-based theranostics*. Beilstein Journal of Nanotechnology, 2018. **9**: p. 2684-2699.
158. A.S. Garanina, V.A. Naumenko, A.A. Nikitin, E. Myrovali, A.Y. Petukhova, S.V. Klimyuk, Y.A. Nalench, A.R. Ilyasov, S.S. Vodopyanov, A.S. Erofeev, P.V. Gorelkin, M. Angelakeris, A.G. Savchenko, U. Wiedwald, A.G. Majouga Dr, and M.A. Abakumov, *Temperature-controlled magnetic nanoparticles hyperthermia inhibits primary tumor growth and metastases dissemination*. Nanomedicine, 2020: p. 102171.
159. U.K. Cheang and M.J. Kim, *Self-assembly of robotic micro- and nanoswimmers using magnetic nanoparticles*. Journal of Nanoparticle Research, 2015. **17**(3): p. 145.
160. J. Katuri, X. Ma, M.M. Stanton, and S. Sánchez, *Designing Micro- and Nanoswimmers for Specific Applications*. Accounts of Chemical Research, 2017. **50**: p. 2-11.
161. T. Li, J. Li, K.I. Morozov, Z. Wu, T. Xu, I. Rozen, A.M. Leshansky, L. Li, and J. Wang, *Highly Efficient Freestyle Magnetic Nanoswimmer*. Nano Letters, 2017. **17**: p. 5092-5098.
162. W. Chao, P. Fischer, T. Tyliczszak, S. Rekawa, E. Anderson, and P. Naulleau, *Real space soft x-ray imaging at 10 nm spatial resolution*. Optics Express, 2012. **20**(9): p. 9777-9783.
163. W. Kuch, *Magnetic Imaging*, in *Magnetism: A Synchrotron Radiation Approach*, E. Beaurepaire, et al., Editors. 2006, Springer: Berlin, Heidelberg, New York.

164. J. Wu, T. Cheng, C. Lu, X. Zhou, X. Lu, and C. Bunce, *Spin-Dynamic Measurement Techniques in Handbook of Spintronics*, Y. Xu, D.D. Awschalom, and J. Nitta, Editors. 2016, Springer: Dordrecht, Heidelberg, New York, London.
165. D. Rugar, R. Budakian, H.J. Mamin, and B.W. Chui, *Single spin detection by magnetic resonance force microscopy*. *Nature*, 2004. **430**(6997): p. 329-332.
166. K.W. Eberhardt, S. Mouaziz, G. Boero, J. Brugger, and B.H. Meier, *Direct Observation of Nuclear Spin Diffusion in Real Space*. *Physical Review Letters*, 2007. **99**(22): p. 227603-1-227603-4.
167. A. Krasnyuk, A. Oelsner, S.A. Nepijko, A. Kuksov, C.M. Schneider, and G. Schönhense, *Time-resolved photoemission electron microscopy of magnetic field and magnetisation changes*. *Applied Physics A: Materials Science & Processing*, 2003. **76**: p. 863-868.
168. A. Kuksov, C.M. Schneider, A. Oelsner, A. Krasnyuk, D. Neeb, G. Schönhense, C. De Nadaï, and N.B. Brookes, *Investigating magnetization dynamics in permalloy microstructures using time-resolved x-ray photoemission electron microscope*. *Journal of Applied Physics*, 2004. **95**(11): p. 6530-6532.
169. X.M. Cheng and D.J. Keavney, *Studies of nanomagnetism using synchrotron-based x-ray photoemission electron microscopy (X-PEEM)*. *Reports On Progress In Physics*, 2012. **75**(2): p. 026501.
170. R. Wiesendanger, I.V. Shvets, D. Bürgler, G. Tarrach, H.J. Güntherodt, J.M.D. Coey, and S. Gräser, *Topographic and Magnetic-Sensitive Scanning Tunneling Microscope Study of Magnetite*. *Science*, 1992. **255**(5044): p. 583-586.
171. S. Krause, A. Sonntag, J. Hermenau, J. Friedlein, and R. Wiesendanger, *High-frequency magnetization dynamics of individual atomic-scale magnets*. *Physical Review B*, 2016. **93**(6): p. 064407-1-064407-7.

172. S. Loth, M. Etzkorn, C.P. Lutz, D.M. Eigler, and A.J. Heinrich, *Measurement of Fast Electron Spin Relaxation Times with Atomic Resolution*. *Science*, 2010. **329**(5999): p. 1628-1630.
173. L. Reimer and H. Kohl, *Transmission Electron Microscopy Physics of Image Formation*. 5 ed. 2008, New York: Springer.
174. H. Ali, D. Negi, T. Warnatz, B. Hjörvarsson, J. Ruzs, and K. Leifer, *Atomic resolution energy-loss magnetic chiral dichroism measurements enabled by patterned apertures*. *Physical Review Research*, 2020. **2**(2): p. 023330-1-023330-6.

11. List of publications and conference contributions

Peer-reviewed journals:

T. Schaffers, R. Meckenstock, D. Spoddig, **T. Feggeler**, K. Ollefs, C. Schöppner, S. Bonetti, H. Ohldag, M. Farle, and A. Ney, *The combination of micro-resonators with spatially resolved ferromagnetic resonance*. Review of Scientific Instruments, 2017. **88**(9): p. 093703-1-093703-10. Reference [45]

F. Scheibel, B. Zingsem, **T. Feggeler**, R. Meckenstock, D. Spoddig, M. Farle, and M. Acet, *Magnetic anisotropy of single-crystal antiperovskite Mn_3GaC studied by ferromagnetic resonance and dynamic magnetic-response simulations*. Physical Review Materials, 2019. **3**(5): p. 054403-1-054403-5. Reference [52]

T. Schaffers, **T. Feggeler**, S. Pile, R. Meckenstock, M. Buchner, D. Spoddig, V. Ney, M. Farle, H. Wende, S. Wintz, M. Weigand, H. Ohldag, K. Ollefs, and A. Ney, *Extracting the Dynamic Magnetic Contrast in Time-Resolved X-ray Transmission Microscopy*. Nanomaterials (Basel), 2019. **9**(7): p. 1-13. Reference [46]

B. Zingsem, **T. Feggeler**, A. Terwey, S. Ghaisari, D. Spoddig, D. Faivre, R. Meckenstock, M. Farle, and M. Winklhofer, *Biologically encoded magnonics*. Nature Communications, 2019. **10**: p. 4345. Reference [11]

N. Josten, **T. Feggeler**, R. Meckenstock, D. Spoddig, M. Spasova, K. Chai, I. Radulov, Z.A. Li, O. Gutfleisch, M. Farle, and B. Zingsem, *Dynamic unidirectional anisotropy in cubic FeGe with antisymmetric spin-spin-coupling*. Scientific Reports, 2020. **10**(2861): p. 1.

S. Pile, **T. Feggeler**, T. Schaffers, R. Meckenstock, M. Buchner, D. Spoddig, B. Zingsem, V. Ney, M. Farle, H. Wende, H. Ohldag, A. Ney, and K. Ollefs, *Non-standing spin-waves in confined micrometer-sized ferromagnetic structures under uniform excitation*. Applied Physics Letters, 2020. **116**(7): p. 072401-1-072401-5. Reference [30]

Submitted manuscripts / Preprints submitted to arXiv:

B. Zingsem, **T. Feggeler**, R. Meckenstock, T. Schaffers, S. Pile, H. Ohldag, M. Farle, H. Wende, A. Ney, and K. Ollefs, *Evaluation protocol for revealing magnonic contrast in STXM-FMR measurements*. arXiv:1901.10595 [cond-mat.str-el] (2019). Reference [103]

T. Feggeler, R. Meckenstock, D. Spoddig, C. Schöppner, B.W. Zingsem, T. Schaffers, H. Ohldag, H. Wende, M. Farle, A. Ney, and K. Ollefs, *Direct visualization of dynamic magnetic coupling in a Co/Py bilayer with picosecond and nanometer resolution*. arXiv:1905.06772 [cond-mat.mes-hall] (2020). Reference [48]

T. Feggeler, R. Meckenstock, D. Spoddig, B. Zingsem, H. Ohldag, H. Wende, M. Farle, M. Winklhofer, and K. Ollefs, *Spatially resolved imaging of GHz magnetization dynamics of a magnetic nano-particle chain inside a magnetotactic bacterium*. 2020. Submitted to ACS Nanoletters 2020.

Patents:

B. Zingsem (30 %), M. Farle (10 %), **T. Feggeler (30 %)**, and I. Iglesias (30 %), *Tubular nanosized magnetic wires with 360° magnetic domain walls*, **United States Patent No.** US 10,614,902 B1, **Assignee:** Universität Duisburg-Essen (Essen, DE), **Current CPC Class:** G11C 19/0808 (20130101); G11C 11/155 (20130101); G11C 11/161 (20130101); G11C 11/14 (20130101); G11C 11/1675 (20130101); G11C 11/1673 (20130101), **Current International Class:** G11C 19/02 (20060101); G11C 19/38 (20060101); G11C 11/14 (20060101); G11C 19/08 (20060101); G11C 11/16 (20060101), United States (2020).

Conference contributions:

I. Iglesias, **T. Feggeler**, Zi-An Li, A. Terwey, M. Farle (2016). *Magnetic nanoparticles and core/shell micro- and nanowires: experiment and MuMax3 simulations*, poster presented at Cenide annual celebration, Essen, Germany.

T. Feggeler, R. Meckenstock, Zi-An Li, D. Spoddig, I. Radulov, K. Skokov, O. Gutfleisch, M. Farle (2017). *Temperature dependent Ferromagnetic Resonance of FeGe samples*, poster presented at 633. Wilhelm und Else Heraeus-Seminar “Spin Orbit Dynamics”, Bad Honnef, Germany.

T. Feggeler, R. Meckenstock, D. Spoddig, I. Radulov, K. Skokov, O. Gutfleisch, Zi-An Li, M. Farle (2017). *Dzyaloshinskii-Moriya Interaction in FeGe samples: Ferromagnetic resonance and micromagnetic simulations*, poster presented at 2017 DPG spring conference, Dresden, Germany.

T. Feggeler, T. Schaffers, S. Pile, B. Zingsem, C. Schöppner, R. Meckenstock, D. Spoddig, H. Ohldag, A. Ney, M. Farle, H. Wende, K. Ollefs (2019). *Element specific time resolved visualization of spin wave modes with 50 nm resolution using Scanning Transmission X-ray Microscopy Ferromagnetic Resonance*, talk presented at 2019 Joint MMM-Intermag Conference, Washington DC, United States.

T. Feggeler, B. Zingsem, A. Terwey, M. Winklhofer, R. Meckenstock, M. Farle, H. Wende and K. Ollefs (2019). *Micromagnetic simulations for static and dynamic characterization of a linear chain of 20 magnetite nanoparticles*, talk presented at 2019 DPG spring conference, Regensburg, Germany.

T. Feggeler, B. Zingsem, R. Meckenstock, H. Ohldag, M. Farle, H. Wende and K. Ollefs (2019). *Magnetization dynamics of a single Fe₃O₄ nanoparticle chain using Scanning Transmission X-ray Microscopy Ferromagnetic Resonance and micromagnetic simulations*, poster presented at the SpinS Workshop 2019, Mülheim a. d. Ruhr, Germany.

T. Feggeler, B. Zingsem, R. Meckenstock, H. Ohldag, M. Farle, H. Wende and K. Ollefs (2019). *X-Ray detected Ferromagnetic Resonance of a single Fe₃O₄ nanoparticle chain in Magnetospirillum Magnetotacticum*, Poster presented at the IAMnano Workshop, Düsseldorf, Germany.

T. Feggeler, B. Zingsem, R. Meckenstock, M. Winklhofer, D. Spoddig, H. Ohldag, A. Ney, M. Farle, H. Wende and K. Ollefs (2019). *Magnetization dynamics of magnetotactic bacteria characterized by ferromagnetic resonance, micromagnetic simulations and scanning transmission x-ray microscopy ferromagnetic resonance*, talk presented at 2019 MMM conference, Las Vegas, United States.

T. Feggeler, B. Zingsem, R. Meckenstock, M. Winklhofer, D. Spoddig, H. Ohldag, A. Ney, M. Farle, H. Wende and K. Ollefs (2020). *Biomagnonic logic device concepts: A new approach to spintronics?*, poster presented 710. Wilhelm und Else Heraeus-Seminar "Spin Transport in Complex Magnetic Structures", Bad Honnef, Germany.

T. Feggeler, B. Zingsem, R. Meckenstock, M. Winklhofer, D. Spoddig, H. Ohldag, M. Farle, H. Wende and K. Ollefs (2020). *Scanning Transmission X-ray Microscopy detected Ferromagnetic Resonance as technique for the characterization of biomagnonic logic devices*, poster presented at 2nd CENIDE Conference, Bergisch Gladbach, Germany.

DuEPublico

Duisburg-Essen Publications online

UNIVERSITÄT
DUISBURG
ESSEN

Offen im Denken

ub | universitäts
bibliothek

Diese Dissertation wird über DuEPublico, dem Dokumenten- und Publikationsserver der Universität Duisburg-Essen, zur Verfügung gestellt und liegt auch als Print-Version vor.

DOI: 10.17185/duepublico/73563

URN: urn:nbn:de:hbz:464-20201210-154918-3

Alle Rechte vorbehalten.